A MONITORING AND MODELLING LED INVESTIGATION INTO THE DEBRIS FLOW GEOHAZARD IN THE WEST OF SCOTLAND

BRADLEY SCOTT SPARKES

Ph.D.

2019

A MONITORING AND MODELLING LED INVESTIGATION INTO THE DEBRIS FLOW GEOHAZARD IN THE WEST OF SCOTLAND

BRADLEY SCOTT SPARKES

A thesis submitted in partial fulfilment of the requirements for the award of Doctor of Philosophy of the University of Northumbria at Newcastle

This research was undertaken in the Department of Geography Faculty of Engineering and Environment

August 2019

Abstract

Debris flows are a particularly disruptive form of mass movement due to their ability to propagate at high velocities over large distances, to increase in magnitude through erosion and entrainment and to inflict large impact pressures. A number of recent events in Scotland have resulted in widespread disruption and damage, including road closures that require expensive repairs and mitigation installations. Climatic forecasts suggest that such events could become more commonplace.

Scotland's hillslopes afford a rare opportunity to observe interacting processes from source to sink, over a relatively short elevation range. This study uses a combination of monitoring, modelling and mapping to investigate the factors driving debris flows, to characterise the geohazard and to gain insight into debris flows within a wider geomorphological context

Monitoring data encompasses multiple changes over three study sites, particularly a period of intense storminess (winter 2015), during which three major slope failures each in excess of 300 m^3 occurred at the primary study site the Rest and be Thankful. A lack of high frequency and low-magnitude changes at all sites suggests that precursory changes, such as progressive gully loading, may be less significant than first considered. Instead, larger magnitude, low frequency slope failures appear critical for loading channels for future entrainment. Using a combination of primary and secondary data, this study also demonstrates the ability for debris flows to directly scour and develop new gully systems and increase in magnitude via this mechanism.

The runout model RAMMS-DF was found to effectively model the effect of convergent topography on debris flow runout magnitude and direction, proving it to be a useful tool for the appraisal of mitigation efforts, such as catch net distributions. The continuum model however struggled to model channelization, not accounting for rheological changes occurring when flows enter areas containing hydrological flow. Nonetheless, a combination of monitoring and modelling demonstrates that source location relative to topographic confinement, channelisation and entrainment form major components of the debris flow geohazards.

Modelling of observed ephemeral drainage has highlighted the significant interconnectivity of shallow failures with slope drainage. It is hypothesised that such interconnectivity may be significant in triggering slope failures, as well as the subsequent incision of gullies.

Furthermore, periodic drainage switching may explain an observed propensity for spatial clustering of slope failures.

Synthesis of these findings highlight the role of debris flows within a geomorphic continuum and presents a conceptual model which hypothesises that successive scouring debris flows connect to rapidly form long gully systems, a mechanism of paraglacial sediment evacuation. At the Rest and be Thankful, recent debris flow activity towards the centre of the slope, and resultant gully development, may be acting to increase the gully density and match that of other slope areas where the gullies are already well developed. Low gully maturity may therefore be indicative of a future hazard. These findings call for hazard management and mitigation approaches to better account for drainage pathways and sediment cascade mass balances.

Table of contents

Table of figures

Table of tables

List of interchangeable detected change codes

Change name (Acronym)	**Alternative code**
Storm Desmond Landslide1 (SDLS1)	RabT1C
Storm Desmond Landslide 2 (SDLS2)	RabT1B
Storm Frank Landslide 1 (SFLS1)	RabT1A

List of abbreviations

Abbreviation	Full length text
AOI	Area of interest
CANUPO	CAractérisation de NUages de Points (point cloud vegetation classifier/algorithm)
C2C	Cloud-to-Cloud
C2M	Cloud-to-Mesh
DEM	Digital Elevation Model
dGPS	Differential Global Positioning Systems
DoD	DEM of difference
ERT	Electrical Resistivity Tomography
FOV	Fields of View
GC	Glen Coe
GCP	Ground Control Point
GO	Glen Ogle
GPR	Ground Penetrating Radar
I2I	Interval to interval
ICP	Iterative Closest Point
IDW	Inverse Distance Weighted
InSAR	Interferometric Synthetic Aperture Radar
LGM	Last Glacial Maximum
LoD	Level of Detection
M3C2	Multiscale Model to Model Cloud Comparison
MSA	Multi Station Adjustment
MTA	Multi Time Around
PDF	Probability Density Function
Quick Terrain Modeler	QT
RabT	Rest and be Thankful
RAMMS-DF	Rapid Mass Movement Simulation (software)
RMS	Root Mean Squared
RSS	Root Sum Squared
SLOPOV	Special Law of Propagation of Variances
SRRB	Scottish Road Research Board
SfM	Structure from Motion
SRNLS	Scottish Road Network Landslide Study
TIN	Triangulated irregular network
TLS	Terrestrial Laser Scanning
UAV	Unmanned Aerial Vehicle

Acknowledgements

I would first like to thank my supervisors, Dr Mike Lim, Dr Stuart Dunning and Prof John Woodward for their invaluable expertise and support throughout this project. Thank you first to Mike for your involvement in this project from its inception and for stepping up as my first supervisor. Your unwavering support and care throughout have made all the difference in me completing this mammoth undertaking. Stuart, your enthusiasm and support from my time as a young undergraduate was one of the main reasons I chose to pursue this PhD. At times I have questioned myself and this pursuit, but I'm now glad I made the decision and stuck with it, due in no small part to your advice. I have grown both as an academic, but also as a person, and will forever be grateful for your reassurance when it was needed. John, I would sincerely like to thank you for climbing aboard my project when the time demanded it. You have consistently helped me to see the bigger picture and I particularly owe a lot to you for helping me in the final push to submission.

I would like to thank the Transport Research Laboratory (TRL), in particular Professor Mike Winter, for their continued support of this project from its conception to completion. I have thoroughly enjoyed the opportunity to work closely with Mike Winter, particularly out in the field. I deeply appreciate your input into the number of reports we have written, and of course my thesis. Throughout the process your constructive advice has developed my report writing skills, particularly for an industry audience, which should prove invaluable in my career. I would also like to thank the Scottish Road Research Board (SRRB) who helped to fund this research and would like to thank Transport Scotland for their support and involvement throughout. Thanks also to my external supervisor Dr Nick Rosser at Durham University. I am very grateful for your support with technical training in the early stages of my project, as well as your assistance in the field and in processing data.

A big thank you in particular to Tom, Mark and Rupert for your assistance with fieldwork, as well as generally keeping spirits high in the office. Mark, you have helped me climb a mountain (literally and figuratively) during this project, so particular thanks to you for being a great friend. Thank you also to Mike and Emily for putting up with me for a whole year where it really mattered! I'm glad that we've been able to support each other and that we have formed a great friendship in the process. Thank you also to everyone who has come and gone in the PGR office and throughout the department. Shout outs to Mark, Rupert, Tom, Steph, Jack, Sina, Kate, Flavia, Mike, Pete, Scott and Clare for some great memories. I

may have complained about the distractions at times, but I wouldn't have changed anything and am thankful that we were able to help maintain one another's sanity (at times).

Thank you to my family, particularly my mum and dad, for your love and support. There have been times where I've wanted to pack this whole thing in, but your words of advice were pivotal in me sticking the course! I know now, that I wouldn't have forgiven myself for giving up. I would like to dedicate this thesis to the memory of my old friend Callum Westbrook who sadly passed away last year. His passing has reminded me of what's important in life. Friendship, love and laughter. To my old school friends Niall, Rory and Sam, you have been amazing, particularly following this tragic loss and at the most difficult time in my life. Thanks for continuing to make me laugh!

Last, but by no-means not least, I would like to thank my amazing partner of eight years, Olivia. Completing this project has been a great challenge, made even harder by our distance apart. Whilst this project has strengthened my individual character, I feel the whole undertaking has strengthened our bond as a couple. I know that I wouldn't have been able to complete this project if it wasn't for your unassuming support and patience, for which I will always be grateful. I hope this hard work, on both fronts, benefits us both in the years to come.

Declaration

I declare that no outputs submitted for this degree have been submitted for a research degree of any other institution. I also confirm that this work fully acknowledges opinions, ideas and contributions from the work of others.

Any ethical clearance for the research presented in this commentary has been approved.

Approval has been sought and granted by the University Ethics Committee in 2016 (RE-EE-14-141216-54902ae3acadd).

I declare that the Word Count of this Commentary is 48,613 words

Name: Bradley Scott Sparkes

Signature:

Date: 04/08/2019

CHAPTER 1

Introduction

Landslides occur worldwide and can be the cause of death, displacement, costly disruption and damage. Transport infrastructure is particularly vulnerable to landslides, with road and rail networks in the UK having suffered disruption in recent years. In remote, rural areas road networks are essential and alternative routes may be lacking or considerably increase journey times. Debris flows have been identified as the predominant cause of landslide disruption to Scottish road infrastructure (Winter *et al.*, 2005), particularly along trunk roads which connect remote communities. Some 77,779 deaths worldwide have been attributed directly to debris flows in the period 1950 to 2011 (Dowling and Santi, 2014), although the actual count may be higher due to the common association of mass movement consequences with triggering mechanisms, such as earthquakes and storms (Petley, 2012). Whilst debris flows have proved disruptive in Scotland over recent years, their high frequency affords a unique opportunity to examine a rarely observed phenomenon in the natural environment, of which this thesis aims to capitalise on in order to better understand the geohazard.

Most shallow landslides and debris flows are triggered by intense rainfall (Guzzetti *et al.*, 2005), often during storm events. Current climate change forecasts indicate that the incidence of intense rainfall events may increase in the UK, which could lead to an increase in sediment mobilisation and debris flows (Winter and Shearer, 2015). Kovanen and Slaymaker (2015) remark that an upturn in the number of noted natural hazard events may mark the beginning of a new disturbance regime, however the role of climate change in this is uncertain. Intermittent renewal of glacigenic sediment reworking have been triggered by factors such as anomalous climatic events, raising uncertainty about the longevity of the paraglacial period (Cossart, 2008) which has previously been considered over no more than 10^3 year timescales (Church and Slaymaker, 1989).

Previous studies have quantified erosion and deposition of sediment emerging from catchment termini (Schurch *et al.*, 2011a; Schürch *et al.*, 2011b) and much is known about the relative efficiencies of hillslope and channelised debris flows (Iverson, 1997). Entrainment is known to increase debris flow magnitudes when propagation occurs through channels for instance (Milne, 2008; Iverson, 2014), however there is uncertainty about the process by which these accumulations have come to reside. Curry (1998) and Martin *et al.*

(2017) attribute gully accumulations to sidewall processes however the relative contribution and timing of this source, prior to or triggered by a passing flow for example, is unclear. Further still, many investigations have focused on the large magnitude primary reworking of glacigenic sediment, however little attention has been paid to later renewed or delayed sediment reworking, small sediment mobilisations and potentially temporarily disconnected secondary stores.

The magnitude of a debris flow influences the hazard intensity and the probability of encounter, both important elements of a Quantitative Risk Assessment (QRA), thus derivation of a magnitude-frequency relationship can be invaluable (Hungr *et al.*, 2008). Knowledge of when and where debris flows will occur, as well as their size, speed and runout path are also crucial to effective hazard assessments (Iverson, 2014). Debris flow hazard assessments commonly rely on the assumption that a supply of sediment is inexhaustible and may therefore overstate the hazard of an area in which the supply of material is dwindling (Glade, 2005) and not consider an area where accumulation may be taking place. Potential sources of material, temporary stores and recharge zones require consideration, as these can influence eventual debris flow magnitudes (Bovis and Jakob, 1999). Entrainment has long been recognised as a significant factor in the final debris flow magnitude and thus hazard (Benda and Cundy, 1990) and such behaviour has been reported in Scottish debris flows by Winter et al. (2006) and Milne et al. (2010). Knowledge of debris flow magnitude and frequency can also form a rational basis for the design and implementation of mitigation structures, which are increasingly being utilised in Scotland, as well as providing inputs into landscape evolution models (Bovis and Jakob, 1999). The rates and variability of sediment production, storage and transport in debris flow catchments, are particularly unclear and have not received sufficient study (Berger *et al.*, 2011; Schurch *et al.*, 2011). A better understanding of these patterns would significantly aid our understanding of the debris flow geohazard.

The lack of a continuous record of landslides is cited as one of the main shortcomings of quantitative hazard assessments (van Westen *et al.*, 2005; Corominas *et al.*, 2014). In alpine basins, the frequency of debris flows is enough to represent a significant risk to infrastructure, but typically not enough to yield sufficient monitoring data over a short time (Marchi *et al.*, 2002). Characterisation of slope failures, particularly via quantification, has also been limited by difficulties in accessing the steep terrain upon which they manifest (Bennett *et al.*, 2012). Much like the surge in activity immediately after deglaciation (Curry, 1998), the renewal and recent upturn of slope activity in the Scottish Highlands provides a

rare opportunity to observe and characterise the role of debris flows as an agent of paraglacial denudation and landscape evolution. Recently active sites, among others, include Dunkeld, the Rest and be Thankful, Cairndow, Glen Ogle, Invermoriston and Glen Kinglas (Winter et al. 2005; 2006; 2009). Unlike many active debris flow sites in continental Europe, such as the Illgraben torrent in Switzerland for example, such sites afford a unique opportunity to observe the debris flow phenomena, encompassing geomorphic activity from source-to-sink, with relative ease.

In the face of climatic uncertainty, this study aims to further characterise debris flow phenomena, the hazard and related processes to better inform future management and understanding. The principal role of this chapter is to review the current understanding of the debris flow phenomenon and the other geomorphological processes and forms with which it interacts.

1.1 Landslides

Landslides are a major agent of landscape evolution, denuding slopes of material ranging in size from small particles to entire mountain sides and submarine coastal shelfs. Landslides act under the influence of gravity to efficiently erode hillslopes (Korup *et al.*, 2007) until they reach some form of equilibrium. The earth surface is however continually perturbed by a range of agents, from tectonic activity and glaciation to climatic changes and human influences. Landslides are most prevalent in active mountainous regions such as the Himalayas and New Zealand, where earthquakes and seasonal rainfall are common triggers. Slope activity is also frequent in glaciated environments, where a complex combination of processes over different timescales, such as freeze-thaw and melt induced rises in hydrostatic pressure (Haeberli *et al.*, 1997), degrade rock slopes.

To a lesser degree slope failures are still common in regions exposed to relatively gentle processes such as fluvial erosion and weathering. Recently exposed rock faces have been found to be more vulnerable to failure after the unloading of ice, as residual stress release takes place, with particular concentrations across internal joints and the development of sheeting joints (Wyrwoll, 1977; Hencher *et al.*, 2011; McColl, 2012)**.** Such stress releases can lead to failures immediately during and after deglaciation, but lags can also occur depending on the rock characteristics (Wyrwoll, 1977). Lag times of more than 5 kyr have been noted by Ballantyne *et al.* (1998, 2014) in Scotland, although glacio-isostatic rebound, seismic activity and gravitational spreading are also considered to be influential. More pronounced lags have also been observed and are anticipated (Le Roux *et al.*, 2009; Sanchez *et al.*, 2010;

McColl, 2012; Ballantyne and Stone, 2013; Ballantyne *et al.*, 2014; Cossart *et al.*, 2014; Coquin *et al.*, 2015). Many deglaciated environments are also laden with material from times of extensive glacial erosion. Glacial till which sat at the base of the ice is found in-situ as a veneer across many landscapes and material which previously failed onto the surface of a glacier can also be found after melt has lowered it onto lower slopes, often as stacked lateral moraines (Ballantyne, 2008), reassembling it back on the hillslope so it can perhaps fail again. Compared to events such as rock slope failures, mobilisation of these deposits is considered a secondary process (McColl, 2012).

1.1.1 Debris flows

1.1.1.1 Classification

The definition of a debris flow has been subject to much debate. Today, the most commonly accepted classifications stem from the work of Varnes (1954, 1978) who classified mass movements firstly based upon their constituent material and secondly the mechanism of propagation influenced by gravity. The definition of the term 'slide' is implicit, however the term 'flow' can easily be confused with similar failure mechanisms such as avalanches. Takahashi (2014) characterises a flow as the irreversible shearing deformation throughout the entirety of a mass. In comparison, an avalanche undergoes less deformation, under the influence of lower saturation levels, with no obvious sorting occurring (Hungr *et al.*, 2001).

Delineation between material types, for example what constitutes 'mud' or 'debris', has also been a matter of discussion. Hungr *et al.* (2013) differentiate between these two examples, stating that the former often contains a high proportion of clay, making it characteristically plastic, whereas the latter contains an unsorted mixture of sand, gravel, cobbles and boulders as well as other fine materials. In contrast to 'earth' which is considered to contain less than 20% coarse material (Hungr *et al.*, 2001), 'debris' has a greater volume of coarse material, roughly 50%, the definition of coarse being sediment with a diameter greater than 2mm (Varnes, 1978).

Debris flows are characteristically similar to 'hyperconcentrated flows', however the latter contains a higher proportion of fluid and therefore travels under a greater influence of fluid mechanics (Pierson and Costa, 1987), whereby minimal inter-particle interactions and friction occur. Many researchers have since employed a 50-60% solids volume as a threshold to delineate between the two (Pierson and Scott, 1985; Pierson and Costa, 1987; Iverson, 1997; Vallance and Scott, 1997), below which flows can be described as hyperconcentrated. Takahashi (2014) however cites debris flows in Japan with solid volume concentrations as low as 35%, thus confusingly suggesting that a flow heavily dominated by fluid may be regarded as a debris flow. Pierson (2005) cautions that sediment concentration alone cannot be used to delineate between debris flow and hyperconcentrated flow for example, stating that grain size distribution and grain density are also important. Furthermore, it is worth noting that a landslide may transition backwards and forwards between different flow types, particularly as a result of entrainment, with no limit on the number of transitions in a single event.

For the purposes of this research, a debris flow is considered to predominantly consist of heterogeneous solids (Hungr et al., 2001), with a smaller proportion of fluid. Irrespective of the solid to fluid ratios used for classification, it is the significant quantity of water that permits debris flows to be highly mobile, travel at extremely rapid velocities in excess of 10 m/s, and to cover very large runout distances (Varnes, 1978; Cruden and Varnes, 1996; Hungr et al., 2014; Iverson, 2014), even on low slope angles. This combination of speed with the capacity to carry large clasts and boulders enables debris flows to inflict strong impact pressures upon contact, underpinning the significant threat debris flows pose to people and infrastructure.

Recent work has also sought to subcategorise debris flows themselves. Takahashi (1991, 2014) recognises three principal forms of debris flow, namely; stony-type flows, turbulent-muddy-type flows and viscous flows. Classification between sub-types of flow is based upon the ratio of three controlling factors, namely the Reynolds number, Bagnold number and Relative depth, which are summarised in figure 1.1.

Immature debris flows are representative of two-phase flows, diverting from a single macro-scale rheological classification, although this is perhaps considered a more realistic representation of flow conditions (Larcan *et al.*, 2006; Iverson and Ouyang, 2015). Such flows

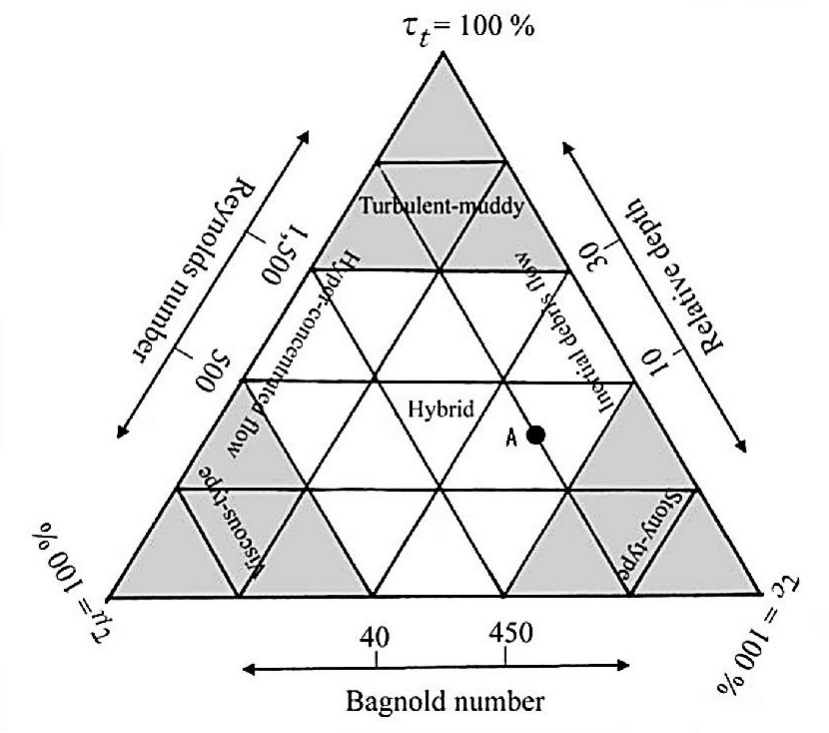

Figure 1.1 - Classification scheme for debris flow sub-types. The area marked A represents hybrid- flow somewhat resembling a stony-type flow. (Takahashi, 2014)

include the plug-type flow, in which non-submerged particles can override a flow otherwise described as mature (Armanini *et al.*, 2005) (figure 1.2). A single classification is not always suitable for the entirety of an event however, both in terms of full landslide categories and debris flow sub-categories, as landslides may initiate as one form but develop into another (Hungr *et al.*, 2014), a factor which can undermine modelling attempts.

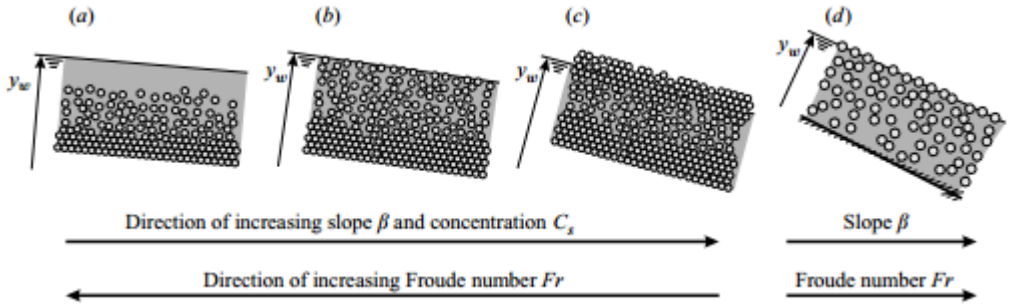

Figure 1.2 - Typologies of debris flow as described by Armanini et al. (2005) including (a) loose bed, immature flow (b) loose bed, mature flow (c) loose bed, plug flow and (d) solid bed flow.

Debris flows typically occur across three successive areas, namely the initiation, transport and deposition zones (Hungr, 2005). The abundance of often unconsolidated and over steepened regolith provides the ideal conditions for loose avalanche and flow like failures to initiate upslope. Material availability is in fact considered one of the fundamental prerequisites for debris flow occurrence (Zimmermann *et al.*, 1997; Bovis and Jakob, 1999; Helsen *et al.*, 2002; Ballantyne, 2004; Glade, 2005; Brayshaw and Hassan, 2009). Slope gradient is also a significant factor in debris flow occurrence, controlling the magnitude of shear stress. Debris flows usually occur on slopes angles above 30° (Ballantyne, 1981, 1986; Innes, 1983; Curry, 1998) and do not typically occur above angles of 46° (Innes, 1983) due to an inability for unstable material to reside at such angles for a significant period of observable time (Heald and Parsons, 2005). Localised topographic hollows may also concentrate hydrogeological and hydrological flow, resulting in locally elevated saturation levels and the frequent initiation of shallow failures (Matsushi, Hattanji and Matsukura, 2006; Sidle and Bogaard, 2016). While steep slopes increase the likelihood of landsliding, the presence of certain vegetation types can increase slope stability by intercepting rainfall and drawing water from the soil, providing matric suction and root binding of the soil. Furthermore in 72% of the cases studied by Guthrie *et al.* (2010) forest cover was found to arrest debris flow mobility within 50 m. Over mature trees and shallow rooted vegetation introduce instability.

Gullies and slope depressions are features particularly prone to landslides due to localised oversteepening and the propensity for persistent locally elevated groundwater levels. Gully

formation has been observed in the sediment mantled slopes of Svalbard immediately following deglaciation, thus representing a form of paraglacial sediment reworking distinct from debris flows (Mercier *et al.*, 2009). Gullies can also magnify debris flow magnitudes, due to significant aggradations of quasi-stable material which can potentially become entrained.

1.1.2 Material properties and structures

Sediment and soil characteristics exert a strong influence over slope stability. As debris flows are usually facilitated by block failure in the source area, the Factor of Safety (FoS) approach offers a simplified explanation for the initiation of such events. This approach accounts for the balance of shear strength with shear stress. The FoS approach is expressed as:

$$F = \frac{s}{\tau}$$

Equation 1

whereby s is the shear strength of soil and τ is the shear stress. When the shear stress value exceeds that of shear strength, the FoS value would be less than 1 and therefore failure is assumed to occur. In contrast, greater shear strength than shear stress results in a FoS value greater than 1, and thus stability is assumed.

The Mohr-Coulomb criterion expresses the components of shear strength (s) as:

$$s = (\sigma - p)\tan\varphi + c$$

Equation 2

where (σ-p) represents the effective normal stress, ϕ is the cohesionless friction angle and c is cohesion. As can be seen, the equation accounts for the impact of pore pressures (p) by subtracting these from the normal stress (σ) to give an effective stress value. If the pore pressure value increases, the overall shear stress value decreases as particles are pushed apart and no longer lock together as effectively. The second element of the equation, cohesion, is directionless and represents the strength of bonds between particles.

The key characteristics that predispose a soil to failure range from microstructures such as soil particle arrangement and inter-particle bonds to mesostructures such as tension cracks, and macrostructures such as major heterogeneities (D'Elia *et al.*, 1998; Leroueil, 2001). The hydraulic conductivity of a soil, the rate at which it is able to draw in water from sources such as rainfall or snow-melt, also determines material response when exposed to an influx of fluid (Reid *et al.*, 1997) due to different rates in pore pressure rises which reduce the effective shear stress.

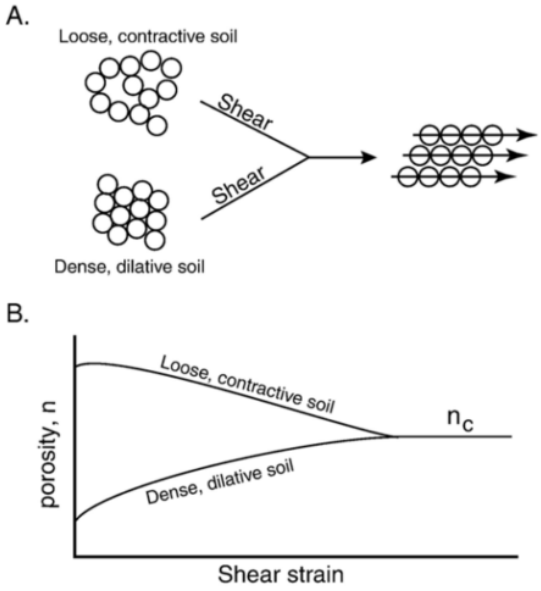

Figure 1.3 - Critical state porosity: contraction and dilation (Gabet and Mudd, 2006)

High porosity soils have larger water retention capacities, and thus can subdue rapid rises in pore pressures at shear surfaces, generally at the interface between soil and bedrock (Mukhlisin *et al.*, 2006). Soil density also influences shear behaviour, with denser soils requiring higher pore pressures than loose soils before mobilisation can occur (Iverson, 2000). These critical state responses arise due to dilation in dense soils (Reynolds, 1886) which can inhibit complete failure and only result in small episodic movements (Schulz *et al.*, 2009) and contraction of loose soils which has a positive feedback effect on pore pressures (Schofield and Wroth, 1968; Iverson, 2005a). Several studies have however shown that natural and experimental debris flows can propagate from dense soils, whereby dilation initially arrests movement, but a secondary onset of contraction occurs stimulating increases in pore pressures by much the same mechanism as in loose soils (Fleming *et al.*, 1989; Gabet and Mudd, 2006; Iverson *et al.*, 2010). Matric suction, or negative pore pressures, have been shown to contribute significantly to a slope's shear strength and thus the Factor of Safety

(Rahardjo *et al.*, 1995; Fredlund *et al.*, 1996). At larger scales, cracks and macropores increase the hydraulic-conductivity of a slope or slope region, resulting in rapid pore pressure rises at soil and bedrock interfaces (McDonnell, 1990). Features such as tension cracks can arise as a result of gradual reductions in shear strength and creep or by sudden stressors such as earthquakes (Mitchell *et al.*, 2005).

The development and collapse of preferential drainage networks, such as soil pipes, can lead to sudden rapid rises in pore water pressures, triggering failures in areas that might otherwise be considered stable (Pierson, 1983; Uchida *et al.*, 2001). Soil pipes are thought to develop due to a multitude of different processes, from drainage exploitation of animal burrows, linking of macropores that have developed due to vegetation root growth and decay, or weather related expansion and contraction (Lu and Godt, 2013). Soil pipes also range in size, from long continuous networks to sub-metre scales (Sidle *et al.*, 2001; Sidle and Bogaard, 2016). A study by Jones *et al.* (1997) found that almost 30% of Britain could be susceptible to soil pipe erosion, with upland areas such as the Western Scottish Highlands covered in the soils most susceptible to piping. Observations of pipes emerging from landslide headscarps has led to theories that preferential flow directly into source areas may be a triggering mechanism (Pierson, 1983). Soil pipes may also lead to the development of visible gullies, via collapse and continued routing of flow through the remaining depression (Swanson *et al.*, 1989; Faulkner, 2006; Wilson *et al.*, 2013). Macropores can introduce instabilities, particularly where multiple flow routes converge (Sidle and Bogaard, 2016), however natural pipe flows and similar man-made drainage systems have also been found to effectively reduce susceptibility to failure by also dissipating elevated pore water pressures (Uchida, 2004; Sun *et al.*, 2010).

In addition to soil structures, soil or drift composition can significantly influence the likelihood of failure, a factor that some engineers have capitalised on to artificially benefit stability (Rahardjo *et al.*, 2008). Milne *et al.* (2012) for example found that a higher silt fraction enables a soil to sustain larger increases in pore water pressure prior to shearing. Variations in grain size distribution have also been found to influence the mechanism of failure (Xenaki and Athanasopoulos, 2003) with flow slides found to arise from finer sands as opposed to retrogressive failure in coarser sand (Wang and Sassa, 2003). The presence and ratio of fine particles, such as clay, can significantly influence the shear strength of a soil (Stark and Eid, 1994). Chen *et al.* (2010) for example found that gravel soils with moderate clay contents (5-10%) required less rainfall to trigger when compared with soils containing low (2.2-5%) and high (>10%) clay contents.

Abundant debris flow activity in Scotland has been observed on slopes mantled with coarser grained regoliths, which may be attributed to the higher permeability of the soils and therefore their potential for rapid pore pressure increases (Ballantyne, 1986). Soil composition is largely influenced by the origin rock and influences a number of factors from grain sizes to mineral content (Trenter, 1999; Winter *et al.*, 2017). The surface on which such deposits reside can be just as significant as the composition of the material itself. Underlying lithologies of high permeability may facilitate enhanced drainage, dissipating pore pressure increases at the soil and rock interface. Impermeable rock surfaces enable fluid accumulation, particularly in topographic depressions, leading to the development of large pore pressures (Harp *et al.*, 1990; Matsushi *et al.*, 2006) and a resultant reduction in shear strength. Whilst such characteristics can aid interpretation of slope stability, particularly through lab and flume experiments, natural heterogeneities, which themselves can influence stability, are often not accounted for (Sidle and Bogaard, 2016). Heterogeneity of soil properties over a hillslope scale may impact hydrology and therefore introduce variations in slope stability (Fan *et al.,* 2016a).

1.1.3 Preparatory factors

Variations over time and space are essential considerations when analysing landslide risk (Van Asch *et al.*, 1999). Prepatory factors can be considered over a range of time frames. Whilst rainfall has an impact on the transient and seasonal stability of a slope or slope area, over longer time periods the general stability of these areas can be considered to be deteriorating or 'ripening' due to multiple factors such as weathering and jacking by vegetation roots (Nettleton *et al.*, 2005). Weathering acts to change the soil properties, affecting shear strength and the susceptibility to failure. One such mechanism may include progressive pedogenesis or podzolisation, by which migration of minerals or organic matter within a soil mass may alter its hydraulic transmissivity and therefore how it responds to a subsequent storm (Ballantyne, 2004). Brooks et al. (1995) conceptualised the reduced stability of a mature soil strata, relative to an early Holocene soil profile, due to the development of a dominant illuvial B-horizon at a depth of around 0.3 – 1 m below the surface. This lower permeability layer, which does not exist within the early Holocene profile, enables elevated pore water pressures to develop and has also previously been found to enable development of macropores containing lateral subsurface flows (Ghestem et al., 2011).

Soil shear strength may reduce as a result of ice swelling (Fang, 1991) and freeze thaw cycles (Qi *et al.*, 2008). Clay-rich regoliths may also arise from the fracture and shearing of

metamorphic rocks (Sidle and Bogaard, 2016), creating heterogeneities or shifting the aforementioned clay ratio of existing soil and thus potentially altering its hydrological response. Lourenço *et al.* (2006) found during flume experiments that the washout of sands, a process that can occur in soil masses over long time scales, led to initiation of failures. Pedogenesis also progressively alters the hydraulic transmissivity of a soil over longer timescales, increasing susceptibility to failure due to the rapid intake of water (Ballantyne, 2004). The addition of organic material to soil can both increase and decrease susceptibility to failure (Ekwue, 1990).

Wildfires have been found to rejuvenate gullies and increase debris availability (Hyde *et al.*, 2007), conditioning and increasing the likelihood of debris flows. Cannon *et al.* (2001a) concluded that wildfires led to changes in soil composition, producing a significant quantity of fine grained wood-ash which contributed to debris flow activity in the earliest post-fire storms. Fires are also responsible for creating hydropohobic soils, which can enhance erosion rates (Cannon *et al.*, 2001b). The removal of vegetation by wildfire also plays a role in unbinding soil and generally enhancing soil mobility. Bare soils are prone to surface erosion processes such as rain drop impact, ravel, surface wash and rilling (Staley *et al.*, 2014). Similar erosion can also arise as a result of anthropogenic activity, such as the felling of tree plantations and the burning of heather for example, both of which are commonly exercised in Scotland.

Chen *et al.* (2015a) point to large population increases, the removal of forest and the increase of tilled land as a major cause of increased slope denudation in Qionghai, China. Trees benefit soil stability by reducing soil moisture through evapotranspiration and interception of rainfall, but also by the effects roots have on binding soil (Sidle, 2005). Removal of vegetation also impacts the incorporation of organic matter into soil, logging may therefore remove the benefits trees have on holding water and therefore attenuating rapid rises pore pressure rises. The progressive failure of a slope can be better understood by considering the variety of complexities and spatio-temporal variability involved in the overall stability of the slope material.

1.1.4 Triggers and failure mechanisms

Landslides are typically triggered by a relatively distinct and short-lived event. Rainfall is recognised as the predominant triggering mechanisms of shallow landslides (Sidle and Bogaard, 2016), particularly debris flows (Ballantyne, 1986), although Volcanism (Capra *et al.*, 2010; Procter *et al.*, 2014) and forest fires (Nyman *et al.*, 2011) are also less common

triggers. Short duration, high intensity rainfall events have the most potential to rapidly increase pore pressures in shallow landslides. Rapid influxes of fluid may also be contributed by rapid snowmelt. Infiltration of water into soil can result in pore pressure rises in interstitial pore spaces, forcing apart particles, reducing friction, and commonly triggering liquefaction in aforementioned loose contractive soils (Iverson, 2005a; Takahashi, 2014).

Pore pressure rises may be focused at the interface between lower-permeability underlying strata and the overlying soil, or between soils of different permeabilities (Galeandro *et al.*, 2013), resulting in a distinct shear surface and often an initial translational failure (Hutchinson, 1988). Over longer timescales, and less frequently linked with shallow landslides, the water table may rise upwards from the bedrock to create saturated basal conditions (Montgomery *et al.*, 1997; Leroueil, 2004). In addition to reducing the effective normal stress by increasing pore pressures, the added weight of the accumulated water will also induce a larger degree of stress (Galeandro *et al.*, 2013; Sidle and Bogaard, 2016).

Failure is most likely when antecedent rainfall is high (Winter *et al.*, 2005). High antecedent conditions can arise from steady but long duration rainfall, which saturates soil, overcomes matric suction and provides a platform upon which intense rainfall can build and trigger failure. Chen *et al.* (2015b) found that debris flows in Taiwan required higher mean rainfall intensities than other landslide types during short rainfall events, but that triggering thresholds were broadly similar to other landslide types during longer sustained periods of rainfall. High antecedent conditions have been found to almost double the runout distance and velocity of a debris flow from a 20° slope, relative to a 30° slope under reduced antecedent conditions (Take *et al.*, 2015). They have also been found to have an impact on debris flow magnitude (Wieczorek and Glade, 2005; Baum and Godt, 2010). The importance of antecedent conditions was highlighted in a study by Wieczorek (1987) which analysed 22 storms in California between 1975 and 1984 and found that debris flows only occurred if seasonal antecedent rainfall surpassed 280mm.

Antecedent conditions can be conceptualised by considering a leaky barrel (Wilson, 1989; Wilson and Wieczorek, 1995). For example, over wet seasonal cycles the water level within the barrel will rise as the net balance is a surplus of water, whereas during the summer for example, the level in the barrel is more likely to fall due to reduced input. To account for the impacts of both transient and persistent rainfall, Caine (1980) developed a global intensity-duration threshold for rainfall triggering. Larsson (1982) was however critical of Caine's work, noting that a number of flows have occurred below his calculated threshold. Instead,

regional and local thresholds are considered to better account for local geomorphic variations and are therefore more reliable (Guzzetti *et al.*, 2007). It is also considered that such thresholds are more effective for triggering in shallow soils, as opposed to deep seated failures which may have a wider range of complexities involved and often much larger lag times (Napolitano *et al.*, 2016).

While increases in pore pressures are perhaps the most common trigger of debris flows, decreases in matric suction, or negative pore pressures, have been observed to trigger instabilities after wetting (Sasahara and Sakai, 2014; Wu *et al.*, 2015). Rainfall and increased pore pressures may trigger a debris flow directly at source, but it is not uncommon for debris flows to first initiate as another form of failure, such as a rigid translational slide, after which transformation occurs (Iverson, 1997a; Ballantyne, 2004, 2008). Iverson (1997a, 2014) states that one mechanism of transition from slide to flow is the change in state of translational energy to 'granular temperature', the agitation of constituent particles within a mass, akin to the kinetic behaviour of atoms that constitute thermal temperature. Takahashi (2014) found that transformation to flow developed from the enlargement of a basal liquefied layer. Iverson (2000) also demonstrated that loose loamy sand transformed after shearing due to the rapid transfer of weight onto the interstitial fluid, rapidly inducing high pore pressures. In flume experiments, Takahashi (2014) found that the transition from slide to flow developed throughout the runout stage and included a period of flow-slide propagation, highlighting that a debris flow hazard may not always be obvious.

Debris flows have also been observed emerging from earthflows (Malet *et al.*, 2004) and slower moving landslides (Reid *et al.*, 2003), particularly by entrainment of coarser material in the case of earthflows. Debris flows may also arise when a failed mass enters a channel and is able to mix with water (Johnson and Rahn, 1970; Richardson and Reynolds, 2000). Whilst other mass movement forms may transition to debris flow, debris flows themselves may transition into hyperconcentrated flows, typically by mixing directly with stream flow (Pierson and Scott, 1985). In addition to increases in pore pressures, debris flows can also be triggered by exfiltration and slope toe removal, or directly from surface runoff erosion over an open hillslope (Takahashi, 2004). Triggering by direct surface runoff can be imagined in a similar way to a firehose being directed at the material (Griffiths *et al.*, 2004). Debris flows may also initiate directly within an existing stream or gully, either by direct failure of in-situ material and mixture with flowing water (Takahashi, 2014), or by flash floods that bulk up by entraining material residing in their path (Zhou *et al.*, 2013). Such flows will often continue

as a channelised flow and may transition into another form dependent upon the entrainment of water and additional sediment.

1.1.5 Ruout and channelisation

Runout will commence under the influence of gravity, with the conversion of gravitational potential energy to kinetic energy, positive pore fluid pressures and heat (Iverson, 1997b). Although topographic controls on runout are perhaps most important, de Haas *et al.* (2015) on the basis of his own studies claimed that debris flow composition can have just as much bearing on flow properties. Debris flows seldom runout under steady-state conditions, with rheological changes occurring throughout flow (Iverson and Vallance, 2001; Iverson *et al.*, 2010) and heterogeneities throughout flow masses commonplace (Hungr, 2000). As such. many simplistic viscoplastic fluid modelling attempts, such as the most commonly ascribed Bingham and Herschel-Bulkley models (Calvo *et al.*, 2015), are ineffective (Hungr, 2000; Iverson and Denlinger, 2001; Iverson, 2003). Such models idealise flow as a single continuum of which different strain stress relationships arise. Newtonian flow describes a fluid in which shear stress is linearly proportional to the rate of strain, although such conditions rarely arise in debris flows due to the solid-phase influence on viscosity. The other common fluid models and their behaviours under shear stresses are shown in figure 1.4 and include the dilatant fluid. In the dilatant fluid model, ascribed to stony-type flows, mobility is reduced under increased shear stress as this reduces the ability for inter-grain collisions to disperse clasts throughout the mass and thus facilitate flow (Takahashi, 2014). Such grain to grain collisions were hypothesised by Bagnold (1954) after he observed the generation of a dispersing layer within his shear experiments.

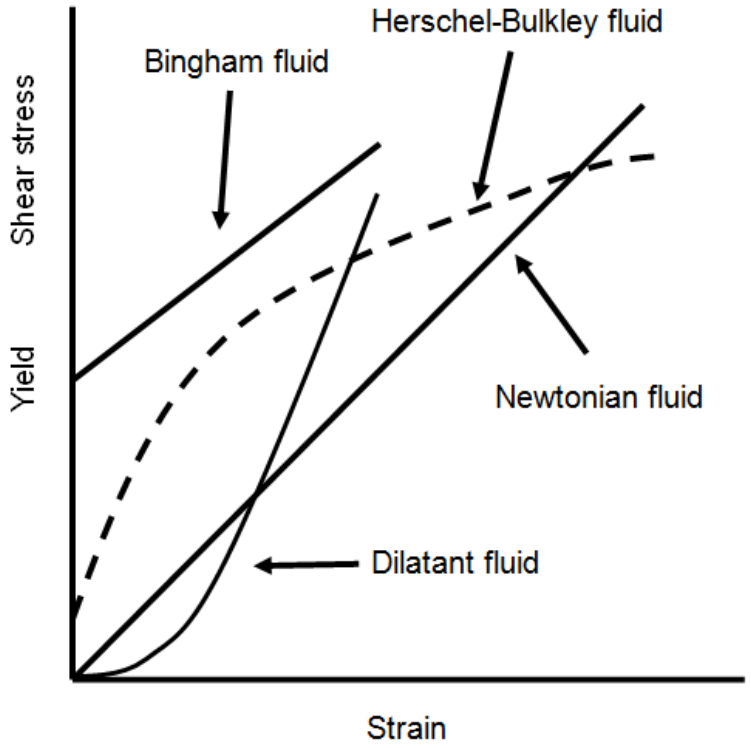

Figure 1.4 - Newtonian and non-newtonian viscoplastic fluid models. Behaviour under application of stress. Adapted from Takahashi (2014).

Single-phase models have been found to calculate large differences in runout distances and velocities (Jeong and Park, 2016). Instead natural debris flows are often best considered as two-phase phenomena, particularly as observations have shown that solid and fluid phases can travel at vastly different velocities (Pudasaini, 2012). Modelling of debris flows using a two-phase approach has become increasingly popular. Two-phase models do not neglect the role of interstitial fluid as the single-phase models do, but account for them and their interaction with the solid-phase of the mass (Takahashi, 2014). Continuum models are however still used abundantly (Schraml *et al.*, 2015; Gregoretti *et al.*, 2016; Vennari *et al.*, 2016) perhaps due to the capability to perform back-analysis with limited event information which can be a challenge to collect. Debris flow mobility is fundamentally modelled using depth integrated conservation of momentum equations (Iverson, 1997; Iverson, 2005b), in which mobility is influenced by changes in velocity and mass.

Iverson and Denlinger (2001) have favoured the Mohr-Coulomb equation to explain the shear stresses that operate to drive flow and this has generally been found to agree with Bagnold's inter-grain collision model (Iverson, 2005b). However, according to Legros (2002)

many natural landslides travel much further than the coulomb model would predict, highlighting the difficulty in parameterising these mass movements. Whilst masses with a higher fraction of fine particles require higher pore-pressure rises to trigger shearing, they can be much more mobile after failure (Mukhlisin *et al.*, 2006). Flows with a higher proportion of fines are able to sustain high pore pressures throughout propagation by minimising drainage of interstitial fluid (Wang and Sassa, 2003; Iverson *et al.*, 2010; Kaitna *et al.*, 2016).

Flows may travel along planar paths in which topographic routing of flow is not apparent, a form of flow often referred to as a hillslope flow. Alternatively, a flow may route into a well defined or subtle topographic depression or continue down it if initiated there, as a channelised flow (Hutchinson, 1988). Gullies may contain higher topographic variability, a factor that Iverson *et al.* (2010) noted to reduce flow velocity, however this did not have any bearing on runout distance.

Gullies and channels down which debris flows propagate represent sources for volume growth, both by entrainment by of additional debris and of water, which increases flow mobility. Entrainment in channels can take place either by scour of the gully floor or from collapse of channel banks (Iverson, 2014) and has been observed to increase debris flow size significantly (Hungr *et al.*, 2008), by an order of magnitude in some cases (Benda and Cundy, 1990; Milne, 2008). Theule *et al.* (2012) observed during two debris flows in South East France, that more than 92% of the final flow volume could be attributed to channel scouring. Entrainment has been observed at a grain-by-grain scale (Reid *et al.*, 2011) and en-masse (de Haas and van Woerkom, 2016). Schurch *et al.* (2011) during monitoring of the Illgraben torrent, noted that increased flow depth led to larger magnitudes of erosion. This relationship supports previous findings by Brayshaw and Hassan (2009) who highlighted that larger aggradations of gully sediment required higher magnitude events in order to trigger release.

Gully formation and development are effective processes in the erosion and stabilisation of hillslope sediments, a significant component of paraglacial glacigenic sediment denudation (Curry, 1999). Gullies are primarily thought to develop from rills and ephemeral gullies as part of a wide continuum (Poesen *et al.*, 2003), but may also form from developing macropores and soil pipes (Faulkner, 2006), ultimately resulting in an effective link between hillslope and fluvial systems (Harvey, 1992).

Ephemeral gullies are not objectively defined in the literature (Grissinger, 1996; Poesen *et al.*, 2003), however they are typically considered to be small channels less than approximately 0.5 m in depth, which form where overland flow is concentrated by surrounding converging topography (Poesen, 1993). They differ from Rills which typically measure only a few centimetres in depth and form somewhat stochastically (Casalí *et al.*, 2015) and fully formed gullies which are at least 0.5 m in depth (Bocco, 1991). They can be further delineated by their tendency to contain transient hydrological flow repeatedly reactivated in the same place by intense precipitation (Bull and Kirkby, 1997; Kirkby and Bracken, 2009) differing from established gullies which typically contain at least a small degree of persistent hydrological flow owing to their larger size. Gully formation has principally been attributed to fluvial incision and upslope propagation (Harvey, 1992), requiring a critical drainage area to sufficiently concentrate an erosive flow (Poesen *et al.*, 2003). Once formed, convergent gully networks concentrate successive storm rainfall events, reactivating ephemeral gullies and enabling their enlargement (Kirkby and Bracken, 2009). This process may elicit a positive feedback effect by concentrating greater volumes of flow, thus gradually increasing erosive power (Poesen *et al.*, 2003). Although the equifinality of gullies has been acknowledged (Harvey, 1992; Kirkby and Bracken, 2009), the significance of mass movements and their interrelationship with gully development has been largely overlooked, with gullying principally linked to fluvial processes (Bocco, 1991). Focus on gullies as purely fluvial forms is unlikely to explain the development of all gully systems (Harvey, 1992) and has undermined development of a wider conceptual understanding of the landforms (Bergonse and Reis, 2011).

1.1.6 Entrainment

Scour is typically minimal when flows override dry basal sediments (Reid *et al.*, 2011) and can even have a negative feedback effect by reducing the overall fluid ratio (Iverson *et al.*, 2011). In contrast, saturated sediments yield much larger volumes to entrainment (McCoy *et al.*, 2012). Sassa (2000) credited easier incorporation of saturated sediments to a mechanism whereby sudden impact loading of the deposits caused a rapid increase in pore pressures and a reduction in friction. Following much the same mechanism, Iverson *et al.* (2011) discovered during experiments at the USGS flume, Oregon, that entrainment of saturated basal sediments increases flow mobility. Iverson *et al.* (2011) also noted that the contractive behaviour of some basal sediments upon shear resulted in a further source of rapid pore pressure increases. Both the coarse front of a flow and inter-surge flow have been observed to entrain material (McCoy *et al.*, 2012), however others have noted erosion

limited to just the passage of a granular flow front (Berger *et al.*, 2011; de Haas and van Woerkom, 2016)**.** During flume experiments, de Haas *et al.* (2015) found that increases in the coarse-material fraction increased runout, an observation that was attributed to the formation of confining levees and increased inter-grain collisions. It was noted however that excess accumulations of coarse grains in the head of the flow inhibited mobility.

Entrainment is not necessarily limited to preconditioned material. McCoy *et al.* (2013) installed a series of erosion bolts in the Chalk Cliffs of Colorado to measure debris flow potential to directly scour the base of a bedrock gully. After the passage of eleven flows in a four year period, erosion of between 36 to 64mm was noted and could be attributed to both coarse flow fronts and inter-surge flow. A basal deposit of around 5cm in thickness, twenty times the median bed sediment grain size, was also noted to shield the bed from erosion.

The development of a coarse debris flow front has been noted by several observers and researchers (Sharp and Nobles, 1953; McCoy *et al.*, 2012; Iverson, 2013; Takahashi, 2014), this occuring due to the stratification of velocities (Takahashi, 2014). The granular head of a flow is then continually pushed by the subsequent finer-flow in its wake (McCoy *et al.*, 2010;

Figure 1.5 - Screenshot of a debris flow front supporting very large boulders, recorded along the Illgraben debris flow channel in Switzerland, 22nd July 2016. Video by Pierre Zufferey of WSL, screenshot from Dave Petley AGU landslide blog (2016).

Iverson, 2013), a mechanism that Takahashi (2014) has likened to that of a bulldozer. Further vertical grading within flow deposits, have been noted and attributed to Bagnold's (1954, 1968) inter-grain collision model of dispersion (Takahashi, 2014). Debris flows are capable of transporting large boulders, sometimes in excess of ten metres in diameter (Iverson, 2014). A recent debris flow in the monitored Illgraben channel was recorded by a camera and can be seen to be transporting very large boulders near the flow front (figure 1.5). Accumulation of boulders and coarse material at the head of a flow will act like a mobile dam (de Haas and van Woerkom, 2016), slowing the flow.

Instances of intermittent debris flow surges are abundant in the literature (Sharp and Nobles, 1953; Davies, 1986; Arattano *et al.*, 2012; Iverson, 2014; de Haas and van Woerkom, 2016). Some debris flows may even be comprised of hundreds of surges (Liu *et al.*, 2009) which can occur over many days (Sharp and Nobles, 1953; Davies, 1986). Furthermore, each surge can have a unique set of flow properties (McCoy *et al.*, 2010), a factor which may undermine runout modelling attempts. Surge behaviour has been attributed to spatially and temporally distributed sediment sources that mobilise independently (Okuda *et al.*, 1978). Kean *et al.* (2013) hypothesise that the exhibition of surge behaviour may be due to reduced transport capacity in low gradient reaches, a storage process aptly described as a 'sediment capacitor'. Given that elevated pore pressures have been found to persist within material long after cessation of movement (Kaitna *et al.*, 2016), the proposed sediment capacitor model appears realistic.

1.1.7 Deposition

Debris flow deposition usually occurs when the slope gradient reduces to below approximately 10° (Rickenmann, 2005), however flows have been known to continue carrying boulders at gradients as low as 5° (Ballantyne and Harris, 1994). Deposition has been found to be more likely when the flow depth reduces (Schürch and Densmore, 2011). And where spreading occurs, increasing the surface area subject to friction and reducing the overall momentum of the mass (Fannin and Wise, 2001).

Highly saturated debris flows commonly deposit as broad fans, whilst in contrast higher viscosity flows with lower water contents will typically form elongate tracks (Milne, 2008). The deposit's pore fluids may subsequently remain elevated for a considerable number of days, or even months (Iverson, 2014), potentially enabling remobilisation by a following surge. Eventually the deposit will dewater, causing the constituent clasts and particles to interlock, returning the flow back to a near-rigid mass (Iverson, 1997). This concretion like

dewatering can subsequently prove problematic when it comes to clear debris from around and on infrastructure such as roads. Successive flows along the same path, or terminating in the same reach, produces stratified debris cones.

1.2 Paraglaciation

The secondary failure of glacigenic sediment was first noted as 'paraglacial' by Church and Ryder (1972) after recognition that recently deglaciated basins in Canada were outputting much larger volumes of sediment than equivalent unglaciated basins. Ballantyne (2002a) argued that paraglacial reworking, also preconditioned by the action of deglaciation itself Ballantyne (2002a, 2002b), represented a momentary stage in the wider geomorphic cycle, in which geomorphological processes, also observed in landscapes unaffected by glaciation, work at an accelerated rate to relax processes back to a 'non-glacial state'.

Aware that paraglacial processes also occurred abundantly in unglaciated environments, Benn and Evans (1998) proposed that the paraglacial descriptor should be restricted to use for the period whereby rapid environmental readjustment took place. Ballantyne (2002a,b) introduced the concept that different geomorphic forms, such as drift-mantled slopes and glacial forelands, took different amounts of time to readjust. Mercier *et al.*, (2009) have observed a full sequence of paraglacial slope adjustment (i.e. gully incision and stabilization) over timescales as short as a few decades after deglaciation, however renewed and delayed paraglacial sediment reworking has been observed several thousands of years after deglaciation (Curry, 1998; Jakob and Friele, 2010). Studies in the Scottish Highlands have demonstrated renewed or prolonged paraglaciation several millennia after deglaciation (Brazier *et al.*, 1988, 1989; Ballantyne and Benn, 1996; Ballantyne and Whittington, 1999; Curry, 1999, 2000; Ballantyne, 2003; Ballantyne and Stone, 2004; Ballantyne *et al.*, 2014; Strachan, 2015). Church and Slaymaker (1989) introduced a considerable extension to the longevity of paraglacial activity, discussing glacially influenced processes in larger basins operating at timescales in excess of 10,000 years after deglaciation. Other studies have also demonstrated the long-lasting and intermittent nature of paraglaciation, for example the erosion of previously dormant drumlins along the coast of North America (Hein *et al.*, 2012; Forde *et al.*, 2016), recent debris flows in the Cheekye basin, British Columbia (Jakob and Friele, 2010) and continued paraglacially dominated sediment budgets in the Karakoram Mountains, Asia (Iturrizaga, 2008).

Benn and Evans (1998, 2014) state that the paraglacial period theoretically ends upon cessation of elevated sediment yield rates, however ambiguity remains regarding the role of

renewed and sediment reworking. The end of the paraglacial period is perhaps dependent upon scale and the ratio of glacially conditioned activity relative to that of other agents, particularly as non-glacial rates of erosion are difficult to quantify. Ballantyne (2002b) recognised that the reworking of paraglacial sediment could continue long after the initial rush of activity during deglaciation, this potentially lasting several millenia due to prolonged activity or rejuvenation.

1.2.1 Theoretical sediment models

Several theoretical models have sought to outline the temporal flux of glacigenic sediment, returning previously glaciated environments back to some form of equilibrium. Observations of disproportionate sediment yields from large tributaries paved way to the first model, often cited as the 'sediment wave model' (Slaymaker, 1987; Church and Slaymaker, 1989). It was first hypothesised that a sediment wave which had already peaked in smaller basins and hadn't yet transpired in basins larger than 30,000 km², was working its way down through the fluvial network, peaking in larger basins progressively through time (figure 1.6). This model was favoured by Ashmore (1993) and Church *et al.* (1999) for its harmonious fit with similar observations in Canada, however Kovanen and Slaymaker (2015) note that the model does not account for changing sediment sources and sinks over time.

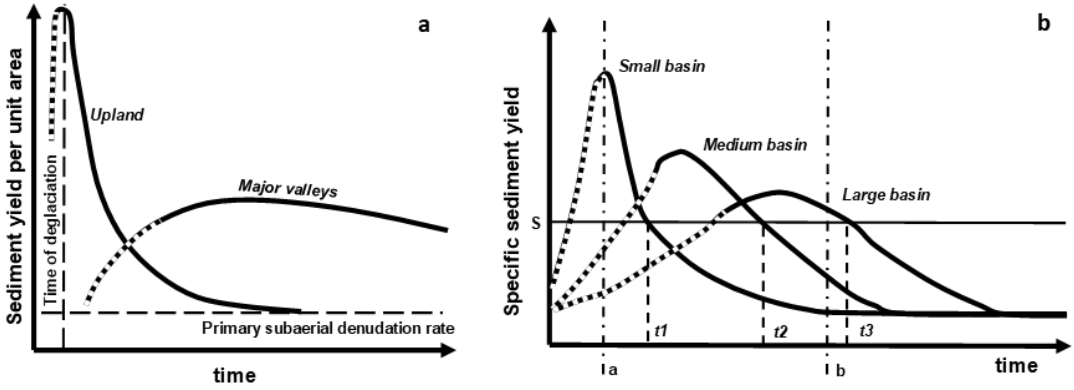

Figure 1.6 - Paraglacial sediment wave models (redrawn) **(a)** As first depicted by Church and Slaymaker (1989) **(b)** As modified by Harbor and Warburton (1993) to better highlight the progression of the sediment wave through time.

Also criticising the sediment wave model for its unrealistic lagging of glacigenic sediment release and reworking in larger basins, Ballantyne (2002b) instead favoured a paraglacial exhaustion model approach which was first utilised by Cruden and Hu (1993) and considers a finite supply of material which decays roughly exponentially, much like the half-life of a radioisotope. While differing, both theoretical models agree that the paraglacial response is generally most rapid during and after deglaciation, after which rates of sediment release

decelerate. Ballantyne (2002b) himself conceded that both models could be used to conceptualise glacially conditioned sediment reworking depending upon the significance of secondary mobilisation and entrainment of paraglacial sediment stores.

Whilst the exhaustion model may better encompass transient sediment stores across a range of different scales, it was developed as an idealised steady-state model where sediment stores eventually stabilise. Recent reactivations or intermittent pulses of glacigenic sediment triggered by factors such as anomalous climatic events have raised uncertainty about the temporal scale of the paraglacial period (Cossart, 2008), particularly when sediment exhaustion and stabilisation are considered to mark the end of the paraglacial period (Ballantyne, 2002b, 2003). Some glacigenic sediment sources can become decoupled from the sediment cascade and thus exhaustion may become heavily protracted (Cossart and Fort, 2008; Hoffmann, 2015). In Gredos Gorge, Central Spain for instance, Muñoz-Salinas *et al.* (2013) estimate that 70% of glacigenic sediment still persists long after deglaciation, with mobilisation only occurring during high discharge events.

Determining the duration of the paraglacial period is a challenge (Orwin and Smart, 2004; Etienne *et al.*, 2008) impaired by a lack of clarity regarding normal background rates of activity at different spatial scales. This challenge is further compounded by climate change symptoms such as increased rainfall, which have been heavily linked with mass movements (Ballantyne, 2002a; Stoffel and Huggel, 2012). Hewitt (2006), Slaymaker and Kelly (2007) have gone so far as to question whether glaciated landscapes can truly revert back to equilibrium prior to successive periods of glaciation, typically over timescales of 20,000-30,000 years. This area of research clearly requires greater attention, particularly through quantitative studies of renewed paraglacial sites.

1.2.2 Sediment cascades

Sediment delivery and transport has long been recognised as a sporadic system, likened to that of a "jerky conveyor belt" (Ferguson, 1981) over a range of timescales. Influxes of sediment at the drainage basin scale are considered to be driven stochastically by rainstorms and other perturbations, sometimes resulting in spatio-temporal variations in sediment fluxes and storage (Benda and Dunne, 1997). The detachment and transfer of sediment between different geomorphic zones may occur efficiently or inefficiently depending on the sediment connectivity (Bracken *et al.*, 2015). Landslides are the primary geomorphological mechanism of sediment release (Densmore *et al.*, 1997; Brardinoni and Church, 2004) and are an important component of the landscape-scale sediment cascade (Rosser, 2010).

Erosion, deposition and transport in debris flow prone landscapes is however poorly understood and has not received sufficient examination (Berger *et al.*, 2011; Schurch *et al.*, 2011), and knowledge of coupling between the hillslopes on which debris flows occur and the channels in which they are transported is often lacking (Rosser, 2010).

Debris flows have primarily been considered as an agent of sediment evacuation, however they have also previously been identified as an agent of rill development and gully scour after wild-fire in the USA (Gabet and Bookter, 2008) as well as a general driver of gully scour (Stock and Dietrich, 2003). Recent evidence has also highlighted the ability of debris flows to erode bedrock channels (McCoy *et al.*, 2013), one mechanism of which includes collision and shatter by large clasts that form part of the flow mass (Stock and Dietrich, 2006). The role of debris flows as an agent of landscape evolution has received little further attention however. Key questions therefore remain about the role of debris flows as an agent of erosion and slope denudation.

1.3 Hazard and Risk

Quantitative risk assessments (QRAs) are increasingly carried out at the site level, to highlight the standing of debris flows in the context of locally stipulated risk tolerances. These assessments are typically preceded by wider qualitative and semi-quantitative analyses, where hazards and their associated risks are first identified at the national scale for instance. This may conform to the framework set out by van Westen *et al.* (2006), in which data on environmental and triggering factors is collected and analysed, along with an inventory of past events to assess spatio-temporal and intensity probabilities.

1.3.1 Hazard and risk Assessment

The risk (R) for a single landslide scenario, of a landslide of magnitude M_i, at a distance of X from the landslide source, can be expressed using the equation set out by Corominas *et al.*, (2014)

$$Risk\ (R) = P(M_i)\ P\left(X_J \middle| M_i\right)\ P\left(T \middle| X_j\right) V_{ij}\ C$$

Equation 3

where $P(M_i)$ is the probability of occurrence of a landslide of magnitude M_i, $P\left(X_J \middle| M_i\right)$ is the probability that the landslide of intensity j will reach the point at distance X from the source, $P\left(T \middle| X_j\right)$ is the probability of the element at risk being at the point X distance from the

source, V_{ij} is the vulnerability of the element at risk to the landslide of magnitude i and intensity j, and C is the value of the element at risk.

An estimate of hazard probability and of the vulnerability of the element at risk, the latter of which is underpinned by knowledge of flow characteristics at the point of impact as well as the characteristics of the element at risk, are essential to any assessment (Jakob *et al.*, 2012). The magnitude of a debris flow influences the hazard intensity and the probability of encounter, both critical elements of a risk assessment, thus derivation of a magnitude-frequency relationship can be invaluable (Hungr *et al.*, 2008). Knowledge of debris flow magnitude and frequency can form part of a rational basis for the design and implementation of mitigation structures, as well as providing inputs into landscape evolution models (Bovis and Jakob, 1999). Care must be taken however, as use of regionally derived magnitude-frequency relationships can lead to incorrect predictions due to variations in slope morphology. Where possible, site-specific analysis should therefore be prioritised over generalized observations (Hungr *et al.*, 2008).

1.4 Thesis aims and objectives

The main aim of this research was to characterise the Scottish debris flow geohazard and the associated geomorphological controls and influences adjacent to the Scottish trunk road network. This was in response to a high frequency of disruptive failure at the Rest and be Thankful.

A review of the literature on landslides and debris flows, as well as reports on debris flow activity in Scotland, identified some key objectives and research questions which were within the scope of this research project.

The three key objectives are outlined below, with their respective research questions and some additional overarching questions with the benefit of all the objectives met and synthesised together at the end of the study.

1) **Mapping**; in order to understand the rates of activity at the main site, in context with the surrounding area, as well as to build up a base understanding of activity at the site and supplementary study sites.
    - What is the nature of historic debris flow and geomorphic activity at the highly active Rest and be Thankful and how does this compare with other study sites?
    - Are failures reasonably homogenous in terms of magnitude and spatial distribution, or are there patterns of spatio-temporal activity which require further investigation?
    - What are the influential characteristics of each study site and are these unique?

2) **Monitoring**; to build a robust picture of activity at the main site, and supplementary sites for comparison, and characterise the nature of activity with a view to potentially better manage and mitigate the hazard. For example, does the slope exhibit precursory changes which can be used to anticipate future activity and hazard potential?
    - Is long-range Terrestrial Laser Scanning suitable for monitoring geomorphic change in a complex vegetated environment? Most studies have previously focused on lower range and less vegetated environments.
    - Is debris flow propagation, and a resultant significant hazard at the road level, reliant upon sediment accumulations within the gully prior to failure?

- If so, what are the predominant sources of these gully material stores and the debris flow entrainment sediment budget?
- What is the spatio-temporal nature of the debris flow geohazard at RabT?
- How does the seemingly high level of activity at RabT compare with other trunk road adjacent mass movement prone slopes?
- Does a second study-site (Glen Ogle, which has itself caused disruption to the trunk road network), of lower frequency and higher magnitude, exhibit significant small detectable changes?

3) **Modelling**: to further understand the nature of the debris flow geohazard, particularly in relation to slope channels which may be of significance in facilitating runout and hazard development. Furthermore, to be able to critically appraise mitigation efforts
    - How effective is a continuum runout model, RAMMS-DF, at simulating the Scottish debris flow geohazard?
    - What does a model tell us about the nature of the debris flow geohazard, particularly at the Rest and be Thankful, a site where multiple runout hazard zones are likely?
    - How does the current hazard mitigation approach at the Rest and be Thankful tally with the nature of the debris flow geohazard? For example, are catch nets configures and distributed optimally given the better understood nature of the hazard?

And finally, within a broader discussion and synthesis of all the above, the following questions arose:

- What is the likely driver of such a high frequency of activity at the main study site (the Rest and be Thankful)?
- Which processes influence the activation of different slope areas and can this be used to anticipate future debris flow activity?
- Are debris flows an effective agent of the rapid gully erosion/propagation found at the site?
- Do the different objectives of this study lead to a coherent conceptual model of debris flow activity, on which further research can develop?

Chapter 2

Debris flows in Scotland: background and key study sites

2 Introduction

Debris flows in Scotland are generally relatively small by global classification standards, such as that proposed by Jakob (2005), however this has little bearing on their disruptive potential. Events that only impact metres of road are capable of affecting areas much larger than the size of Hong Kong (Winter, 2014), largely due to the remote nature of communities and the sparsity of alternative route options, an effect called the vulnerability shadow (Winter and Bromhead, 2012). Winter *et al.* (2016) estimate that a debris flow in 2007 at RabT, accrued total direct damage and remediation costs between £1.7M and £3M (at 2012 prices). Tourism represents a significant contribution to the Scottish economy, particularly during the summer, thus events at this time of the year can be particularly disruptive (M. G. Winter and Shearer, 2017).

A recent review of debris flow deposit dating studies in Scotland indicates an upturn in activity over the last 700 years, although the cause is unclear (Ballantyne, 2018). Factors such as burning, deforestation and grazing may have preferentially disposed sites to failure (Innes, 1983; Hinchliffe, 1999; Ballantyne, 2018). A study by Reid and Thomas (2006) suggests that a climatic stabilisation between c. 7.5 ka and 550 BP may have reduced rates of sediment reworking by enabling the colonisation of vegetation and establishment of peat cover. Scotland's natural forest cover is said to have reached its maximum extent some 3-4 k yr BP, long after the last glacial maximum (LGM) (Smout et al., 2007), although this was considered to be far from the dominant land type (Darling, 1968). The cause and timing of a major reduction in woodland cover is a matter of debate, however Elm decline in the British Isles, some 5.5 k yr BP, appears to mark the decline, this followed by a dramatic collapse in Scots Pine coverage some 4.4 k yr BP and rapid anthropogenic clearing around the same period (Smout et al., 2007). Woodland clearance and burning have continued to this day, with recent such activity (last 500 years) associated with debris cone erosion by Brazier et al. (1988) for example. Many authors however point to extreme rainfall and storm events as the contributor to increased debris flow activity, perhaps linked to longer-term climatic changes (Brazier and Ballantyne, 1989; Hinchliffe, 1999; Reid and Thomas, 2006). Grove (1972)

analysed data on mass movements in Norway between 1650 and 1760 and found that the influence of the Little Ice Age caused a significant increase of activity in this period. A combination of these factors may therefore be responsible for the observed increase in activity.

Landslide events have been well documented across Scotland, from relatively early mapping and lichenometric dating by Innes (1983), to subsequent publications by, for example, Ballantyne (1986), Winter et al. (2005; 2006; 2009), Milne et al. (2009), the British Geological Survey (BGS 2007) and Strachan (2015), not to mention several private geotechnical reports. By far the most comprehensive of these was the 2005 Scottish Road Network Landslide Study (SRNLS) (Winter *et al.*, 2005), which gave recommendations for a network-wide hazard scoring approach based upon identified predisposing factors. The report summarised the topographic influences of failure and recognised the potential role of streams and gullies, which Milne *et al.* (2010) later highlighted as playing a major role in amplifying the hazard during a large magnitude event at Glen Ogle in 2004. The report also served to review and highlight key sites and areas of carriageways that had been subject to hazardous debris flow activity in recent years and set out the plan for a semi-qualitative regional hazard and risk assessment which was reported by Winter *et al.* (2009).

This SRNLS work forms the basis for this study, in which key sites in Scotland have been selected for repeat monitoring and change detection, to lend further, more detailed, insight into the debris flow phenomenon, hazard and other related geomorphological factors. This chapter presents some key study sites and a justification for their selection, as well as a summary of their past activity and their different characteristics.

2.1 Road network hazard ranking

Debris flows are typically initiated from the inherently unstable veneers of glacigenic sediment that have been deposited across the sides of many formerly glaciated valleys (Mattson and Gardner, 1991; Ballantyne and Benn, 1994, 1996). In Scotland, these arose during the LGM and Younger Dryas some 26 k – 10 k years ago. The extent of the LGM is shown in figure 2.1. Drift mantled slopes, typically comprised of stacked lateral moraines (Ballantyne, 2018), are the primary source of debris flows and gullying (Ballantyne, 2002). The failure of these glacial deposits is dependent upon a range of factors, particularly slope angle and topographic features such as channels, which were comprehensively reviewed in the SRNLS (Winter *et al.*, 2005). A follow up hazard mapping study (Winter *et al.*, 2009) on 3,200 km of the trunk road network, split 53 % of the strategic road network into three

categories. One of these categories included 19 % of the road network (figure 2.2), with these sites requiring further detailed study due to the identification of a potentially significant hazard. These sites were subject to detailed inspections, initially over the course of a year, resulting in a set of scores for exposure to the landslide hazard. Of 126 sites, 66 were given high or very high hazard rankings (risk).

The SRNLS was undertaken in response to the debris flows that affected the trunk (strategic) road network in August 2004 at the A83 at Cairndow, the A9 at Dunkeld and the A85 at Glen Ogle. At Glen Ogle, a total of 31 debris flows were identified (Milne *et al.*, 2010), including the two major events that reached the road, between which road users were trapped resulting in helicopter evacuations (Winter et al. 2005; 2006; 2009). The Rest and be Thankful (RabT) was also well known for debris flow activity prior to 2005 and has gained much attention over recent decades for its high frequency of slope activity, disruption to the A83 trunk road and the communities it serves. Anecdotal evidence suggests that debris flows at the Rest and be Thankful (A83) have occurred annually, on average, between approximately 1989 and 2007. Since 2007, an average of around two events per year has affected the road.

Glen Ogle (A82) and the Rest and be Thankful (A83) were both identified as very high hazard (risk) sites in the SRNLS implementation study (Winter *et al.*, 2009), with Glen Ogle ranked tenth and RabT ranked twelfth. Both of these sites are highlighted here and have been selected for further study for a number of reasons. First, RabT has been chosen for its high frequency of debris flow activity which is far in excess of a typical 10-50 year recurrence interval (Ballantyne, 2002) thus presenting the greatest potential to yield insight into the Scottish debris flow phenomenon. Secondly, the Glen Ogle site has demonstrated one of the largest magnitude (8,500 m^3) debris flow events on record in Scotland (Milne *et al.*, 2010), and stratigraphic evidence suggests that the site has produced similar events in the past (Milne et al. 2009), indicating that the site is prone to a very different magnitude-frequency of events. Third, these two sites in particular are easily accessible, free of obstructions and can be observed from within the 2 km limit of a Riegl LMS-Z620 terrestrial laser scanner.

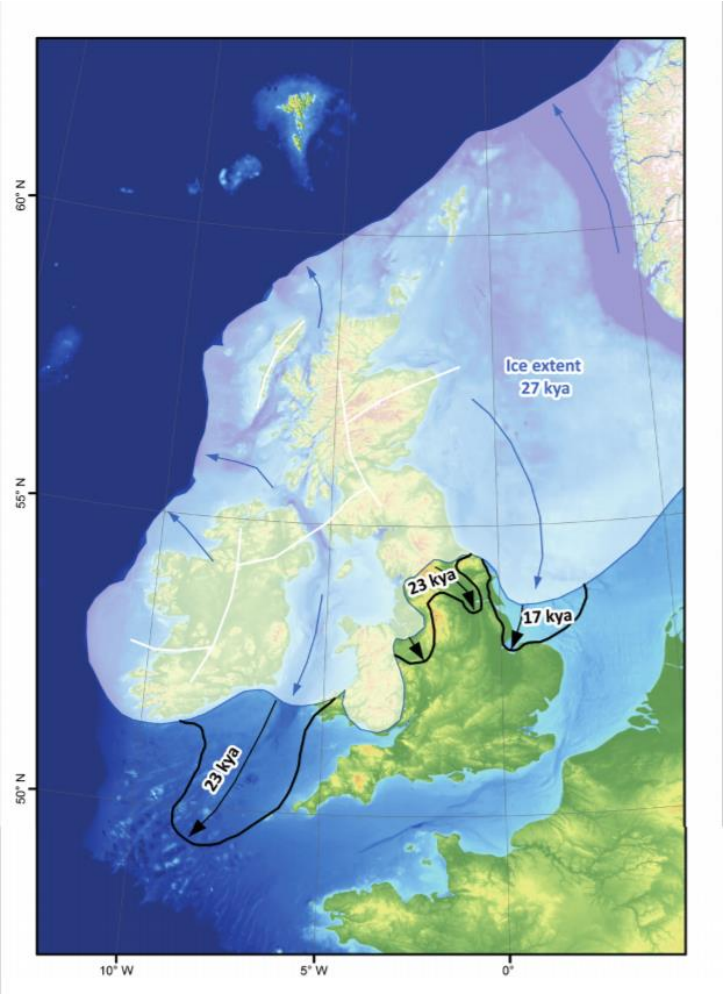

Figure 2.1 - A map of the LGM extent in Britain (Clark et al., 2012), principally 27 k years before present, although with some spatio-temporal variation.

A third study site, Glen Coe (A82) has also been chosen to supplement RabT and Glen Ogle, particularly due to its significantly different geological and geomorphological characteristics. This was thought to potentially give rise to a different set of observable processes, thus lending insight into a different form of landslide hazard, or a different sub-type of debris flow. Glen Coe was not initially identified as a site of high or very high risk in the SRNLS (Winter *et al.*, 2009) but was, instead, highlighted as in need of further study and assessment as a result of its more unique geomorphological characteristics. Following this, the site was eventually found to fall within the upper quartile of risk scores. In contrast to RabT and Glen Ogle, the A82 at Glen Coe has experienced limited disruption by landsliding since the events

of the late-1980s/early-1990s. The site was again chosen due to its relative ease of access and low scan ranges.

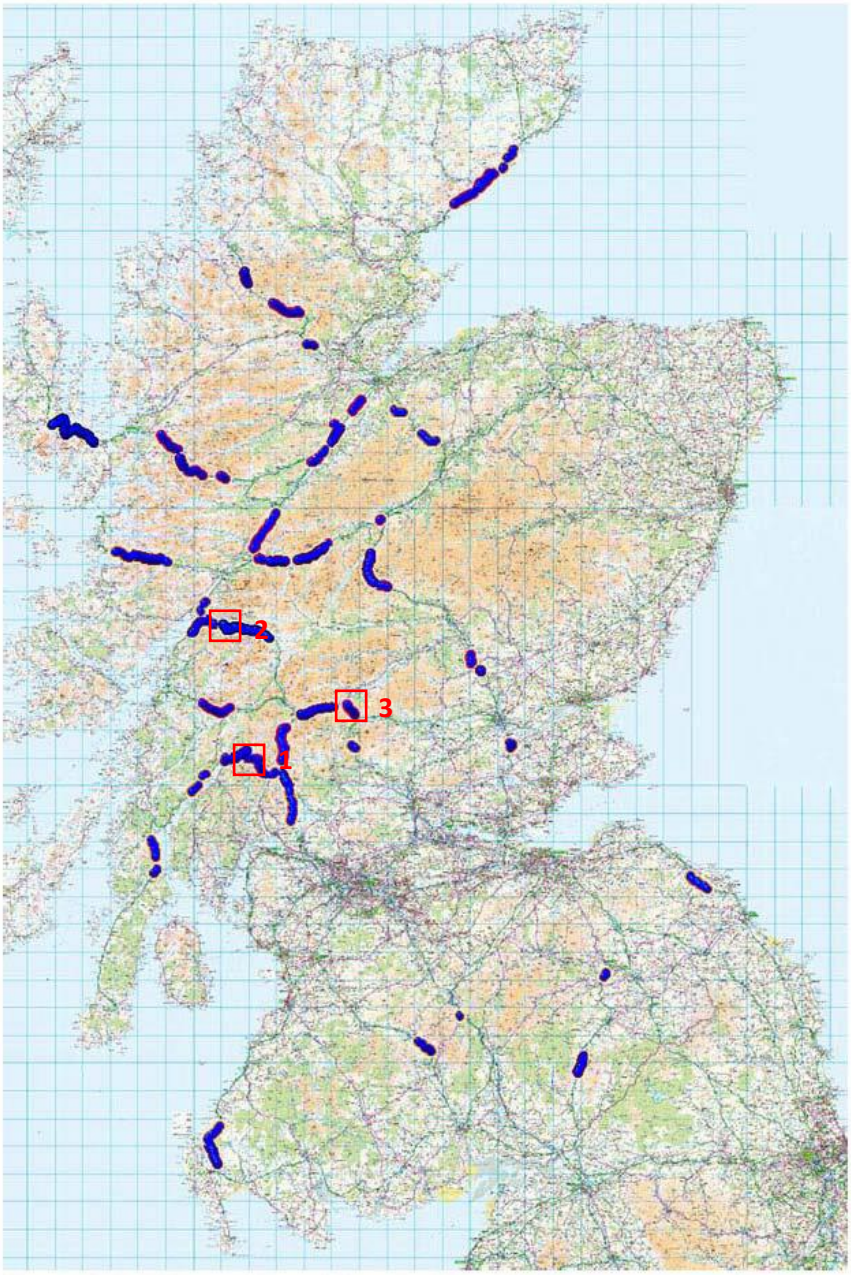

Figure 2.2 - The results of the SRNLS: Implementation study GIS and mapping analysis. These sites were identified for their hazard potential and were further analysed in more detail to attribute hazard scores and identify key sites of risk (Winter et al., 2009). The three study sites 1) RabT, 2) Glencoe and 3) Glen Ogle are also marked for reference.

Figure 2.3 shows the locations of the three chosen sites across Scotland. Their relatively close proximity to one another was an additional benefit to their selection. A more detailed description of each site, including photographs and maps, is presented herein.

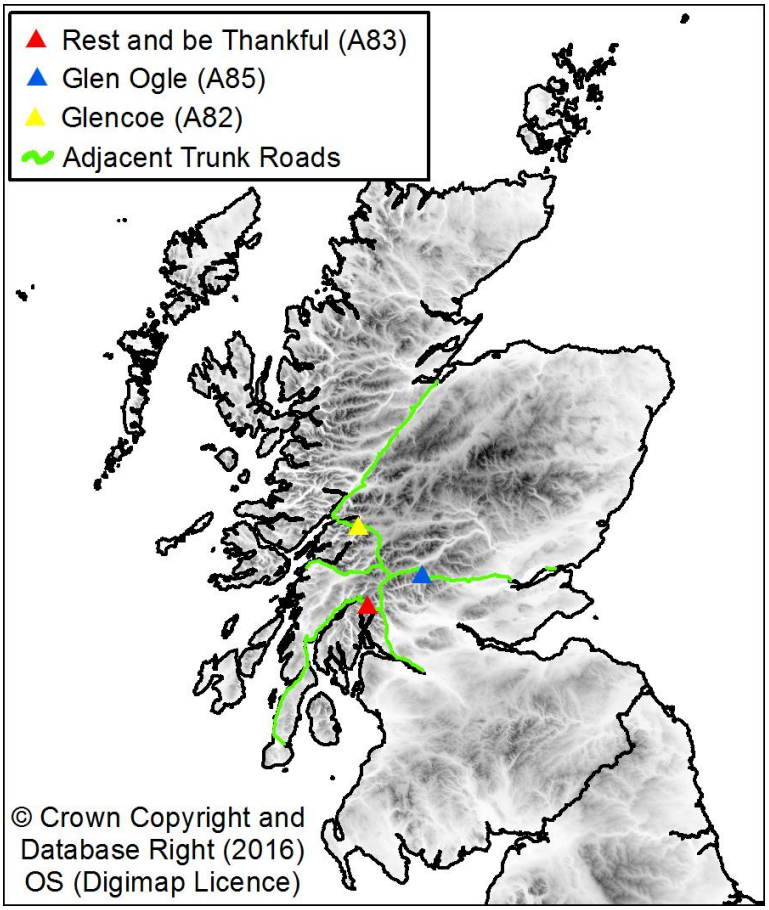

Figure 2.3 - The three study sites chosen for monitoring during this project

2.2 The Rest and be Thankful (A83)

The debris flow prone RabT slope is above the A83 trunk road in Glen Croe, approximately 100 km north-east of its terminus in Campbeltown in Argyll & Bute. The main slope (shown in figure 2.4) measures an average of 32° and rises approximately 530 m from the floor of the valley (133 m.asl) to a convex head before rising a further 198 m up to the peak of Beinn Luibhean. The bedrock consists of low-grade pelite, psammites and mica-schists (BGS, 2018), with an overlying layer of poorly sorted glacial drift (up to 3 m thick) which is densely gullied (lateral gully density of *c.* 18/km) and interspersed with shallow scars, levees and debris cones. The drift deposits are heterogeneous, containing material ranging in size from large clasts to small grains, peat and clay. The superficial layer at RabT is abundant with sands, derived from the underlying psammitic schist, the matrices of which are susceptible to a high number of debris flows in Scotland (Ballantyne, 1991; Milne *et al.*, 2015).

The slope has a low cover of perennial vegetation, with a few scattered trees evident, however seasonal vegetation, particularly Bracken (*Pteridium*), is widespread from low to

mid-slope elevations. This seasonal vegetation is particularly rife during the summer months, with growth occurring from roughly April through to the winter, dwindling with the onset of frosty conditions and dieback. It is not uncommon for the Bracken at RabT to reach a high density with a canopy height in excess of 1 m.

Figure 2.4 - A photo of the Rest and be Thankful. A high number of gullies are evident across the slope. The A83 can be seen running along the bottom portion of the photograph.

The Loch Lomond readvance (Younger Dryas) was focused on the Western Highlands, with its maximum southern extent within the vicinity of RabT (figure 2.5). The site was therefore exposed to renewed glaciation, and periglaciation when the ice was not at its maximum extent (Ballantyne, 2018). This likely resulted in the advanced production and perturbation of drift cover at RabT and the surrounding area, compared to equivalent slopes not proximal to the readvance. RabT is also situated in one of the wettest areas in the UK (> 3000 mm/yr; Met Office 2016) and such intense rainfall patterns are considered a major contributory factor to the rate of activity at the site. The rate of activity at RabT is however far from unprecedented in Scotland, especially when accounting for variations in mean annual rainfall across the country. The gully density at the Drumochter Pass, Cairngorms, when normalised for mean annual precipitation, is slightly greater than that at RabT for example (Sparkes et al. 2017). Most reported values also tend to focus on slopes proximal to infrastructure, such as roads, where events cause damage and disruption. Given that the trunk road network in particular only intersect a small proportion of the Scottish hills, it's entirely likely that there are slopes exhibiting even greater levels of activity than RabT.

The A83 is the main route between mid-Argyll and Central Scotland and is essential for local communities, tourism and the movement of goods and services. Glen Croe was established as a major transport corridor with the completion of the Military Road in 1750, this

commemorated by a granite stone at the head of the glen. This route was modified and the A83 itself constructed in the 1930s, with some low level blasting evident in archive newspaper records (Arrochar Heritage, 2019).

Considerable investment has been made to implement mitigation measures at the site due to the high frequency of disruptive failures. A series of warning signs, called wig-wags were installed along the A83 in 2011 to warn road users of elevated landslide potential during periods of heavy rain (Winter *et al.*, 2013; Winter and Shearer, 2017). The most significant physical mitigation effort however has been the installation of debris flow catch nets above the A83 since 2010, to prevent major flow impact with road infrastructure and its users. Catch nets have reduced disruption by debris flows, inhibiting approximately half of the failures since their installation. The phenomena still proves to be disruptive however and further construction works are ongoing as of 2018. Further understanding of the debris flow phenomena and susceptibility is therefore particularly required to aid future mitigation works at RabT, but also at other potential sites that have the potential to be perturbed as a result of climatic changes. A large debris flow in October 2014 for instance was the largest

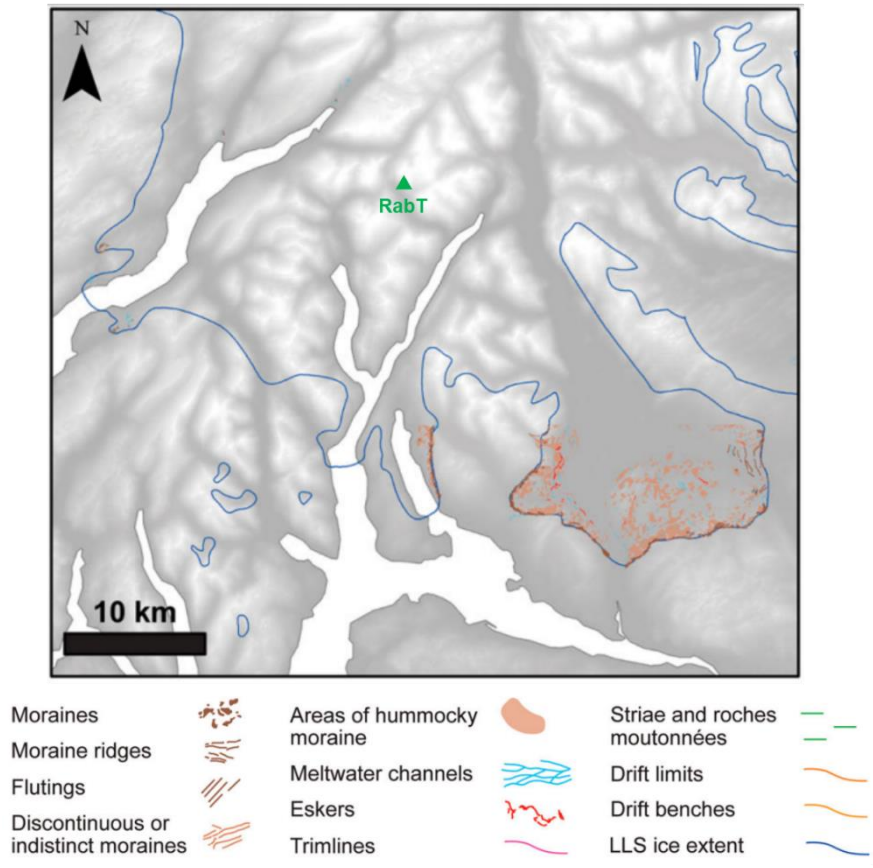

Figure 2.5 - A map of the maximum Loch Lomond Stadial (Younger Dryas) extent, modified from Bickerdike et al. (2016)

recorded at the site (>1,000 tonnes) and resulted in closure of the A83 despite the presence of a catch net along its runout path. Entrainment is considered to have played a major role in this event, potentially doubling the overall magnitude of the flow (Sparkes *et al.*, 2017), however the source and erosion process of this entrained material is not currently well understood. Gullying is known to play a major role in channelizing such flows, and accumulating entrainable materials, thus an understanding of the link between these forms, which are abundant at RabT (figure 2.4), and debris flow activity may be key to better mitigating against the debris flow geohazard.

2.2.1 Pre-monitoring spatial inventory

The location and extent of slope failures prior to April 2015 has been derived from archive photographs and reports generated by road operating companies (on behalf of Transport Scotland). Discernible features were cross-referenced with a hillshade model, derived from a 0.1 m resolution TLS Digital Elevation Model (DEM), and the source areas of these events were mapped. It was possible to map a total of fourteen failures, all of which are shown in figure 2.6. The smallest recorded event mapped measures 59 m^2 in area. It is highly likely that a number of events smaller than this have occurred at RabT, thus demonstrating the scope for monitoring to significantly benefit event records and to carry out more detailed inspection of the debris flow phenomena at the site.

Initial inspection of these mapped events indicates a degree of clustering, both spatially and temporally, with the three events to the top-left (north-west) of the slope all occurring within 16 months of one another for example. A second cluster is located to the right (south-east) of the figure, with three events occurring within fourteen months of one another. This cluster is neighboured by another event which occurred in 2008. A third cluster, near the centre of the figure, includes three events which occurred within two years of one another, as well as an event which occurred previously in 2007. This clustering is of interest because it may indicate some spatially variable control on the likelihood of failure, whether this be localised soil or lithological conditions (Lorente *et al.*, 2002), vegetation or hydrological variations (Beguería, 2006) or some other variable.

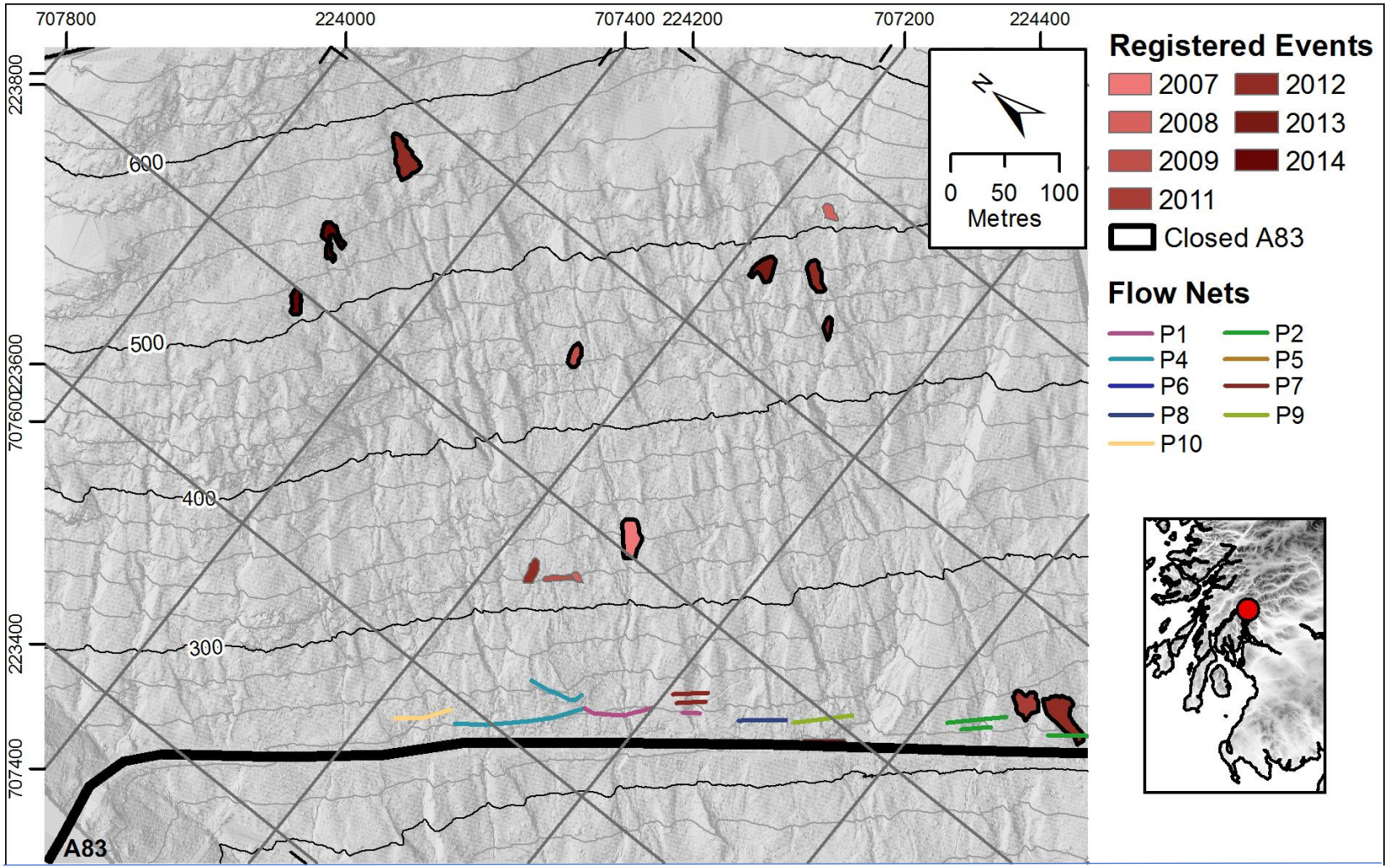

Figure 2.6 - A spatial inventory of events recorded at RabT prior to this research project. Nine of the thirteen mapped events have resulted in road closures.

2.2.2 Further mapping

A geomorphological map of RabT (figure 2.7) was drawn to highlight prominent geological and geomorphological features, as well as identify potential relict landslide scars prior to the events recorded and mapped in the spatial inventory. Twenty six relict scars have been mapped with high certainty thanks to the occurrence of prominent features, such as headscarps and lateral scarps, within the high resolution hillshade data. A further 31 medium certainty scars and 87 low certainty scars were also mapped. A higher proportion of scars is mapped to the north-west of the slope, much of the scars are interspersed with rock outcrops. The density of well incised gullies is also slightly higher towards this extent of the slope and reduces markedly from the centre of the figure and further towards the south-east. A variation in the length of these gullies is also notable, with some running up to the very top of the main slope portion (> 500 m a.s.l), where the drift cover thins and the slope angles begin to decrease. In contrast to the well-defined gullies to the north-west of the site, some of those to the south-east of the site are less developed and consist of truncated regions. The join of these truncated gully regions, with other gullies, is not so well defined and therefore hard to map with certainty.

Figure 2.8 shows an example of debris flow activity mapped away from the main slope, but just 3 km to the west. This activity indicates that the main RabT slope is not unique, at least regionally, and has received a particularly high degree of attention due to its proximity to, and impact on, the A83 trunk road.

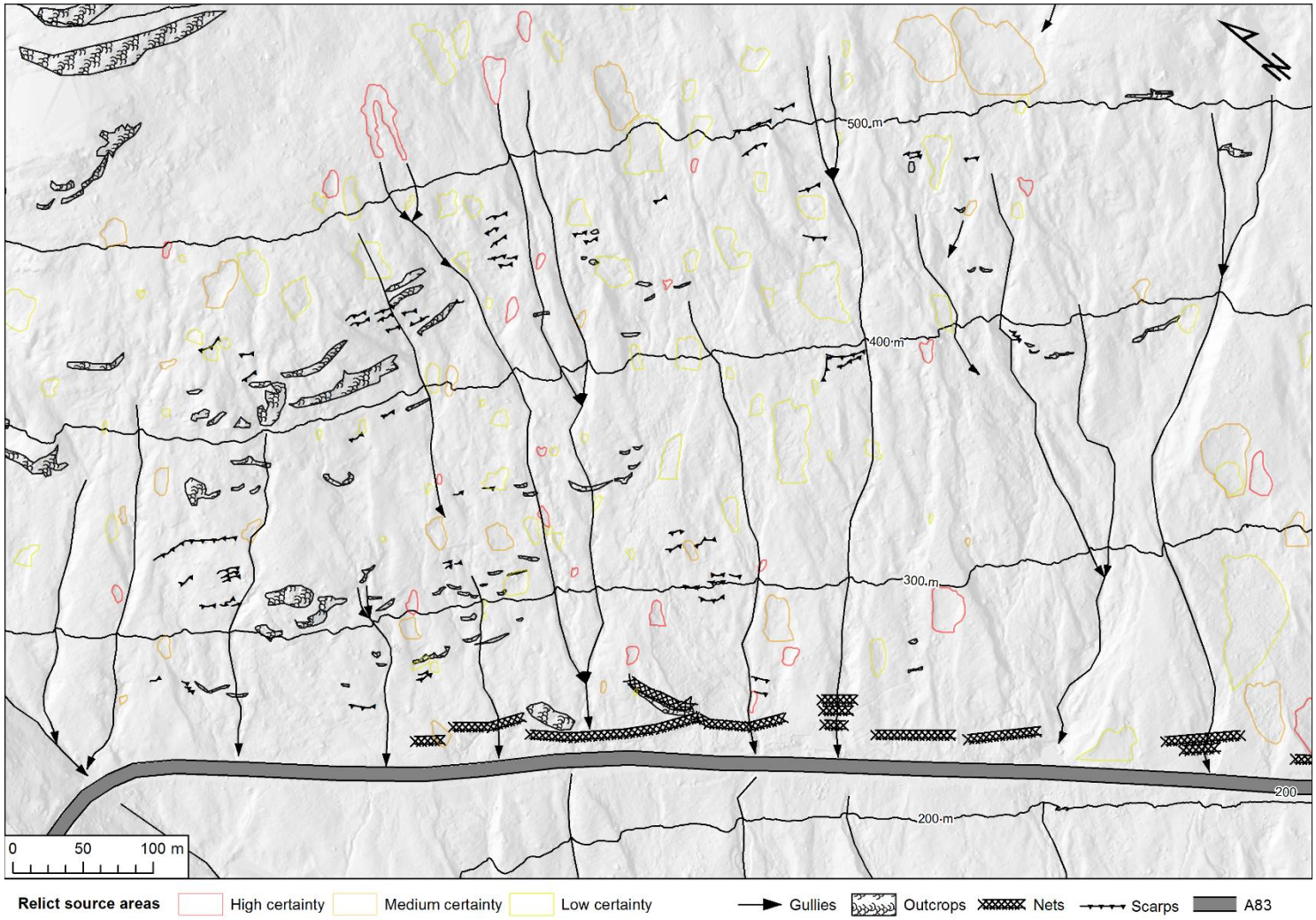

Figure 2.7 - A geomorphological map of RabT, with relict scars of high, medium and low certainty mapped.

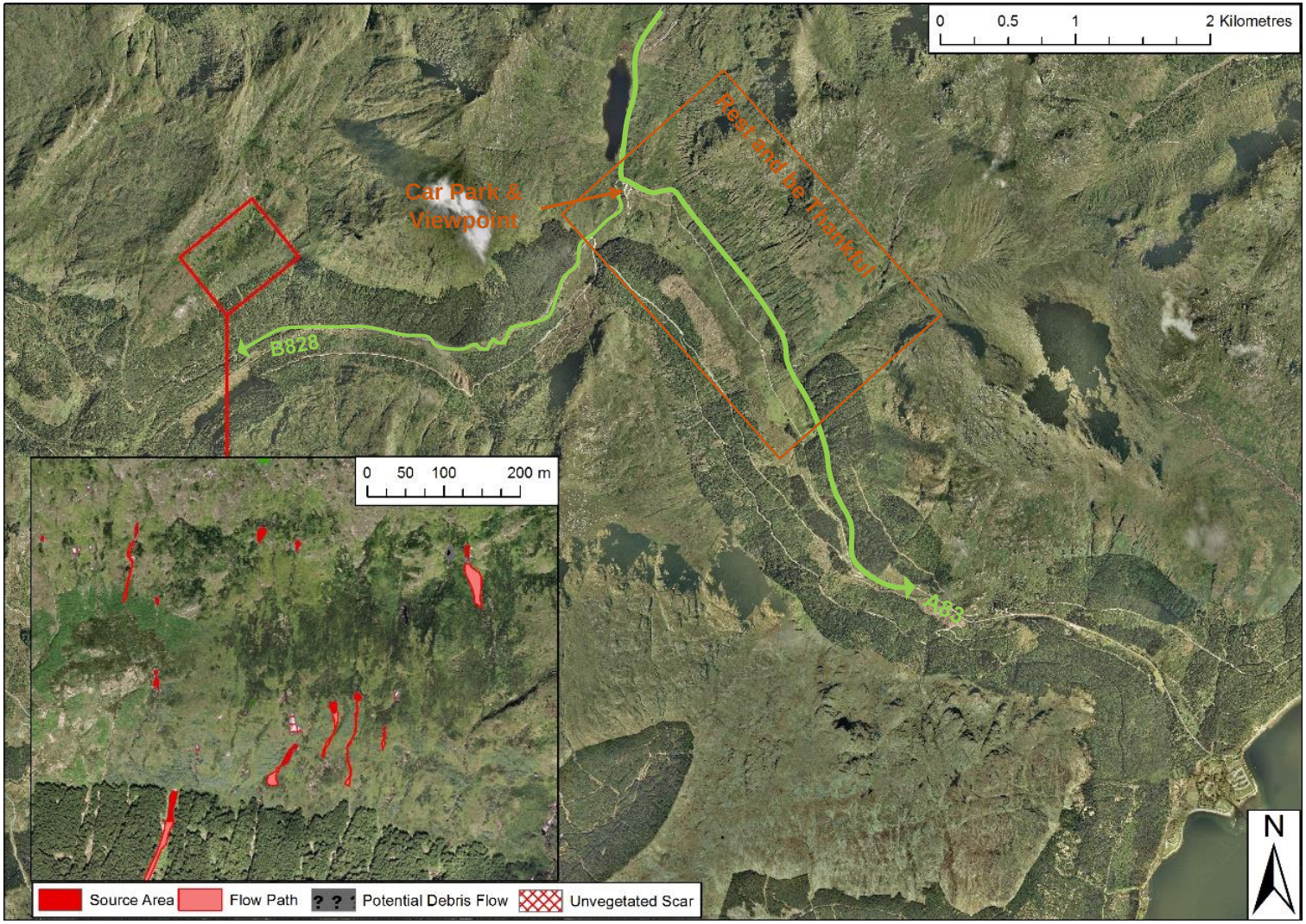

Figure 2.8 - An example of prominent debris flow activity, away from road infrastructure, within a few kilometres of RabT

2.3 Glen Ogle

Glen Ogle is located some 60 km north of Glasgow. The slope, subject to two of the largest recorded debris flows in Scotland, in 2004, is located on the south-west facing side of the glen, below which the A85 trunk road runs from Perth in the east to Oban in the west. The site is characterised by schistose bedrock covered by a layer of glacial drift deposits and colluvium. In contrast to RabT, established gullying is limited and only two continuous gullies are recognised within the study area. Small incised channels and hollows with gully potential are however recognised in inter-gully slope regions, thus future gully propagation may be possible. The slope is broadly a similar gradient to that of the RabT, although the source area of the largest debris flow in 2004 was a much smaller 21° (Milne et al., 2010), demonstrating that triggering mechanisms and conditions cannot always be constrained with ease.

Vegetation cover at the site is broadly similar to the RabT, with rife low to mid elevation Bracken (*Pteridium*) cover outside of the winter months, as well as some higher elevation Heathers (*Calluna Vulgaris*) which do not experience as much variable and rapid seasonal growth patterns. The slope is also occupied by isolated patches of dense deciduous trees, particularly around the smaller southernmost gully (2) described below.

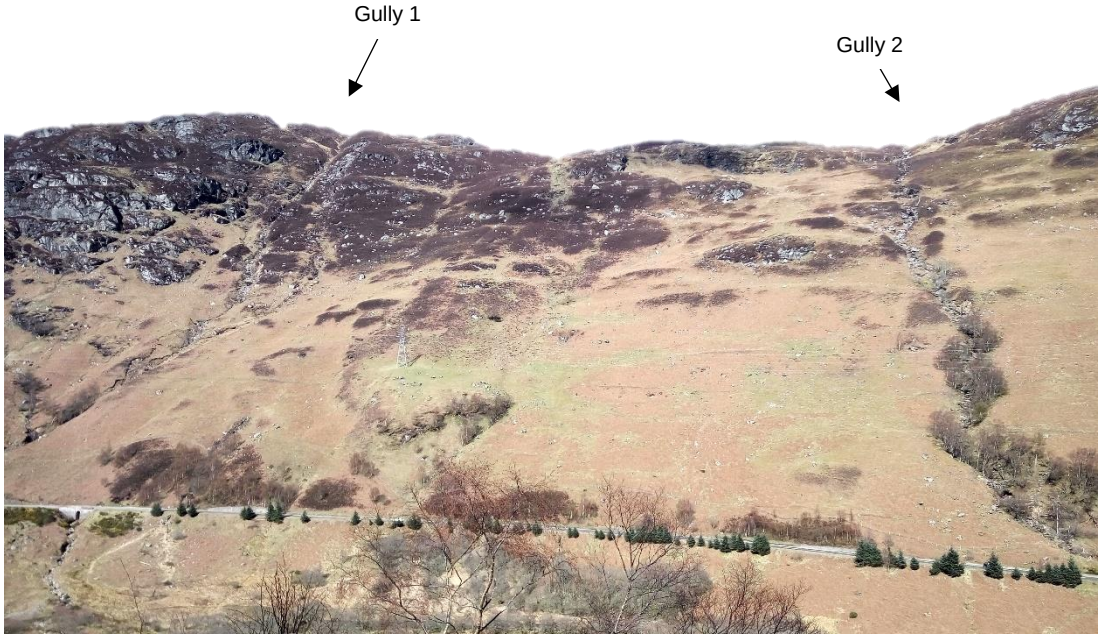

Figure 2.9 - A photo of Glen Ogle. The two main gullies subject to debris flow in 2004, between which a number of vehicles were stuck, are annotated to the left and right.

Figure 2.9 shows a photograph of the slope, in which the two main gullies are annotated. Gully 1 at the north-west extent of the slope played host to the largest debris flow in 2014,

which mobilised from a source area approximately at 600 m.asl. The failure entrained some 8,000 m^3 of material along gully 1 before impacting the A85 (Milne *et al.*, 2010). Another debris flow mobilised along gully 2 to the south-west, isolating some 57 people on the A85 between the two gullies (Winter and Shearer, 2017).

The large magnitude of the 2004 failures at Glen Ogle, and minimal activity since then, characterises the site as having a different magnitude-frequency to RabT. This is further evidenced by geomorphological mapping, from a high resolution hillshade model (figure 2.10) which indicates a much lower count of relict feature, such as prominent scars. Despite a low frequency of recent activity at the site, stratigraphic evidence suggests multiple instances of historic landsliding (Milne et al. 2009) and thus potential for future activity. Uncertainty about continuation of this trend, and hazard potential at the site, necessitates further characterisation however.

Milne (2008) found that a significant proportion of the large 2004 debris flow was derived from erosion and transport of gully material during the runout phase. Given the low frequency of hazardous activity at the site, the state of potential recharge of gully accumulations is of particular interest. Little is known about current activity at the site and whether it possesses the potential to yield further sediment on the scale of the events seen in 2004. The detection of potential gully accumulations, from sediment influxes or in-situ mobilisations, could for example characterise the site as akin to a 'sediment capacitor' whereby the gullies fill with material and periodically empty resulting in a large debris flow surge (Kean *et al.*, 2013). A wide number of alternative mechanisms could also be dominant, or indeed absent, of which this research aims to characterise.

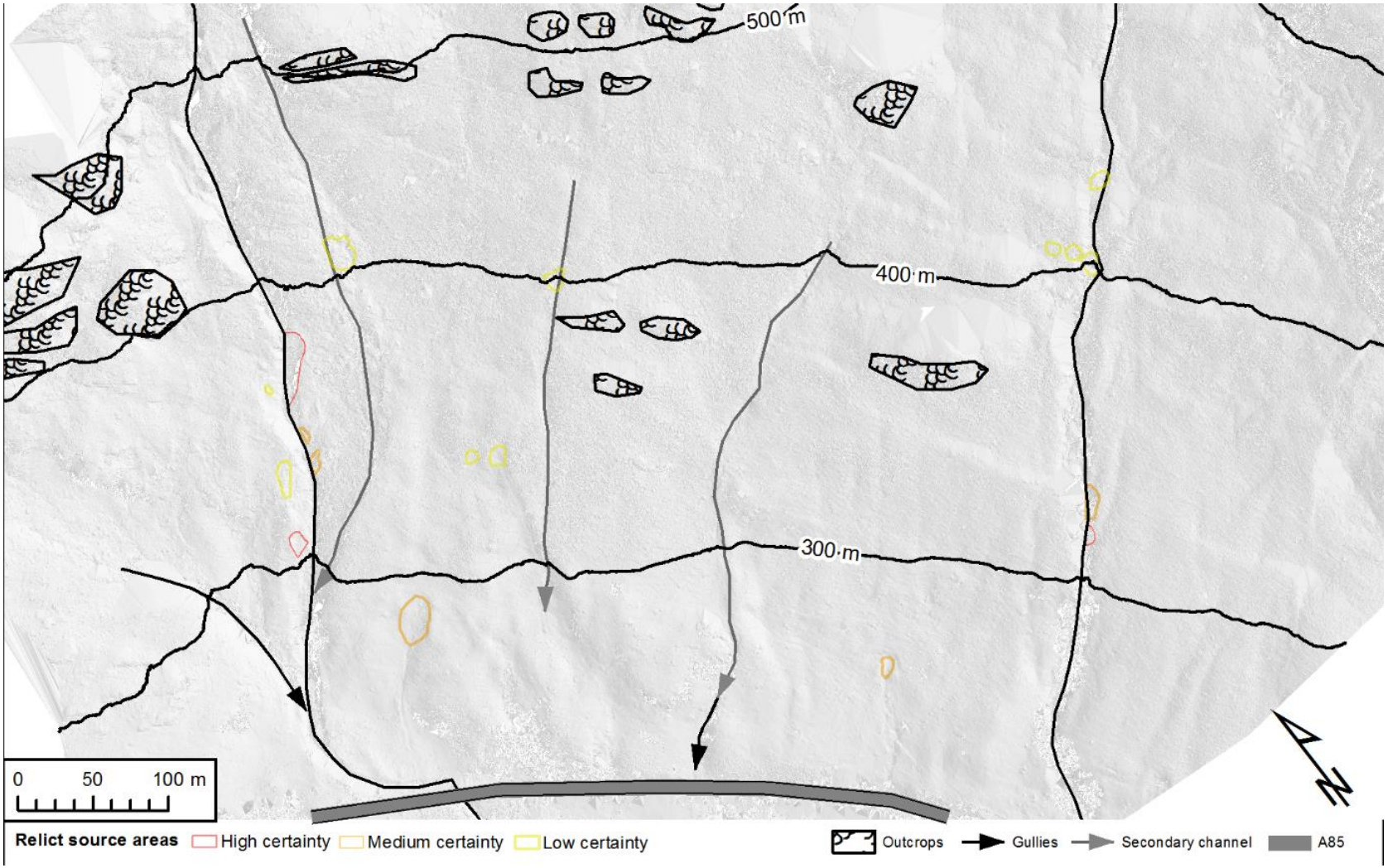

Figure 2.10 - A geomorphological map of Glen Ogle, with relict scars of high, medium and low certainty mapped.

2.4 Glen Coe

The pass of Glen Coe (A82) is located some 100 km north north-west of Glasgow, and just 18 km south of Fort William. The site is characterised by much steeper, primarily Andesitic, bedrock faces (BGS, 2018) with a number of incised gullies. Overlying sediments are limited to much coarser debris, with cones at the foot of the steep rock faces and alluvial fans emerging from below the gullies. Gullies throughout the Glen Coe pass also contain accumulations of degraded sediment. In contrast to both RabT and Glen Ogle, material at Glen Coe is coarse with limited fine grains. Much like Glen Ogle, the slopes are covered in widespread bracken and heather, with the latter particularly dominant amongst the higher and steeper rock faces. Deciduous trees are also present, although at a higher density than at RabT and Glen Ogle.

The pass is particularly popular with tourists, with popular resting points situated proximal to the slopes, raising concerns about the geohazard potential. The main pass of Glen Coe contains two main viewing points and car parks at which cars and coaches of tourists frequently park and caravans often reside. A small debris flow occurred to the west of the Glen Coe pass (NGR NN 21455 75707) in August 2014 and accumulations of material were identified by a Scotland Transerv engineer in December 2012 (above the car park at NGR NN 16801 56948 and at Achtriochtan Farm at NGR NN 15693 57149) (Personal comms, 2018).

A number of unvegetated debris fans indicate potential continual sediment reworking, although the magnitude and frequency of such activity is unknown. Little is also known about whether the overlying slopes are actively recharging these fans with fresh material. Should fresh accumulations or active reworking of existing material be taking place, this may pose an increased hazard. The same could be said of the gullies should these actively be accumulating material from the rock faces. A principal aim of this research is to again monitor such activity in order to characterise the activity and geohazard potential. It is hoped that the contrasting characteristics of the Glen Coe study site will shed light on a different set of processes to those operating at RabT and Glen Ogle, providing a better understanding of a variety of landslide geohzards.

2.5 Summary

Several studies have examined the incidence of slope failures across Scotland and the associated risks. The most detailed of these studies have examined specific events in detail, from on-slope investigations to laboratory based characterisations of events. One high level study in particular, the SRNLS, has looked nationally at the major factors which predispose slopes in Scotland to failure and pose a hazard. Such factors include large quantities of erodible glacigenic sediment, particularly in locations when located on steep and gullied slopes overlooking major trunk road infrastructure.

Thus far, there have been limited detailed studies into the geomorphology of debris flows at the individual slope level in Scotland, particularly in terms of their spatio-temporal distribution. For the most part, such studies have not been possible due to a lack of concentrated activity at one, or few, accessible sites, and the limited means to document, quantify and compare events. This has not been a problem unique to Scotland, as worldwide researchers have historically tried to recreate events in laboratory settings, in flume experiments for example. Whilst these experiments have been highly effective in examining the mechanics of individual runout events, there have been major limitations in characterising the interaction of events across a slope, including with other processes such as hydrology.

This chapter has demonstrated that highly active, accessible sites and regions have been highlighted by studies such as the SRNLS. With the provision of higher range and accuracy TLS techniques, it is possible to examine specific sites in greater spatio-temporal detail than previously possible. Three key sites with contrasting characteristics, such as magnitude-frequency of activity, have been selected for monitoring and characterisation, with RabT in particular representing a good opportunity to yield unique data on the debris flow phenomenon and its interaction with other events and processes at an individual slope scale. This opportunity is demonstrated by a pre-existing record of past events which has been collated into a map, this representing a good base to which further monitoring can be compared to build up a robust understanding of spatio-temporal debris flow activity.

CHAPTER 3

Characterisation of landslide dynamics, processes and hazard through remote monitoring of recently active slopes

3 Introduction

This chapter characterises landslide activity, particularly debris flows, through application of remote surveys and change detection. The understanding of landslide processes within a wider geomorphological context has previously been undermined by a lack of observation data, owing to the difficulty in observing the often sporadic natural phenomena in remote locations (Iverson, 1997). Characterisation of slope failures, particularly via quantification, has previously been limited by difficulties in accessing the steep terrain upon which they manifest (Bennett *et al.*, 2012). An incomplete record of landslides is a major weakness in quantitative assessment of hazard (van Westen *et al.*, 2005). With the adoption of mitigation techniques, such as debris catch nets, it is important to characterise the geomorphic behaviour of debris flows. Factors such as hillslope gully deposition are of major significance due to the widely-observed magnitude increases that can occur during debris flow propagation, when flows erode and entrain such sediment stores. Little is known about hillslope sediment budgets and gully recharge sources, yet knowledge of these is important and underpins our understanding of geohazard potential and severity (Milne *et al.*, 2010). Furthermore, questions remain regarding the role of debris flows as an agent of landscape change, although complete quantitative data from natural debris flows is required to support any laboratory or theoretical understanding (McCoy *et al.*, 2010). Spatio-temporal identification and recording, for an extensive landslide database is also important for analysis of trends, in rainfall intensity-duration studies for instance.

The use of remote sensing to investigate earth surface processes has increased significantly in recent years and has become a well-established discipline (Abellán *et al.*, 2016). Such techniques serve to shed light on many questions relating to the geomorphological factors driving landslides and characterisation of the phenomena to aid management strategies for

the geohazard. A number of techniques exist to detect and characterise different phenomena, including landslides. These range from individual geotechnical installations such as GPS (Gili *et al.*, 2000), extensometers (Herrera *et al.*, 2017), scour sensors (Berger *et al.*, 2011) and optical camera set-ups (Travelletti *et al.*, 2012), often targeted at singular large landslides, to sensor networks targeted at multiple zones deemed to be prone to failure, with the hope that displacement properties or environmental conditions can be recorded (Reid *et al.*, 2008). Ultrasonic and seismic signals have shown recent promise for the identification of event timings and surge behaviour, and have proven effective at ranges of over several kilometres (Arattano *et al.*, 2012; Kogelnig *et al.*, 2014). Such techniques can be useful for precise temporal identification and quantification of change in one or two dimensions, as well as for deployment in early warning systems, however they do have limited capabilities to measure and characterise smaller stochastic events across a wider area.

Remote sensing increasingly forms part of natural hazard management approaches (Corominas *et al.*, 2014) and 3D data collection has gained utility in standalone analyses (Collins *et al.*, 2007; Dunning *et al.*, 2009, 2010) as well as repeat monitoring projects (Lim *et al.*, 2005; Rosser *et al.*, 2005, 2007; Kasperski *et al.*, 2010; Abellán *et al.*, 2014; Kuhn and Prüfer, 2014; Kromer *et al.*, 2017). A new development in the former, is that of object identification, whereby data can be automatically analysed at a range of resolutions to recognise and characterise major morphological features (Van Den Eeckhaut *et al.*, 2012). Repeat monitoring has emerged as a particularly effective method to highlight previously unnoticed changes that may represent precursors or signal important geomorphological driving processes (Neugirg *et al.*, 2016). The capability of 3D techniques to capture data over a wide area is particularly useful for monitoring small shallow failures and debris flows, the domains of which can be difficult to anticipate and instrument.

The range of repeat monitoring techniques has developed significantly, from carefully calibrated photogrammetric techniques and slow single-pulse distance measurements, to rapid aerial and terrestrial laser scanning (ALS and TLS), multi-view stereo Structure from Motion (SfM) photogrammetry, Interferometric synthetic aperture radar (InSAR) and even high resolution spaceborne optics. The emergence of low cost and user-friendly SfM techniques (James and Robson, 2012; Westoby *et al.*, 2012) has prompted a number of research projects in the earth sciences. Kaiser *et al.* (2014) for example found TLS to be impractical when surveying gully erosion and development in rough terrain in Morocco, whereas SfM offered a lightweight, mobile solution which minimised shadowing issues. The SfM approach has been aided by improvements in low cost aerial platforms, however these

platforms are often necessary to cover wide areas (Glendell *et al.*, 2017) and are not always suitable or dependable depending on the environment and weather conditions. SfM is also heavily reliant upon a well distributed network of ground control points (GCPs), the deployment of which can comprise a significant portion of the survey effort (James *et al.*, 2017). SfM and photogrammetry have been criticised for shortcomings relating to changes in illumination conditions (Nadal-Romero *et al.*, 2015) and poor image quality (Carbonneau *et al.*, 2003), as well as centimetric accuracy which is not always suitable for deformation monitoring. InSAR offers a significant improvement in the monitoring of millimetric deformations of the earth's surface, whether conducted from a satellite (Strozzi *et al.*, 2005), including the use of reflectors (Froese *et al.*, 2008) or performed using a ground-based system (GB-InSAR) (Barla *et al.*, 2017). GB-InSAR is however prone to issues relating to large sudden changes (Kromer *et al.*, 2015), typical of shallow landslides, can be more complex to set up and offers a significantly lower spatial resolution compared to TLS (Abellán *et al.*, 2014).

TLS enables the collection of high resolution data over a wide area (Brasington *et al.*, 2012). Lim *et al.* (2005) for instance used a combination of photogrammetry and TLS along a hard rock cliff in Yorkshire and were able to collect data showing site-specific variations in erosion patterns, relatable to cliff geotechnical properties. Such findings demonstrate the utility of monitoring and provide a greater understanding of site-specific erosional regimes, allowing for more effective management practices to be carried out. Many researchers have used TLS to monitor in-channel distributions and fluxes of sediments due to the passage of debris flow (Bremer and Sass, 2012; Theule *et al.*, 2015). Schurch *et al.* (2011) for example studied erosion and deposition dynamics in the Illgraben debris flow channel using TLS, amongst other instrumentation, and found flow depth to exert a fundamental control on the magnitude of erosion as well as its distribution. Comparable studies on sources of material into such channels has been lacking however, with these often limited to techniques such as repeat stereophotogrammetry (Coe *et al.*, 1997; Veyrat-Charvillon and Memier, 2006) which is not particularly useful for identifying small changes (Perroy *et al.*, 2010). Studies such as that by Bremer and Sass (2012) have combined airborne laser scanning (ALS) data with TLS data to quantify debris flow erosion and deposition over a wide extent, however these have also been undermined in the detection of small changes due to large inherent errors. More recently, Loye *et al.* (2016) have demonstrated the benefits of a higher resolution TLS approach to monitor channel sediment influxes, important to debris flow discharge, from the hillslope zone, and found rockfalls to be a major contributor to accumulations.

TLS platforms are now capable of rapidly collecting data up to ranges of 6 km using technologies such as 'multiple time around' (MTA) processing implemented within the Riegl VZ line of terrestrial laser scanners (Riegl, 2017a and 2017b). This has opened up opportunities to reliably conduct change detection at distances in excess of several kilometres (Fey and Wichmann, 2017). Fischer *et al.* (2016) for example have recently been able to monitor annual changes in alpine glacier mass balances using a 6 km range scanner. TLS systems are also able to collect data at such a pace that oversampling can become problematic, resulting in large quantities of high-resolution data. Opportunities have been recognised in redundant data however, with de-noising and calibration capable of reducing the level of detection (LoD) to a similar accuracy as radar systems (Kromer *et al.*, 2015)

Reductions in the weight of Lidar systems has seen the more recent adoption of Unmanned Aerial Vehicle (UAV) based laser scanning (Glira *et al.*, 2016), which offers advantages such as a reduction in occlusion, however this is a relatively new approach undergoing continual development. Researchers are increasingly looking towards semi-permanent and permanent installations and automation of the change detection process (Williams *et al.*, 2017), with a view towards near-real-time monitoring applications (Kromer *et al.*, 2017). TLS platforms are also now capable of automatically augmenting 3D data with high resolution photographs, often using built-in cameras, however researchers also choose to supplement this data with additional installations (McCoy *et al.*, 2010), such as standalone cameras which can record higher temporal resolution data with minimal effort and cost.

Observations and records at RabT have previously been recorded in photographs and geotechnical reports, however these are frequently limited to those changes which have impacted infrastructure of which can be observed without the aid of specialist survey techniques. Medium to high magnitude events have captured attention, but by doing so they have skewed the appreciation of smaller events and the processes that underpin activity at all scales. Much like the surge in activity immediately after deglaciation (Curry, 1998), the renewal and recent upturn of slope activity in the Scottish Highlands provides a rare opportunity to observe and characterise the role of debris flows as an agent of paraglacial denudation and landscape evolution, as well as to characterise the geohazard. The provision of frequently active study sites and advances in long-range remote sensing techniques now provides a foundation on which broader more-detailed observations can be made and robust field evidence can be gathered. This research capitalises on that opportunity through the inter-annual and intra-annual monitoring presented herein.

3.1 Methodology

3.1.1 Terrestrial Laser Scanning (TLS)

Long-range laser scanners have been used to repeatedly survey each study site. A 2 km range Riegl LMS-Z620 has been used for most surveys, whilst two surveys were carried out with a 4 km range Riegl VZ-4000. Both scanners use the time-of-flight principle, which relies upon the emission and return of a near-infrared laser pulse, typically 500-600 nm wavelengths for terrestrial laser scanners (Dong and Chen, 2017). The overall travel time of this pulse is halved to calculate the travel distance based upon its known speed (Uren and Price, 2010), and this is subsequently multiplied by a manufacturer calibrated constant to account for atmospheric conditions. In test conditions, at range of 100 and 150 m respectively, Riegl provides accuracy values of 10 mm and 15 mm for the LMS-Z620 (Riegl, 2010) and VZ-4000 (Riegl, 2017b), with both scanners having a precision of 10 mm.

Each measurement results in a distance measurement, saved in X, Y, Z cartesian format, with the scanner representing the origin (0, 0, 0) by default. A collection of these points is referred to as a point cloud. Co-ordinates directly relate to the scanner's orientation and beam exit angle, the former of which is controlled using a panning mechanism and the latter of which is controlled by an internal rotating mirror. Riegl scanners also record the intensity of the returning pulse, which is governed by factors such as atmospheric conditions, target reflectance and surface orientation (incidence angle) relative to the scanner (Kaasalainen *et al.*, 2011).

The VZ-4000 and LMS-Z620 record with minimum angular stepwidth changes of 0.004° (Riegl, 2010) and 0.002° (Riegl, 2017b) respectively, with respective angular resolutions of 0.002° and 0.0005°. This spacing enables a high density of points to be collected, even at large ranges. The spacing of these points is often used as a direct measure of resolution, particularly optimistically by the manufacturers (Pesci *et al.*, 2011), however this overlooks the role of the laser beamwidth (Jaboyedoff *et al.*, 2012). The VZ-4000 and LMS-Z620 emit pulses, which emerge with circular footprints of 18 mm and 14 mm respectively (orientated perpendicular to the direction of travel). Beam divergence occurs at a rate of 0.00015 m/m for both scanners (Riegl, 2010, 2017). This divergence has the effect of increasing the beam width with distance, reducing the capacity for the scanner to resolve fine details at greater distances (Uren and Price, 2010). Scanners resolve measurements from the peak return of pulse energy (Pirotti *et al.*, 2013). Maximum pulse energy is concentrated towards the centre of the beam footprint and decreases radially outwards in a 2D Gaussian distribution (Teza *et*

al., 2007; Pesci *et al.*, 2011), thus measurements are typically centre-biased. However, if only the edge of the beam is reflected, and the scanner attributes this measurement to the centre of the beam, shape distortion can occur (Lichti *et al.*, 2005). According to Pesci *et al.* (2011), features measuring 1/3 of the beamwidth, or larger, should be discernible.

A point spacing equivalent to the beamwidth might notionally negate gaps between points, however centre bias of measurements invalidates this. Lichti and Jamtsho (2006) comment that major overlap of points, from low point spacing relative to the beam width, can result in blurring of fine features. They instead recommend an approach whereby the point spacing should be no more than 86 % of the beam width. This criterion is, however, most applicable to scenes where planar surfaces are orientated normal to the scanner. Schürch et al. (2011), for example, explain that incidence angles also affect the beamwidth, and thus the overlap of points is likely to vary with the complexity of the surface.

The older Riegl LMS-Z620 records discrete returns, i.e. one point per pulse emitted, whereas newer scanners such as the VZ-4000 are capable of full-waveform analysis (Dong and Chen, 2017), using echo-digitisation to delineate between layers spaced more than 0.8 m apart (Pirotti *et al.*, 2013), such as vegetation and the ground surface. This technology has proven particularly useful for forestry studies. Discrete return scanners can be unsuitable when surveying layered surfaces, such as sparse vegetation, resulting in the scanner resolving multiple points in the half-space between canopy layers or between the vegetation and the true ground surface, an effect commonly called 'Mixed Pixels' (Lichti *et al.*, 2005; Hodge *et al.*, 2009). The same effect can arise from echo digitization scanners however; in cases where surface layers are spaced less than 0.8 m apart, where normally the scanner would digitize two measurements, only one will be recorded somewhere between the multiple layers.

Variations in surface reflectance characteristics, such as roughness, darkness and moisture content, can affect point return distributions and quality (Pesci and Teza, 2008; Soudarissanane *et al.*, 2011), an effect which is exaggerated with increased incidence angles (Williams *et al.*, 2017). Increases in range will also decay the intensity of the pulse return, particularly when atmospheric conditions are poor. This is clear in point cloud data from older scanners, such as the LMS-Z620, where the reflectance values are uncalibrated. Newer scanners, on the other hand, correct the reflectance values, enabling direct comparison and classification of surfaces across the scene, regardless of range (Höfle and Pfeifer, 2007; A Abellán *et al.*, 2014).

A number of factors, including environmental conditions, will affect the precision and accuracy of a TLS survey, with multiple sources of uncertainty propagating to have a detrimental impact on the LoD. Although the impact of many of these factors can be reduced, through approaches such as point averaging, inherent systematic errors can only be rectified through repeat instrument and survey calibration (Kromer et al., 2015). One such approach is to perform self-calibration, the repeat surveying against a known reference point, from which an instrument can be adjusted until accurate measurements are resolved (Lichti et al., 2010).

Such activities are particularly important for studies demanding very high accuracies, in civil engineering applications for instance, however may not prove feasible in other applications where there are time constraints, where very high accuracies are not necessary, particularly given other influential factors in the environment and inherent in long-range TLS application. Quality checks, during the registration of congruent surfaces, may serve as an effective alternative to ensure instrument measurement consistency (precision) for the purposes of relative, rather than absolute, change detection routines.

3.1.1.1 Data Acquisition

A total of 35 surveying days were observed throughout the project (table 1), with approximately 46 individual surveys (discrete sites or sub-site surveys) completed over this time. Over 100 individual scans were collected over the course of the project.

Monthly and bi-monthly survey intervals were anticipated for the Rest and be Thankful (RabT) and the other two sites respectively. Insufficient windows of opportunity, owing to poor weather conditions at the desired time of surveys, proved problematic however. Data were instead collected as close to this regime as possible. The frequency of surveys at Glen Ogle (GO) and Glencoe (GC) were reduced due to lower than anticipated levels of detectable change. Focus was shifted to data collection around the winter months which have historically exhibited greater levels of slope activity.

Table 3.1 - Observed survey days numbered sequentially from earliest to latest. Survey days at Glencoe included between two to three surveys owing to the individual single-scan setups and discrete sub-sites.

	2015												2016												2017												2018			
	1	2	3	4	5	6	7	8	9	10	11	12	1	2	3	4	5	6	7	8	9	10	11	12	1	2	3	4	5	6	7	8	9	10	11	12	1	2	3	4
RabT			1	3			5		8	10		13		14		16	19		21		22		25	27	29	30		21							34		35			
Glen Ogle			2	4			6		9	11						17	20				23		26					32												
Glencoe							7			12				15		18					24			28				33												

3.1.1.2 Site-specific survey set-ups

Point spacings were primarily chosen based upon the highest feasible resolution within the given time constraints. Stipulated spacings remained constant, to ensure consistency, despite occasional use of the much faster Riegl VZ-400. However, it is considered that more optimal point spacings (86 % overlap) would have been regularly achievable using the VZ-4000. The largest consequential point spacing, for all three study sites, was 0.096 m (600 m range) at GO. In comparison, the smallest event recorded at RabT, prior to monitoring, measured 59 m^2 (equivalent to a 7.7 x 7.7 m idealised square). A regularly subsampled point cloud of 0.2 m spacing, is more than adequate for the detection of changes measuring < 0.1 m^2, although it is worth noting that later processing increases the minimum detectable change footprint. That said, changes of a similar magnitude are still realistically detectable.

Given that shallow landslide magnitude frequency studies are often bound by a lowest magnitude in the order of 1-10 m^2 (Larsen *et al.*, 2010; Gao *et al.*, 2018) and 10 m^3 (Francesco Brardinoni and Church, 2004; Stoffel, 2010), a maximal point spacing of 0.096 m is considered more than adequate to detect changes much smaller than previously recorded across Scottish study sites. In some cases, high resolution surveys required separate scan datasets, per position, due to computational limitations (RAM related). Some surveys were also split, or stopped altogether and resumed, to avoid short-lived inclement weather conditions which reduced point returns and overall data quality.

RabT (A83)

Surveys were conducted from two scan positions, both opposing the slope (below Beinn Luibhean). These positions are shown in figure 3.1, in which the visibility from each position has been modelled using a 5 m resolution NextMap digital elevation model (DEM). A combination of both scan positions results in good overall slope coverage with minimal occlusion. These scan positions were supplemented by a third position (antenna shown to the west of figure 3.1), at OSGB coordinates 229500 707180. Table 3.2 summarises all of the surveys, the scan positions and instrument utilised.

Table 3.2 – A detailed collation of the survey dates, scanning apparatus and positions utilised. The survey # relates to that shown in table 3.1

Survey #	Date	Scanner used	Plinth scan position	Station scan position	Third scan position	Comment
1	17/03/15	LMS-Z620	✓	✓	✗	Scanner vibration
3	20/04/15	LMS-Z620	✓	✓	✗	Scanner vibration
5	29/07/15	LMS-Z620	✓	✓	✓	
8	08/09/15	LMS-Z620	✓	✓	✓	
10	16/10/15	LMS-Z620	✓	✓	✓	
13	06/12/15	LMS-Z620	✓	✓	✓	
14	11/02/16	LMS-Z620	✓	✓	✓	
16	19/04/16	LMS-Z620	✓	✓	✓	
19	24/05/16	LMS-Z620	✓	✓	✓	
21	26/07/16	VZ-4000	✓	✓	✓	
22	19/09/16	LMS-Z620	✓	✓	✓	
25	26/11/16	LMS-Z620	✓	✓	✓	
27	17/12/16	LMS-Z620	✓	✓	✓	
29	29/01/17	LMS-Z620	✓	✓	✓	

30	03/02/17	LMS-Z620	✓	✓	✗	Limited weather window
31	27/04/17	VZ-4000	✗	✓	✓	Plinth data corrupted (MTA)
34	16/11/17	LMS-Z620	✓	✓	✓	
35	23/01/18	LMS-Z620	✓	✓	✓	

Instrument stability was a concern (Hartzell *et al.*, 2015), particularly owing to the large scan ranges and the potential for small movements to propagate into large offsets. Data collected in March 2015 was found to contain a significant vibration signal during registration. This related to windy conditions and the small point of contact between the laser scanner and a tribrach. Subsequent surveys were thus carried out using a wide (levelled) tripod base, but with the scanner directly mounted onto the tripod plate for a more stable configuration. Data were acquired using a stipulated point spacing of 0.18 m at a range of 1,000 m (approximately the centre of the slope), equivalent to 37 pts / m^2. This required an average angular stepwidth of 0.01°. Laser pulse divergence (Riegl LMS-Z620) resulted in a normally orientated footprint diameter of 0.164 m at a range of 1,000m.

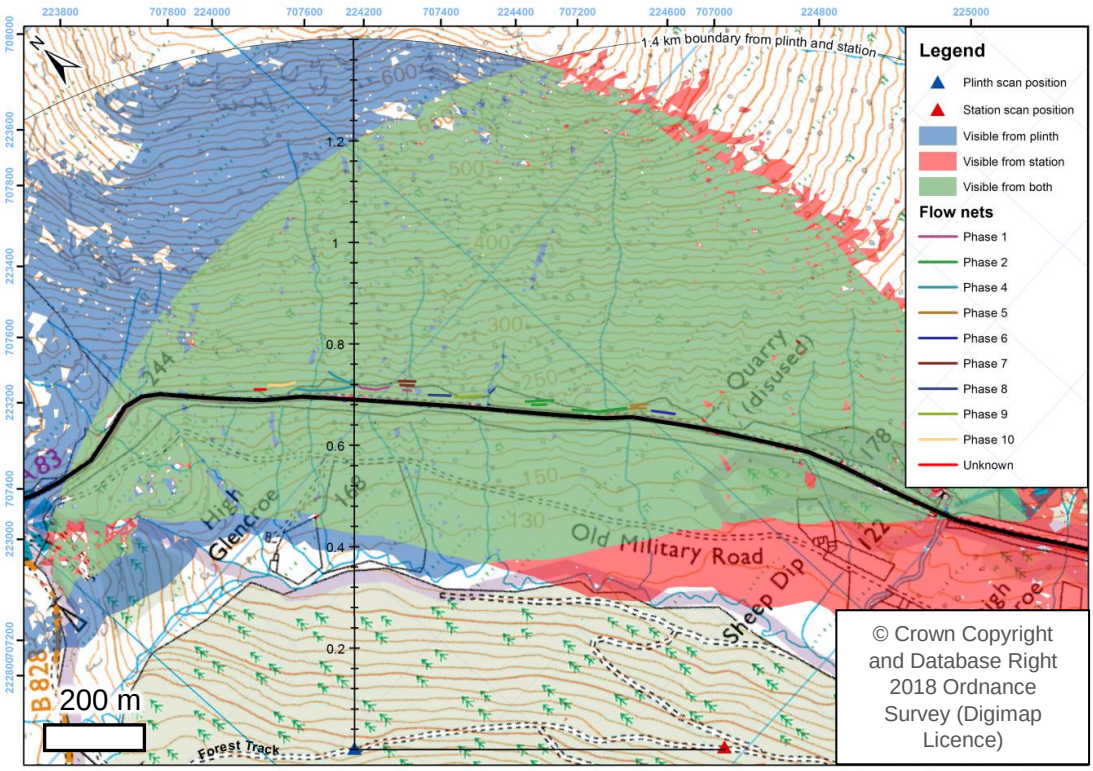

Figure 3.1 - Viewshed analysis for the RabT. 2D scan distances are represented by the vertical scale bar, although this does not account for difference in height between the scan position and different regions of the slope. For example, parts of the slope towards the 1.4 km 2D boundary are at an elevation of around 600 m, ~350 m higher than the scan positions, thus the actual 3D straight line distance is 1443 m.

A smaller point spacing, of 0.141 m, would have satisfied Litchi and Jamtsho's (2006) recommendation of an optimal 86 % beam footprint overlap, however it was not possible to regularly achieve this with the LMS-Z620, given time and weather constraints. It is considered that regular use of the VZ-4000 would have enabled fulfilment of this criterion, however this would have only been satisfied for a narrow elevation band, due to the sloping nature of the study site. This would have also varied more for oblique scan positions. Furthermore, Pesci *et al.* (2011) found that an 86% overlap recommendation was somewhat pessimistic, with a resolution 1/3 the beam width achievable. Thus the optimal resolution may have conceivably been much higher and far beyond what was feasible. Single surveys yielded data with small gaps between points, spanning approximately 0.016 m at a range of 1,000 m. These gaps shrink with decreased range, and disappear below a range of 500 m (as shown in figure 3.2).

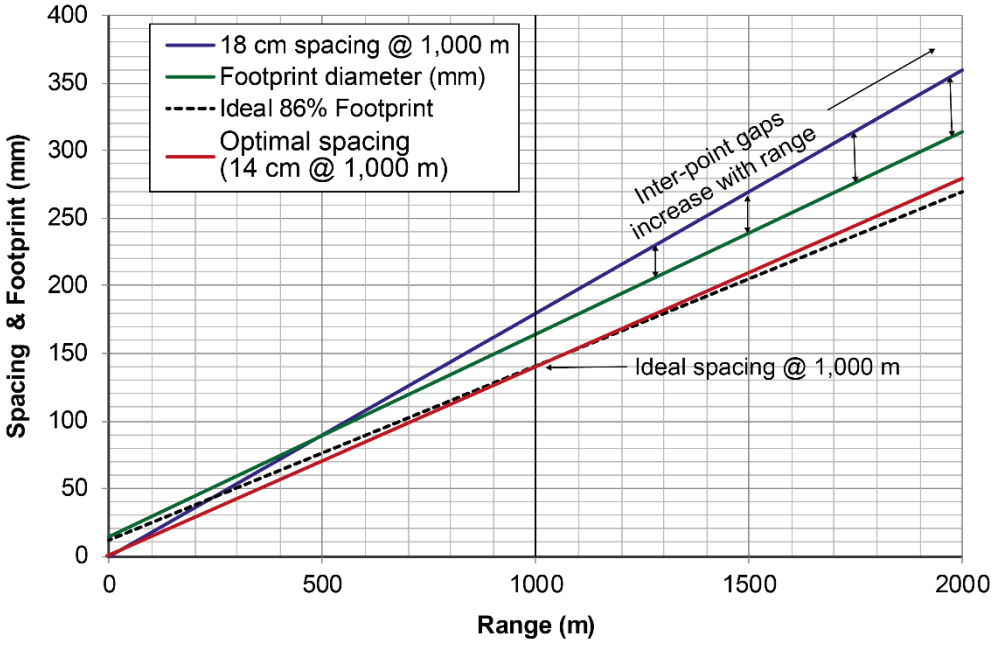

Figure 3.2 - A plot showing the increase in inter-point gaps, from a range of ~ 500 m , due to the laser beam divergence increasing at a smaller rate, per metre, than that of the point spacing. The red line signifies the ideal point spacing of 0.14 m at 1,000 m range, although this was not regularly achievable in this study and, despite the offset being relatively small, would have only ensured the optimal 86 % footprint overlap within a narrow range band due to the sloping nature of the site.

Minimal gaps were also desired at higher elevations, in order to detect small changes which may be occurring at a sub-decimetre scale (Lichti and Jamtsho, 2006; Pesci *et al.*, 2011). Merging non-coincident points, from multiple positions, reduces these gaps. Whilst this improvement has not been quantified, it can be observed when comparing individual point clouds with merged point clouds (figure 3.3). This oversampling, or 'correlated sampling', can reduce resolution limitations from single scan sampling intervals, limiting the final data resolution to the equivalent of the beam footprint size (Milenkovic´ et al., 2016).

Pesci *et al.* (2011) reported no significant decline in data quality from oversampling, and alluded only to the unnecessary time wasted in collecting such data. Significant overlap between points, has however been shown to result in blurring of fine details elsewhere (Lichti and Jamtsho, 2006). This prompted Nguyen *et al.*, (2011) to subsample their data, an approach of which was replicated in this study and is discussed later in this chapter.

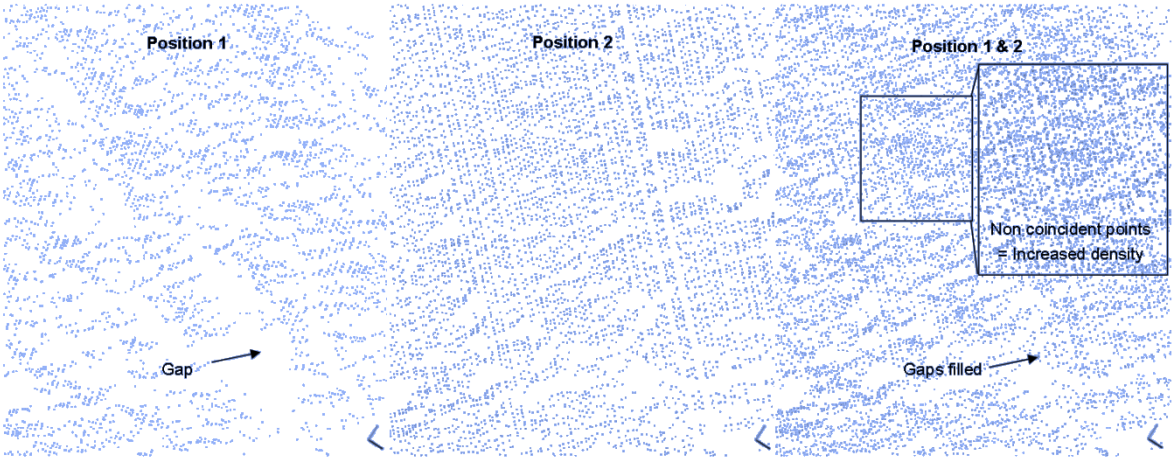

Figure 3.3 - A demonstration of how non-coincident points, from multiple positions, can increase the effective final point density.

Glen Ogle (A85)

Surveys at GO were conducted from the opposite side of the glen to the slope on which two major debris flows occurred in 2004 (figure 3.6). A breakdown of the surveys, instrument and positions utilised, are shown in table 3.3.

Oblique features, particularly gullies, again necessitated a multi-station set-up (shown in figure 3.4) to acquire adequate survey coverage. The majority of the slope was within 1 km of the four scan positions, although a 1.4 km radius (the same as that included in figure 3.1 for RabT) is included in figure 3.4 for context. A point spacing of 0.016 m, at a range of 1,000 m, was again adopted for consistency with that used at RabT. This again resulted in a point density of approximately 37 pts / m^2.

Table 3.3 - A detailed collation of the survey dates, scanning apparatus and positions utilised at Glen Ogle. The numbered positions are detailed in figure 3.4

Survey #	Date	Scanner used	Position 1	Position 2	Position 3	Position 4
2	18/03/15	LMS-Z620	✓	✓	✓	✗
4	21/04/15	LMS-Z620	✓	✓	✓	✓
6	30/07/15	LMS-Z620	✓	✓	✓	✗
9	09/09/15	LMS-Z620	✓	✓	✓	✓

11	17/10/15	LMS-Z620	✓	✓	✓	✓
17	21/04/16	LMS-Z620	✓	✓	✓	✓
20	25/05/16	LMS-Z620	✓	✓	✓	✓
23	22/09/16	LMS-Z620	✓	✓	✓	✓
26	25/11/16	LMS-Z620	✓	✓	✓	✓
32	28/04/17	VZ-4000	✓	✓	✓	✗

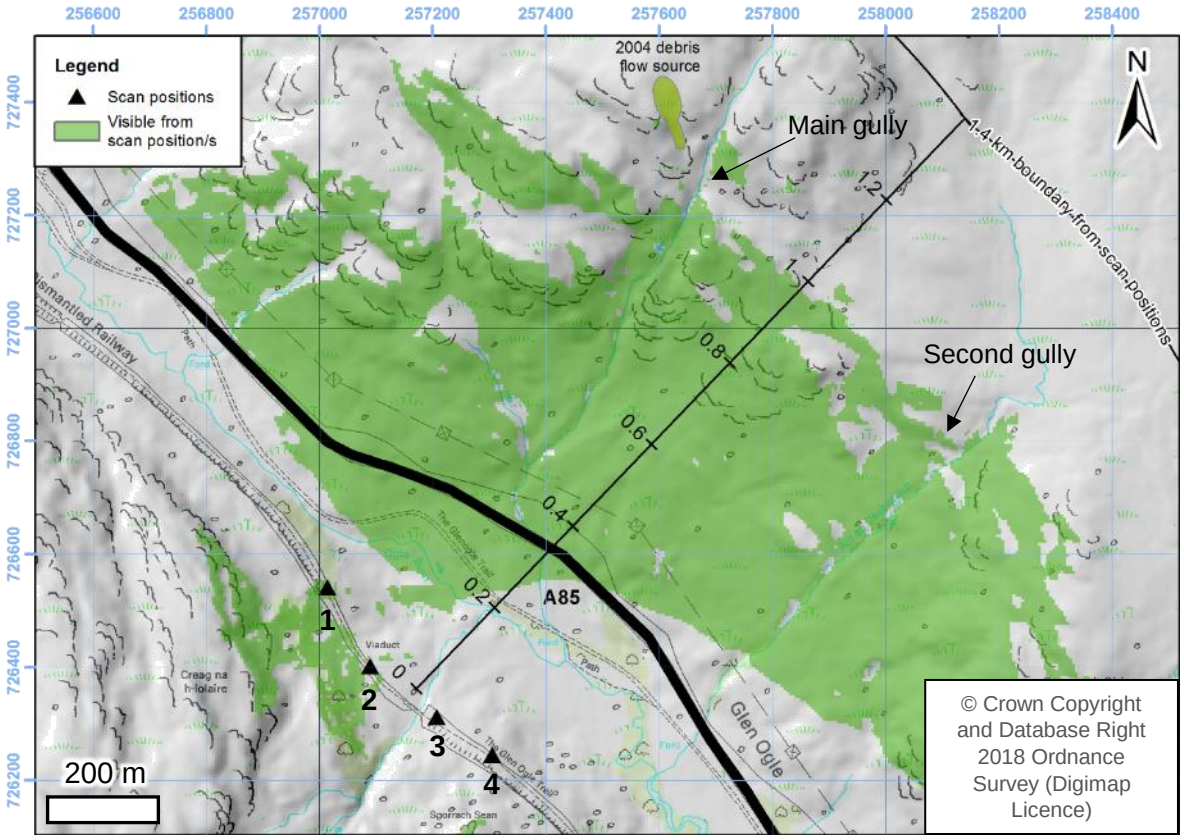

Figure 3.4 - Viewshed analysis (based upon NextMAP DEM) and scan positions for Glen Ogle. 2D scan distances are represented by the diagonal scale bar, but again this does not represent the true scan distance accounting for elevation.

Glencoe (A82)

Glencoe (GC) contained three separate areas of interest (AOI), necessitating three scan positions. These include two resting points (car parks) to the east of figure 3.5 (1 & 2), above which steep slopes and debris cones are found, and a hazard to road users is potentially anticipated (Scotland Transerv and Transport Scotland, 2012). A further site to the west, close to Achtriochtan farm (3 in figure 3.5), was also surveyed to encompass a seemingly active alluvial fan headed by steep rock faces intersected by deep gullies. This area is characterised by coarse un-vegetated deposits, incised by multiple streams.

Multi-station surveys, at each sub-site, were deemed of limited additional benefit and were not adopted due to time and access constraints. Resultant data for the main areas of interest, the debris fans and cones, were occluded in places, although the resultant data was deemed adequate for the identification of major changes, particularly in close proximity to the road and on rock faces. Table 3.4 summarises all of the surveys across the three positions.

The GC AOIs encompassed wide fields of view (FoV), thus requiring significantly longer scan times than RabT and GO. The AOIs were closer (within 600 m), thus a lower point spacing of 0.33 m, at a range of 1000 m (0.198 m at 600 m; equivalent to ~26 pts / m^2), was adequate to capture a similar point density to the other sites. Whilst the interpoint spaces were larger than those at the previous two sites (0.096 m), they are considered small relative to the desired magnitudes of detectable change, particularly rockfalls which Abellán *et al.* (2011) only detected down to a magnitude of around of 1 m^3 . Other studies have detected much smaller rockfalls (Rosser *et al.*, 2005; Santana *et al.*, 2012; Williams *et al.*, 2017), although at much smaller ranges, often in sparsely vegetated environments. For context, if a rock mass spanning 0.5 m x 0.5 m (idealised as a square i.e. later in figure 3.19) were to detach from a rock face at a range of 600 m from the laser scanner, the number of points covering the area would range between approximately four and nine (16 - 36 pts / m^2), thus any change of this magnitude would likely be identified in subsequent change detection processing where a density filter of 5 pts / m^2 is applied. Detection of ~1 m^2 sized changes on the slope would be considered a major improvement over current records of small mobilisations emerging at road level, at Glencoe, in the order of > 10 m^2 (Personal comms). Furthermore, it is not clear whether larger failure are still actively occurring at Glencoe, as these have not been recently recorded by road maintenance authorities.

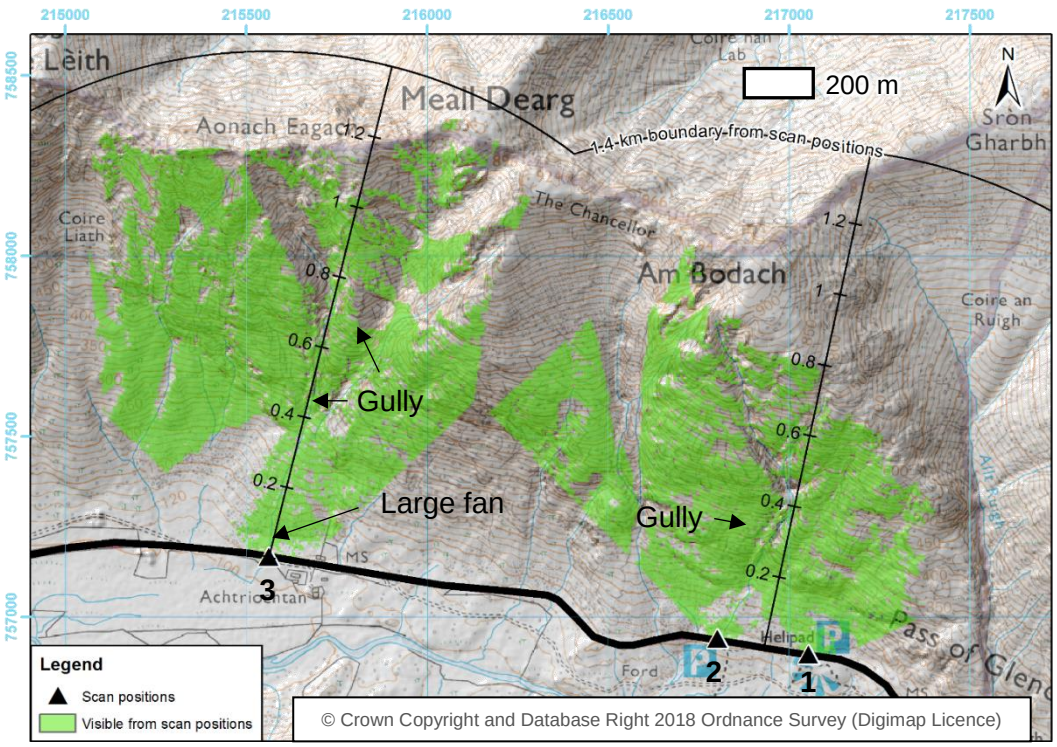

Figure 3.5 - Viewshed analysis (based upon NextMAP DEM) and scan positions for Glencoe (numbered). 2D scan distances are represented by the sub-vertical scale bars, but again these do not account for elevation

Table 3.4 - A detailed collation of the survey dates, scanning apparatus and positions utilised at Glen Ogle. The numbered positions are detailed in figure 3.5

Survey #	Date	Scanner used	Position 1 (stop)	Position 2 (stop)	Position 3 (fan)	Comment
2	30/07/15	LMS-Z620	✓	✓	✓	
4	18/10/15	LMS-Z620	✓	✓	✓	
6	13/02/16	LMS-Z620	✓	✓	✓	
9	21/04/16	LMS-Z620	✓	✓	✓	
11	22/09/16	LMS-Z620	✓	✓	✓	
17	17/12/16	LMS-Z620	✓	✓	✓	
20	28/04/17	VZ-4000	✓	✓	✓	

Figure 3.6 shows a final map of all three study sites and the respective scan positions for each. Here the relative scales of each site can be better appreciated, with the pass of Glen Coe being particularly large, justifying the need for multiple individual scan positions.

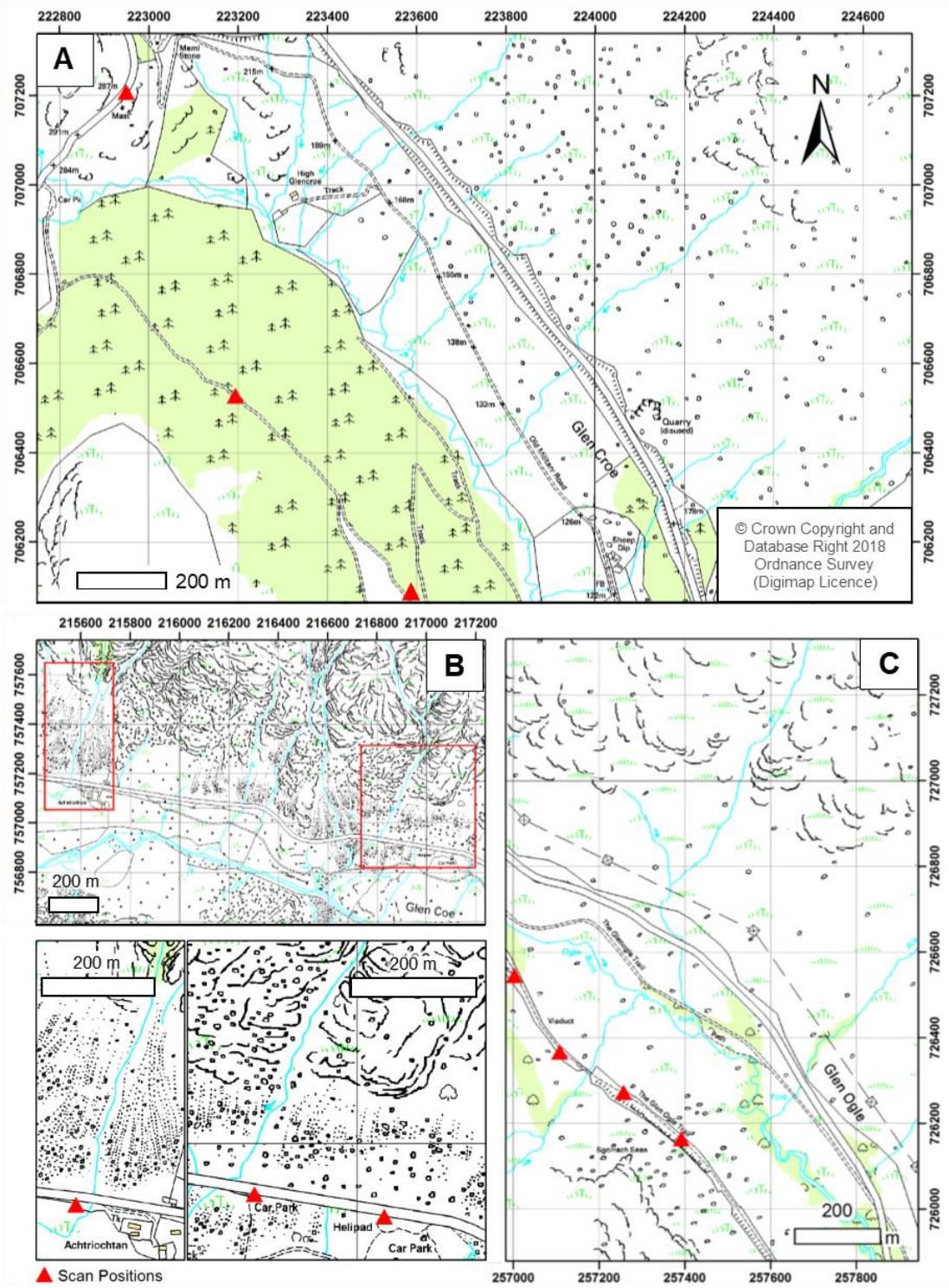

Figure 3.6 –Scan positions across all three study sites A) The Rest and be Thankful, B) Glen Coe and C) Glen Ogle

3.1.1.3 Scan Co-Registration

Multi-station surveys at RabT and GO required co-registration to assemble complete site-wide point clouds. Use of targets, as tie-points, is common in laser scanning studies (Giussani and Scaioni, 2004; Schürch *et al.*, 2011; Montreuil *et al.*, 2013; Liang *et al.*, 2014; Goodwin *et al.*, 2016), particularly to avoid a large contribution to the eventual cumulative error, uncertainty, or propagation of variances. Target positions can be difficult to resolve in long-range applications however, particularly as scan resolutions are generally lower (Corsini *et al.*, 2013) and beam widening occurs, typically rendering the approach ineffective (Akca, 2007).

An iterative closest point (ICP) algorithm (Besl and McKay, 1992) matches contiguous planes, or points, within triangulated sub-sets of an overall point cloud, and aims for the lowest possible standard deviation (plane to plane distance) in each iteration. This approach has been deemed effective at long ranges (Fey and Wichmann, 2017) and was thus the favoured approach in this study. A plane matching approach, implemented in RiScan Pro v 1.5.9 (Riegl, 2011), was utilised in this case.

Multi-station

Surveys at RabT and GO were registered to central reference clouds. The central scan position was used as the base for multi-station registration (left and right survey positions) as this minimised variation in incidence angle between the scans for ICP registration and maximised the overlapping area. This is in contrast to registering the left scan to the right scan for example, where the overlapping zone would be minimal and incidence angles would have varied significantly, potentially negatively affecting the registration effort.

Point clouds were first cleaned of moving objects, reflection and solar radiation artefacts in order for these not to be factored into the ICP process. High resolution fine scans were then coarsely registered within the software package RiScan Pro v 1.5.9 (Riegl, 2011) using four well distributed and contiguous control points. These were typically the corners of man-made features, such as buttressing walls. A coarse registration with a standard deviation of less than 1 m was deemed satisfactory, as this allowed subsequent refinement using RiScan Pro's ICP algorithm.

Spatially distributed point cloud sub-sets were chosen to avoid spatial bias and minimise over-reliance on zones of lower accuracy (high-range and obliquity areas for example). Subsections containing minimal vegetation were chosen to avoid irregularities related to variable laser penetration from different scan positions. Clean regular surfaces, such as rock

faces, were instead preferred, particularly as large beam footprints are largely inconsequential in such areas. A variety of surface orientations were chosen to ensure alignment on all three axes. Registrations were verified using cross-section profiles, of distributed surfaces of varying orientation, within the software package Quick Terrain Modeller (QT).

Interval-to-interval

Following multi-station registration, point clouds were merged and imported into a temporal registration project in Riscan Pro. Data were subsequently registered using the same approach outlined above. The first survey dataset, with minimal seasonal vegetation signal, was used as the base scan, to which every successive survey was registered to. This is in contrast to Schürch *et al.* (2011), who favoured sequential alignment of temporal scans, to ensure the optimal matching and minimal error introduced by an accumulation of changes from the first scan dataset.

The approach used in this study was at the cost of overall positional accuracy owing to compounding errors and potential drifting of sequential scans over time (Williams *et al.*, 2017), however this was not considered a major problem in this study, especially as changes only tend to affect a discrete element of the slope over shorter monitoring time-spans. Instead, known changes and areas of fluxing vegetation were omitted from temporal co-registration. The benefit of this base survey registration approach was that it minimised vegetation signal and allowed any survey to be compared to another, whereas a sequential survey technique, such as that used by Schürch *et al.* (2011), may have introduced a drifting effect in the case of large time differences between surveys.

As with the multi-station adjustment, a good distribution of cross section profiles, through all co-registered datasets (using QT), were analysed to verify registrations. Cross-section profiles were again used to verify the registration quality. An example of the features used at RabT, and their respective cross-sections, is shown in figure 3.7.

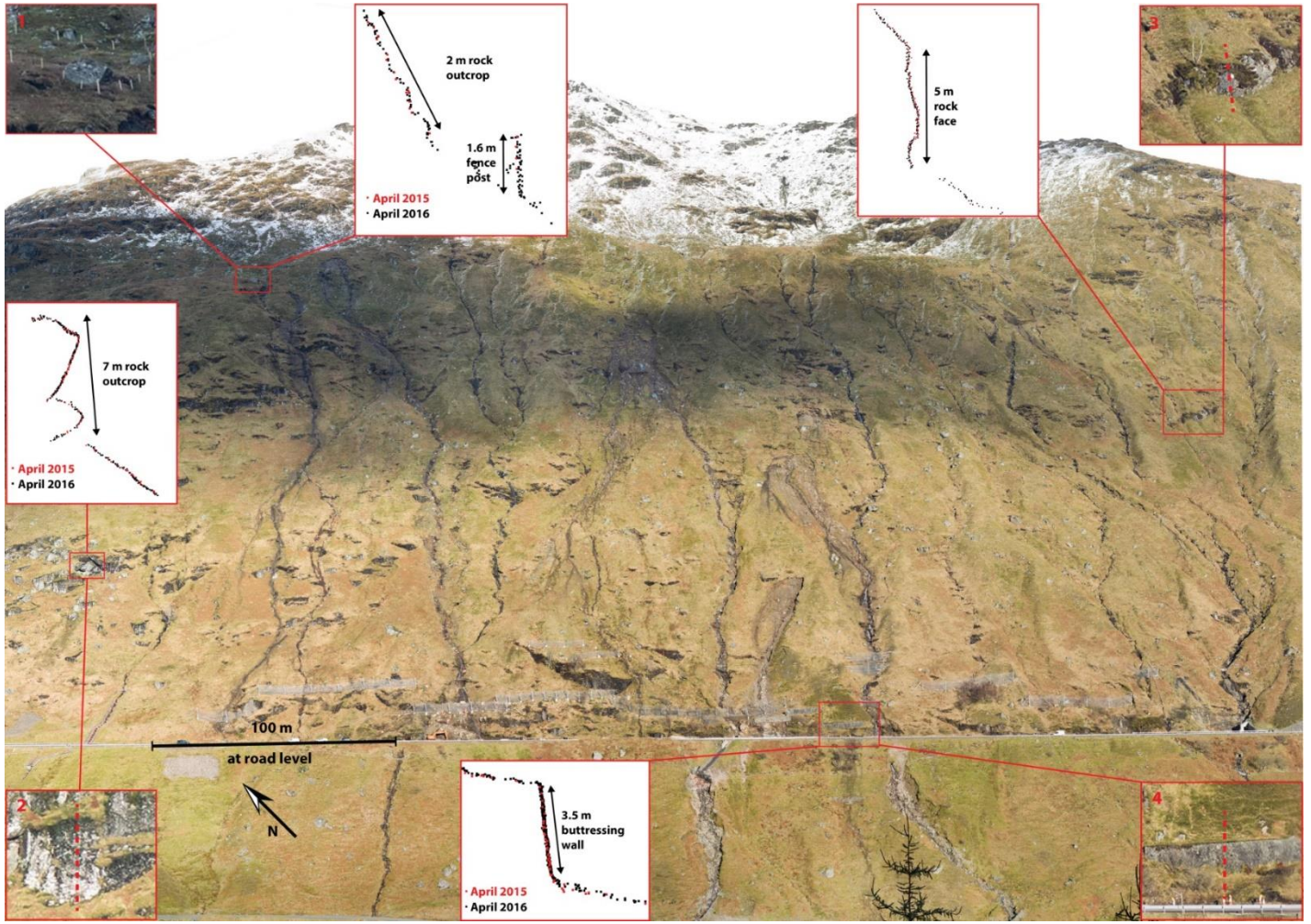

Figure 3.7 - A sample of the surfaces used for validating good scan co-registration (April 2015 to April 2016 in this case). These incorporate well distributed features, with faces orientated in different directions, to maximise the optimal point cloud alignment on all three axes.

3.1.1.4 Post-processing

Perennial vegetation was manually clipped from the data, using the CloudCompare v 2.9.1 (2018). roughness field as a guide, due to it either completely obscuring the true ground surface or producing mixed pixels. The same areas were clipped in future datasets, using these points as a mask with the Cloud-to-Cloud (C2C) distance tool. Artificial features, including catch nets, were also clipped from the datasets. An automated algorithm, CANUPO (Brodu and Lague, 2012), was trialled for this, but was not effective with the given scan resolutions at large ranges.

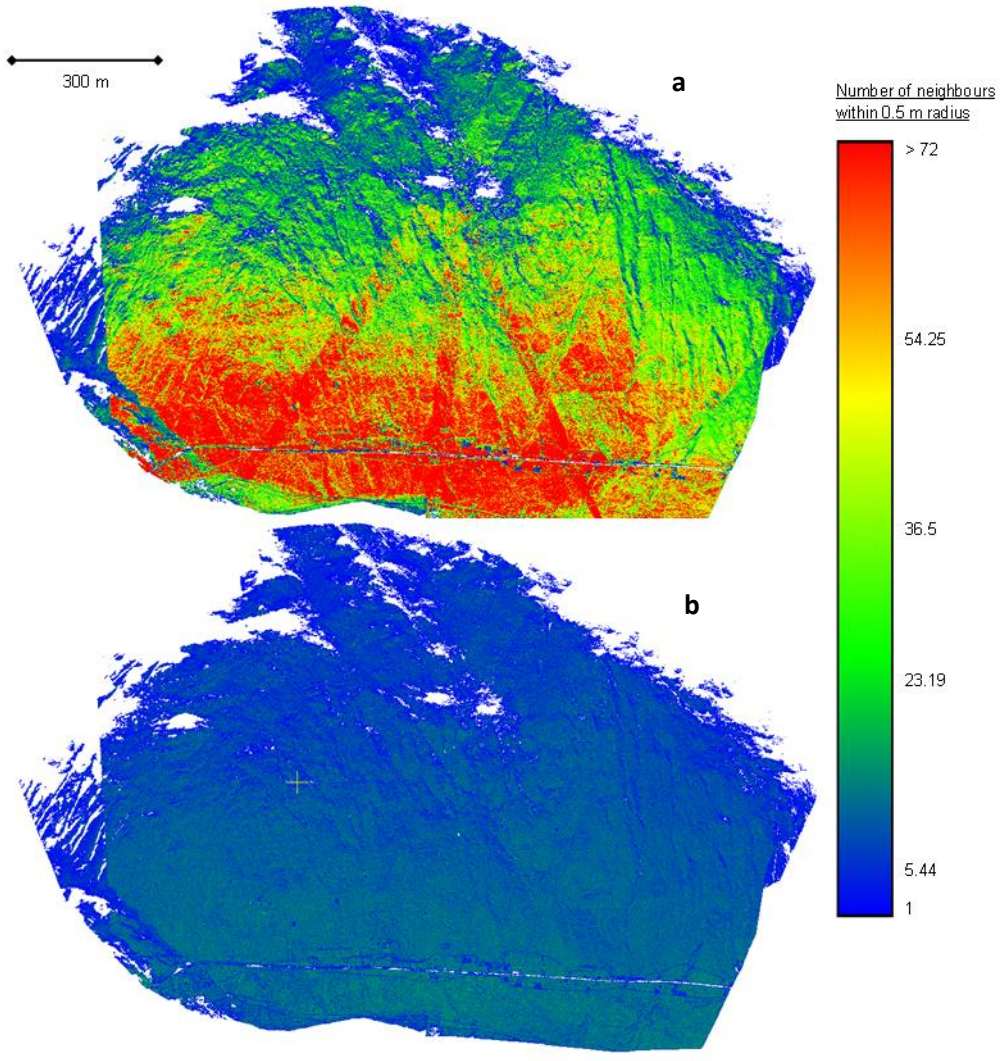

Figure 3.8 – Point cloud densities after co-registration a) prior to subsampling, showing a general reduction in resolution with distance upslope and away from the scan positions, b) after subsampling to 0.2 m spacing the point cloud density is more homogenous and thus change detection and processing is less spatially biased.

The sloping nature of the study sites resulted in lower point densities at higher elevations. This biased the change detection, and subsequent analysis, towards the bottom of the slope. Registered and merged point clouds were thus subsampled within CloudCompare, resulting in a relatively even lateral and vertical distribution of 5 points / m, or 25 pts / m^2 (0.2 m spacing).

Figure 3.8 shows the point cloud densities at RabT before and after this process. This created a relatively homogenous point cloud, enabling later use of a density filter to remove isolate noise, from the change data, without bias towards higher density areas. Following the density filter, the theoretical minimum detectable change footprint remains < 0.1 m^2.

3.1.2 Error Quantification

Multi-station adjustment and temporal registration introduce errors, which propagate as explained by the 'special law of propagation of variances' (SLOPOV) (Ghilani and Wolf, 2006), to reduce the effective LoD. Such errors must be quantified to confidently detect change (Martinius and Naess, 2005). The Root Mean Square (RMS) error approach for independent error sources (Taylor, 1997) is widely used in TLS studies to estimate uncertainty (Schürch *et al.*, 2011; Westoby *et al.*, 2016; Cook, 2017) and reduces the LoD compared to a relatively conservative summative approach.

The RMS errors for each survey, calculated using the standard deviation of registration residuals (RiScan Pro), are shown in table 3.5.

This uncertainty is further compounded by instrument accuracy and environmental factors (Jaafar *et al.*, 2018). Long range terrestrial laser scanning, for example, introduces greater measurement uncertainty compared to shorter range applications (Hartzell *et al.*, 2015; Telling *et al.*, 2017). Riegl report accuracies of 10 mm (100 m range) and 15 mm (150 m range) for the LMS-Z620 (Riegl, 2010) and VZ-4000 (Riegl, 2017b) respectively, however these values significantly underrepresent uncertainty at increased distances.

Attempts were made, during this study, to collect independent control points for an objective empirical quality assessment specific to the environment. This is often a vital task, particularly where the data is intended for use in engineering design, as a combination of different factors from atmospheric conditions to surface roughness for example, can significantly impact the quality of a survey.

Long-range total stations are capable of surveying points with a much smaller uncertainty range of approximately ± 0.001 m (Leica, 2019). This was the preferred quality assurance

approach, to which repeat Riegl fine scans were to be compared to quantify both the precision (repeatability) and accuracy of the device's measurements. These efforts were unfortunately hampered, on a number of occasions, by poor and changeable weather conditions which obscured the field assistant and prism, eventually necessitating the reliance on values reported by other researchers.

Castagnetti and Bertacchiniab (2014) for example estimated the LMS-Z620 measurement uncertainty to be approximately ± 0.1 m at a range of 1.2 km, whilst Fey and Wichmann (2017) calculated uncertainty of ± 0.036 m for a VZ-4000 scanning a 45° surface at a range of 1 km. The latter, better constrained conditions, were considered to best match those in this study, and were therefore adopted as a simplified, but conservatively isotropic measure of instrument uncertainty, including for monitoring at shorter ranges and lower incidence angles.

3.1.2.1 Final Cumulative Uncertainty

Maximal Multi Station Adjustment (MSA) and Interval to Interval (I2I) error values for each site (red in table 3.5 and table 3.6) were used to calculate final uncertainty (F_u) values propagating from registration errors and instrument uncertainty. This approach has been previously been implemented in TLS studies by Barnhart and Crosby (2013) for example and is founded on the principle of the SLOPOV (Ghilani and Wolf, 2006). In this study, the Root Sum Square (RSS; Equation 4), or variance formula, took the form:

$$F_u = \sqrt{{MSA_1}^2 + {MSA_2}^2 + I2I^2 + InsErr^2}$$

Equation 4

where MSA represents the multi-station registration error (RMS) for each respective interval, $I2I$ represents the interval-to-interval registration error (RMS) and $InsErr$ represents instrument error. Resultant maximal final cumulative uncertainty values are shown in table 3.7.

Table 3.5 – Root mean square (RMS) Multi-station adjustment (registration) errors. Maximal values are marked in red.

Study site	Date	Registration Error (RMS, m)
RabT	20th April 2015	0.0405
"	29th July 2015	0.0298
"	8th September 2015	0.0485
"	16th October 2015	0.0281
"	6th December 2015	0.0404
"	11th February 2016	0.0367
"	19th April 2016	0.0328
"	24th May 2016	0.0252
"	11th July 2016	**0.0543**
"	19th September 2016	0.0396
"	26th November 2016	0.0434
"	17th December 2016	0.0394
"	29th January 2017	0.0472
"	3rd February 2017	0.0285
"	27th April 2017	0.0271
Glen Ogle	21st April 2015	0.0404
"	30th July 2015	0.0376
"	9th September 2015	0.0459

"	17th October 2015	0.0430
"	21st April 2016	0.0336
"	25th May 2016	0.0355
"	22nd September 2016	0.0445
"	25th November 2016	**0.0505**
"	28th April 2017	0.0174

Table 3.6 - Interval to interval registration errors (RMS). Maximal values are marked in red. *The October 2015 dataset collected at Glen Ogle was prone to offset in high-incidence angle areas, and could not be reliably registered to the April 2015 dataset.

Site	Date	Registration Error (RMS, m)		
RabT	20th April 2015	Static		
"	29th July 2015	0.0299		
"	8th September 2015	0.0287		
"	16th October 2015	0.0261		
"	6th December 2015	0.0272		
"	11th February 2016	0.029		
"	19th April 2016	**0.0321**		
"	24th May 2016	0.0285		
"	11th July 2016	0.0178		
"	19th September 2016	0.0315		
"	26th November 2016	0.0308		
"	17th December 2016	0.0276		
"	29th January 2017	0.0286		
"	3rd February 2017	0.0321		
"	27th April 2017	0.0259		
Glen Ogle	21st April 2015	Static		
"	30th July 2015	0.0277		
"	9th September 2015	0.0244		
"	17th October 2015	N/A*		
"	21st April 2016	0.0307		
"	25th May 2016	0.0235		
"	22nd September 2016	0.0311		
"	25th November 2016	**0.0339**		
"	28th April 2017	0.0262		
		Position 1	**Position 2**	**Position 3**
Glencoe	30th July 2015	Static	Static	N/A
"	18th October 2015			Static

"	12th February 2016	0.0153	0.0166	0.0235
"	20th April 2016	0.0199	0.0166	0.0235
"	17th September 2016	0.0181	0.0169	0.0157
"	18th December 2016	0.0179	0.0238	
"	27th April 2017	**0.0375**	**0.0251**	**0.0276**

Table 3.7 - Maximal final uncertainty values calculated using the maximum registration error values marked in red in table 3.5 and table 3.6. The Glencoe values are lower due to no requirement for multi-station adjustment.

Study Site	Maximal F_u (m)
RabT	± 0.088
Glen Ogle	± 0.084
Glencoe	± 0.052

3.1.3 Transformation to real-world co-ordinate space

Change data were transformed from their arbitrary local co-ordinate system to Ordnance Survey National Grid coordinates within CloudCompare. Three well distributed control points (corners of engineered structures) were surveyed using a Trimble dGPS and were also fine-scanned during a TLS survey. The control points were postprocessed using Trimble Business Centre and Ordnance Survey Rinex data (baseline) collected at Oban (Ordnance Survey, 2017). Transformation using the three control points resulted in an RMSE error of 0.217 m. A resultant 4x4 transformation matrix, a combination of a rigid 3x3 rotation and a 3D translation, was saved for application to future datasets using CloudCompare's 'Apply Transformation' tool.

3.1.4 Change detection

Once registered, point cloud data can be compared using a multitude of different methods and approaches outlined in this section. This includes a novel workflow to negate seasonal vegetation fluxes.

3.1.4.1 Change detection on slopes with dense, seasonally fluxing vegetation

Survey data are conventionally differenced sequentially, from one scan interval to the next, to produce a high temporal resolution catalogue of change. These calculations can be prone to uncertainty from the presence of vegetation (Fan *et al.*, 2014). Approaches to negate this issue include surface classification using 3D data (Brodu and Lague, 2012), use of targets (Franz *et al.*, 2016) and filtering of ground returns using full waveform analysis (Wagner *et al.*, 2008; Anderson *et al.*, 2016).

Issues also arise where vegetation growth and die-back occur (Fan *et al.*, 2014), with this producing a false change signal (figure 3.9a). This is particularly problematic when the vegetation cover is dense and widespread, often the case across much of Scotland, as such areas cannot simply be filtered and removed. Should part of the vegetated slope fail, conventional change detection will account for the depth of vegetation loss in addition to the actual depth of geomorphic loss (figure 3.9b). A new change detection approach has therefore been necessary to negate this effect.

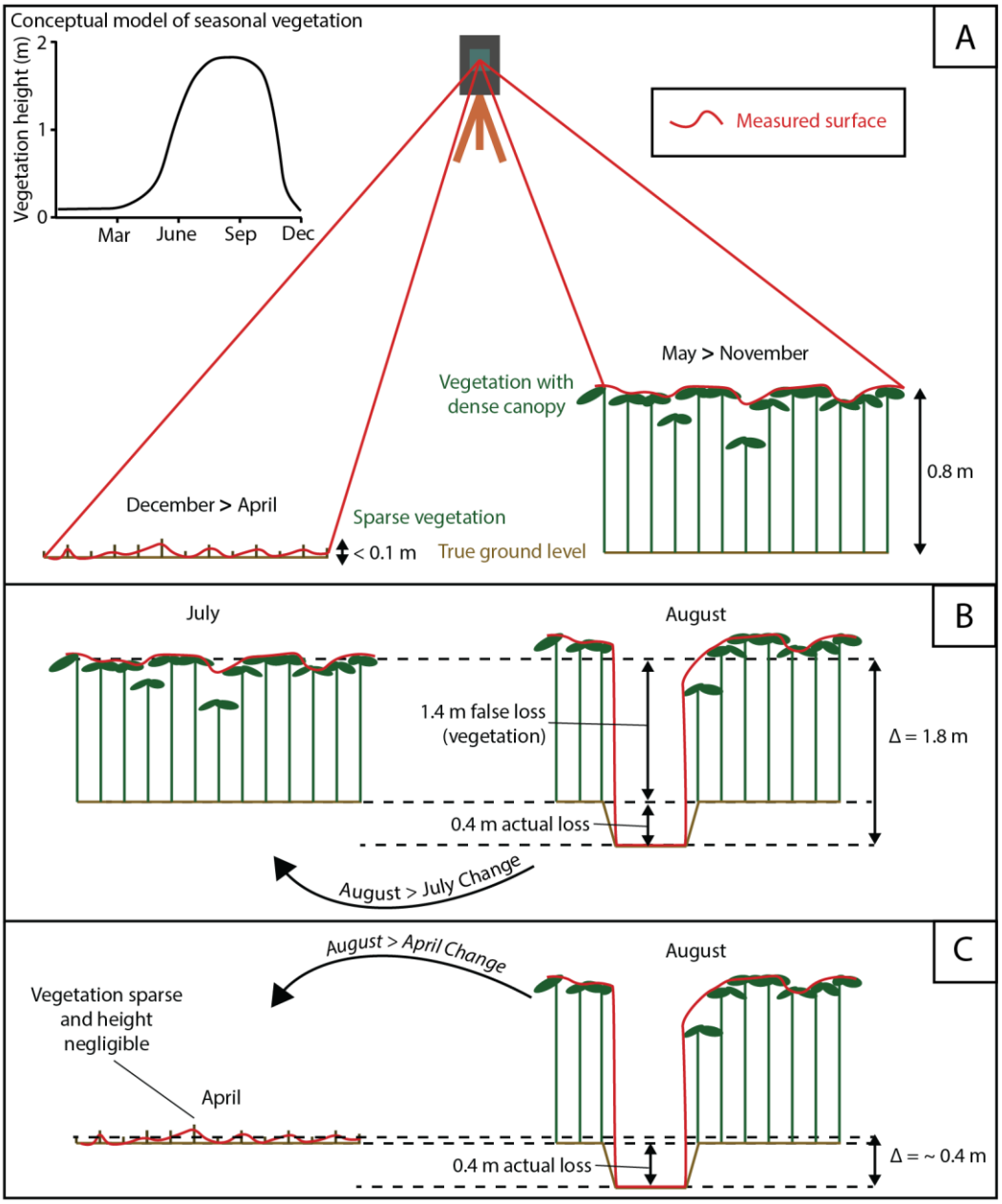

Figure 3.9 - The role of seasonal vegetation fluxes in the change detection scheme a) A dense vegetation canopy provides a false representation of true underlying topography. B) Comparison of a vegetated dataset with another vegetated dataset gives the impression that a large degree of loss has occurred. C) Comparison of a vegetated dataset with a basal topography dataset, prior to vegetation growth, provides a more representative account of true loss. One caveat is that vegetation growth introduces undesired gain, this must therefore be ignored and monitoring of gain must take place using a different approach.0

Growth occurs from a baseline, immediately following winter die-back, after which vegetation, particularly dense bracken, proceeds to develop beyond heights of 1 m. This vegetation does not typically die back beyond the baseline level, thus any change below this is usually a true geomorphic change (figure 3.9c). This theory is the basis for a new change detection approach, in which losses can be detected all year round, relative to the baseline

dataset. The February to April period is the best time of year to conduct a baseline survey, as adequate die-back and minimal regrowth have occurred here. Annual change detection in this study uses baseline datasets collected in April. Gains are much harder to detect using such an approach and have thus only been quantified on an annual basis.

3.1.4.2 Calculating and Processing Change

Interpolated point clouds, forming digital elevation models (DEM), are commonly subtracted to create a DEM of difference (DoD) and therefore detect change. This works well on relatively planar study sites, such as rock walls and cliffs, although re-orientation of the data is still necessary to ensure that subtractions are calculated on the Z-axis of the GIS environment being used. The DoD approach cannot account for areas that significantly differ to this orientation however, necessitating manual separation and processing of such regions (Barnhart and Crosby, 2013).

Interpolation can introduce false topography where mixed pixels, artefacts or occlusion occur in the raw data. The introduction of false topography may explain a near 25% overestimation of rockfall volume loss found by Benjamin *et al.* (2016) compared to several 3D change detection mechanisms which were all more closely in agreement with one another. Furthermore, interpolation of 3D data to a 2.5D system, removes the potential for post-processing using 3D change properties. C2C change detection consists of a measurement between one point and its closest neighbour in the comparison cloud. Because this can be calculated in any direction, unrealistically large measurements can occur, particularly in occluded regions. Abellán *et al.* (2009) found that noise related to the method obscured the true change signal. The cloud-to-mesh (C2M) method overcomes some of these problems, particularly orientation of the calculation, but still relies upon the closest neighbouring points and introduces interpolation issues similar to those of the DoD approach, particularly in complex areas with large roughness (Olsen *et al.*, 2015).

Abellán *et al.* (2009) found that the normal Gaussian distribution of noise, from direct C2C comparisons, could be reduced using a nearest neighbour averaging approach, leveraging point cloud redundancy. The (M3C2) algorithm (Lague *et al.*, 2013) can be considered a hybrid change detection method, which adopts a similar approach and negates many of the negatives of DoD, C2C and C2M. M3C2 has gained wide acceptance within the Geomorphological community over recent years (Abellán *et al.*, 2016). The M3C2 algorithm calculates the difference between two point clouds by using core points in a reference cloud (demonstrated in figure 3.11). Circles of a user defined radius are drawn around each core

point, within which the mean depth of the neighbouring points is sampled. A cylinder is then projected using the local orientation (user defined sampling radius), out towards the comparison cloud. Points from the comparison cloud, falling within this cylinder, are also averaged and then compared with those sampled from the reference cloud, to provide an overall change value. Use of a normal direction optimises the process on complex and rough surfaces (Barnhart and Crosby, 2013), including steep breaks of slope (Beer *et al.*, 2017) which are intermittently present across RabT and GO, and most prominent at Glencoe. The technique also ignores cylinders with a low-density of points, to ensure high confidence in the change detection.

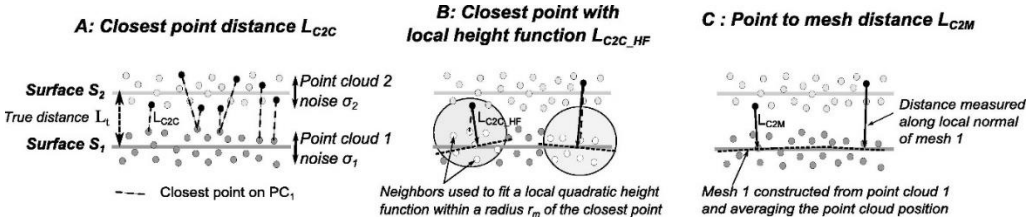

Figure 3.10 - A comparison of different 3D change detection techniques *(Lague* et al*., 2013)* A) Cloud to Cloud distance which may both overestimate and underestimate the actual distance as a result of noise B) Cloud to Cloud with height function which does not account for the original surface orientation and C) Point to Mesh which still retains the origin cloud noise issue from C2C.

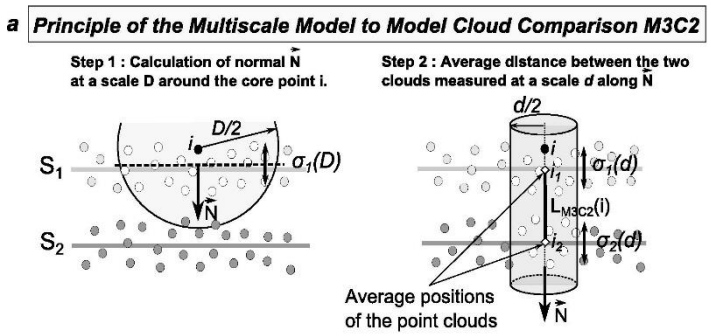

Figure 3.11 - A breakdown illustration of the M3C2 change detection method *(Lague* et al*., 2013)*. This demonstrates the normal calculation for correct orientation of the comparison cylinder (shown in step 2) which is projected from the reference cloud to the comparison cloud, the mean surfaces within which are subsequently compared

M3C2 was the preferred change detection technique in this study, owing to the large size of the study sites and variable complex surfaces. The method also provides a statistical significance parameter for each calculation (95 % confidence based upon equation 4), as well as a measure of the standard deviation (roughness), which can be used to clean up the change data.

The M3C2 algorithm also calculates and outputs a statistical significance value for each cylinder, derived by considering a combination of the isotropic registration error (or cumulative error in this case) and sub-cloud roughness. This is calculated using equation 5:

$$LOD_{95\%}(d) = \pm 1.96 \left(\sqrt{\frac{\sigma_1(d)^2}{n_1}) + \frac{\sigma_2(d)^2}{n_2}} + reg \right)$$

Equation 5

where σ_1 and σ_2 represent the roughness values of two respective clouds, both n_1 and n_2 represent the number of points contained within each cylinder (subcloud) of diameter d, and reg represents the maximal final uncertainty calculated (F_u calculated in section 4.2.2.3).

Lague *et al.*, (2013) state that the above equation is optimal for subclouds of n > 30. Although the number of points used in this study is lower (i.e. 21 as shown in figure 3.12), tests by Lague et al. (2013) have shown that the equation is effective on natural surfaces with as few as 5 points. Barnhart and Crosby (2013) highlight that this statistical approach removes small magnitudes of change and thus may result in a net underestimation of change. This is an unavoidable and necessary step in long distance studies such as this, where levels of uncertainty are relatively high. Furthermore, this effect is insignificant in the case of the larger magnitude changes which are of particular interest to this study.

M3C2 Change Detection

M3C2 calculations were conducted in CloudCompare v 2.9.1 (2018). A 0.5 m radius cylinder was utilised, orientated by a 0.5 m normal radius. Each calculation cylinder was anticipated to contain approximately 21 points, based upon a 0.2 m subsampled point spacing (figure 3.12). The orientation radius was considered just large enough to account for changes in slope, but not too small to be affected by surface noise or roughness. Change values were projected onto, and stored within the reference point cloud containing the original surface morphology.

Table 3.8 – Typical effective $LOD_{95\%}$ thresholds for each study site, based upon use of the aforementioned maximal error values

Site	$LoD_{95\%}$
RabT	± 0.194 m
Glen Ogle	± 0.183 m
Glencoe	± 0.085 m

3.1.4.3 Post change detection filtering

Changes deemed statistically insignificant were removed following the M3C2 calculation. The resultant LoD values, at a confidence interval of 95% ($LoD_{95\%}$), are shown in table 3.8.

Although most of the vegetation signal was cleaned and negated against, using filtering and non-sequential change detection, residual noise was evident in the change data. This noise may have related to patches of un-filtered long grass, edge effects and mixed pixels. A large proportion of this was cleared using M3C2's standard deviation field (roughness surrounding each core point), both on its own and with a 0.5 m radius Gaussian filter in CloudCompare v 2.9.1 (2018).

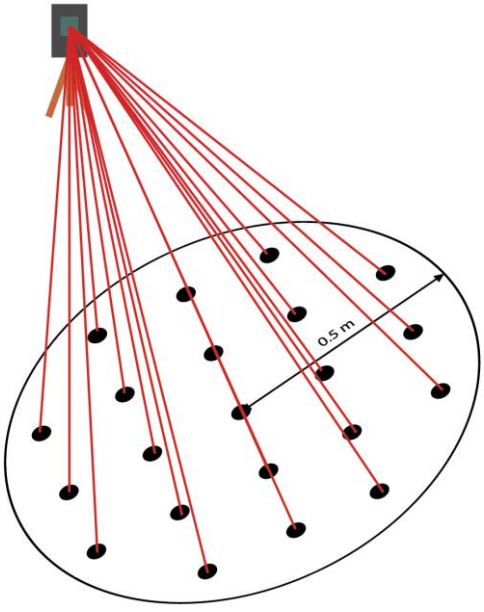

Figure 3.12 – Idealised data collection from a terrestrial laser scanner. In this case, a 0.5 m radius circle is drawn around a nodal point. A point spacing of 0.2 m results in 20 neighbouring points falling within a 0.5 m radius of the nodal point.

Remaining noise, verified using high resolution photographs, was clearly composed of both loss and gain signals. The remaining M3C2 change data were split into respective 'loss' and 'gain' point clouds. Splitting both signals effectively reduced the point density of noise to a value below that of the true coherent change. This left clusters of 'true' change points, at a higher density than the surrounding noise, enabling a density filter to be applied in a similar fashion to that employed by Tonini and Abellan (2014). Points with less than four neighbours within a 0.5 m radius (equivalent density of ~5 pts / m^2) were filtered from each cloud at this stage. This compares with the subsampled point density (0.2 m spacing) of 25 pts / m^2.

After this, CloudCompare's Connected Components tool was used to split the change into coherent patches. These were all manually verified, using a combination of detailed 3D examination, bounding box dimensions and high resolution photographs. Cross-section sampling (QT) was used to more precisely examine changes which could not be verified by visual inspection alone. The change data, with the pre-change surface morphology, was first saved as an ASCII file. The Z axis value of each point was then changed to represent the M3C2 values, after which the change was again saved for a second time.

3.1.5 Volume Calculation

CloudCompare was deemed optimal for complex processing of the 3D data, with the inherent 3D properties of the data retained up until this point, thus enabling the full 3D dataset to be fully exploited as opposed to other studies where data are quickly simplified to a 2D or 2.5D format (A Abellán *et al.*, 2014). CloudCompare did not, however, enable a straightforward calculation of volumetric change from the remaining data. Change data were therefore imported into ArcGIS for a relatively straightforward volume quantification.

Volumes were calculated by multiplying the mean depth of change by the area of the change domain. Use of a 2.5D surface area was necessary at this stage, due to ArcGIS truncating the length of the change domain polygons (as explained in figure 3.13). The original morphology files were imported and converted into a triangulated irregular network (TIN) file at this stage, before being broken up into discrete areas and the domains of each being converted into a shapefile. The 2.5D format of a TIN was not considered problematic, due to a minimal number of overhangs at RabT and GO. A 2.5D surface area was calculated using the 'polygon volume' tool.

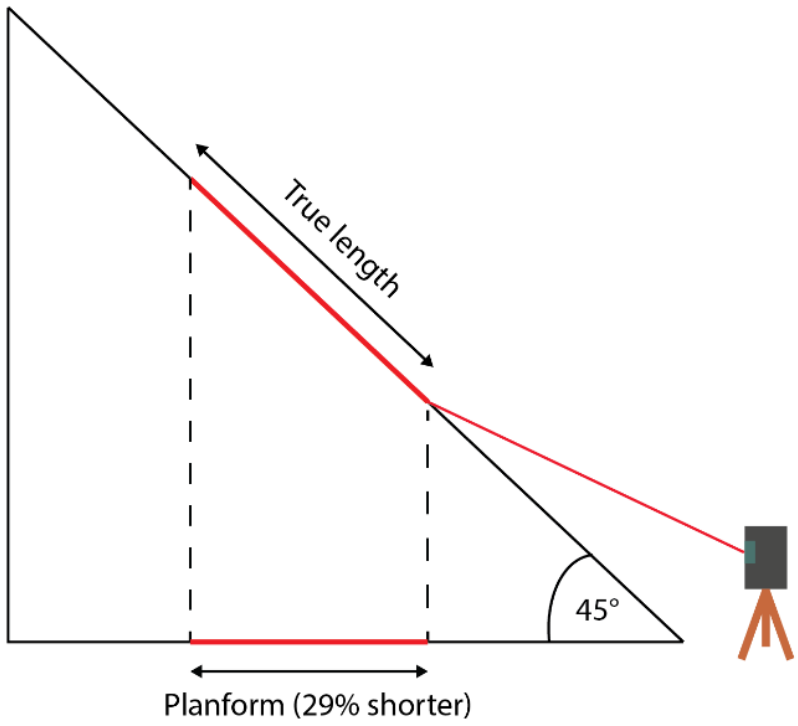

Figure 3.13 - An example of how a 2D polygon area calculation in ArcGIS underestimates the true area of a change patch orientated along a slope

Mean (M3C2) values were appended to each change polygon through interpolation (Inverse Distance Weighted; IDW) of M3C2 points into a 0.1 m DEM and sampling using 'Zonal Statistics'. The attribute table of mean depths were checked for errors which may have been introduced by the workflow. Surface areas were multiplied by the mean change values to give the volume change (m3) for each polygon. The mean change approach was favoured, over summing each 0.01 m2 cell and dividing by 100, due to the simplicity of joining values with 3D surface area values. Both approaches resulted in the same change values. This workflow was eventually automated using ArcGIS model builder, the outline of which is shown in figure 3.14.

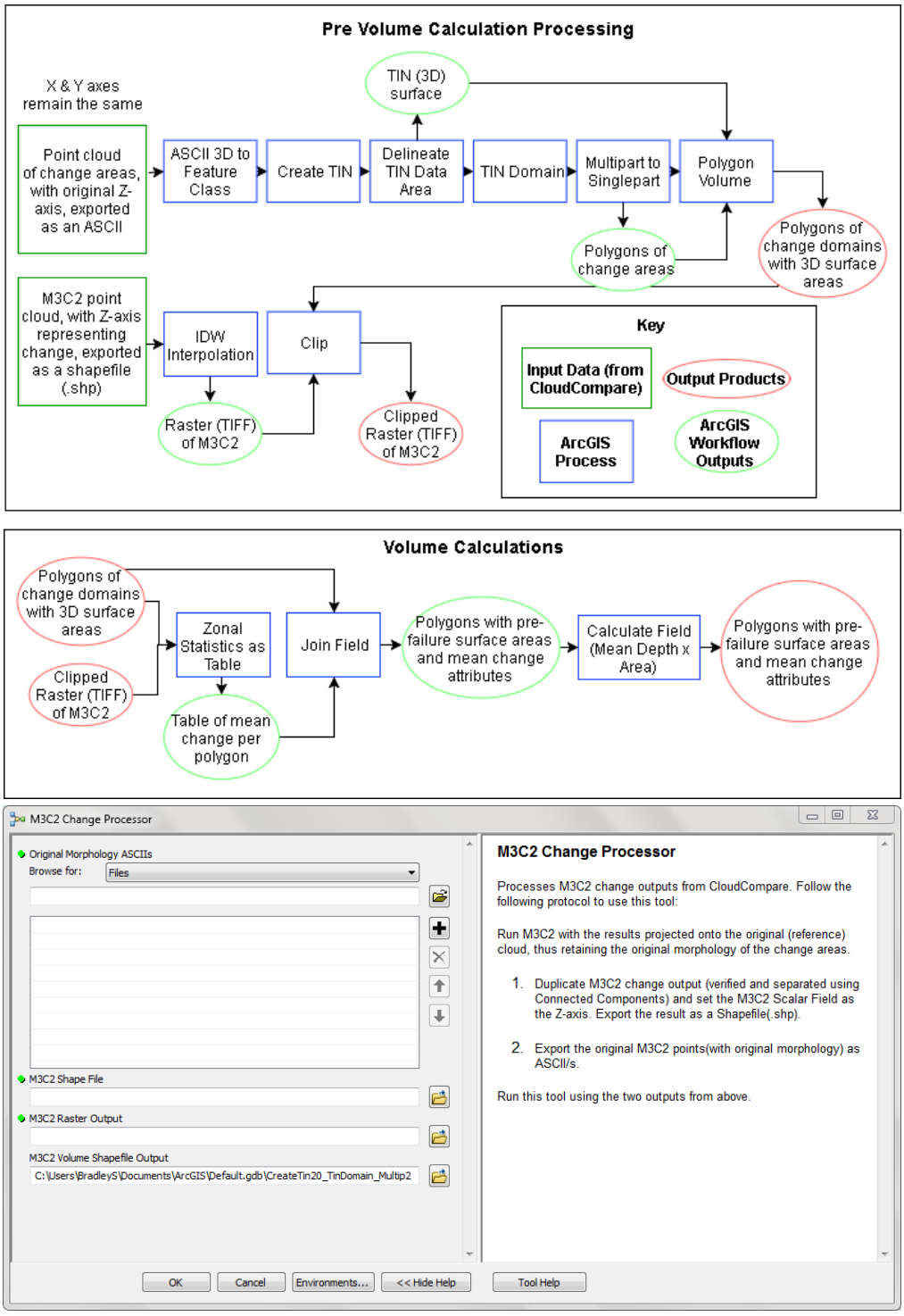

Figure 3.14 - Top) The workflow developed to power the tool. The user inputs the M3C2 ASCII in its original state (directly from CloudCompare) as well as a shapefile of the M3C2 results where the Z axis values have been substituted for the M3C2 values. The original morphology files are used to generate shapefiles and calculate the true 3D surface area, whilst the M3C2 values (shapefile) are interpolated into a raster, from which the mean change per polygon is sampled and multiplied by the true surface area to give the volumetric change. Bottom) The GUI developed within ArcGIS for input and processing of data directly from CloudCompare.

3.1.6 Temporal interpretation of accumulated change

Sequential change detection produces change isolated to each survey interval (figure 3.15a), which is desirable for ease of temporal change interpretation. Non-sequential change detection results in accumulation of changes throughout the year (figure 3.15b) which can complicate temporal interpretation, parti cularly where superimposition occurs. To isolate changes to their respective survey intervals (figure 3.15c), accumulated changes were masked using a relatively simple subtraction approach. Each change interval was subtracted from the next interval, removing the prior known changes and leaving new changes since the earlier interval. For example, subtracting change between April to June, from change between April to July, would result isolate change occurring only between June and July.

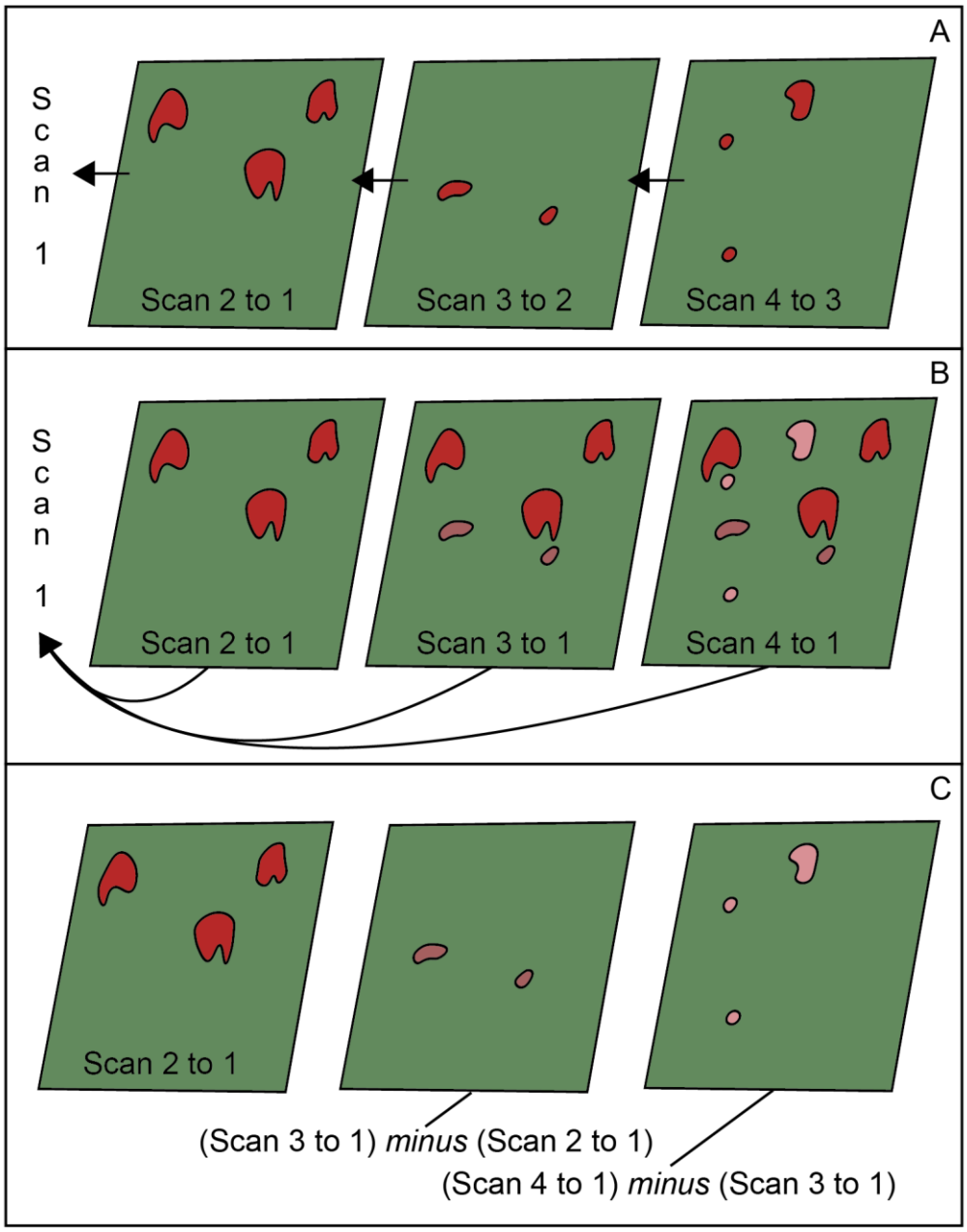

Figure 3.15 - Masking unconventional change data to obtain data that can be interpreted much like; (A) conventional change data. (B) An unconventional change approach results in 'stacked' change. (C) Subtraction of preceding change results in isolated change, much akin to conventional change data.

Masking was conducted within ArcGIS (workflow shown in figure 3.16), by subtracting preceding losses using 'Raster Calculator'. This required both datasets to be matching in extent, and for all 'NoData' values to be replaced with '0' values, as calculations could only be processed on the latter. Subtraction resulted in a raster dataset containing both negative and positive values. Negative values represented areas in which new loss had been detected, whilst positive values represented areas in which superimposed loss had been detected (two negative values, the most recent interval of change being larger than the former). The latter of these were changed to negative values for consistency.

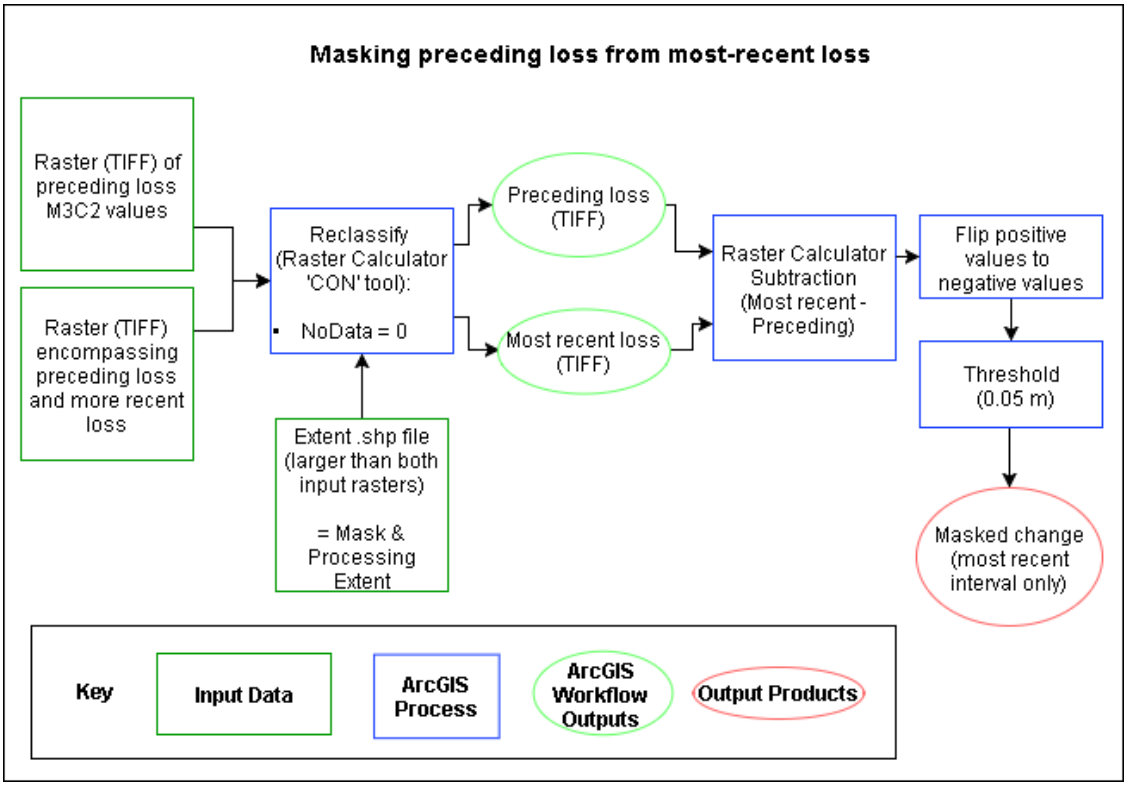

Figure 3.16 - The loss masking workflow, used to isolate change to intra-annual intervals.

Following masking, data were cleansed of small residual artefacts relating to minor raster misalignment and differences falling within the range of instrument uncertainty. The masked rasters were first thresholded to 0.05 m, slightly larger than the aforementioned 0.036 m instrument error at a large range. Data were subsequently cleaned by converting the masked rasters into shapefiles and using the 'minimum bounding geometry' tool within ArcGIS to highlight and remove polygons with a width of just 0.1 m (figure 3.18), equivalent to the raster resolution and thus the maximum expected offset between rasters.

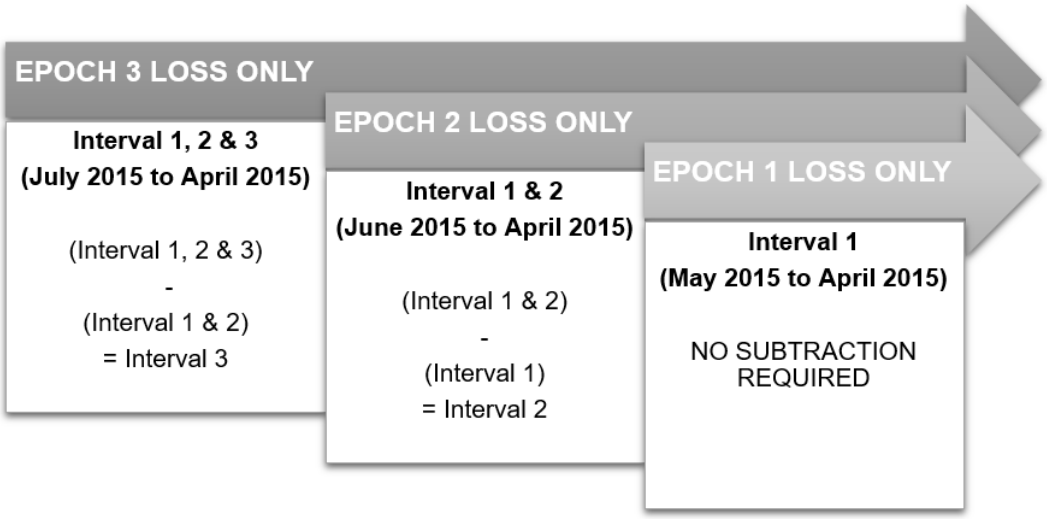

Figure 3.17 - A loss masking regime to isolate 'stacked' losses to their discrete respective epochs

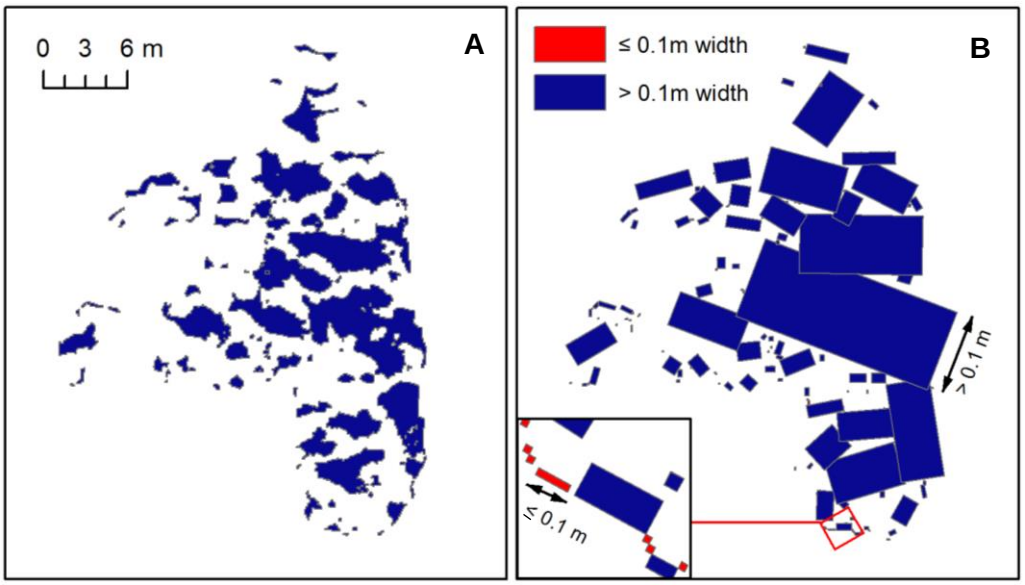

Figure 3.18 - Cleaning edge-effects (residuals) from post-masking polygon data, using a minimum-width (0.1 m) polygon filter. A) Original data prior to cleaning. B) The same area (and scale) with 'Minimum Bounding Geometry' rectangles calculated for each original polygon. Those marked in red have a width less than or equal to 0.1 m, and are thus filtered.

3.1.7 Limitations

Laser attenuation, related to dark, wet and oblique surfaces (Abellán *et al.*, 2014), resulted in areas of no data coverage, particularly around gullies and streams. This was mainly found to be an issue at the base of the gullies, with the sidewalls returning satisfactory point coverage for the most-part. This effect relates to the energy output of the laser scanner used, with the 2 km range LMS-Z620 found to be more susceptible to attenuation than the 4 km range VZ-4000. Flat slope area will also be occluded, particularly at high elevations relative to the laser scanner, where an ample proportion of the beam footprint is unable to hit the surface. Failures are less likely to occur in such areas, however deposition could occur should a debris flow runout into such a zone. Debris flow runout and deposits are also prone to spreading, resulting in a high width to depth ratio, thus producing a potentially large spread of material below the LoD threshold (Bremer and Sass, 2012). Considering that deposits are likely to spread over flat areas and mobilise into occluded gullies, it is clear that the discussed limitations primarily relate to detection of gains, rather than losses. Considering the intra-annual masking approach is only applicable to losses, it is notable that this study is best suited to, and prioritises, the detection of losses. As a result, the change detected and presented is considered a conservative representation of actual change on the slopes.

Differences in surface obliquity, roughness and other surface parameters may also influence the distribution of errors, so that they are anisotropic. It can be a challenge to quantify a dynamic value for uncertainty and a fixed, isotropic, LoD threshold was used in this study to simplify matters. A conservative isotropic approach to error ensures that the maximum anisotropic uncertainty is accounted for across the entire point cloud. A single LoD ensures consistency in measurements across the area of interest, which can be important when relative event magnitude quantification is desired (Williams *et al.*, 2017), however it can result in the omission of small changes below the threshold. This is unlikely to be an issue for the detection of landslide scars, even small ones, as these are likely to measure more than 0.194 m and typically have a low width to depth ratio. The dimensions of change polygons are not necessarily true to the actual dimensions of the change on the slope, due to the aforementioned influence of a large beam footprint and inter-point spaces. The exterior boundary of a change will typically fall somewhere between the points, and seldom aligns perfectly with the sampled points. As a result, the change detection will underestimate the true footprint of the change, particularly for smaller changes where the resolution (point spacing) to change size is relatively low. This degree of underestimation will vary, depending upon the alignment of points within the domain of the change. Figure 3.19 shows how an

idealised 0.5 m x 0.5 m change could be sampled by a minimum of four points, or a maximum of nine points, based upon a 0.2 m point spacing. The former results in an 84 % underestimation of the actual change size, and the latter underestimates this by 36 %. Table 3.9 shows how the relative underestimation is smaller for changes of increasing size.

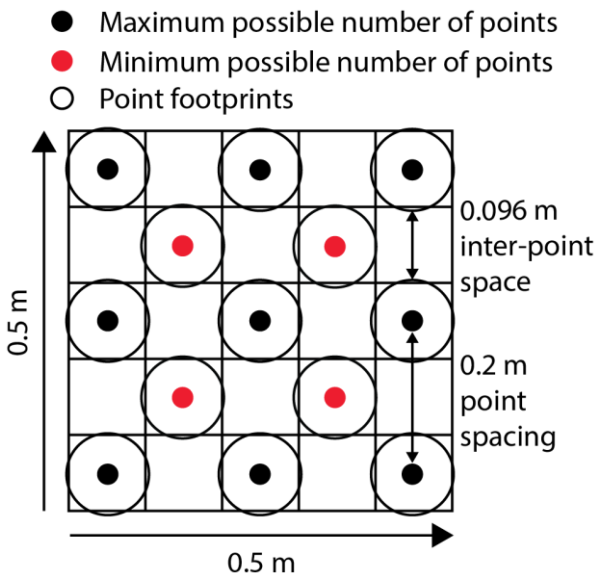

Figure 3.19 - The minimum and maximum point coverages for an idealised 0.5 m x 0.5 m square area at a range of 600 m from the laser scanner (assuming an evenly distributed 0.2 m point spacing on a surface orientated normal to the laser scanner). An oblique surface would yield non-circular point footprints, with an uneven spacing.

Table 3.9 - Example of greater relative underestimation of change dimensions at smaller magnitudes

Square Side Dimension (Area)	Minimum number of points (0.2 m spacing)	Maximum Percentage Underrepresentation	Maximum number of points (0.2 m spacing)	Minimum Percentage Underrepresentation
0.5 m (0.25 m²)	4	84 %	9	36 %
1.5 m (2.25 m²)	49	36 %	64	13 %
4.5 m (20.25 m²)	484	13 %	529	4 %

3.2 Results

The monitoring results are presented in this section. Inter-annual change is shown for all three study sites. At RabT, 127 patches of loss were detected over a 33 month period. In comparison, six losses were detected at GO over a 24 month period, and seven losses were detected at GC over a 21 month period. The large number of changes at RabT have been masked into their respective survey intervals and a figure for each is also presented. Detailed analyses of these changes is presented in section 3.3.

3.2.1 RabT

Figure 3.20 shows a complete inventory of all changes detected at RabT between April 2015 and February 2018, along with the change references used throughout this chapter. The convention used for these references is a combination of the site code (acronym) i.e. 'RabT', the monitoring year in which the change occurred i.e. '1' and the change letter i.e. 'A'. Large magnitude events, triggered by storms, are also displayed with additional labels.

3.2.1.1 Year 1 (April 2015 – April 2016)

The first year of change, detected between April 2015 and April 2016, is shown in figure 3.21. This includes both loss and deposition. 73 losses were detected over this period, although some of these are clustered polygons relating to the same change. The majority of changes (60%) are concentrated within a 180 m wide central region of the slope, accounting for just 20 % of the monitored area. Furthermore, these changes include all three of the largest changes (RabT1A, RabT1B and RabT1C; winter storm events). There are ten significant clusters of change, of which the largest is RabT1C, a 630 m^3 landslide triggered on 5th December (intra-annual interval 4) during Storm Desmond (thus also referred to as SDLS1; Storm Desmond Landslide 1). The source area measured a mean depth of 1.5 m, with a maximum depth of 3 m and was detected within in a topographic hollow with a mean gradient of 34.7°. RabT1C propagated 60 m down towards the A83, with no sign of deposition along this extent. Flow was arrested by the P1 catch net 20 m upslope of the carriageway.

The second largest change, also a landslide, was RabT1A. RabT1A was triggered on 30th December (interval 5), during Storm Frank (thus also referred to as SFLS1: Storm Frank Landslide 1), and was found to measure 485.6 m^3. The source area was on a 33.9° gradient prior to failure. SFLS1 measured an average depth of 0.7 m, with a maximum depth of 1.86 m. The source area retained numerous soil rafts which were evenly distributed and interspersed around the source area, giving the loss polygon its incoherent boundary. A large proportion of deposition (157.0 m^3) was detected immediately below the source area. The

majority of the failed mass appears to have continued downslope into a channel 54 m downslope, along which it eroded at least 29 m^3 from the sidewall before reaching the road. It is estimated that this mobile mass represented 67.7 % (328.6 m^3) of the original failed volume, although this was likely smaller accounting for deposition below the LoD threshold. A survey based estimation of deposits, using Rinex baseline processed DGPS to trace the outline of gully material, and a stake to probe the mean depths, suggests that around 137 m^3 of material resides within the gully area below the point of inflow (over 100 m length). Clearly some of this material may have been present prior to SFLS1, however the survey confirms the presence of large volumes within the gully. The flow mass also impacted the same P1 flow net (since emptied) as SDLS1. The P1 net did not fully prevent spillage onto the carriageway as before during SDLS1, thus it is assumed that a significant volume mobilised down to road level.

The third largest change, RabT1B, occurred on 6th December (interval 4). This 356 m^3 landslide also occurred during Storm Desmond (thus also referred to as SDLS2) and mobilised from a 30.3° gradient source area measuring a mean 0.66 m depth, with a maximum depth of 1.43 m. SDLS2 deposited approximately 52.9 m^3 (14.9 %) of its source volume immediately downslope of the source area and a small quantity of material was observed behind two phase 7 catch nets downslope. The majority of the initial source volume was therefore inferred to have propagated 57 m towards the gully to its south. Occluded data did not allow accurate calculation of the sediments deposited behind the P7 nets, however reconstruction from a bulge in the upslope flow net (1 m high at the centre), inferred to represent the deposit depth, puts the estimated volume at around 29 m^3 (8.1 % of the source). This would suggest that approximately 77 % (274 m^3) of the source mass was deposited within an occluded area of gully, somewhere between the point of inflow and the P7 catch nets. However, this volume was likely significantly less when accounting for the LoD threshold. More deposition is therefore likely to have occurred on the slope. A survey based estimation of deposits, again using DGPS and depth probing, suggests that only around 21 m^3 of material resides within the gully area below the point of inflow. Accounting for material in the net, and assuming the gully was bare prior to SDLS2, this suggests that approximately 50 m^3 of material was actually deposited within the gully. This equates to 14 % of the overall flow mass, rather than 77 % and clearly highlights a high level of uncertainty relating to the detection of deposition. This breakdown of volumes also clearly indicates that the SDLS2 event deposited a large proportion of material on the open hillslope.

The timings of these events are known due to their impact on the A83 road and increased observations at this time. An additional 13.9 m^3 landslide, RabT1D, was also detected in the first monitoring year, although the timing of this is not clear from the annual change alone. Further small losses were detected and are detailed in the following intra-annual sections. The smallest change polygon was 0.21 m^3, although this was comprised as part of SFLS1. Further changes not highlighted within the figure were detected and are presented in Appendix 1. These were however small and isolated polygons, with relatively large uncertainty, thus not necessitating particular attention.

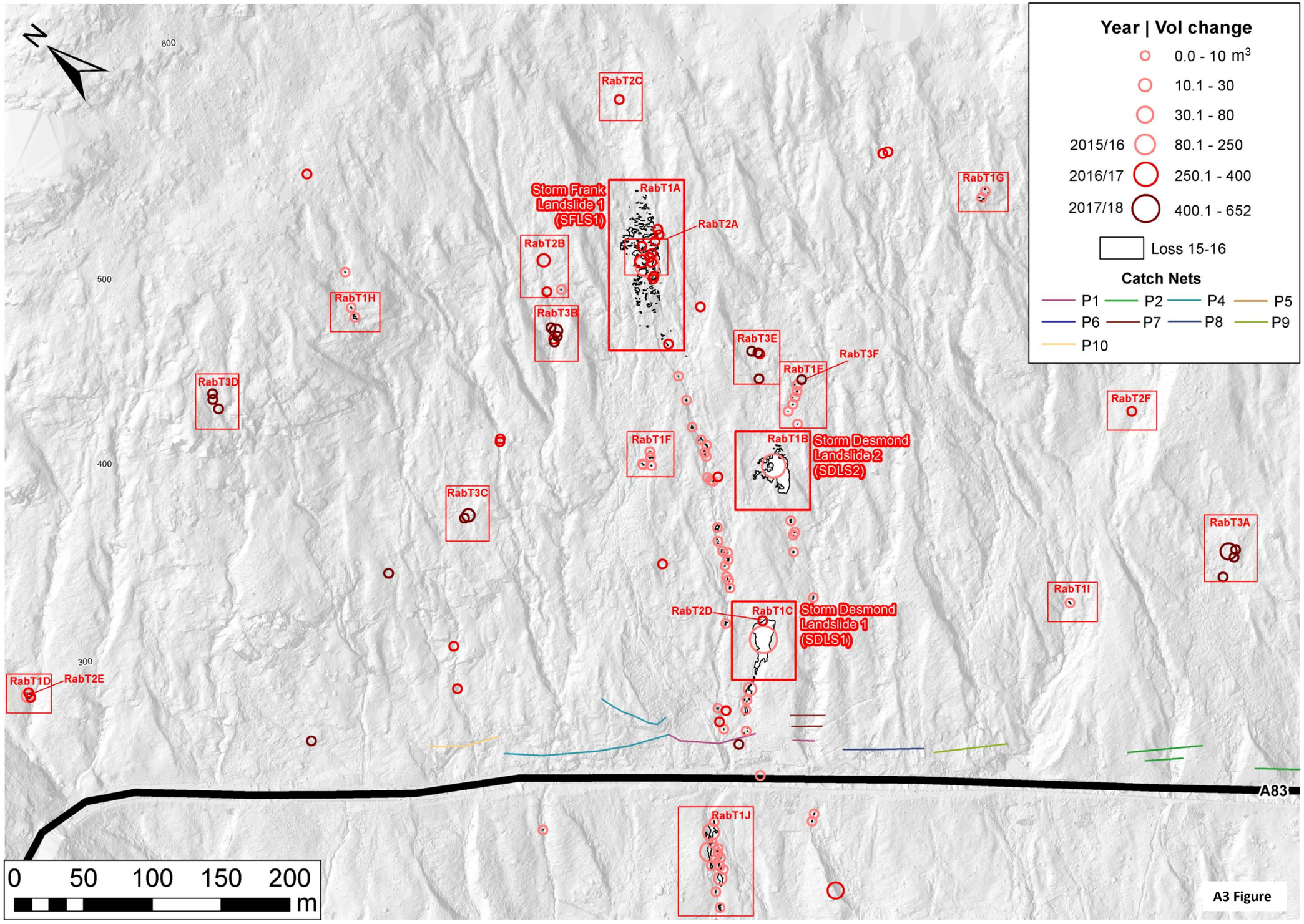

Figure 3.20 – A complete record of all losses recorded at RabT between April 2015 and February 2018. Circles represent each change magnitude and are particularly used for small changes which are otherwise not visible at this scale. The references used within the figure are used in all other change figures throughout this chapter, allowing this to be used as a reference figure. The backdrop to this figure is a TLS DEM derived hillshade model.

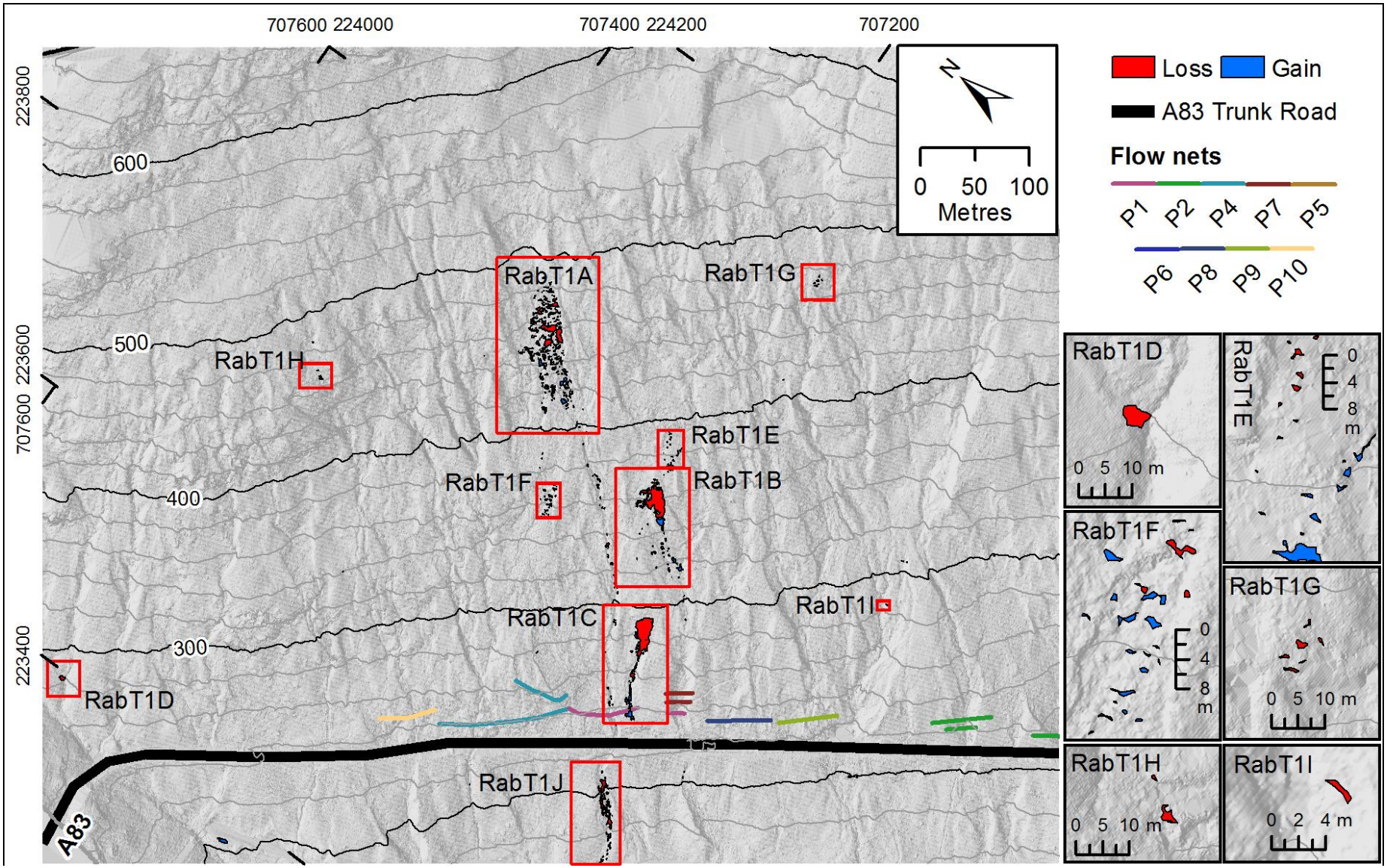

Figure 3.21 - Change from 20th April 2015 to 19th April 2016.

Early monitoring intervals (1, 2 and 3)

Figure 3.22 shows the changes detected over the first three monitoring intervals. RabT1D is shown here, in the first monitoring interval, and thus is known to have occurred at some point between 20th April 2015 and 29th July 2015. RabT1D was a small shallow failure on the margin of a gully at the top (north-west) of the glen, just 90 m upslope of the A83. The source area was detected on the margin of convergent topography which may host transient flow. This is also at the confluence with a major gully known to contain hydrological flow. No deposits were detected in the vicinity or were visible in a follow up inspection. The failure appears to have fully mobilised and evacuated the hillslope and was potentially aided by hydrological flow.

A smaller change, RabT1I, was also detected. This appears to represent movement at a small headscarp on the margin of a major gully, low down on the slope. This area has shown repeated activity throughout all three intervals and thus may represent propagation. This was found to measures 2.5 m x 0.4 m and had an estimated volume of 0.51 m^3 in the annual change data. Reworking of sediment below the A83 trunk road (RabT1J) and the phase 1 culvert was also detected, primarily during the first interval.

First storm interval (4; Desmond)

Figure 3.23 shows the detected losses masked to the period encompassing Storm Desmond (from 16th October to 6th December 2015). The SDLS1 (RabT1C) polygon in this interval is 224 m^3 smaller than that calculated in the annual change detection. This clearly demonstrates that the source area was subject to at least two changes in the first monitoring year.

In addition to RabTI, which was detected in intervals 1-3, three additional small changes were detected in this interval. RabT1E represents shifting of sediment, rather than a fully formed failure, just 35 m east of the SDLS2 source area (also RabT1B). RabT1F represents sediment movement below the SFLS1 landslide found in the next interval. This change is along the secondary runout path, or convergent topographic topography, of the flow and this could host ephemeral flow which also flows through the SFLS1 source upslope. Should ephemeral flow be important to the triggering of shallow failures, this change may represent a precursor to future activity within this lateral slope zone.

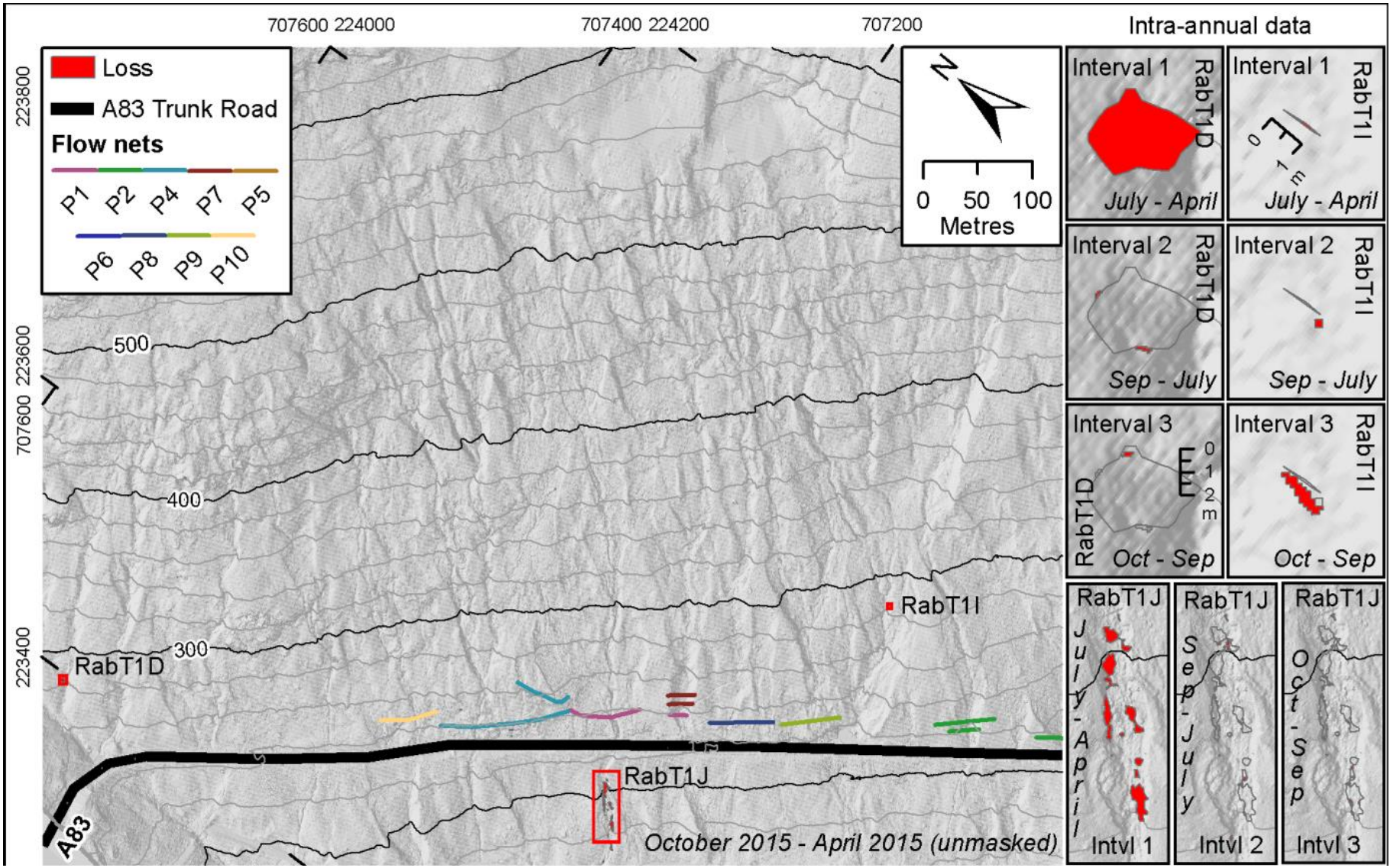

Figure 3.22 - Change from 20th April 2015 to 16th October 2015 period (Intervals 1, 2 and 3).

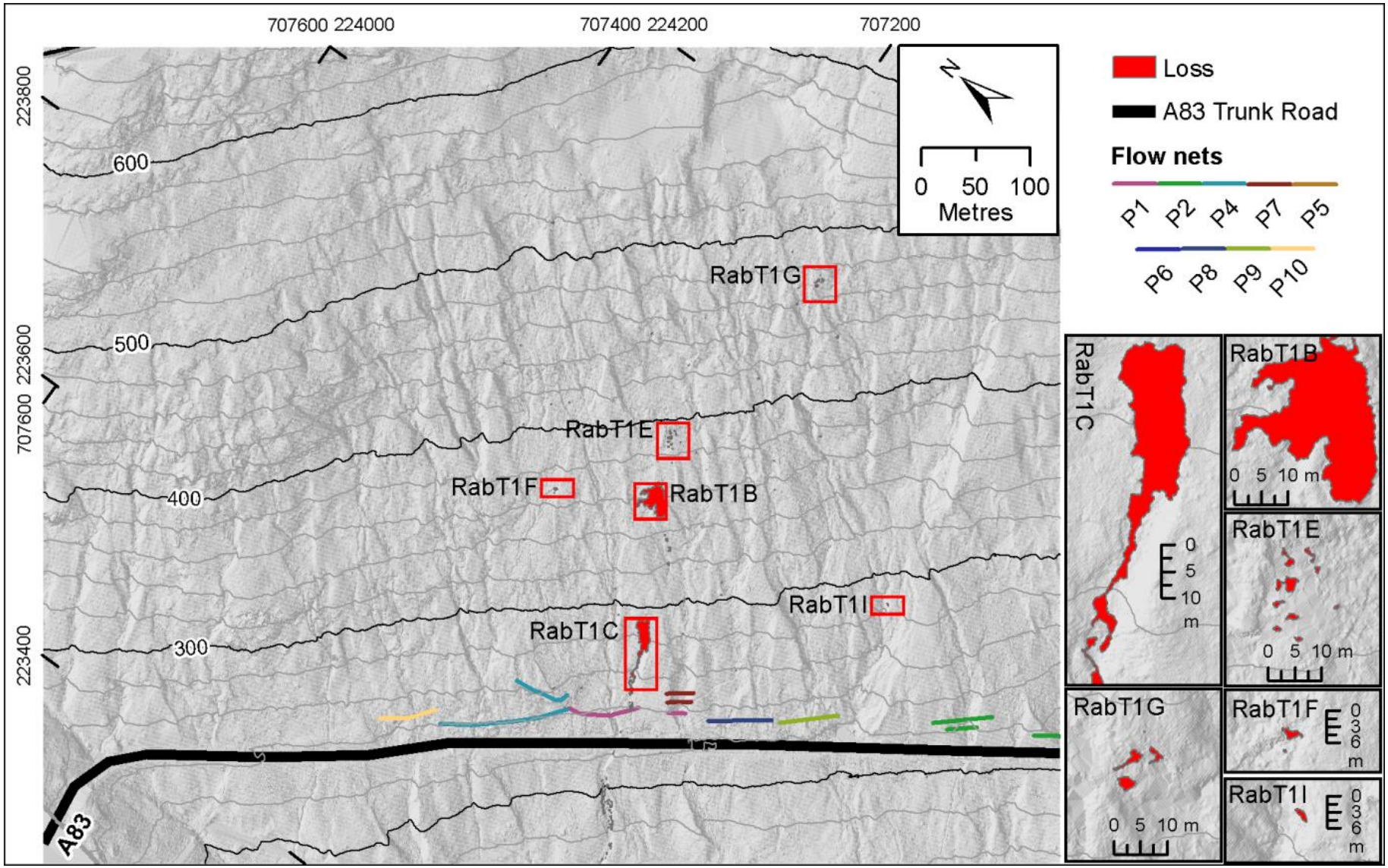

Figure 3.23 - *Change from* **the 16th October 2015 to** *6th December 2015 period (Interval 4).*

RabT1G represents a 4 m^3 shallow failure from the steep head (42°) of a gully. The change was represented by three small polygons rather than one coherent polygon which may have been expected. It is thought that this incoherent cluster of polygons relates to laser attenuation on the dark and distant failure scar, as well as the presence of a soil raft, and that the true volume is larger than 4 m^3. Deposition likely occurred within the occluded gully area below. It is possible that this landslide was triggered at the same time as SDLS1 and SDLS2.

Second storm interval (5; Frank)

Figure 3.24 shows the detected losses masked to the period encompassing Storm Frank (6th December 2015 to 11th February 2016) and SFLS1 (RabT1A). The SDLS1 source area has shown evidence of enlargement after its initial failure (RabT1C (2)). A total sediment loss of around 224 m^3 was detected within the SDLS1 source area after masking. This shows that a significant proportion (36 %) of the total calculated loss volume (630 m^3) occurred in the interval after initial failure. Although interval 5 spans two months, isolation of all the remaining change within this interval suggests that the mechanism of failure was more likely instantaneous than gradual. It is possible that this was triggered at the same time as SFLS1. A further 12.5 m^3 of gully loss (33% of the total detected in the annual change) was also detected below SDLS1 in this interval.

Further change, RabT1F (2), was detected below the SFLS1 source area and corresponds with the shifting of sediment downslope in the preceding interval (RabT1F). Repeated activity here may indicate the continued influence of hydrology. A large magnitude of loss, RabT1J (2), measuring 199 m^3, was also recorded in the phase 1 culvert below the A83, similar to that recorded during interval 1. This culvert lies directly below the SFLS1 gully. Whilst no gain was quantifiable using the method outlined in section 3.1.5, a quick approximation using CloudCompare's 2.5D volume tool determines the deposit volume to be approximately 60 m^3, thus a net loss of approximately 140 m^3 appears to have occurred.

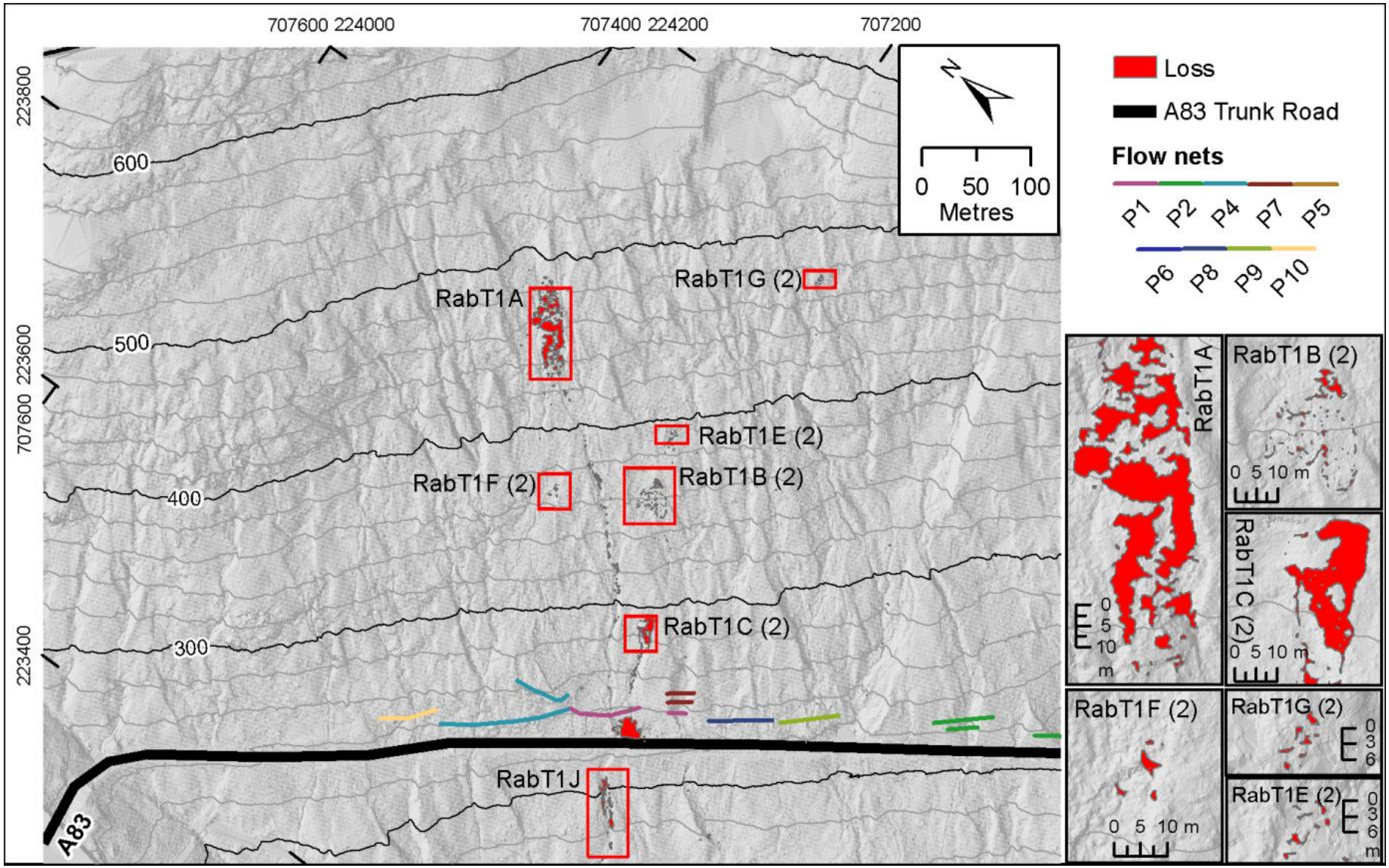

Figure 3.24 – Change from 6th December 2015 to 11th February 2016 period (Interval 5).

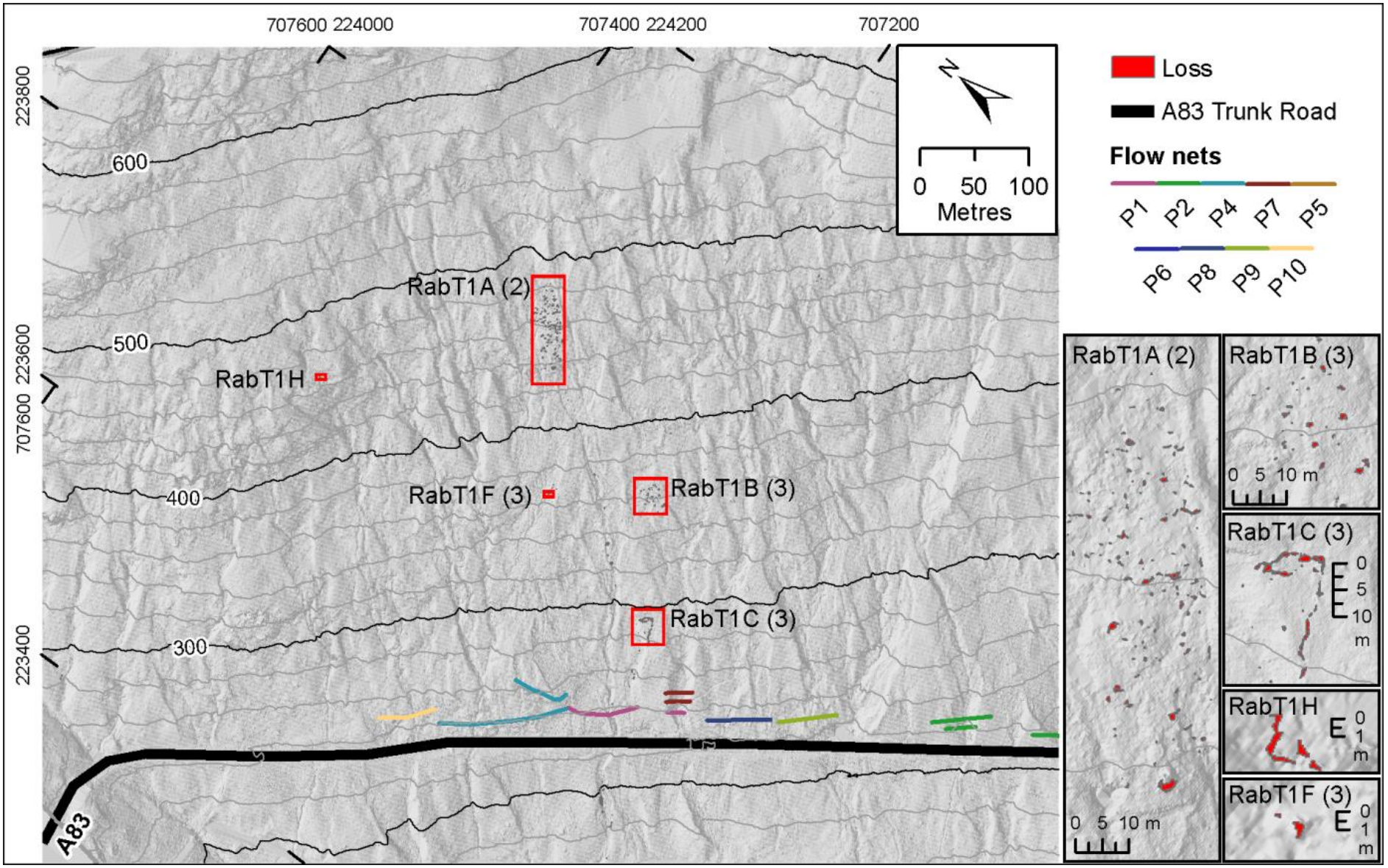

Figure 3.25 - Change isolated (masked) to the 11th February 2016 to 19th April 2016 period (Interval 6).

Post-storm interval (6)

Changes detected during interval 6 are shown in figure 3.25. One new change, RabT1H, was found. This measured 5.2 m^3 and represents another small shallow failure towards the top of a gully (39.2°), similar to that of RabT1G.Further losses include RabT1C (3), at the margins of the SDLS1 source area, particularly at the headscarp. Minor losses were also found in the SDLS2 and SFLS1 source areas (RabT1B (3) and RabT1A (2) respectively). Some of these small changes may represent some residual edge effects, although a cross-section of this change is shown in figure 3.26, demonstrating that masking has detected genuine interval-to-interval loss from the source area headscarp.

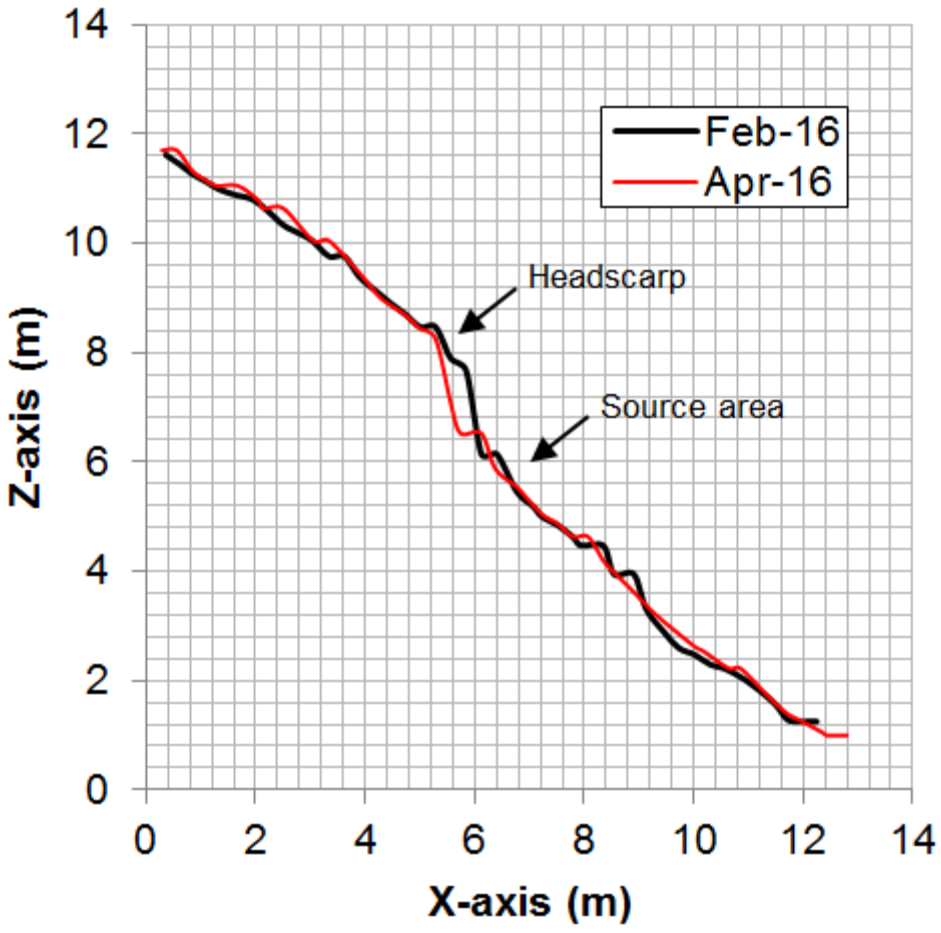

Figure 3.26 – A cross section through the top right of the SDLS1 (RabT1C) source area demonstrates genuine loss from the headscarp.

3.2.1.2 Year 2 (April 2016 – April 2017)

The second year of change, detected between April 2016 and April 2017, is shown in figure 3.27. 34 losses were detected in this interval. This marks a clear reduction in activity compared to the first monitoring year. Many of the detected changes correspond with first year changes, which are included in the figure to aid interpretation. Changes are primarily isolated within the same central band of the slope as those detected in the first year (containing SDLS1, SDLS2, SFLS1, RabT1E and RabT1F). RabT2A (32.5 m^3) represents the largest magnitude loss detected in the second year. The loss occurred within the source area of SFLS1 (RabT1A) and is neighboured by an equivalent volume of deposition just downslope. The mean depth of loss was 0.48 m. Secondary mobilisation of material here matches that found in the source area of SDLS1 (RabT2C) in the first monitoring year (interval 5).

RabT2B and RabT2C represent two new small magnitude shallow failures. These were found to measure 26 m^3 and 8 m^3 respectively, with respective mean depths of 0.74 m and 0.59 m. RabT2B mobilised from the head of a steep (39.9°) gully tributary, or channel, from where the material moved into the larger neighbouring gully. Some material has visibly deposited prior to the gully, although this appears to have spread to a level below the LoD threshold, and hence has not been detected. RabT2C initiated from a steep area (48.0°) high up the slope, directly above SFLS1 (RabT1A). Like RabT2B, this failure has occurred at the top of a pre-existing incised channel. It is considered that this change could be related to hydrology, permanent of transient, flowing through the SFLS1 source area, as hypothesised for RabT1F. RabT2C may also be linked to RabT2A, and SFLS1, given that the former is found directly upslope of the latter. The potential role of ephemeral flow in triggering these failures is discussed later in section 3.3.2.

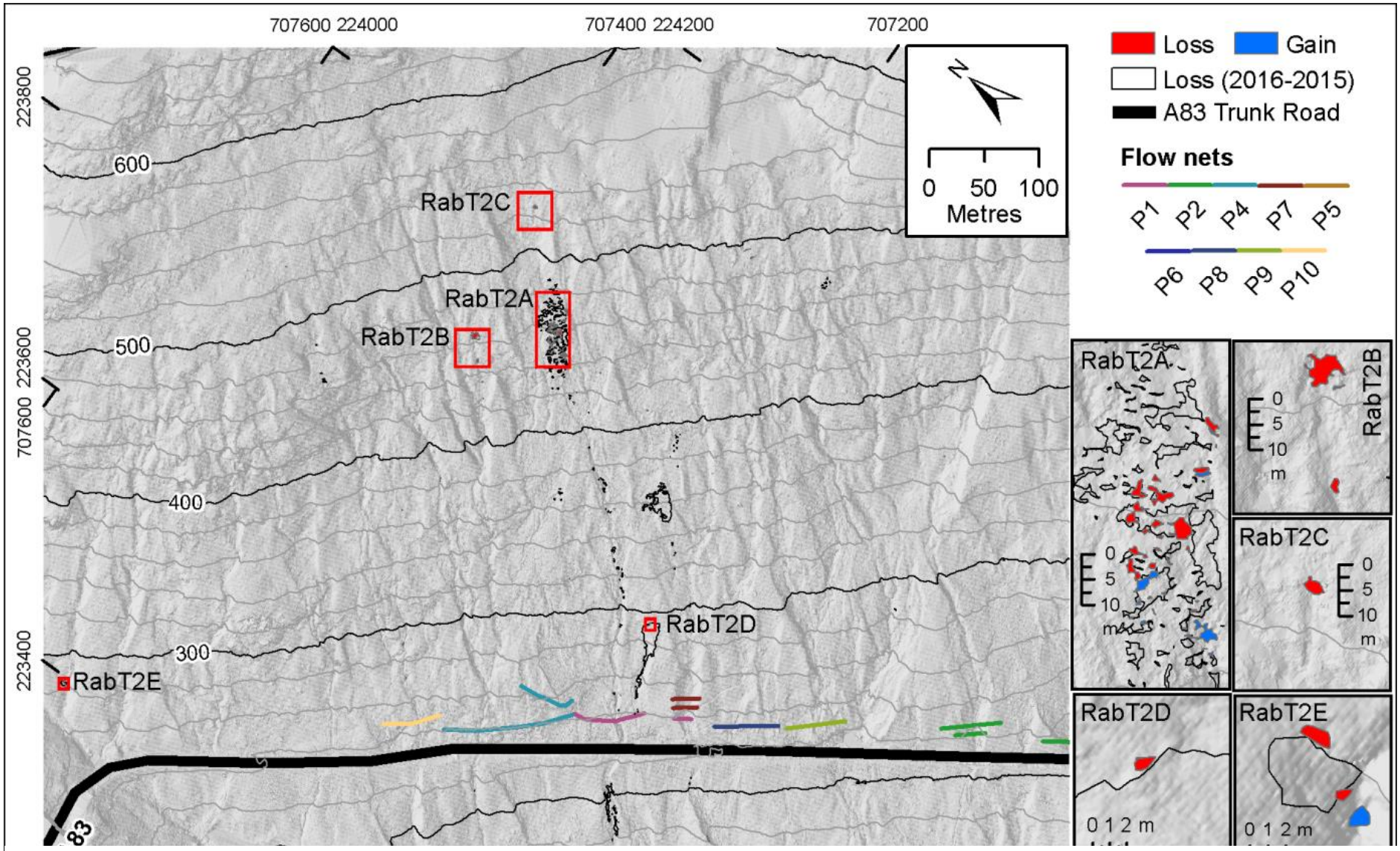

Figure 3.27 - Change from 19th April 2016 to 27th April 2017.

Interval 7 - April 2016 to December 2016

Three changes were detected during this long interval encompassing the summer and early winter 2016 (figure 3.28). The largest change, RabT1A (3), is that of a small 4.8 m^3 loss along the side of SFLS1 (RabT1A). RabT2D represents a small (1 m^3) loss at the headscarp of the SDLS1 source area, which measures a mean depth of 0.63 m and measures 1.3 m across. No deposit was detected below this, likely due to spreading below the LoD threshold. RabT2F is a small 0.65 m^3 loss detected to the south-east of the slope, an area which has been relatively inactive during previous monitoring intervals.

Interval 8 - December 2016 to February 2017

Losses detected in this interval are shown in figure 3.29. RabT2B is found in this interval. The only other change found alongside this is RabT1A(4), another very small change (4.8 m^3) along the side of SFLS1 (RabT1A). This differs from many other intervals where landslides have typically occurred alongside a large number of other changes.

Interval 9 - February 2016 to April 2017

The largest change in this interval is RabT2A. This marks the third consecutive interval in which change has occurred around or within the SFLS1 (RabT1A) source area, clearly demonstrating the residual effect of a large failure. RabT2C, is also isolated to this interval and is found directly above RabT2A and the SFLS1 source area. A link between these two changes has already been hypothesised. Identification within the same interval may further support this hypothesis, as there is potential that the same rainfall event, and streamflow, could have triggered both at around the same time in the interval.

RabT2E corresponds with the summer landslide (RabT1D) detected in the first year of monitoring and primarily consists of 0.7 m^3 headscarp loss which can be seen in figure 3.30, which measures 1.8 m across and has a mean depth of 0.4 m. A further smaller patch of loss was detected, below which 0.8 m^3 of deposition has been detected positioned within the major gully.

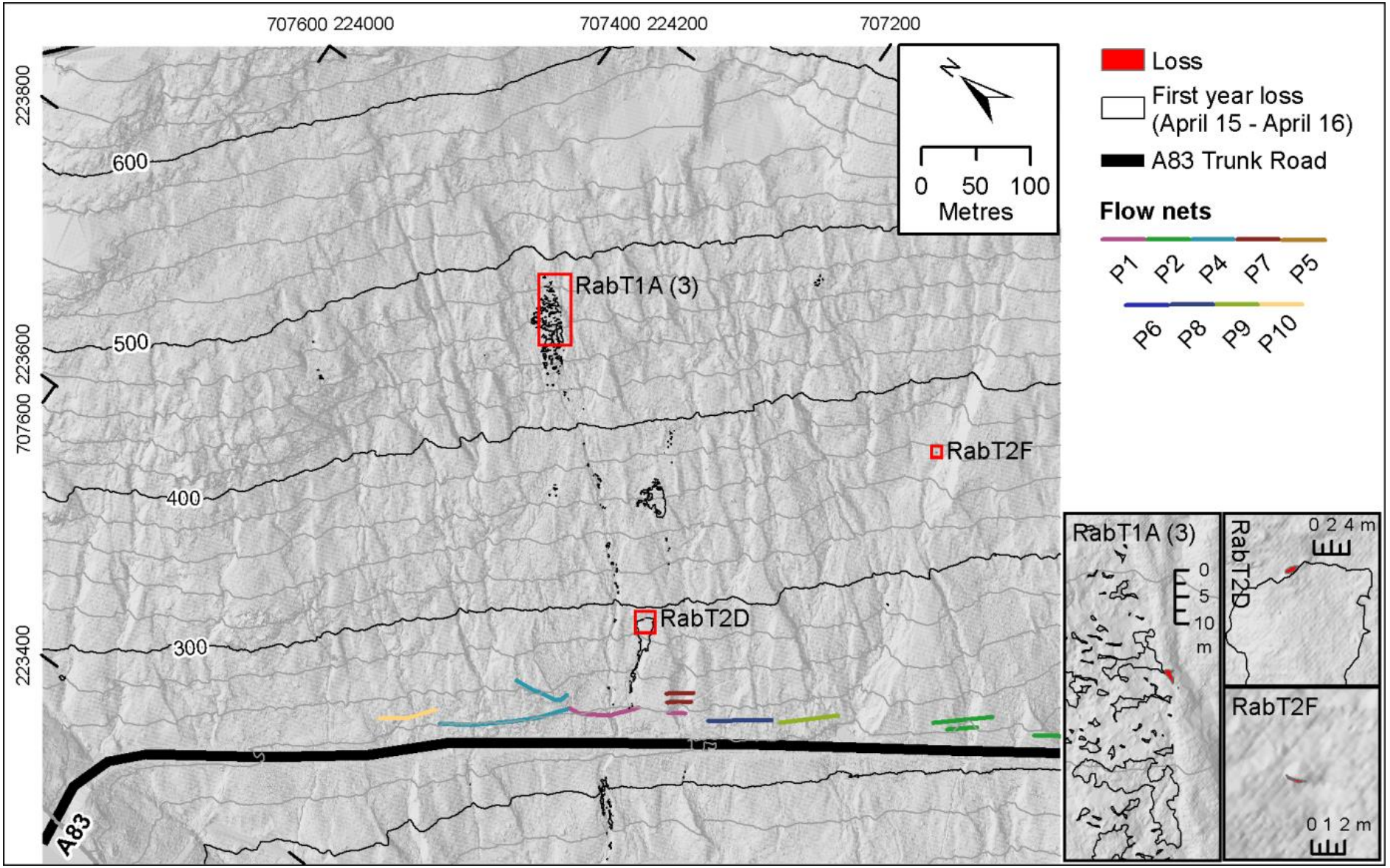

Figure 3.28 - Change from 19th April 2016 to 17th December 2016 period (Interval 7).

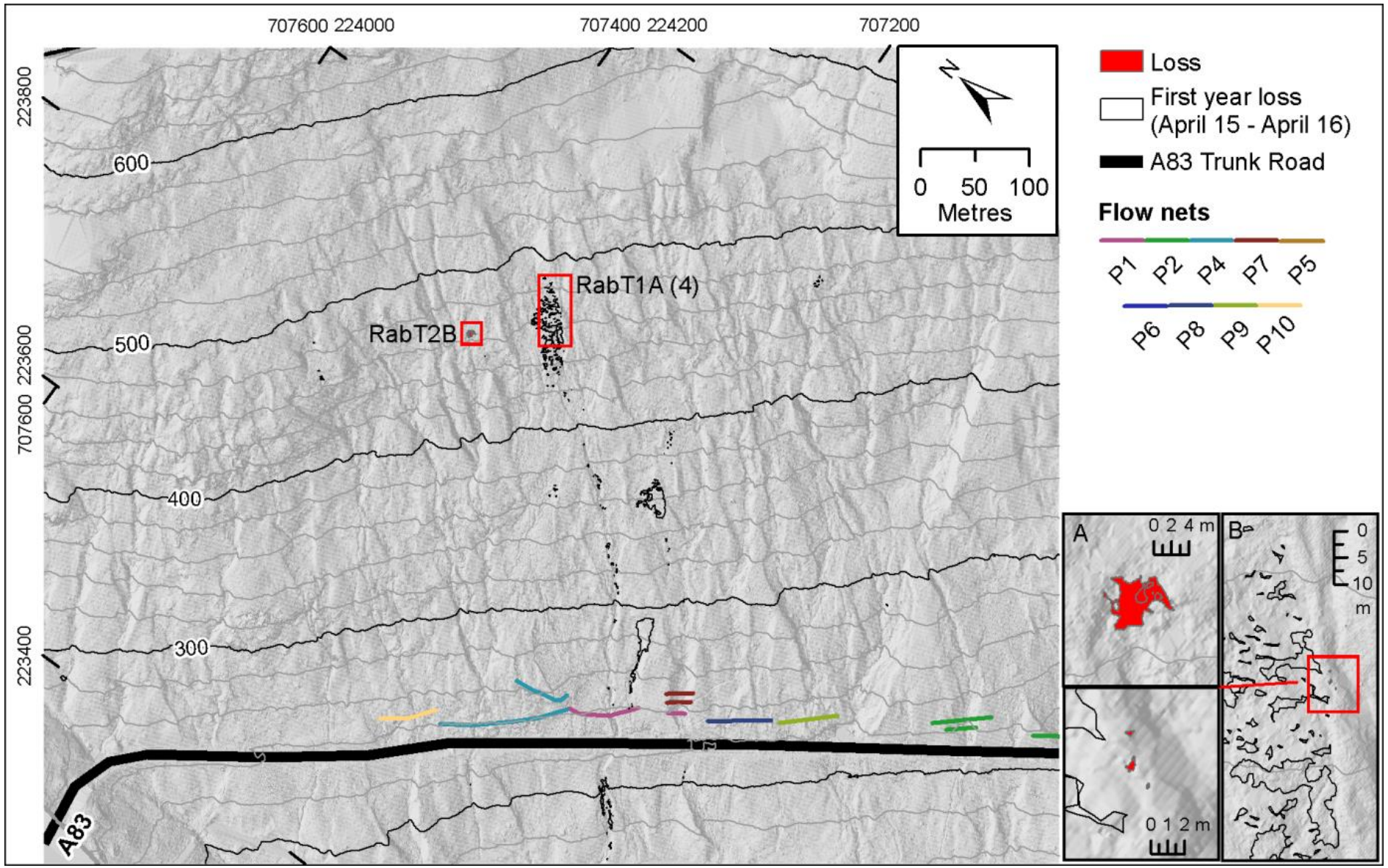

Figure 3.29 - Change from 17th December 2016 to 3rd February 2017 period (Interval 8).

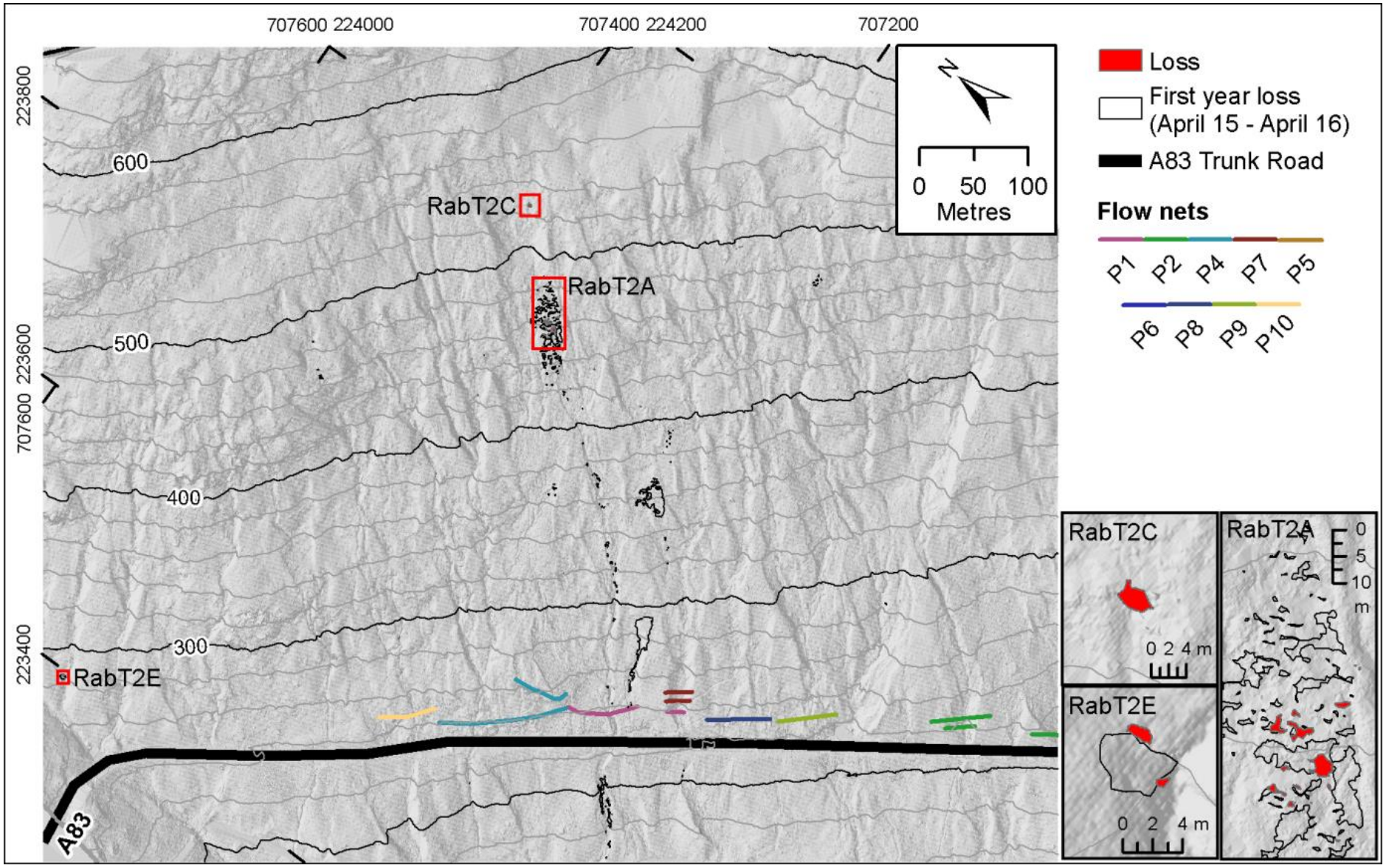

Figure 3.30 - Change from 3rd February 2017 to 27th April 2017 period (Interval 9).

3.2.1.3 Year 3 (April 2017 - January 2018)

Monitoring was continued beyond the initial two-year scope of the project, with two additional surveys conducted around winter 2018. Figure 3.31 shows losses detected between 27th April 2017 and 23rd January 2018. 20 changes were detected in this third monitoring year, although some of these are clustered polygons. Six salient areas are highlighted in total. In contrast to the first two monitoring years, these changes are more evenly distributed across the slope. Deposition is not shown, due to incomplete vegetation dieback.

The largest change, RabT3A, was detected to the south-east extent of the study area. The 58.5 m^3 failure mobilised from a 30.6° gradient open hillslope area, leaving a 0.76 m mean depth source area. The failure is found 60 m directly below a relict landslide scar with a well-defined headscarp. A long linear feature, seemingly a small incised channel, is also visible downslope of RabT3A, as visible in figure 3.32. A lack of confinement has enabled this flow to spread, resulting in rapid deposition and a short runout distance.

RabT3B and RabT3C are the second and third largest changes detected and both also represent shallow landslides. These were found to measure 12 m^3 and 10.9 m^3 respectively, with respective mean depths of 0.71 m and 0.55 m. RabT3B mobilised from a 33° area and is particularly notable due to its occurrence 50 m directly below RabT2B (interval 8: December 2016 to February 2017), along the same channel, the tributary of a major gully.

Interval 10 – April 2017 to November 2017

Losses isolated to this interval are shown in figure 3.33. In this, five of the six failures from the annual change are isolated. These include RabT3A, RabT3B and RabT3C. Whilst the large inter-survey interval period did not allow the timing of these events to be directly estimated, the data did highlight the changes, prompting further investigation using a newly installed camera installation. From this, RabT3A is estimated to have occurred on 7th November, whilst RabT3C and RabT3D were found on around 10th to 11th October and 1st to 2nd October respectively.

RabT3D and RabT3E were also detected within this interval and were found to occur between 21st and 22nd October and 1st and 2nd November respectively. RabT3D, another shallow landslide, was detected on the margin of a gully and was estimated to measure 6.9 m^3, with a mean source depth of 0.7 m. RabT3E was found to represent displacement of a small boulder measuring approximately 2 m across.

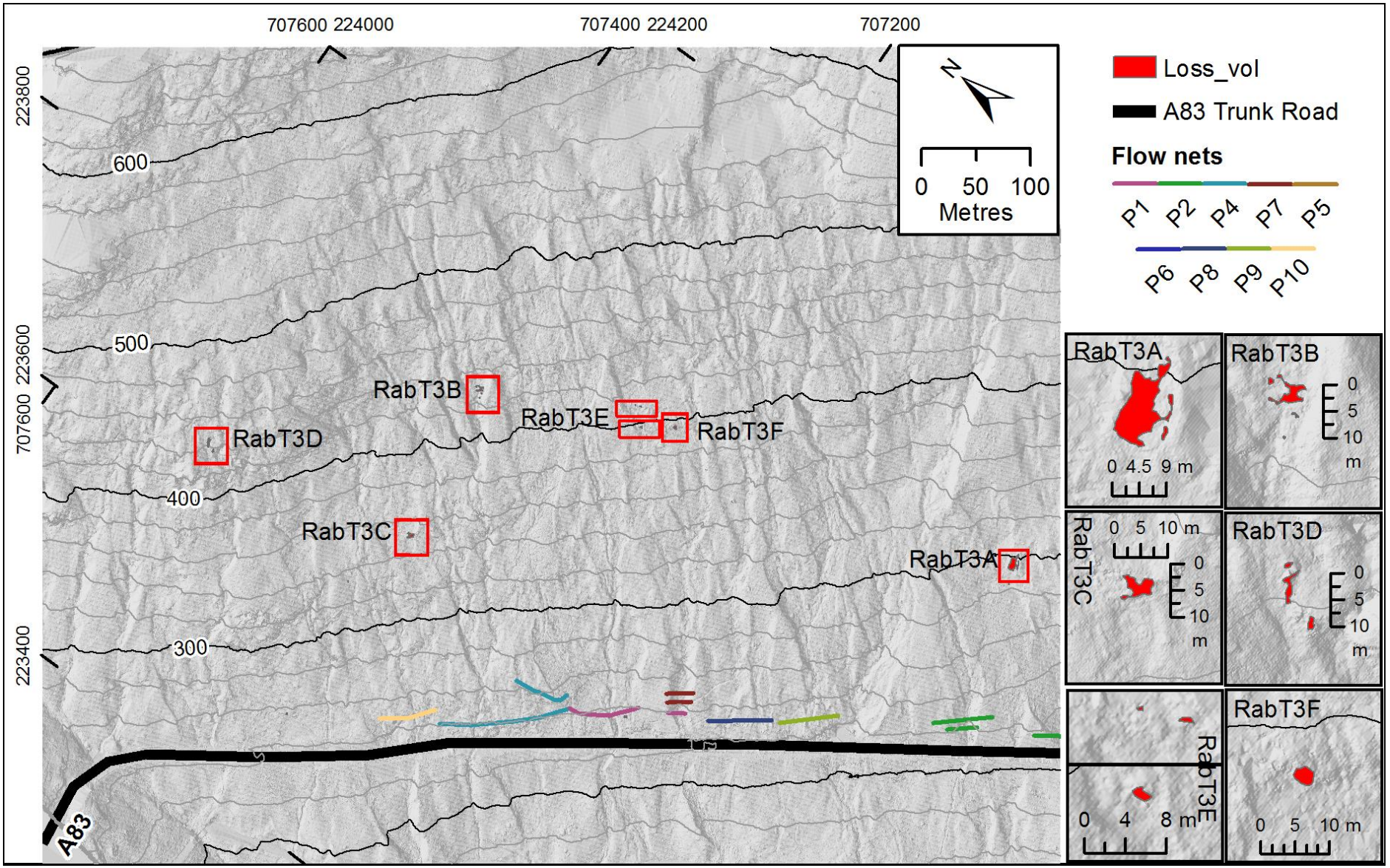

Figure 3.31 - Change from 27th April 2017 to 23rd January 2018.

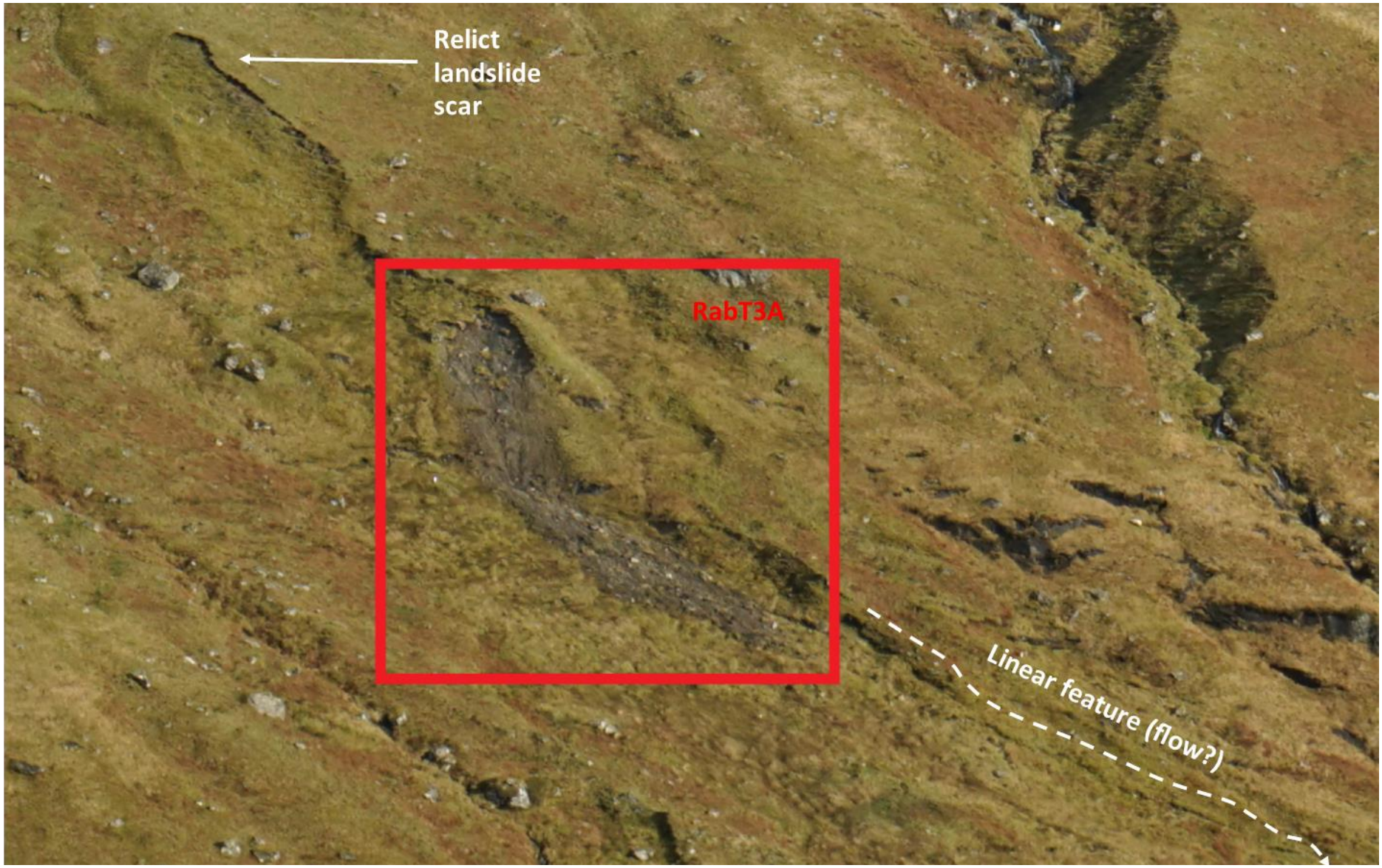

Figure 3.32 - RabT3A was detected directly below a relict landslide scar and appears to occur along a small incised channel

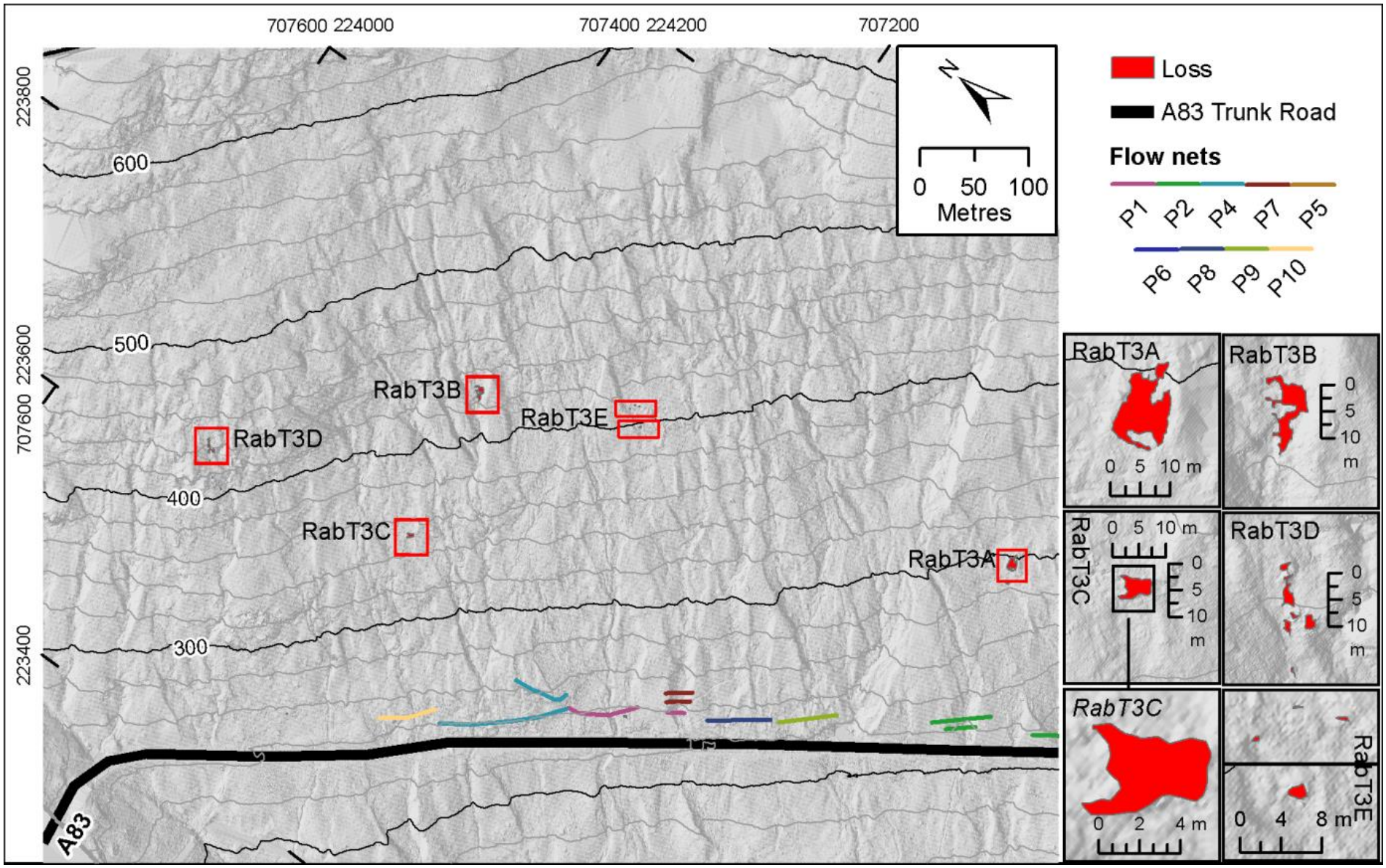

Figure 3.33 - Change from 27th April 2017 to 16th November 2017 (Interval 10*)*.

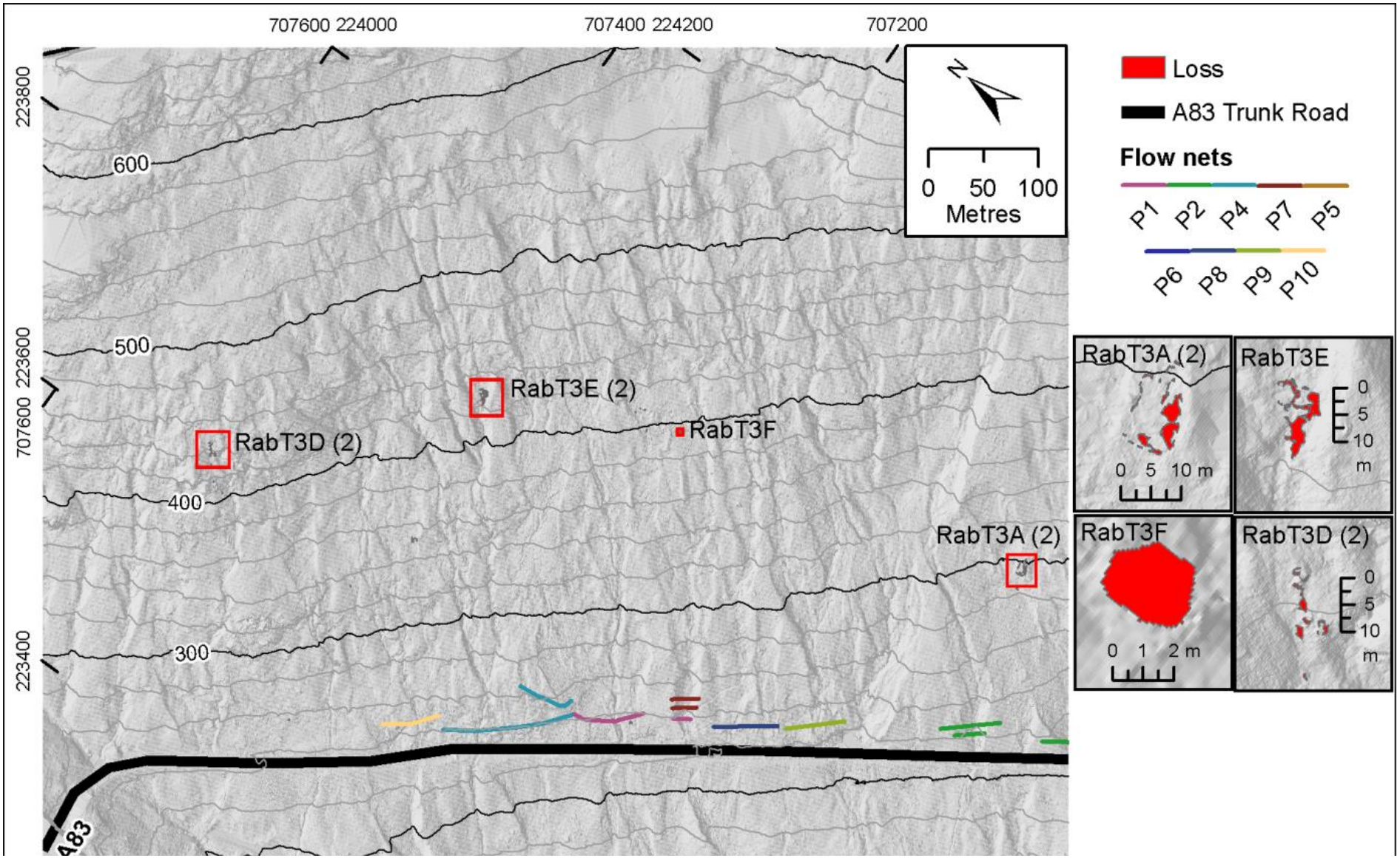

Figure 3.34 - Change from 16th November 2017 to 23rd January 2018. (Interval 11).

Interval 11 – November 2017 to January 2018

Losses isolated to this interval are shown in figure 3.34. The main change detected was RabT3F, a 5.6 m^3 shallow landslide measuring a mean depth of 0.49 m. This mobilisation corresponds with RabT1E, which appears to have been a precursor to RabT3F. Further changes include RabT3A (2) and RabT3B (2), both losses relating to landslides, of the same code, in the previous interval (10). These again clearly demonstrate remobilisations from landslide scars.

3.2.2 Glen Ogle

Five changes were detected at GO in the first year of monitoring, whilst only one significant change was detected in the second year of monitoring. Both years of monitoring data are shown in figure 3.35. The largest changes detected occurred at the head of a lateral gully scar (figure 3.35b: along the second major gully to the south east of the slope). These losses are estimated to be 0.7 m^3 and 0.67 m^3 for year 1 and year 2 respectively. Deposition was not detected below the first-year change, likely due to spreading below the LoD threshold, however this was detected for the second year change. The area prone to these failures is shown in figure 3.36, and shows this to be the only unvegetated scar of its type along the gully. Multiple similar features are found along the length of the main gully to the north-west, although none have demonstrated any detectable change. The other changes detected were too small to quantify.

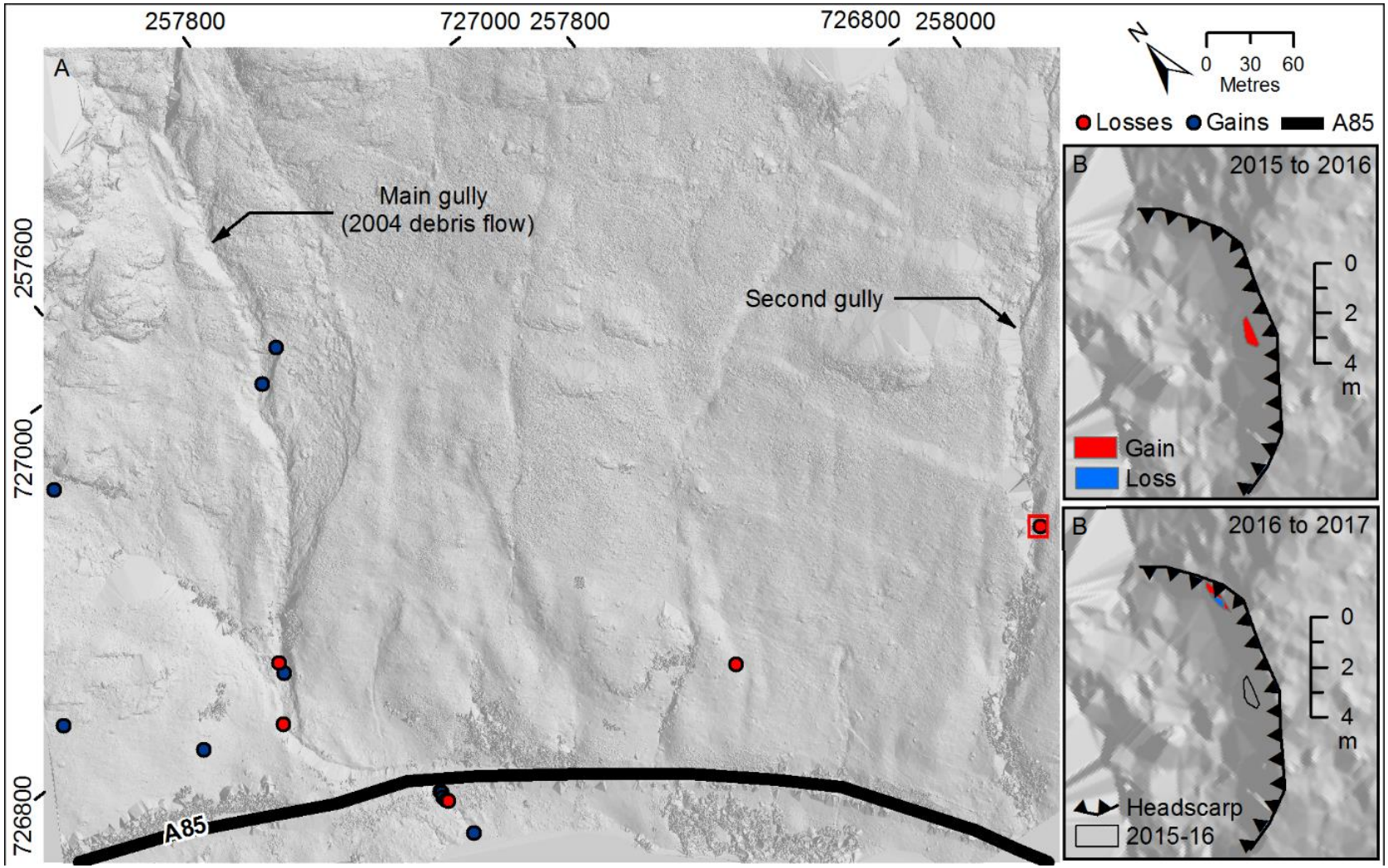

Figure 3.35 - Glen Ogle change recorded between April 2015 and April 2017 A) The main figure portion only shows change recorded between 21st April 2015 and 21st April 2016, no further changes were detected between 21st April 2016 and 28th April 2017, apart from that shown in C) which corresponds with preceding change shown in B).

Figure 3.36 - A photograph of the most active region at Glen Ogle, a lateral gully scar.

3.2.3 Glencoe

Seven changes were detected at Glencoe in the first period of monitoring, between October 2015 and April 2016. No changes were detected in the second whole year of monitoring, between April 2016 and April 2017. Figure 3.37 and figure 3.38 show the results of the first-year monitoring for positions 1 and 2 respectively. At position 1, five small magnitude losses were detected from the rock faces above the debris cones, however these change volumes were too small to accurately estimate (< 0.5 m^2 in area). The largest quantity of change, 5 m^3 of loss and 7.6 m^3 of gain within an incised debris fan, was found close to the road at position 2. Some additional loss was likely occluded a short distance upslope.

No whole-site figure is shown for position 3 as no significant detectable changes were found across the main portion of the study site (alluvial fan). A large rock failure measuring approximately 2000m^3 was however detected high up on the steep (72.4°) rock face above the debris fan (figure 3.39), almost 900 m away from the road. This comprises the largest single failure detected at any site throughout the monitoring period. The failure occurred between October 2015 and April 2016 and measured mean and maximum depths of 1.85 m and 6.35 m respectively. The failed rock unit is classified as being part of the Andesitic

Glencoe volcanic formation, which mobilised into a gully deeply incised into an Etive Dyke to the east (BGS, 2017). The failed area comprised part of a bench, or step, in the bedrock. In addition to the vertical cross section shown in figure 3.39, figure 3.40 shows a lateral cross section through the rockfall. The relatively clean post-failure surface, with little roughness, is indicative of one mass failure, rather than multiple smaller superimposed failures which would be expected to leave a rough surface. The failure appears to be of the block slide (Hungr *et al.*, 2014), or slab (Ballantyne, 1986) type, with the rock mass dimensions being 48.8 m across and 18 m high. The pre-failure surface protruded somewhat in comparison to the surrounding area, whereas the post-failure surface is now at a similar baseline to the rest of the face. The 45° inclination of the scar, down towards a large gully (mean 36° gradient), and a lack of evident deposit on the area immediately downslope, suggests that the rock slab slid rather than toppled. A cross section through limited data in the gully (figure 3.41) indicates the presence of a large coherent slab, with a 20 m long spread of material approximately 1.4 m thick visible downslope. The post-failure surface features a 1.7 m deep lip (approximately 33 m along the cross section) which may mark a discontinuity. This only protrudes in the lower 8 m of the scar and would have inhibited a vertical planar slide, thus suggesting that the rock mass slid normal to the orientation of the scar, towards the area where deposition is observed. Rock failures of this type are common north of the highland boundary, as opposed to rotational rock slope failures (Ballantyne, 1986).

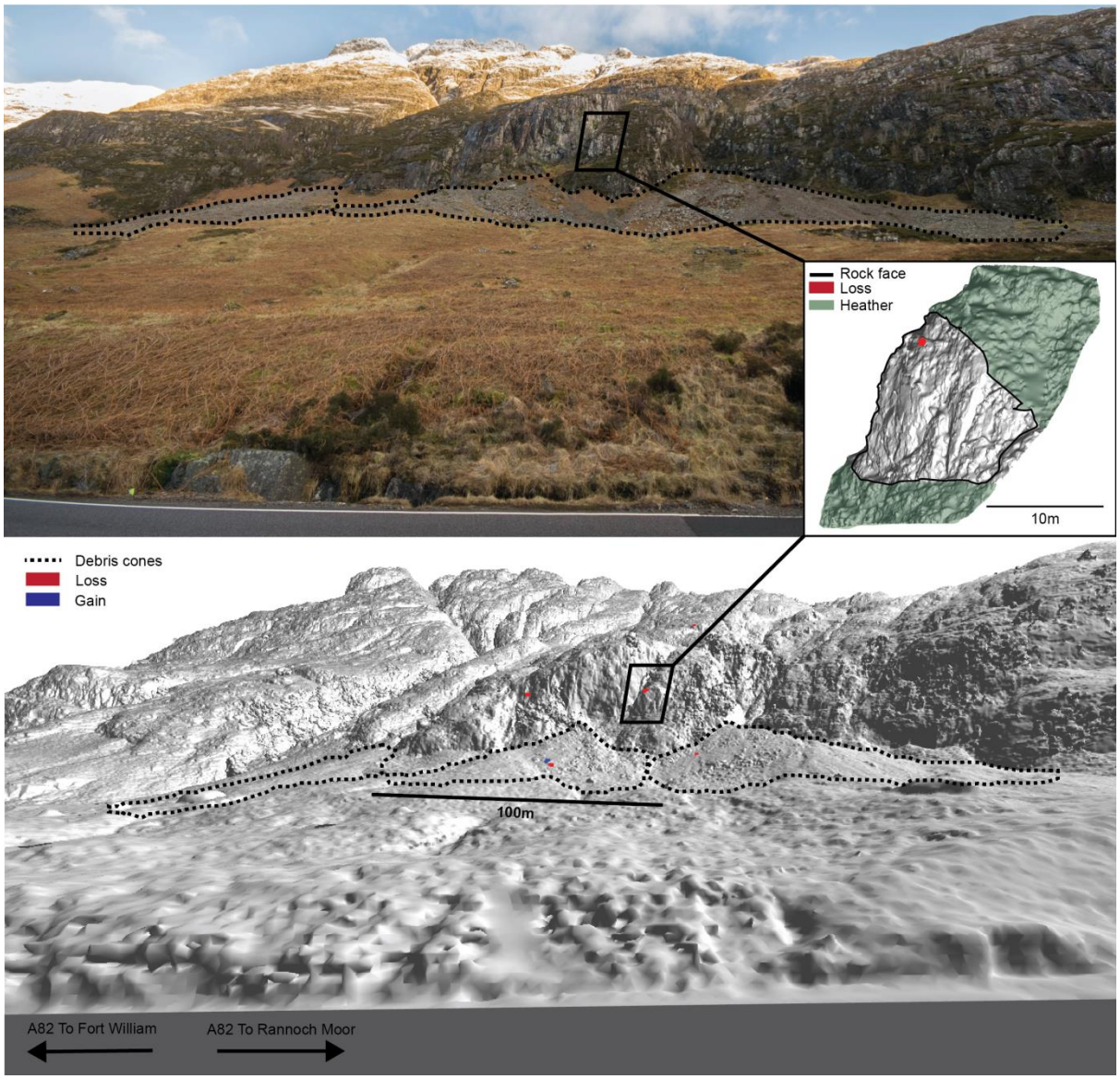

Figure 3.37 - Glencoe year 1 (October 2015 to April 2016) change for position 1

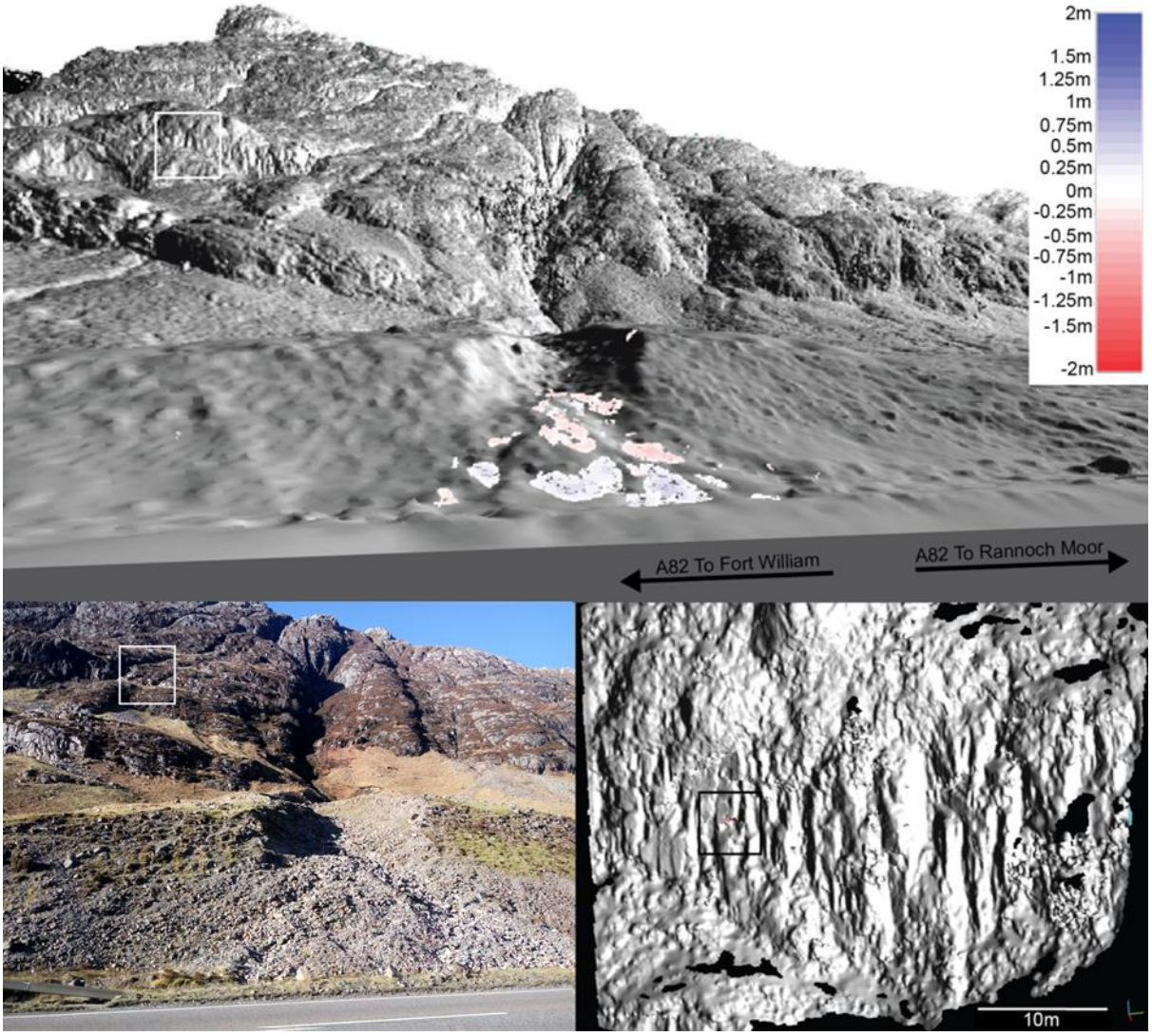

Figure 3.38 – Change detected at Glencoe position 2, in the first year of monitoring (October 2015 to April 2016). The principal changes detected are those within a few metres of the road. Elsewhere, only a very small number of small changes have been detected, such as that displayed in the bottom right.

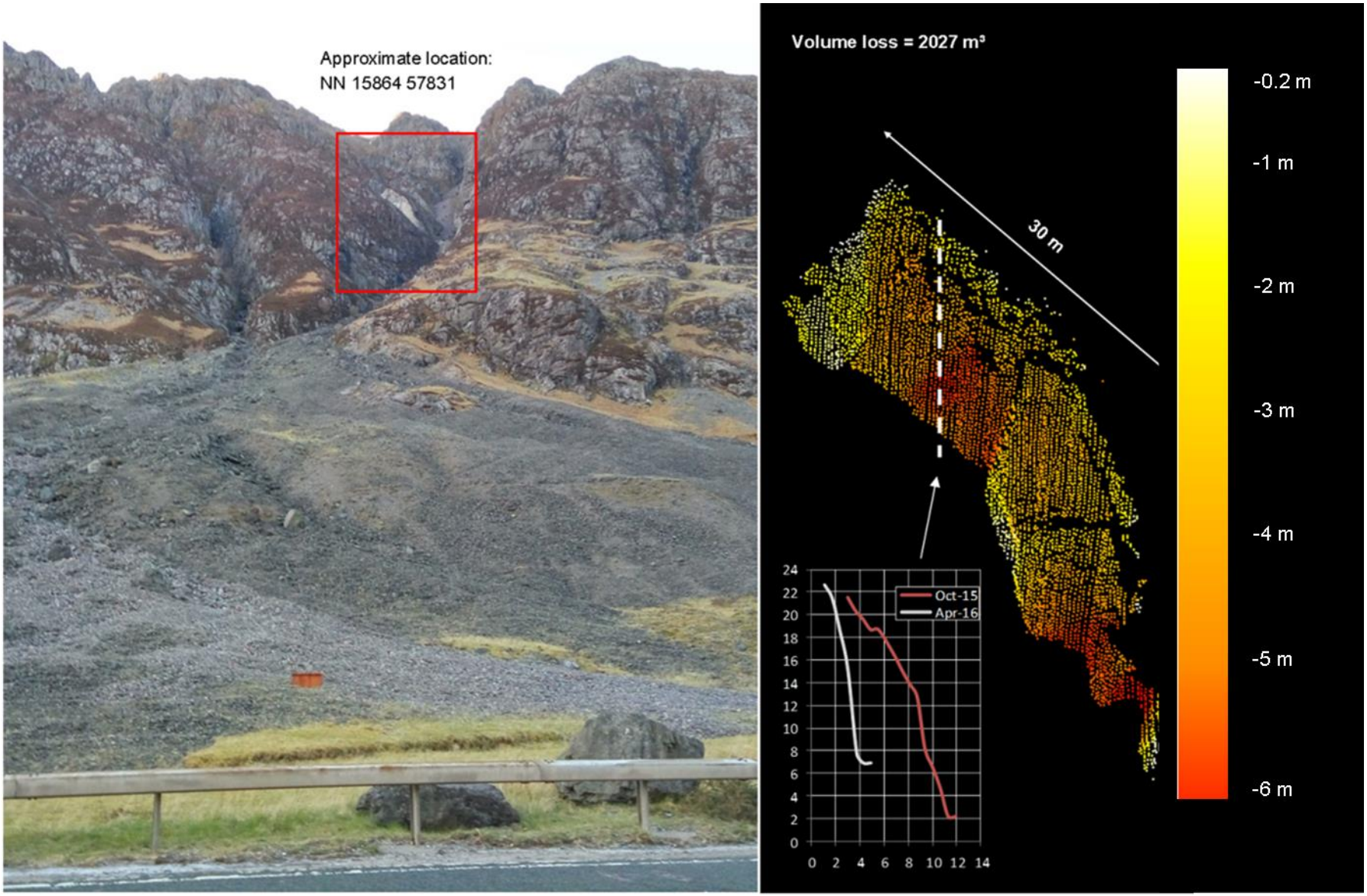

Figure 3.39 - Glencoe year 1 (October 2015 to April 2016) large rockfall detected at position 3

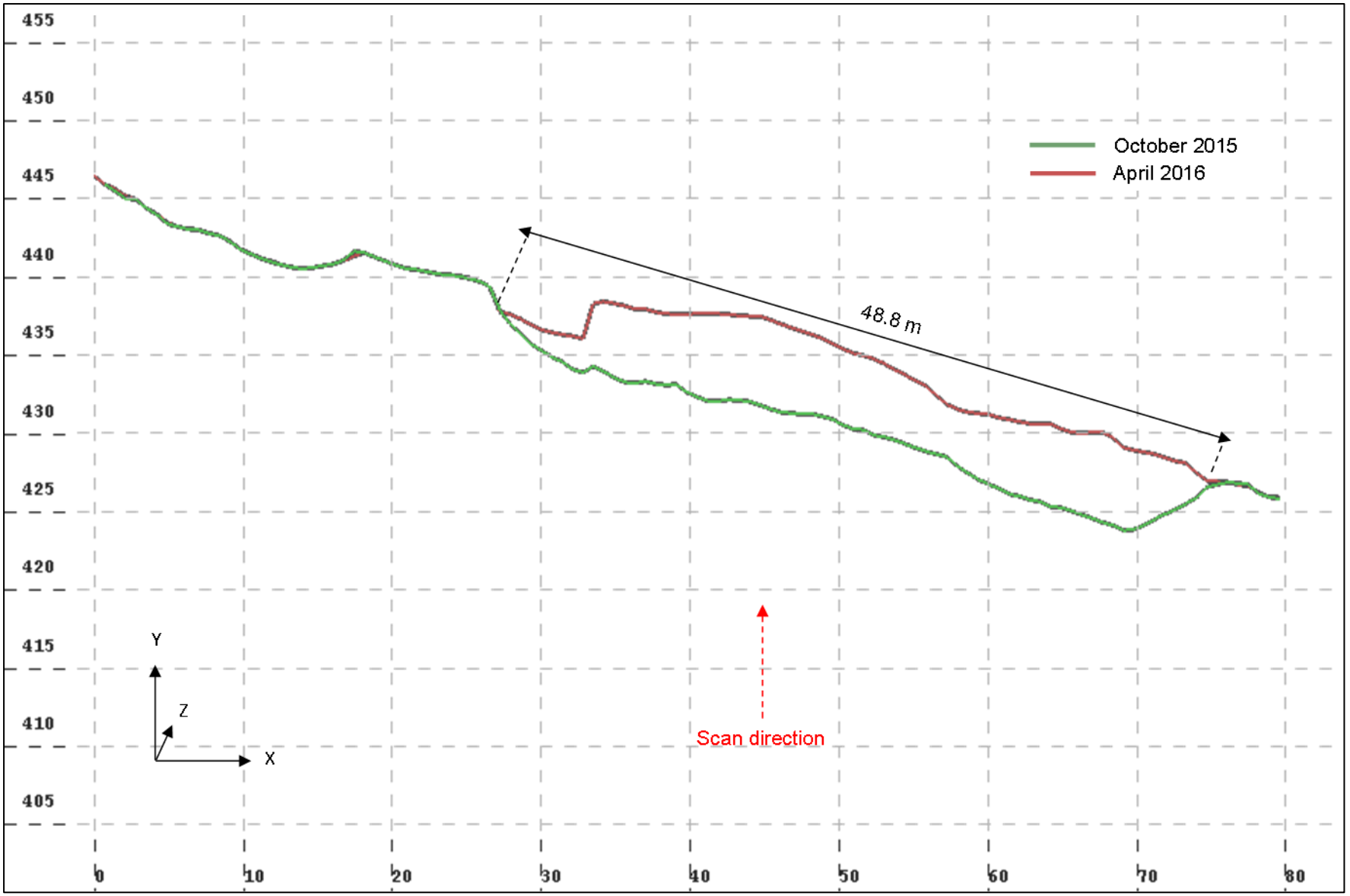

Figure 3.40 - A lateral cross section through the 48.8 m wide rockfall at Glencoe.

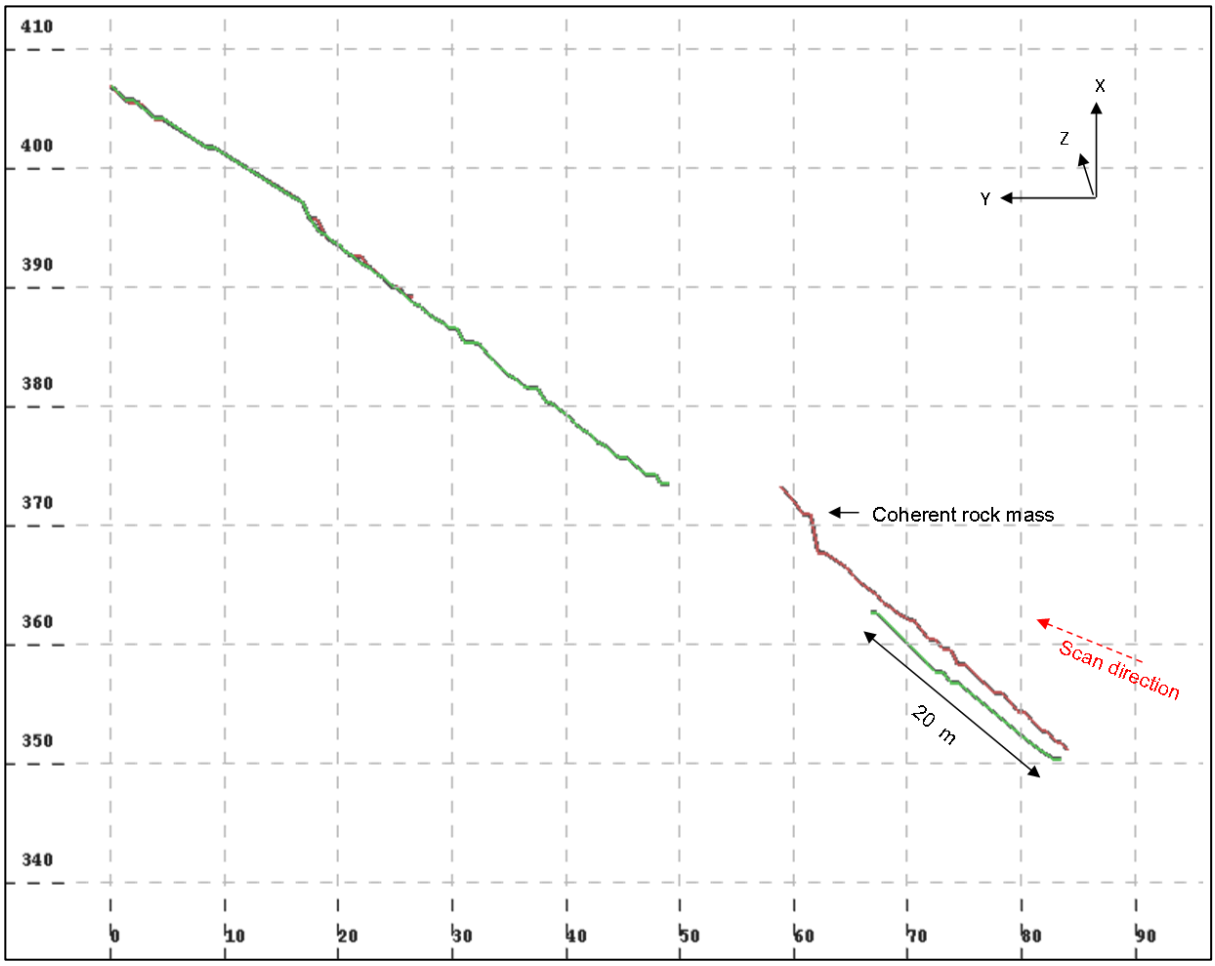

Figure 3.41 - A longitudinal cross section through limited gully data at Glencoe, showing a large coherent rock mass and a thick (1.4 m) layer of deposition below. The area upslope of the gap shows no difference in surface, thus suggesting this area is not prone to vegetation issues. Data was not adequate for change detection using M3C2.

3.3 Analyses

The spatial distribution of shallow failures and debris flow is influenced by topographic and stability factors, including slope angle, convergence, hydrologic conductivity and material properties (Montgomery and Dietrich, 1994). This section provides more detailed analyses of such factors, as well as an examination of rainfall recorded at the time of known events and the magnitude-frequency relationship.

3.3.1 Rainfall

Daily rainfall data, for all three sites, was made available by the Centre for Environmental Data Analysis (CEDA, 2017) and is shown in figure 3.42. Higher resolution data was not available for all three sites, although rainfall intensity-duration threshold studies for shallow failures have historically used databases with a large proportion of events that had rainfall durations of a day or more (Caine, 1980; Guzzetti *et al.*, 2008). Figure 3.42 encompasses the first two years of monitoring, which surveys at GO and GC were limited to. The data show that RabT exceeded a daily forecast threshold of 25 mm, used alongside a 3 hour forecast threshold to activate A83 warning wig-wag signs, much like those used at rail crossings (M. G. Winter and Shearer, 2017), on 57 occasions. This compares with the same threshold being exceeded 29 times at GO and 52 times at GC. Increasing this threshold to 40 mm, for comparison purposes, GO only exceeded this on three occasions. This compares to sixteen occasions at RabT and eleven at RabT. It is notable that the peak of rainfall on 30th December 2015 was recorded at both RabT and GO, yet no failure was detected at the latter, whilst SFLS1 was triggered at RabT.

A further breakdown of daily rainfall, relative to the detected changes, is provided for RabT herein. This includes data for the third monitoring year.

Year 1

Daily rainfall for the first year of monitoring is shown in figure 3.43. Of the first three monitoring intervals, the first received the largest average daily rainfall, this being 8 mm rainfall per day. It is noteworthy that RabT1D and RabT1J were both detected in this interval. The former was most likely triggered by an intense peak in rainfall on 2nd June 2015 (interval 1), where 64 mm of rainfall was recorded. This compares with daily maximums of 71.4 mm and 63.6 mm for 30th December (SFLS1) and 5th December (SDLS1) respectively. The next two intervals, in which only minor changes were detected, received daily averages of 5.7 mm and 6.7mm respectively. The respective maximal rainfall values were 33 mm/day and 46.2 mm/day.

Rainfall during interval 4 was particularly high, with an average of 15.7 mm rainfall per day recorded. In addition to 63.6 mm on 5th December, 54.8 mm was recorded on 6th December (SDLS2). It is noteworthy that 61.6 mm rainfall was detected on 10th November, this being more than the quantity that triggered SDLS2. Average daily rainfall during interval 5 was lower than that of interval 4 with an average of 10.7 mm per day recorded. The interval did however experience a more intense day of rainfall (71.4 mm on 30th December 2015), which coincides with the SFLS1 event. An average of 5.3 mm rainfall per day was recorded in interval 6.

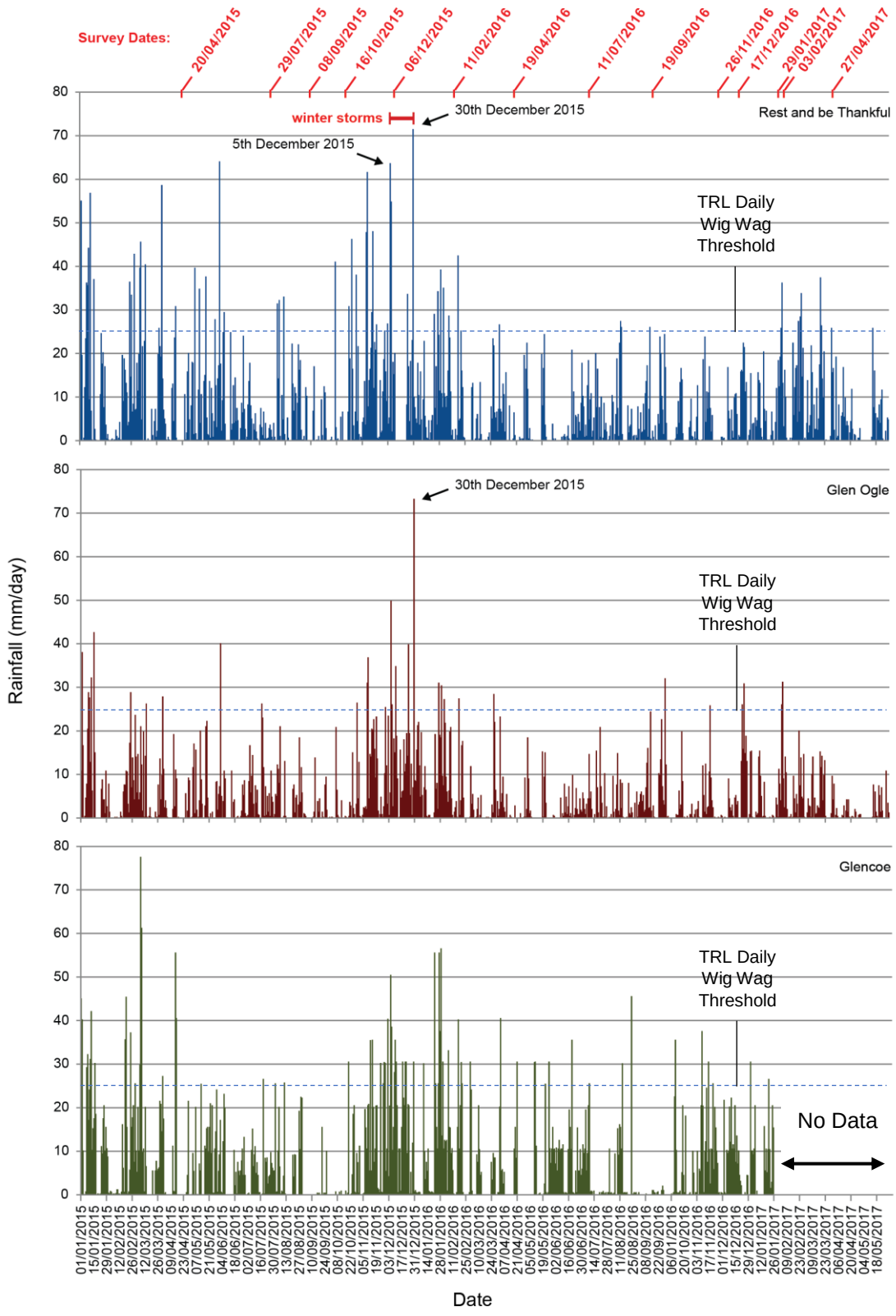

Figure 3.42 – Daily rainfall data for the three study sites, including survey dates for the Rest and be Thankful at the top for reference. 5th December is the date of SDLS1 and SDLS2, whilst 30th December marks the date of SFLS1.

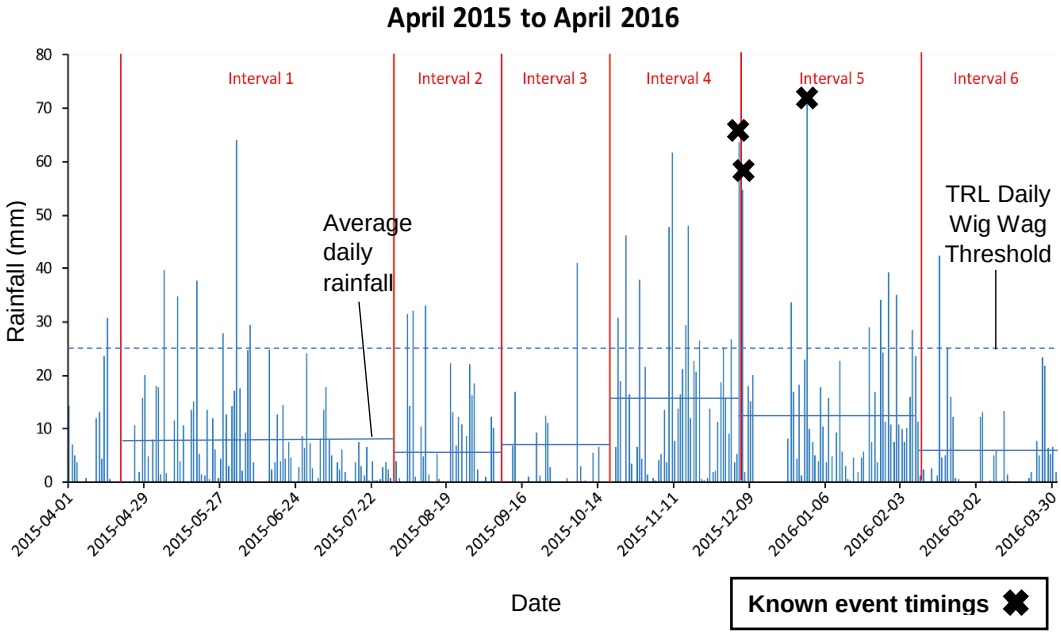

Figure 3.43 - Daily rainfall values, for the first monitoring year, recorded at the top of Glen Croe, RabT (NN 228069) (CEDA, 2017)

Year 2

Figure 3.44 shows daily rainfall data for the second year of monitoring. The mean daily rainfall in interval 7 was 4.6 mm. This was the lowest mean value recorded throughout the monitoring. The 25 mm daily warning wig-wag sign threshold was only surpassed on three occasions in this interval. Rainfall did not once exceed a threshold of 30 mm/day, whereas most other intervals did on at least one occasion. These low values correspond with some of the lowest quantities of detected change.

The mean daily rainfall during interval 8, in which few changes were also detected, was 7.3 mm. A 30 mm/day threshold was only exceeded once at the end of the interval (2nd February 2017). RabT2B was however detected during this interval and may correspond with this particular peak. The mean daily rainfall during interval 9 was the highest recorded throughout the second monitoring year, with 8.3 mm recorded. These quantities are however still considerably lower than those recorded during intervals 4 and 5. Interval 9 was also the most active period, with RabT2A and RabT2C detected. Daily rainfall exceeded 30 mm on three occasions. The largest of these three peaks was a daily total of 37.4 mm recorded on 18th March 2017.

Year 3

Figure 3.45 shows the average daily rainfall for the third monitoring year. Interval 10 saw an average daily rainfall of 9 mm, however the 1st October to 15th November period had a

much higher average of 13.9 mm, thus skewing the overall survey interval average rainfall value. The 25 mm warning wig-wag rainfall threshold was exceeded on sixteen occasions, seven of these falling within the 1st October to 15th November period. During this period, five shallow landslides were detected. All of these occurred on days with rainfall values above the 25 mm warning wig-wag threshold. The smallest quantity of daily rainfall for these was 31 mm. Rainfall in interval 11 was reduced compared to the preceding October and November period, with an average of 9.1 mm per day recorded. This is comparable to the value for the whole of interval 10 however.

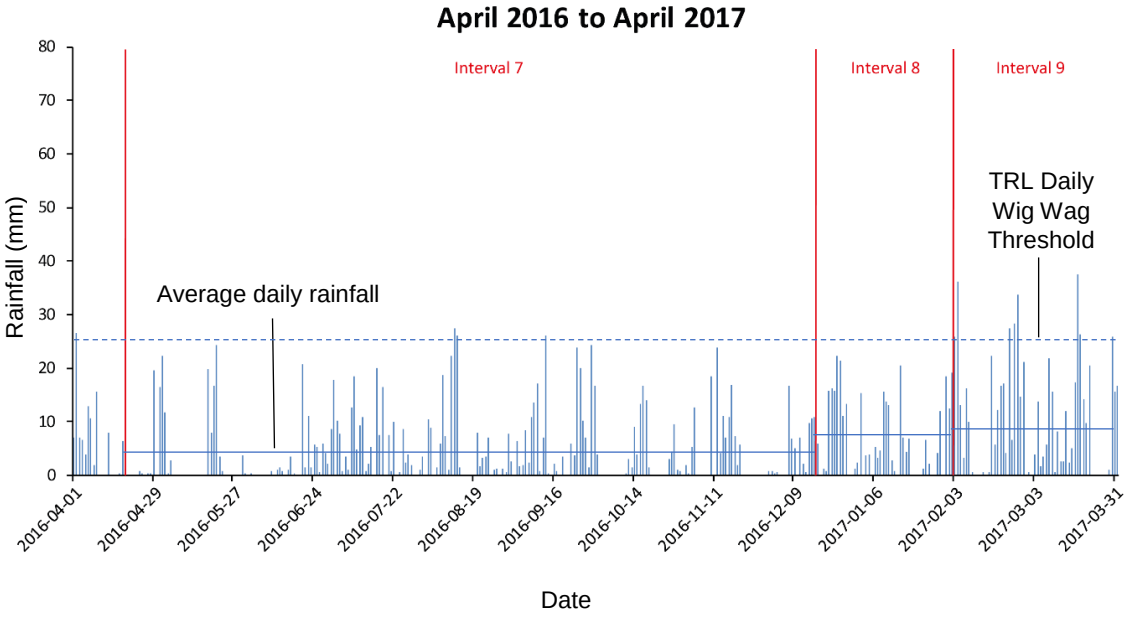

Figure 3.44 - Daily rainfall values, for the second monitoring year, recorded at the top of Glen Croe, RabT (NN 228069) (CEDA, 2017)

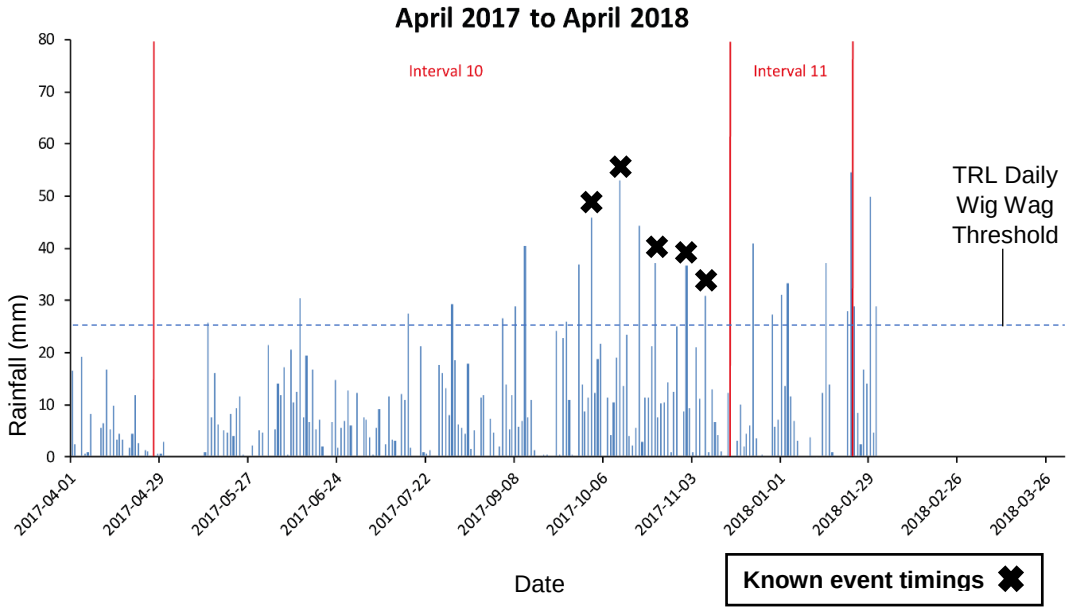

Figure 3.45 - Daily rainfall values, for the third monitoring year, recorded at the top of Glen Croe, RabT (NN 228069) (CEDA, 2017)

3.3.2 *Landslide dimensions and pre-failure topography*

The range of landslides detected at RabT, and the accompanying high resolution topographic data, enables a fairly robust analysis of the pre-failure topography and the dimensions of the failures. The former was examined using a raster dataset of slope angles derived from a 1 m April 2015 TLS DEM in ArcGIS, as well as high resolution pre-failure photomosaics. The latter was examined by aggregating incoherent polygons of the same change and performing a 'minimum bounding geometry' analysis in ArcGIS, to draw polygons around the landslides and derive minimum width and length values.

3.3.3 *Pre-failure topography and features*

Most of the landslides examined were found on or close to steep convex breaks in slope (>40°). In the first year data, both SFLS1 and SDLS2 were footed by steep breaks in slope. SDLS2's break in slope was vegetated, although some small tension cracks were evident. SFLS1 was footed by a scarp measuring approximately 4 m in height. RabT1D and RabT1G were also footed by breaks in slope, although the former was footed by the bank of a gully. In contrast, SDLS1 was headed by a steep scarp, approximately 3 m in height. RabT1G was also found below a steep break in slope. RabT2B and RabT3B (related failures) are exceptions, although the former was found on a more gentle break in slope with a maximum slope angle of 39.3°. RabT2C was found on a particularly steep break in slope measuring 48°. In the final year of monitoring, RabT3C, RabT3D and RabT3F were all found on steep breaks in slope. In contrast, RabT3A was found above two breaks in slope which correspond with large tension cracks in pre-failure photographs.

Figure 3.46 shows the mean slope angles on which all of the detected change polygons were found at RabT. The 30-34.9° range is dominant in this plot and shows that 31 % of the detected changes occurred on slope angles of this gradient. 40 % of the detected changes were found on steeper areas of slope however 29 % of the detected failures were found at slope angles less than 30°.

3.3.4 *Landslide dimensions*

The mean depth of failure for all of the landslides detected at RabT was 0.74 m, however this figure is skewed by the 1.5 m depth SDLS1. Omitting SDLS1, the mean depth of failure was 0.66 m. The year 2 and year 3 mean change depths were both 0.67 m, whilst SDLS2 measured a mean depth of 0.66 m and SFLS1 was similar at 0.7 m. The variance in the mean depths of failure is clearly very small (std dev of 0.264 with SDLS1 and 0.082 without).

The mean width of all detected landslides was 10 m. with SFLS1 having the maximum width of 29 m. All three winter 2015 debris flows skew these figures however, and omission of these reduces the mean width of failure by almost half (to 5.3 m). The mean length of failure meanwhile was 18.9 m, whilst the maximum length was again that of SFLS1, with a value of 85.9 m. Omitting the three largest failures resulted in a mean source area length of 10.1 m.

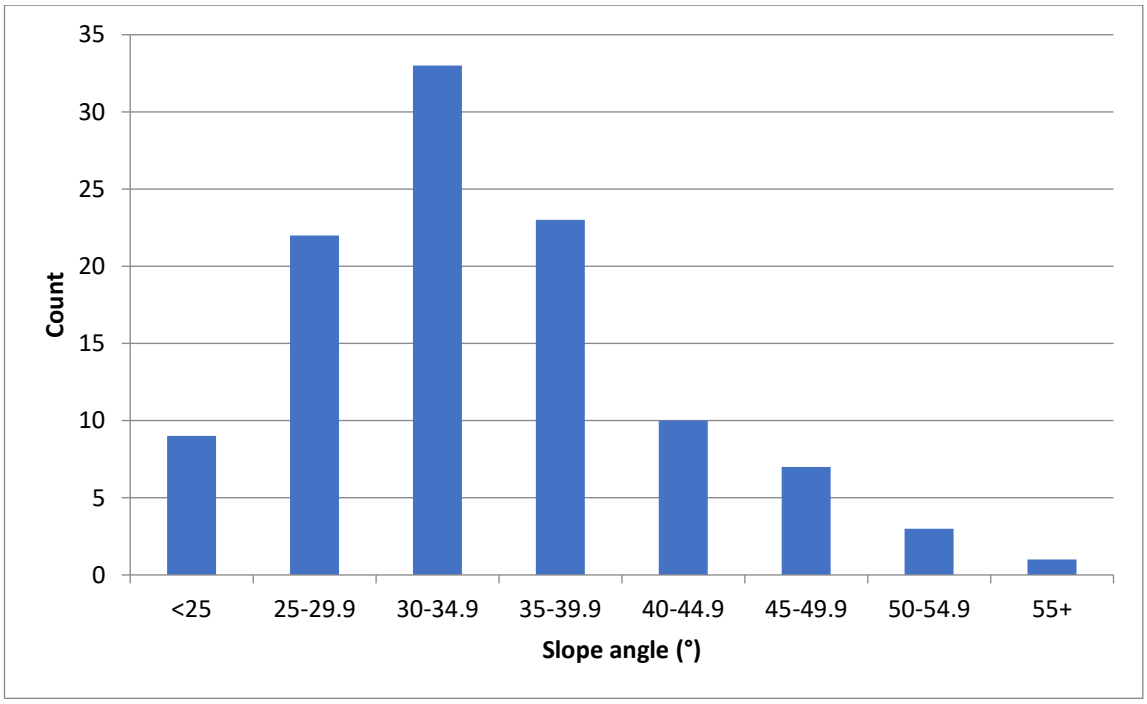

Figure 3.46 – The mean slope angles at which the detected changes were found

3.3.5 Small incised channels and ephemeral flow

In addition to gullies, small incised and ephemeral channels have been observed at RabT during slope walkovers and on detailed analysis of high resolution photographs. Channels have anecdotally been highlighted as a potential trigger of activity. It is thought that transient flow within such systems could be changing over time, although the mechanism of this switching is not particularly well understood. This might explain zonation of first year detected changes within the centre 180m of the slope.

Some of the changes detected at RabT correspond very closely with these features. RabT2B and RabT3B were for example both detected along the same incised channel, within 50 m of each other. Figure 3.47 shows the region around these failures before and after RabT2B. The source area may have been saturated prior to failure, with darker, mottled vegetation present (circled in red), this being characteristic of other saturated areas. This area also coincides with two upslope tension cracks.

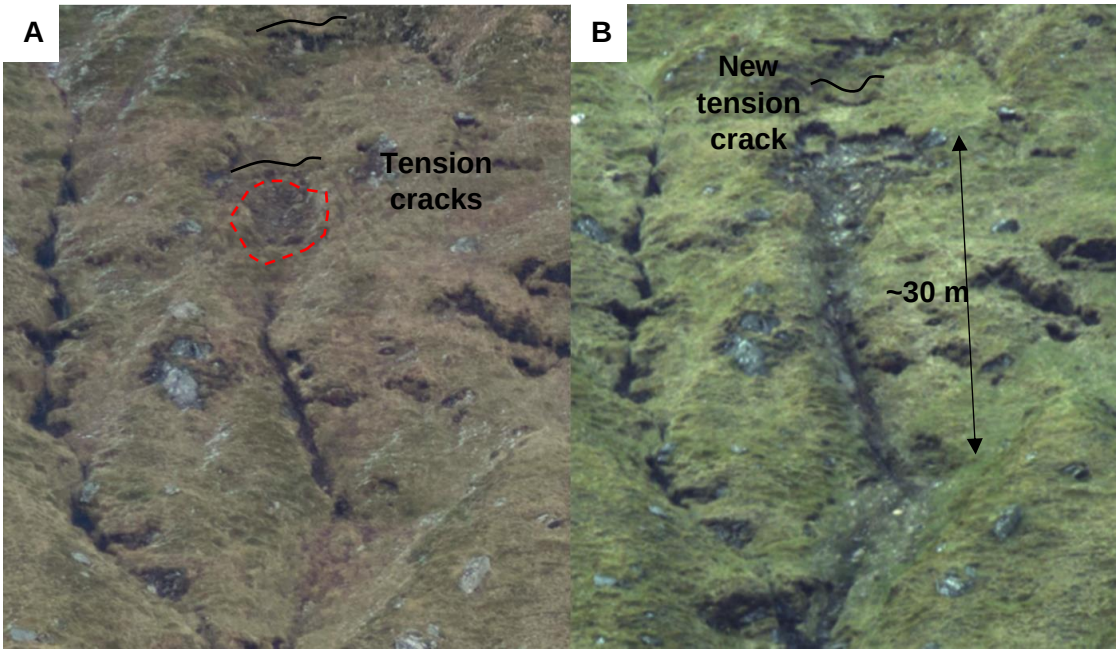

Figure 3.47 - Photos relating to RabT2B. A) Potentially waterlogged ground above an existing gully tributary (February 2016). B) The same area, from which a shallow failure has propagated and subsequently been channelised (February 2017)

Other examples include RabT2C which occurred directly above RabT1A (SFLS1) along a small incised channel visible in figure 3.48. This area, including the SFLS1 source area, demonstrated hydrological flow prior to failure, as visible in figure 3.52. Figure 3.49 demonstrates a clear example of a small channel flowing directly into the source area of RabT1G. This channel was not visible remotely, due to the small size of the feature and the vegetation overhanging the channel margins. Similar channels, also obscured by vegetation, have been observed elsewhere at RabT, including above and around the RabT1B (SDLS2) source area. Similar features are also apparent at GO, although these have not demonstrated any detectable change over the monitoring period.

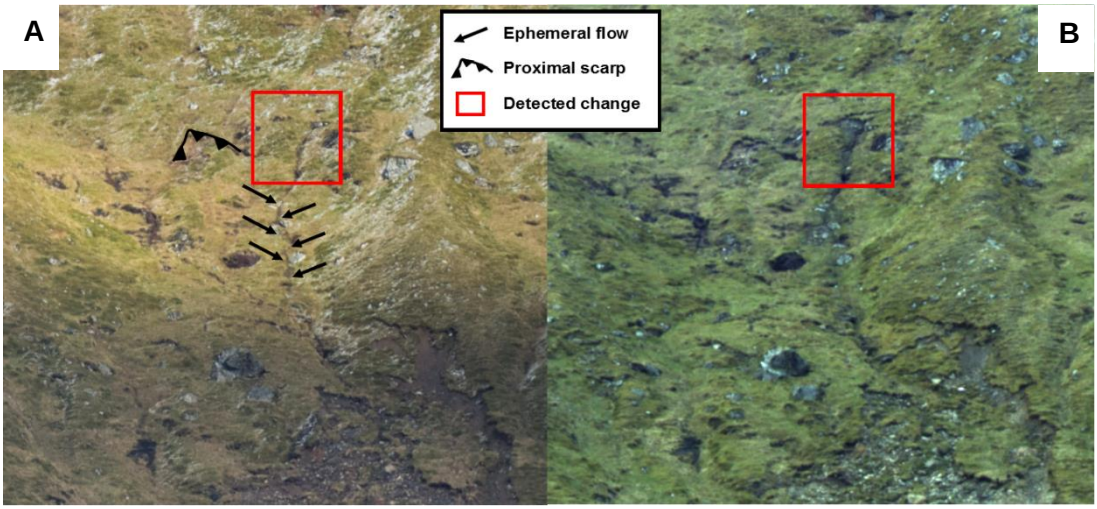

Figure 3.48 - Photos relating to RabT2C A) Taken in February 2016. B) Taken in April 2017. An ephemeral flow line is clearly visible prior to failure.

3.3.6 Modelling concentrated surface flow

Given the availability of high resolution topographic data, modelling was considered an effective way to highlight areas where flow might be expected to accumulate. Hydrological flow paths were modelled within ArcGIS using a 0.1 m resolution digital elevation model (DEM) derived from TLS data (April 2015; prior to the landslides shown). Flow from cells of the same orientation resulted in a raster of flow accumulation, to which thresholds of 2,000 and 5,000 cells (2,000 m and 5,000 m contributing areas respectively) were applied to derive flow routes. These were converted into polylines to produce the results shown in figure 3.50 for the winter 2015 landslide events, SDLS1, SDLS2 and SFLS1.

The 5,000 cell threshold corresponds well with major gullies, but also picks out other areas of interest that are not established gullies. Pipe flow has also been observed during slope walkovers, and it's possible that water may disappear below the surface in these modelled areas. The lower flow threshold of 2,000 cells does not tend to correspond with large gullies, but does appear to coincide with anecdotal observations of very small channels (< 0.5 m width) and may also correspond with ephemeral flow. SDLS2 (figure 3.50b) for example has a major channel modelled along its right-hand margin, although no established gully exists here. A small flow channel with running water was however observed here during a slope walkover in May 2016. This same channel is modelled as originating much further upslope, and runs directly through the centre of detected changes RabT1E and RabT3F. A minor channel (2,000 cells) is also modelled directly through the centre of the SDLS2 source area.

Evidence of flow, namely a linear track of saturated soil, appears to exist in a photo taken within 24 hours of the failure (figure 3.52) although there was no sign of this flow during a slope walkover in May 2016, thus this likely represents ephemeral flow during heavy rainfall.

For SFLS1 (figure 3.50a), modelled flow appears to partially correlate with that observed and annotated in figure 3.52. The major modelled flow-line runs through the top of the source area and continues downslope through detected change RabT1F, where no gully or permanent channel has yet clearly established. This same modelled channel originates further upslope and intersects RabT2C. In comparison to SFLS1 and SDLS2, the SDLS1 source area is not intersected by modelled flow (figure 3.50c), although a small channel (2,000 cells) is modelled directly downslope where major erosion and entrainment occurred. SDLS1 originated within a topographic hollow, which will concentrate flow to the area below, and was approximately double the mean failure depth of SFLS1 and SDLS2, as well as a number of other detected failures analysed in section 3.3.2. The lack of modelled flow and the large depth of failure may indicate a different triggering mechanism to other events.

Figure 3.49 - Evidence of flow running directly into the source area of a shallow failure (RabT1G). Vegetation clearly obscures the feature, thus minimising any chance of surveying ephemeral channel geometry with TLS, particularly at long range where the beam footprint size is large.

3.3.7 Assessment of flow and landslide overlap significance

In order to assess the significance of overlap between detected change and modelled flow, the probability of overlap with modelled flow must be analysed. The mean width of all landslides detected at RabT was 10 m, and thus a moving window of this width was utilised to systematically sample the probability of overlap between a failure and modelled flow. Assuming a generous 1 m flow width (0.5 m being the maximal threshold for an ephemeral gully), approximately 3 % of the slope is covered by modelled flow lines with 2,000 or more contributing flow cells. 9 % of the slope is therefore either covered by modelled flow, or falls within 1 m of it.

This analysis was conducted by breaking the 900 m width of the slope into 0.1 m sections, and assigning a 'yes' value to 3 % of these cells (in blocks of 10 to represent 1m streams) in Microsoft Excel. A window of 10 m width (mean width of failure) was then moved across the entire slope, in 0.1 m increments, to calculate the percentage overlap of a random 10 m source area with a 1 m wide flow line. The same analysis was performed with 9 % stream slope coverage, to account for a buffer of 1 m around the flow lines, which may encompass uncertainty about flow width and saturation conditions.

This analysis suggests a 32.5 % probability that a random 10 m wide failure would overlap modelled flow. The analysis also found a 38.4 % probability that a 10 m window would overlap, or fall within 1 m of, modelled flow. This compares to an actual overlap, of all detected landslides, of 60 % (9 of 15). No additional landslides fell within 1 m of the modelled flow. The mean width of all detected landslides was however skewed by the December 2015 events (SDLS1, SDLS2 and SFLS1). Omitting these event, the mean failure width was 5.3 m. A moving window of this size yielded a smaller probability of overlap with modelled flow, of 18.6 %. Accounting for an additional 1 m either side of the flow lines, the probability of overlap was 24.5 %. This compared with an actual overlap, of all remaining detected changes, of 58.3 % (7 of 12). The actual overlap of small detected changes was therefore more than three times that of random probability.

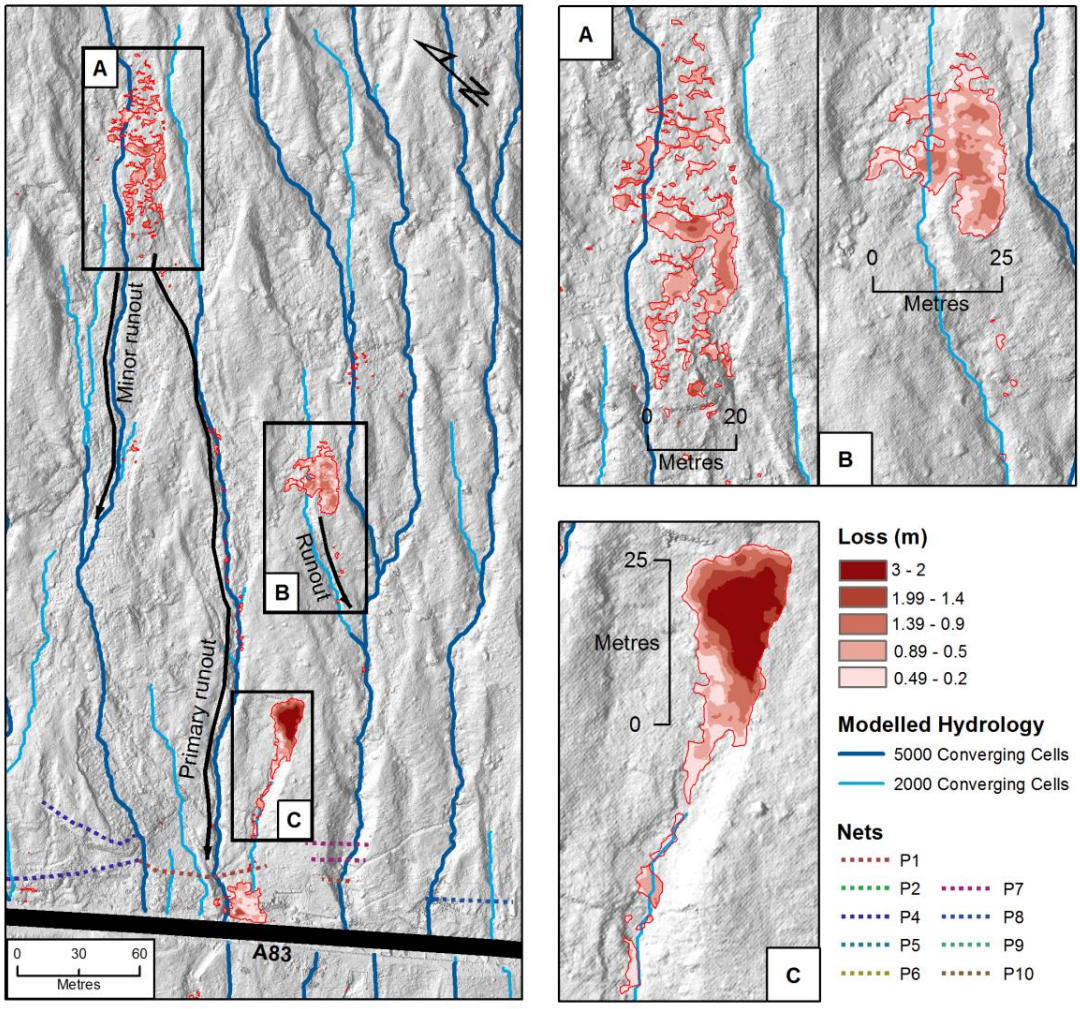

Figure 3.50 - TLS derived change detection encompassing both Storm Frank (SFLS11; A) and Storm Desmond (SDLS2, B and SDLS1, C). Both SFLS1 (A) and SDLS2 (B) failures are visibly intersected by modelled flow above 2,000 cells, whereas the deeper SDLS1 (C) failure is not. Additional losses detected also generally corresponded with modelled flow lines.

Figure 3.51 - A photo taken of the SDLS2 source area within 24 hours of failure. Here there appears to be evidence of hydrological flow (saturation) down the centre of the source area (annotated) which corresponds with modelled flow.

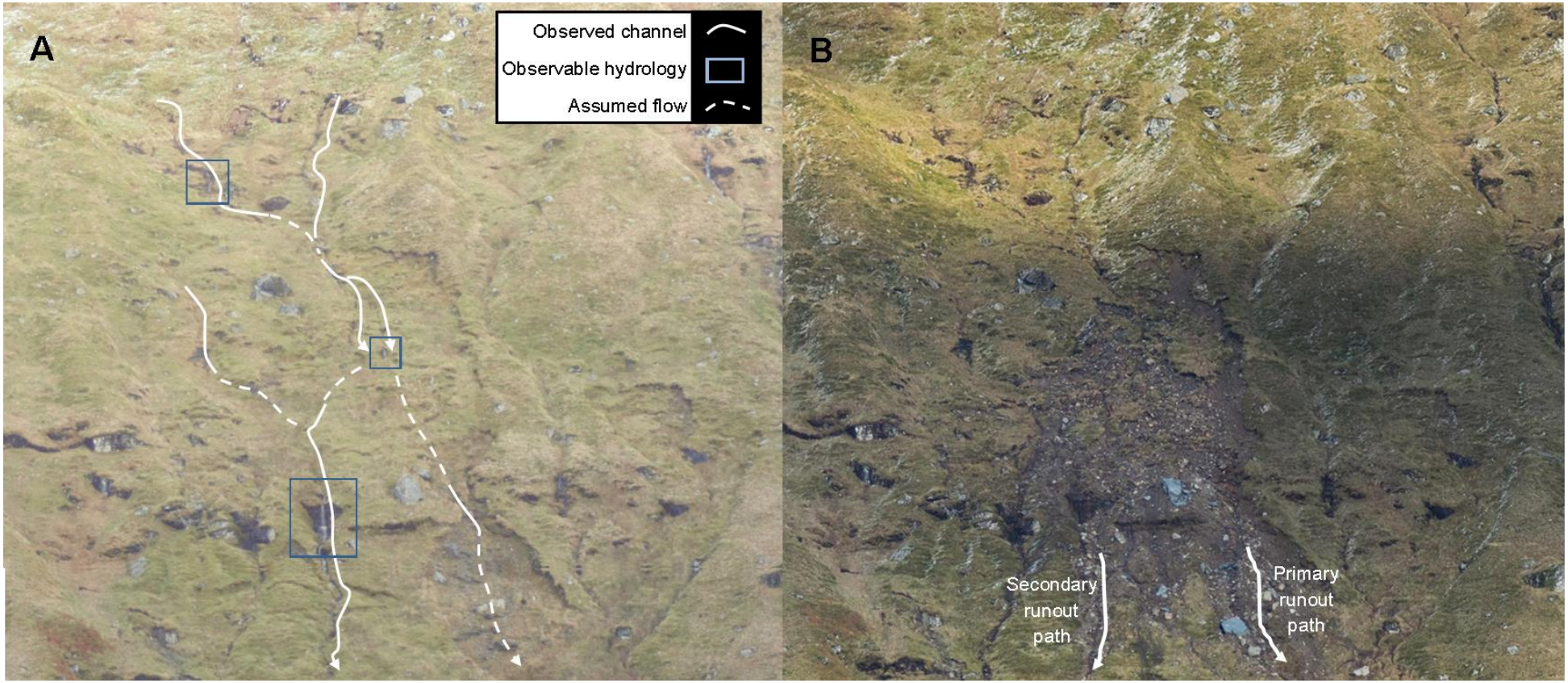

Figure 3.52 – A) A photo of the SFLS1 source region prior to failure in December 2015. This telephoto was taken immediately after the SDLS1 and SDLS2 events and, as such, contains evidence of ephemeral hydrological flow (as highlighted by the blue boxes). Small channels (not active in the photo to the right) are annotated. These appear to re-activate during heavy rainfall and evidently ran through the SFLS1 source region prior to failure. B) The SFLS1 source area, with two runout paths labelled, after failure. Here we can see that the region below the annotated flow has failed. The secondary runout path also coincides with a small flow channel.

3.3.8 Debris flow runout and classification

The landslides detected at RabT varied between the hillslope and channelised types. Of fourteen landslides, eight were primarily of the channelised type and five were primarily of the hillslope type. The volumes of change attributable to each type are 494.1 m^3 (54 %) and 423 m^3 (46 %) respectively. One failure, SDLS1, is not classified as it did not mobilise within a pre-existing channel, although it was bound by convergent topography (hollow) and appears to have eroded a new channel. Although the majority of changes were primarily linked with channels, a high proportion of change was not and therefore are unlikely to have evacuated the slope of the failed material.

3.3.8.1 Analysis of debris flow runout and topography

The runout of the three largest events detected at RabT varied quite significantly. SDLS1 mobilised straight into a catch net without any significant deposition, whereas both SDLS2 and SFLS1 deposited large quantities of material. SDLS2 in particular did not mobilise down to the A83. Figure 3.53, figure 3.54 and figure 3.55 show long profiles of SDLS1, SDLS2 and SFLS1 respectively, including their runout paths. The landslides mobilised from mean source areas gradients of 35°, 31° and 28.7° respectively. In the 20 m immediately downslope, SDLS1, SDLS2 and SFLS1 encountered mean gradients of 30.5°, 32.4° and 36.3° respectively. The overall mean runout slope angles were 30.4° (SDLS1; for 70 m), 31.2° (SDLS2; for 100m) and 32.3° (SFLS1; for 100 m) respectively.

SFLS1 encountered the steepest immediate runout path, but mobilised from the lowest gradient source area. In comparison, SDLS2 emerged from the median source area gradient and mobilised over the median immediate runout path. SDLS2 also mobilised over the median overall slope gradient. It is notable that SDLS1 encountered the lowest gradient topography immediately downslope. The large source depth gradient and initial failure volume would have instead influenced its efficient runout, with this also being aided by convergent topography. Figure 3.56 shows that SFLS1 mobilised over topography with multiple confining features, whereas SDLS2 mobilised over a broad and flat slope region, promoting spreading of deposits below the LoD threshold (visible in the field and photographs). Another factor in the runout and deposition characteristics of these events is their respective influx angles into gullies (figure 3.57). SFLS1 appears to have mobilised along a fairly straight runout path, prior to reaching a gully, whereupon it appears to have entered at an angle of 16°. In comparison, SDLS2's runout path was more oblique, with the detected deposits following a final 25° trajectory into the gully. A large polygon of deposition is highlighted at the margin of the gully in figure 3.56.

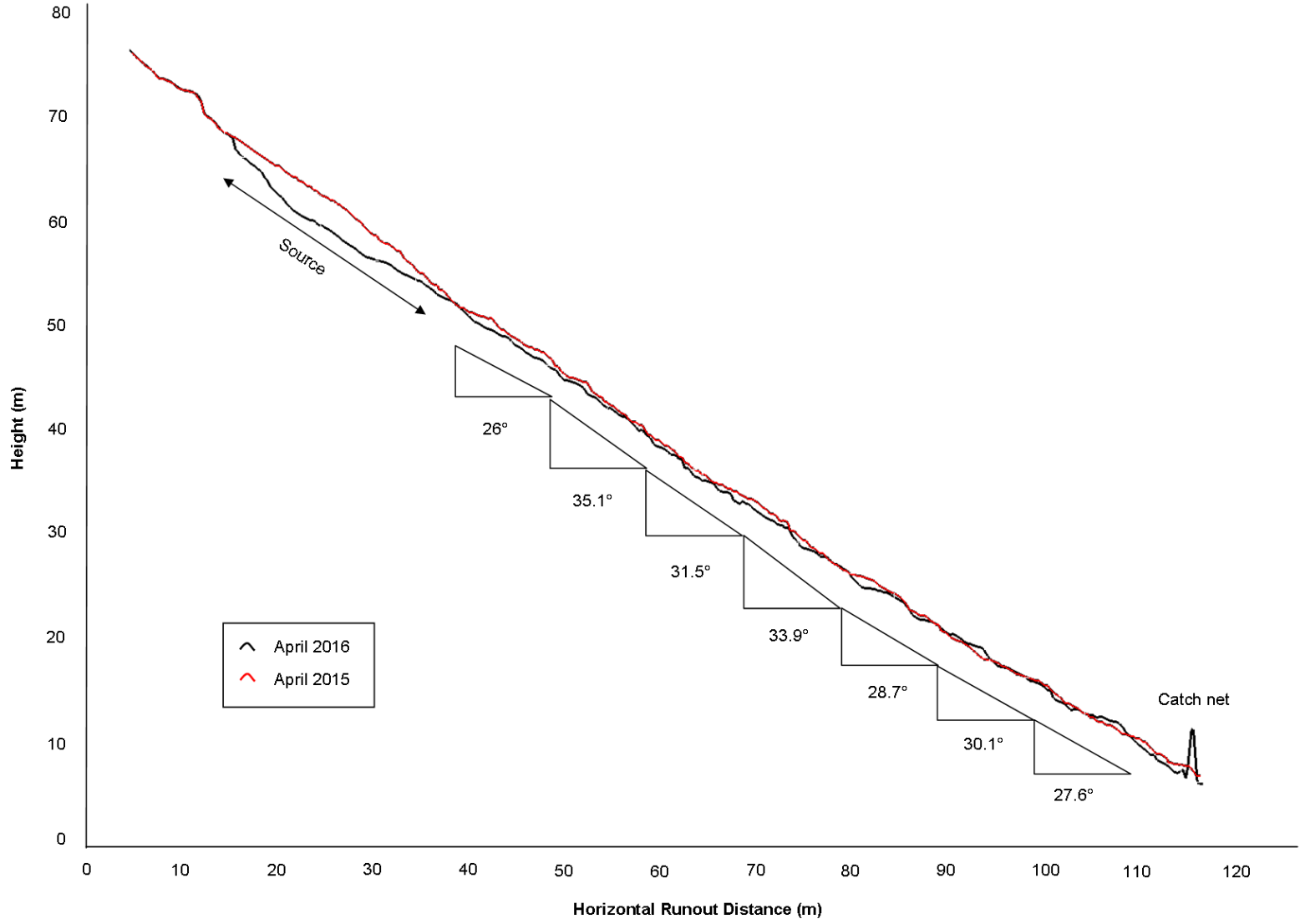

Figure 3.53 - A long profile of the SDLS1 event and its runout path

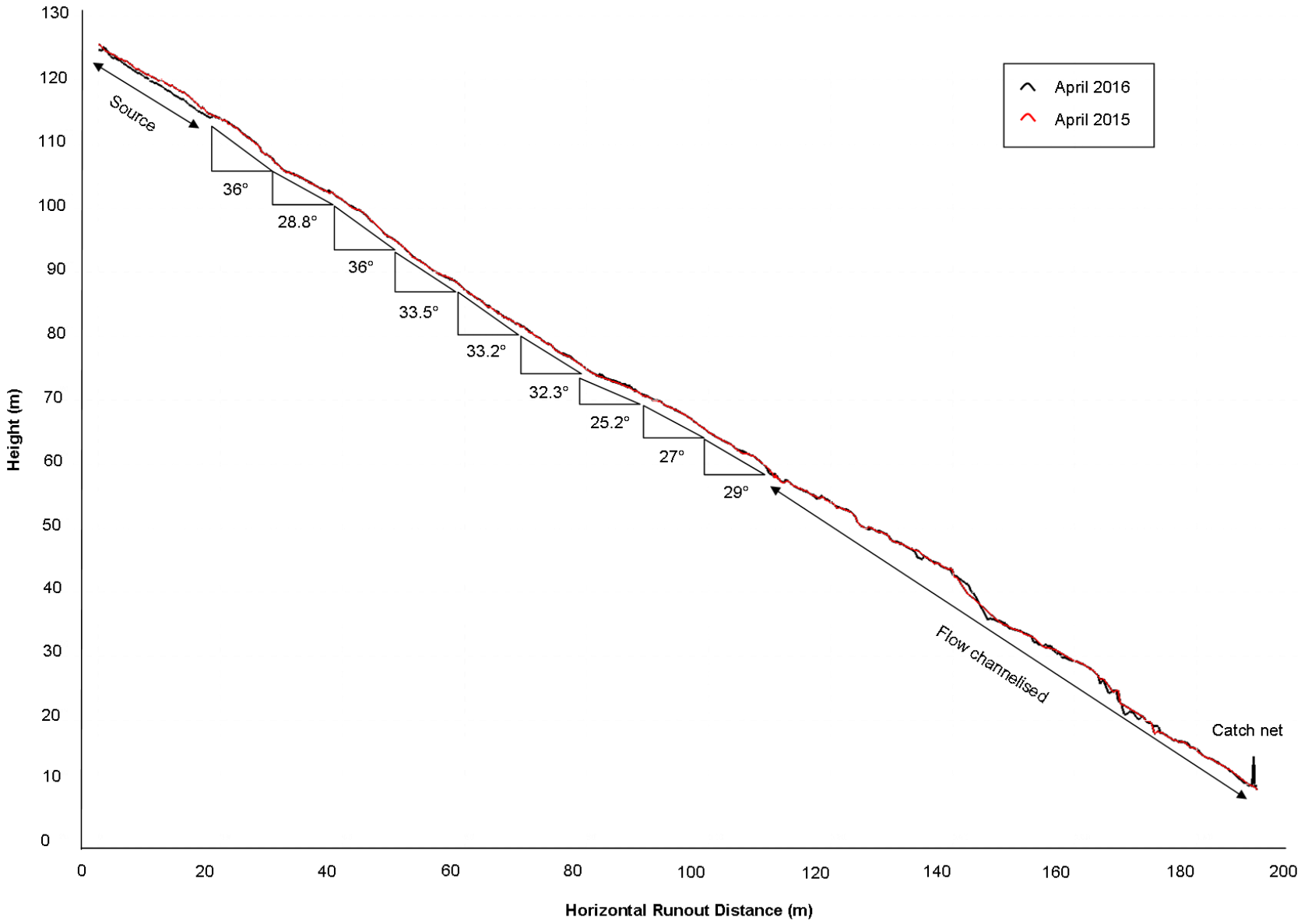

Figure 3.54 - A long profile of SDLS2 and its runout path, including the gully area into which some of the material mobilised.

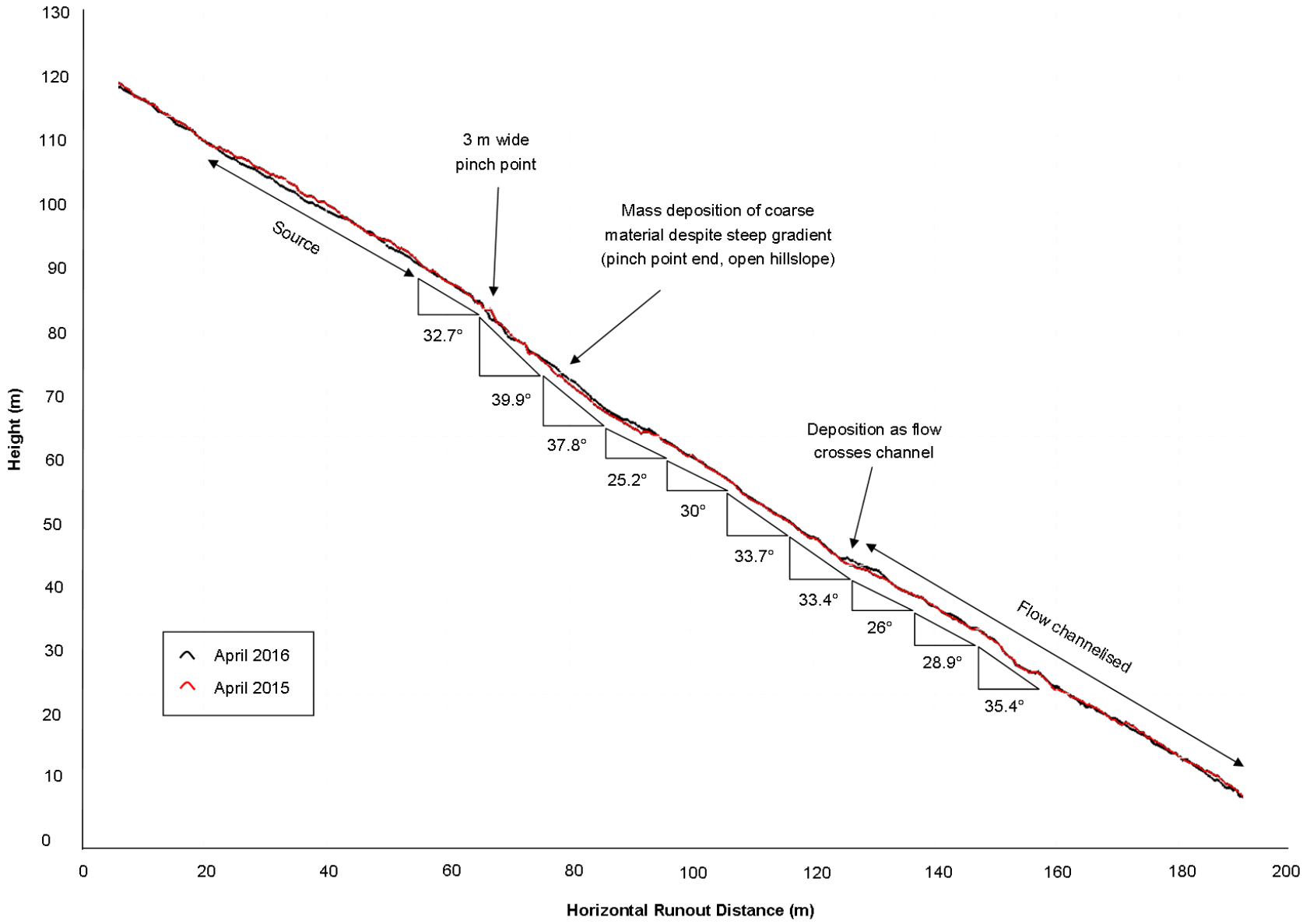

Figure 3.55 - A long profile of the SFLS1 event and its runout path. This includes a short region of gully.

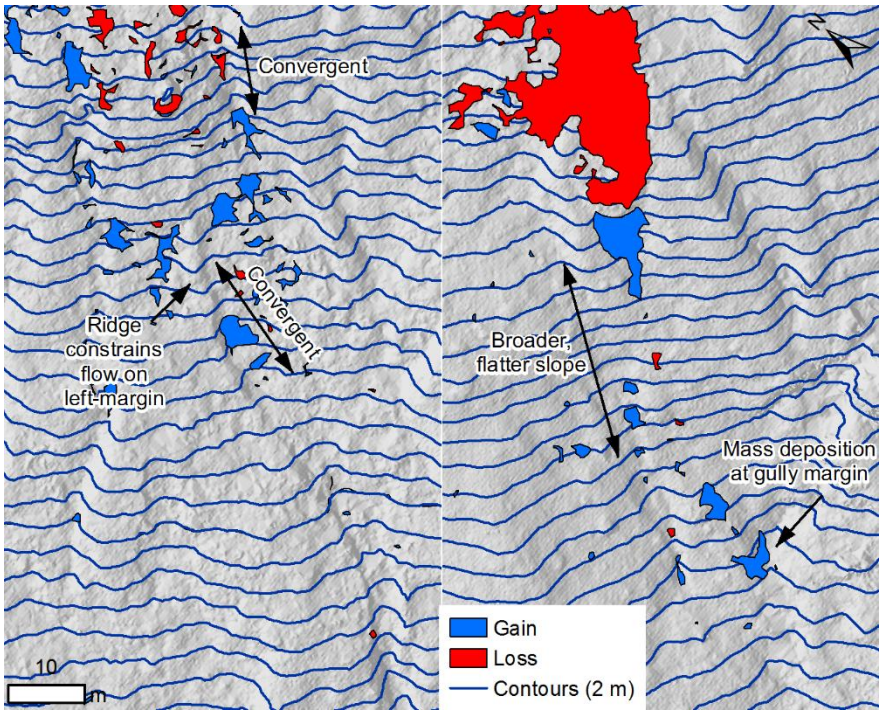

Figure 3.56 - A comparison of the runout topography for SFLS1 (left) and SDLS2 (right). SFLS1 encountered several regions of topographic convergence, as well as at least one confining ridge. SDLS2 mobilised over a very flat region, with limited confining topography.

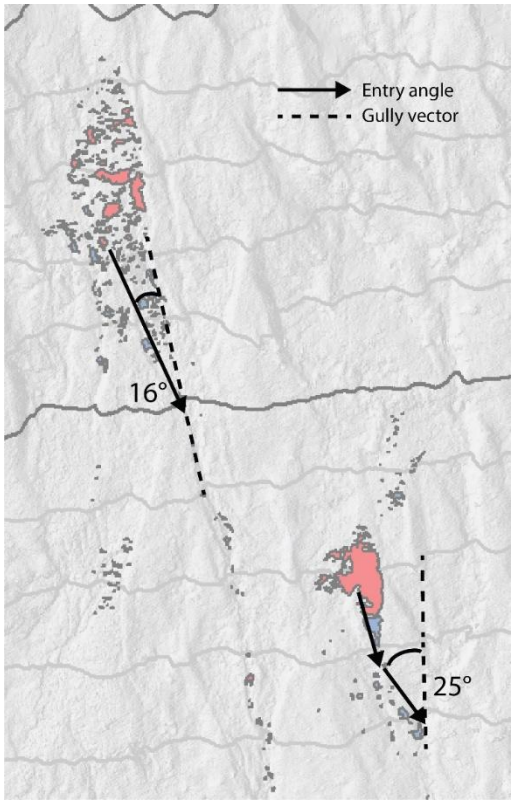

Figure 3.57 - A comparison of gully influx angles for both SFLS1 (left) and SDLS2 (right).

3.3.9 Magnitude Frequency

The probability of occurrence is a principal factor in landslide risk calculations, for which statistical analysis of past activity can be invaluable (Corominas and Moya, 2008). Like many systems in the Earth sciences, the relationship between landslide magnitude and frequency can be characterised by a power-law (Malamud *et al.*, 2004; Brunetti *et al.*, 2009, 2014). This relationship can be used to quantify landslide erosion (Francesco Brardinoni and Church, 2004) and hazard (Hungr *et al.*, 2008). The magnitude-frequency power-law typically covers medium-large magnitude events, with the relationship decaying at the smaller end of the scale, producing a 'rollover' effect (Pelletier, 1997; Malamud *et al.*, 2004). The source of this rollover has been widely debated (Stark and Hovius, 2001; Guzzetti *et al.*, 2002; Brunetti *et al.*, 2009; Frattini and Crosta, 2013), particularly for landscape evolution purposes.

Despite the provision of positionally precise technologies for mapping landslides, such as Lidar, complete inventories of the phenomena can be hard to achieve (Steger *et al.*, 2017). The monitoring data represents a short record of change, yielding a relatively small sample size. This can lead to large uncertainty when performing magnitude frequency analyses, potentially obscuring statistically significant variation (Li *et al.*, 2016). The approach can still prove useful for the comparison of short-term trends however, as long as the limited sample size is considered and the results are treated accordingly. Change data has been analysed to compare the inter-annual records of change and how these may differ due to different factors, such as the late 2015 storm events. The detected change areas have also been used, without depth information, to highlight any inconsistencies and analyse which might be the most effective approach to derive a magnitude-frequency relation from long range TLS change data. Twenty major changes, visible at the figure scale, have been detected at RabT between April 2015 and January 2018. Additional changes have also been detected, resulting in a total of 83 significant changes (N_L = 89) at RabT throughout the nearly three-year monitoring period. This is comprised of 45 changes in 2015/16, 21 changes in 2016/17 and 17 changes in 2017/18.

Data were first processed in ArcGIS, to aggregate multiple incoherent polygons known to represent larger singular changes (i.e. SFLS1 source area). All of the calculated surface areas and volumes, for aggregated and singular polygons, were collated into both annual and overall tables of change. Changes were sorted in ascending order of size, by both area and volume, after which they were counted into bins of equal logarithmic width (Log Δ 0.1) starting with minimum sizes of 0.15 m^2 ($10^{-0.8}$) and 0.25m^3 ($10^{-0.6}$) respectively, ranging up to

maximums of 502 m^2 ($10^{2.7}$) and 631 m^3 ($10^{2.8}$). The actual bin widths increased with the areas and volumes of change (Malamud *et al.*, 2004).

Equation 6, was used to account for these varying bin-widths, to calculate the probability density function (PDF) of each magnitude (Malamud *et al.*, 2004).

$$p(A_L) = \frac{1}{N_{LT}} \frac{\delta N_L}{\delta A_L}$$

Equation 6

where $p(A_L)$ is the probability density, N_{LT} the number of events in the inventory, δN_L is the number of events in the bin, and δA_L is the width of the bin (m^2 or m^3).

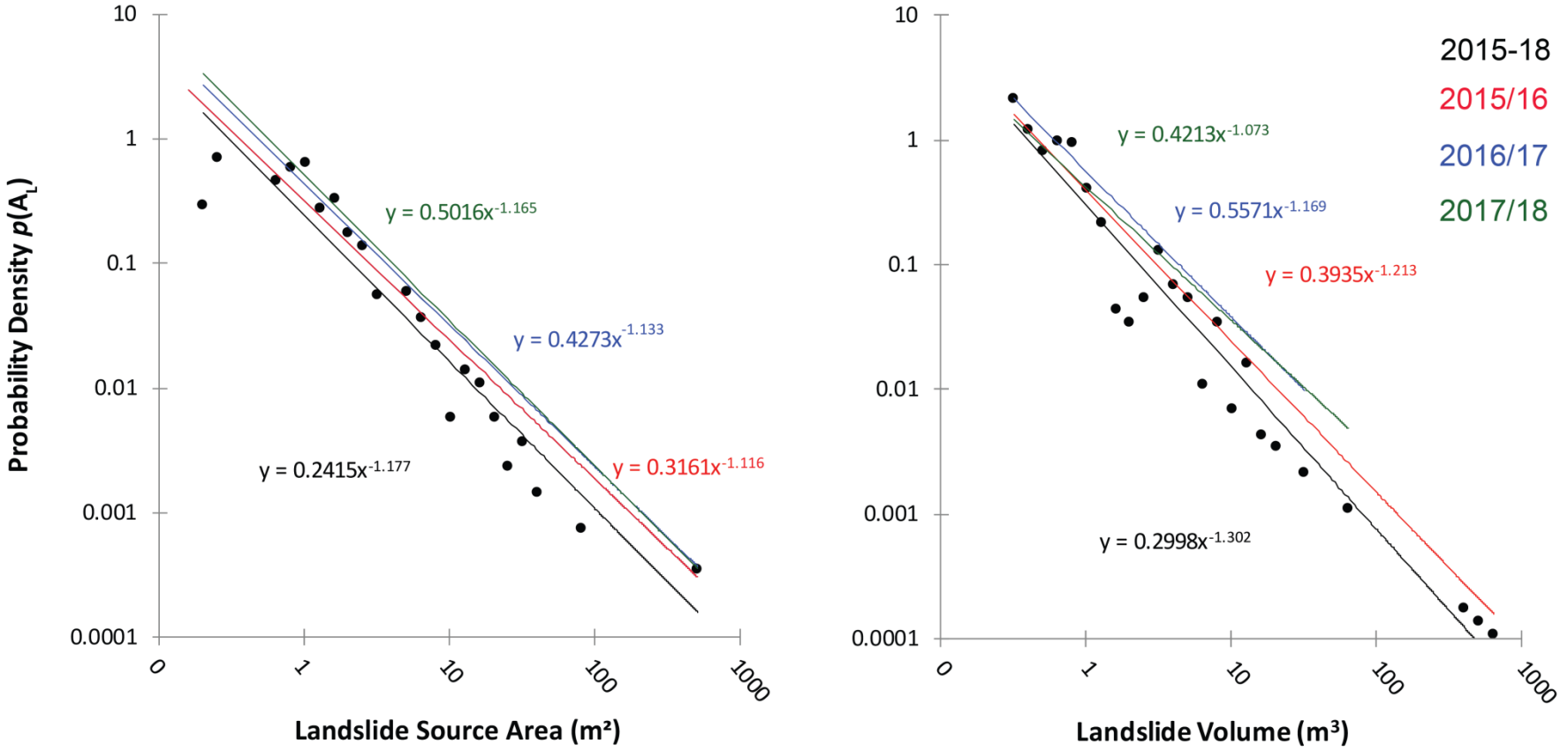

Figure 3.58 – Magnitude frequency plots for the Rest and be Thankful, using both change area (m²) and change volume (m³)

Figure 3.58 shows two plots of the PDF magnitude-frequency relation, the left using detected change areas and the right using calculated change volumes. The area magnitude-frequency relation gives an overall exponent of -1.77, whereas the volume plot results in an exponent of -1.302. The distribution of points within the area plot is reasonably linear (log-scale), whereas the volume plot is split into two sub-sections, with larger volumes observing one trend and smaller volumes (<10 m^3) deviating from this and following another trend. Calculation of change volumes, particularly at large range, adds another element of uncertainty on top of that in the area values. This is likely to dominate for the smaller magnitude events where the relative uncertainty is high and under-estimations of change volumes occurs due to inter-point gaps, as explained in section 3.1.7. This results in an erroneously high number of small magnitude events, hence the high PDF values in this range of the plot. Other studies have used standalone change areas (Hovius *et al.*, 1997; Guzzetti *et al.*, 2002; Malamud *et al.*, 2004), or area derived change volumes to analyse the magnitude-frequency relationship (Guzzetti *et al.*, 2009). This study has found little variance in shallow landslide depths, however these only apply to the medium-large scale shallow failures (figure 3.59). This demonstrates that smaller volumes typically have smaller change depths with lots of variation, making an area to volume conversion not suitable and use of raw change areas the best approach in this study.

Area values give an exponent of -1.116 for the first monitoring year, in which the three largest changes were detected. This is towards the low end of the exponent scale for shallow landslides and suggests a smaller difference in probability between small and large events. Considering that the second and third year exponents are larger, the first-year data demonstrates the capability of a short monitoring period, particularly one containing storm events, to influence a short-term magnitude-frequency relationship. The largest exponent was that of the final monitoring year (-1.165), in which five small to medium sized events were detected. The difference between this, the largest value, and that of the first year (smallest), is 0.049. Over the three monitoring years, events in the 398 – 502 m^2 range represented 3.6% of the detected change. These all occurred in the first monitoring year, in response to the winter storms Desmond and Frank. The corresponding low exponent for this year suggests that storms may exert a small control on the magnitude of events, although this is based upon limited data. Although the sample size is small, the area plot shows some sign of rollover for smaller magnitudes, which is in contrast to the volume plot. This is perhaps indicative that the area values are prone to lower uncertainty than the volumes. For

comparison, the difference between exponents for the volume plot was 0.14, almost three times that of the area plot.

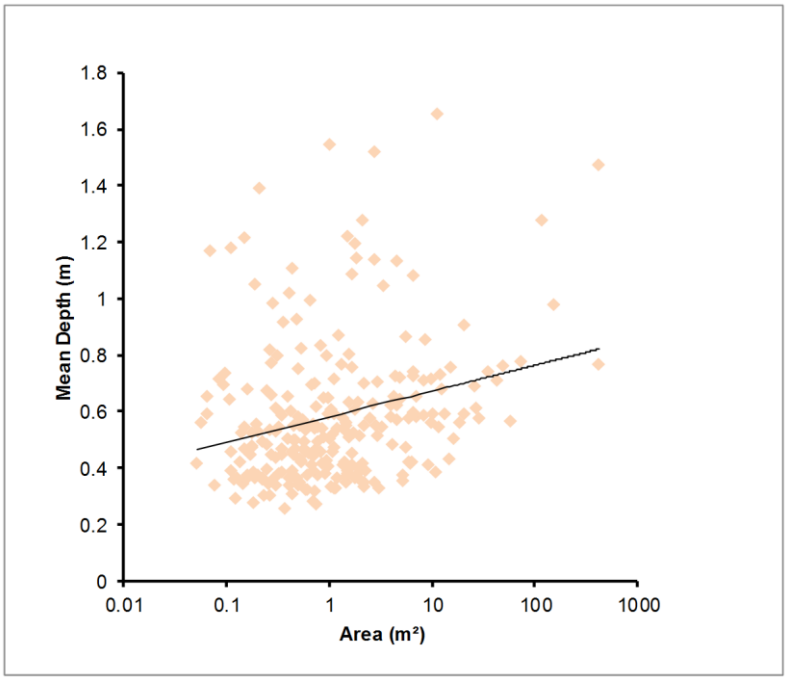

Figure 3.59 - A plot of the detected changes at RabT and their respective mean depths and footprint areas. This data shows a wide distribution of change depths, unlike those for the main landslides detected. This plot particularly demonstrates that use of a fixed value for depth of failure, to estimate change magnitudes (m3) from their areas, would be inappropriate. The mean failure depth of 0.66 m should therefore only be used for medium-large shallow failures, such as those detected at the end of 2015 and during the third monitoring year.

3.4 Discussion and conclusions

RabT has been subject to more than twenty changes throughout the 33 months of monitoring. Glen Ogle and Glencoe have been subject to far fewer changes (10 combined over 24 months). The smallest event within the spatial inventory, introduced in chapter 3, was that of a 59 m^2 shallow failure in 2008. Fewer minor changes were reported within geotechnical reports, however these could not be mapped due to a lack of information about their location. Fifteen changes smaller than this have been detected during the three year monitoring period. Given difficulties in observing some of these failures by remote visual inspection, it is unlikely that these events would have been recorded without the use of TLS based monitoring.

This study has prioritised the detection of new losses, partly due to necessary use of intra-annual masking which follows cycles of seasonal vegetation growth and dieback, but also due to the propensity for deposits to spread and thin (Bremer and Sass, 2012) below the high LoD threshold associated with long range monitoring. This was demonstrated by the SDLS2 event, whereby material was visible along the runout path, but at a thickness below the LoD threshold, hence a lack of deposition data in this area. Nonetheless, the available deposition data appears to prove indicative of the runout trajectory and longitudinal deposition distribution. This LoD could be reduced through use of a single scan position, however this would have reduced the point coverage and further increased occlusion issues. Loss detection, including intra-annual masking, was found to work well, particularly because landslide scars tend to be deeper than the LoD threshold. The mean depth of failure, of the detected landslides, was found to be 0.66 m for example, with minimal variation apart from that of SDLS2 (1.5 m). Whilst monthly, or less frequent, change detection was not able to pinpoint precise event timings, supplementary camera installations proved a useful low-cost tool for this task during the third monitoring year. The change data, particularly through intra-annual masking, did aid a reduction in manual image interpretation to identify the change timings however. This yielded a detailed record of changes at the site, with event timings that can be used to analyse rainfall patterns for instance. No short-term precursors, coinciding directly with a landslide source area, were found. Nonetheless, small detected changes could potentially represent longer term precursors, or indicate an active region of the slope.

The TLS data has enabled quantification of landslide and change volumes, with the M3C2 and ArcMap workflow producing similar change volumes to a 2.5D approach implemented

within CloudCompare. Smaller changes are however prone to relatively large uncertainty, particularly due to limitations arising from a low point spacing and a large laser beam footprint. This is evident through inspection of the volumetric magnitude-frequency plot, in which smaller change volumes (< 10 m^3) have disproportionately high probabilities and a lack of rollover. The uncertainty of small change volumes, discussed in the methodology, is similar to uncertainty identified by Williams et al. (2017) who determined polygons between 0.001 m^3 and 0.01 m^3 to yield volumetric uncertainties of between 80 % and 160 %. It is not uncommon to use landslide area as a proxy for magnitude however (Guzzetti et al., 2005), thus the monitoring data still proves useful for these purposes. All of the annual magnitude(area)-frequency plots returned exponents between 1.1-1.3, typical of shallow soil-based landslides (Larsen *et al.*, 2010). Such values may be used to assess the hazard probability, however this assumes that past trends are indicative of the future (Hungr *et al.*, 2008) and doesn't take into consideration factors such as sediment exhaustion and climatic perturbation.

3.4.1 Characterisation of failures, timings and rainfall

Activity at RabT included three large magnitude failures towards the end of the first monitoring year (December 2015; winter storms Desmond and Frank). Twenty small magnitude failures were also detected. The majority of the detected landslides were smaller than 100 m^3. The maximum daily rainfall values, recorded throughout the study period, were primarily isolated to the late 2015 winter storm period and may have influenced the large magnitude of these failures. The effects of this are visible within the annual magnitude-frequency plots, whereby the first year of monitoring data yielded the lowest magnitude (area)-frequency exponent due to a larger number of large magnitude events. A small inventory size and lack of timings for smaller changes does not enable detailed analysis of the relationship between rainfall totals and event magnitudes, however a relationship of this type was found for shallow landslides, debris flows and rock slides triggered primarily by typhoons, but also frontal storms (Saito et al., 2014). If the frequency and intensity of winter storms is to increase in response to climatic changes (Winter et al., 2010) the implications of such a relationship may be significant. This area therefore deserves more research, which would be aided by a larger inventory of detected change. All of the detected landslides, of known timings, occurred on days where the daily recorded rainfall was in excess of 30 mm. This is slightly higher than the 25 mm/24 hr threshold used to activate warning wig-wag signs, much like train crossing signs, at RabT, however that uses a rolling average on forecast rainfall values and is used alongside an additional three hour forecast threshold (Winter &

Shearer, 2017). This 24 hr threshold is low compared to a value of 200 mm/24hr identified in Hong Kong for instance (Gao et al., 2018).

Rainfall recorded at Glen Ogle exceeded 30 mm/24hr and 40 mm/hr thresholds on 14 and 3 occasions respectively during monitoring. This compare to 38 and 29 times respectively at RabT. This disparity corresponds with longer-term rainfall records, in which RabT receives more than 3,000 mm rainfall per year, whereas Glen Ogle receives between 2,000-3,000 mm per year (Met Office, 2016). Glen Ogle's location further inland, away from the wet west-coast, plays a major role in this lower average annual rainfall. Glen Ogle experienced 31 debris flows during 18th August 2004, all occurring in response to a minimum of 20 mm hr^{-1} rainfall (recorded several kilometres away) (Milne *et al.*, 2010) or potentially the equivalent of a 250-300 year return period (Heald and Parsons, 2005). Glen Ogle experienced a very similar intensity of rainfall to RabT on 30th December 2015, without any detectable change occurring; the site has therefore set a precedent of only being impacted by very high intensity rainfall events, far in excess of those triggering failures at RabT.

Of the events with known timings, five were found to occur between October and November, four between December and February and one between February and April. A further event (RabT1D) was recorded between April and July 2015. Most of these event timings correspond with recent activity, which has fallen between November and January in the winter months (Winter et al., 2005), with the exception of the three events detected in October 2017. The majority of the detected changes (56%) were isolated to the centre of the slope, representing approximately 20 % of the monitored area. Assuming no linked triggering mechanism, other than rainfall, failures might be expected to occur with a stochastic spatial distribution. Spatio-temporal clustering of the three largest failures (SDLS1, SDLS2 and SFLS1), within the centre of the slope in December 2015 is therefore of major interest and continues a trend identified in the spatial-inventory of pre-monitoring events. Monitoring of smaller changes (i.e. RabT1E, RabT1F, RabT2B, RabT2C and RabT3E) within the same zone has further highlighted this clustering.

Slope gradients between 26° to 50° should be accounted for in a first pass hazard assessment (Winter et al., 2005). This range encompasses 87 % of the change detected during this study and thus is considered strongly applicable to RabT. The majority of changes (31 %) were found within a 5° gradient range of 30 - 35°. This includes the three largest events triggered during the 2015 winter storms. Many of the detected landslides were found proximal to breaks in slope, particularly small bedrock scarps. The link between these and failure is not

clear however. The distribution of landslide material between channelised and hillslope runout was fairly even. Just under half of the detected material mobilised on open hillslope areas, thus depositing significant quantities of material as disconnected sediment stores where immediate reworking is limited. Materials deposited within a channel are prone to fluvial reworking and entrainment by the passage of future debris flows, however it is uncertain whether the significant quantity of hillslope deposits are themselves prone to significant reworking. Given the relatively short observation period of this study, these deposits are of further interest, particularly to see whether they may remobilise before revegetating.

3.4.2 Flow accumulation and ephemeral flow

Shallow failures and debris flows at RabT have anecdotally been linked to hydrological switching, and cases of discrete waterlogging have been reported (private unpublished reports) suggesting a mechanism of flow accumulation. Clustering of change within the pre-monitoring spatial inventory and monitoring data is indicative that certain zones exhibit waves of behaviour, before this activity switches elsewhere on the slope. Hydrology may underpin this activity, evidence of which has been found in the form of small incised ephemeral channels during slope walkovers. Observation of flow through source areas was a particular motivation to study such features in greater detail. Milne *et al.* (2010) observed similar flow through the source area of the most damaging flow at GO in 2004, suggesting that such flow may be influential in the surficial triggering of shallow failures. Furthermore, it is noteworthy that soil pipes have been observed during on-slope investigations, and whilst these have been shown to efficiently drain a slope (Sun *et al.*, 2010) they have also been known to clog or collapse, directly triggering debris flows (Tsukamoto *et al.*, 1982; Uchida *et al.*, 2001)**.**

Modelling of flow accumulation in ArcGIS resulted in polylines that corresponded strongly with observed major and minor drainage features on the slope. Flow lines with contributing cells of 2,000 (2,000 m) or more also corresponded with observed ephemeral flow during and following intense rainfall. Inspection of the detected change with these flow lines found some overlap, with flow polylines running directly through the centre of many change polygons or polygon clusters. A systematic sampling analysis found that an average failure of 10 m width had a 32.5 % probability of overlapping this modelled flow. The actual overlap of detected landslides with modelled flow was 60 %. Ignoring the influence of the three largest landslides, due to their higher inherent probability of overlap with flow, 58.3 % of the

remaining twelve landslides were found to overlap modelled flow. This was significantly higher than the associated 18.6 % probability found during systematic sampling.

Although the sample size of landslides was low (15), this analysis gives some initial quantitative indication that discrete hydrological flow may be of significance in the triggering of shallow failures. It is worth considering however, that topography is also an influential variable in the routing of groundwater (Condon and Maxwell, 2015), which is more commonly attributed to the triggering of shallow failures, and that modelled flow may therefore also be indicative of these conditions. The third year monitoring data also marked a departure from the clustering trend, with a greater spatial distribution of failures. This is perhaps a reminder that a diverse range of processes, beyond concentrated surficial, flow influences shallow failures.

3.4.3 Runout potential, deposition and gully recharge

Of the three debris flows triggered by the 2015 winter storms, SDLS2 was the only one not to mobilise towards the road level. Instead, more than half of the failed mass appears to have deposited on the open hillslope. This estimation is based upon the lack of deposits found within the gully below the point of inflow during inspection. This clearly indicates that the hillslope deposition quantified in the annual change (52.9 m^3) is far below the actual likely quantity of deposition (~171 m^3). This is also evident when comparing the deposition data with photographs of the runout path which is covered in a thin spread of material. Unaccounted deposition appears to relate to the LoD threshold used. The smaller volume of the failure compared to SDLS1 and SFLS1, may have contributed towards some of SDLS2's limited runout potential (Davies, 1982; Takahashi, 1991; Legros, 2002), due to a higher ratio of friction to flow footprint (Iverson, 1997). It is worth considering however that the largest Glen Ogle failure in 2004 started as a shallow failure approximately 76 m^3 smaller than SDLS2 (Milne et al., 2010). SDLS1 was also only 27 % smaller than SFLS1, thus other factors appear to have influenced deposition. SFLS1 for example mobilised over a similar length open-hillslope zone, however this contained confining features which would have limited spreading of the flow mass, enabling more material to reach the gully. SDLS2 in contrast mobilised over a 1° flatter hillslope zone with no confining features. Mass deposition prior to reaching the gully suggests that the flat hillslope was the most influential factor in deposition, although it's possible that the flow viscosities may have also varied due to different initial water contents.

SFLS1 also flowed into a gully at a lower influx angle, conserving more of the flow momentum (Brayshaw and Hassan, 2009; Guthrie *et al.*, 2010) than SDLS2 which encountered a bend in its runout path, a common location for deposition to occur (Benda & Dunne, 1987; Benda & Cundy, 1990; Wicherski et al., 2016), including at RabT (Horsburgh, 2009). Gully entrainment by SFLS1 likely promoted increased mobility (Mangeney *et al.*, 2010), particularly due to streamflow saturating basal sediments and the positive feedback of these on flows (Iverson *et al.*, 2011). Mixing with streamflow, a term called debulking, may have reduce the flow viscosity (Pierson and Scott, 1985; Iverson, 1997) and velocity itself. Photographs of a slurry-like mass deposited onto the A83 carriageway by SFLS1 (ForArgyll, 2015) clearly show that the mass contained a large proportion of water, although this cannot be fully appreciated due to rapid dewatering. Increases in mobility, through entrainment of basal sediments and water, is of significance to both mitigation considerations and modelling attempts. the latter because the dilution could vary the flow rheology significantly between source and sink (Crosta *et al.*, 2009).

SDLS1 was much larger in magnitude, coming from a source area approximately double the depth of both SDLS2 and SFLS1 as well as other detected landslides. This failure depth appears to relate to thicker deposits at the bottom of the slope indicative of debris cones (Ballantyne and Benn, 1994). The large depth of failure suggests a different triggering mechanism may have influenced failure, as deeper soils are less susceptible to failure as a result of changes in moisture (Sidle and Ochiai, 2006; Ray *et al.*, 2010). The hollow setting of SDLS1 may be significant, as these features are known to aid accumulation of both thick regolith deposits and flow (Dietrich and Dunne, 1978), as well as sustaining moisture levels for long periods (Knighton, 2014). This hollow also inhibited spreading of the flow, enabling incision of a new truncated channel in a previously vegetated area. Gully erosion through debris flows has previously been observed (Stock and Dietrich, 2003), but the significance of the process in their formation has perhaps been underrepresented owing to a lack of observation data.

Excluding RabT1D, which occurred immediately at the margin of a gully, none of the events detected below the magnitude of SDLS2 are known to have mobilised to road level. High elevation gully and channel headwall events (RabT1G, RabT2B and RabT2C) may have washed down to road level, however it is more likely that these were intercepted by one of the many gully sinks which typically promote deposition (Martin et al., 2017). These failures therefore likely deposited more than 38 m^3 into the gullies, which is more than the detected lateral gully erosion attributable to SFLS1. No evidence of sidewall failure was found prior to

the propagation of SFLS1, suggesting that the debris flow actively eroded this material during runout. No further erosion was detected during the two monitoring years after SFLS1, despite the increased vulnerability of these areas following scour (Martin et al., 2017). The largest debris flow recorded at RabT in October 2014, prior to monitoring, is estimated to have entrained more than 400 m^3 during runout. It's seems highly unlikely that such a significant volume of material was sourced from the sidewalls given the minimal contribution of this source to SFLS1.

The low quantity of activity at GO demonstrates the high-magnitude low-frequency nature of the site. Two small detachments, each less than 1 m^3, were detected at the margin of the second gully to the south-west of Glen Ogle, indicating that small changes were detectable, however these are insignificant. A large debris flow, along the main gully in 2004, entrained some 8,220 m^3 of material (Milne et al., 2010), thus questions remain about the recurrence potential of such a high magnitude event. A lack of detected change over a short observation period sheds little light on this, but may indicate that, unlike RabT, gully sediments accumulate more gradually from degradation of bedrock sources (below LoD). This would be consistent with observation of minimal recharge in the five years following the large 2004 debris flow (Milne et al., 2010) and potentially characterises GO as a supply-limited site (Jakob *et al.*, 2005), although this requires longer-term monitoring. This is in contrast to RabT which has a high gully density (Sparkes et al., 2017) with abundant sediment accumulations and active sources of recharge.

A low quantity of change at Glencoe, mostly limited to small sediment redistribution close to the A82, is also indicative that the site is of a high-magnitude low-frequency character. A large rock mass failure, high up on the slope close to Achtriochtan Farm, into a deep bedrock gully presents a mechanism of accumulation for a potential future channelised runout event. The gully continues upslope for nearly 500 m and measures approximately 36°. An upslope failure could mobilise the sediments, perhaps as a 'rock slide-debris flow' or 'rock slide-debris slide' (Hungr *et al.*, 2013). A large unvegetated alluvial fan at the foot of the slope demonstrates washout of these materials in the past. Change detection on the slopes of Glencoe was a major challenge, even compared to the other two sites. Perennial vegetation is widespread and so only major changes are likely to survive the necessary vegetation filtering undertaken. When events do occur at the site, such as the large detected rockfall, these can be identified with relative ease.

CHAPTER 4

Modelling debris flows: coupling 3D survey data with a dynamic runout model for geomorphological and hazard vulnerability analysis

4 Introduction

Monitoring data (Chapter 3), used alongside an inventory of historic events and geomorphological mapping, have demonstrated the recent succession of debris flows on the slope of the RabT. These data have quantified the magnitude and frequency of slope failures and the scalable relationships that link them. However, data on recent slope changes does not translate to a direct assessment of future trunk road vulnerability to flow events (Corominas and Moya, 2008), and significant preventative action has been taken through the installation of flexible debris flow catch barriers, or nets, at the site (Transport Scotland, 2016b). To date, these have worked with mixed success, stopping one low elevation debris flow (SDLS2) in December 2015, for example, but not completely containing another high elevation flow (SFLS1) in the same month. The difference in net performance is thought to primarily relate to differences in the developed flow volume and impact pressures, with overfill and spill related to both. Correct design specification and strategic placement of the structure relative to the hazard or potential source area is vital to the effectiveness of mitigation structures.

The prediction of debris flow runout is a significant element of assessing its hazard potential (Fell *et al.*, 2008). Extensive mitigation measures that achieve complete protective coverage is cost prohibitive and should be limited to cases where the value is clear (Winter, 2016). Debris flow runout is primarily controlled by the volume and position of the source relative to topographic features in the flow area. Open hillslope areas diffuse flow mobility, but larger flow volumes can overcome this effect and still achieve long runout distances. The influx angle of a flow into a gully also appears to be influential in determining overall runout. Energy

models have previously been used to inform catch net design (Wartmann and Salzmann, 2002; Wendeler *et al.*, 2006), although more recently runout models have utilised monitored impact pressures and flow height information (Ashwood, 2014). Runout models provide cost-effective, repeatable and adaptable tools with which to assess the effectiveness of net placement and to optimise new installations. They can also be used to quickly assess different rheological flow characteristics. Modelling on slopes without predefined tracks requires flow interactions to be simulated over a high resolution DEM (van Westen *et al.*, 2005). The runout model employed in this study is called RAMMS-DF (RApid Mass Movement Simulation; Debris flow), a 2D depth-averaged continuum model developed by the Institute for Snow and Avalanche Research (SLF), part of the Swiss Federal Institute for Forest, Snow and Landscape research (WSL). Dietrich and Krautblatter (2017) have recently shown precise monitoring data to be useful in calibrating the RAMMS-DF runout model.

This chapter presents the results of RAMMS-DF numerical runout modelling to better understand and characterise debris flow hazards. It starts by conducting a sensitivity test of the key model parameters, varying the main input parameters within realistic ranges. Several debris flow events have been detected and quantified at RabT, providing the necessary information to derive rheological parameters and landslide source and flow paths. Back-analysis of several events at the same site is seldom performed but here a comparison between separate events allows assessment of uncertainty and validation of parameters.

Following sensitivity testing, back analysis and validation of RAMMS-DF with respect to inter-event rheological variability, the model has potential to be applied in a predictive manner. Hazard mapping approaches are typically applied at the regional scale, and rely upon a selection of source areas, often based upon an inventory of past events or other analysis (Castellanos, 2008; Blahut *et al.*, 2010)… Luna *et al.* (2014) however highlight the potential for such approaches to overlook new source areas. A hazard mapping approach should account for different flow volumes, linked to a magnitude-frequency relationship (Hürlimann *et al.*, 2008). Selective modelling of the largest recorded flow volume only does not constitute holistic hazard mapping, and ignores the potential for smaller failures to grow as they propagate and entrain material. The RAMMS-DF model is applied at the end of this chapter to demonstrate a new form of susceptibility analysis, from which slope-wide runout potential can be analysed, potentially offering data for a more appropriate approach to hazard mitigation.

The result of this application is the output of an exhaustive runout and susceptibly map, from which source areas of particular concern can be highlighted. This differs from initiation susceptibility approaches (Corominas *et al.*, 2014), in which source areas are first identified and then modelled. The added benefit of this analysis, is that areas of relatively high slope mobility can be identified without making assumptions about source conditions. Highlighted source areas can then be followed up by detailed inspection to assess the hazard. The back-analysed rheological parameters, from the two events monitored in 2015 (SDLS2 and SFLS1), are used to inform this process, including a measure of uncertainty. Lari *et al.* (2014) have performed widespread analysis for rockfalls, but no such mapping approach, using a dynamic model, has been performed for debris flows.

4.1 RAMMS Debris Flow

4.1.1 Model Equations

RAMMS-DF is based upon a 3D numerical code first implemented to model snow avalanches (Christen *et al.*, 2010) and employs a Voellmy-fluid friction model approach (Salm, 1993).

Calculations in the model are made across a Cartesian domain represented by the co-ordinates x and y. The elevation of the terrain, derived from a digital elevation model (DEM), is defined by $z\ (x, y)$. At any time t in the model, the flow height is given by $H\ (x, y, t)$, and the mean flow velocity vectors are given by $U_x\ (x, y, t)$ and $U_y\ (x, y, t)$, in the x and y directions respectively. The mean flow velocity (U) is given by:

$$U = \sqrt{U_x^2 + U_y^2}$$

Equation 7

The direction vector unit (n_U) of the flow meanwhile is given by:

$$\boldsymbol{n}_{\boldsymbol{U}} = \frac{\mathbf{1}}{\boldsymbol{U}} (\boldsymbol{U_x}, \boldsymbol{U_y})^{\boldsymbol{T}}$$

Equation 8

The mass balance of the flow, relating to height, is given by:

$$\partial_t H + \partial_x(HU_x) + \partial_y(HU_y) = Q(x, y, t)$$

Equation 9

where values of Q < 0 result in deposition and Q > 0 result in entrainment (this being irrespective of the entrainment option and resulting only to the initial flow mass).

The depth-averaged momentum balance is calculated in both x and y directions as separate components, using the equations:

$$\partial_t(HU_x) + \partial_x\left(c_x\, HU_x^2 + g_z\, ka_{/p}\, \frac{H^2}{2}\right) + \partial_y\left(HU_x U_y\right) = S_{gx} - S_{fx}$$

Equation 10

and

$$\partial_t(HU_y) + \partial_y\left(c_y\, HU_y^2 + g_z\, ka_{/p}\, \frac{H^2}{2}\right) + \partial_x\left(HU_x U_y\right) = S_{gy} - S_{fy}$$

Equation 11

where c_x and c_y are first-order model corrections which are incorporated to account for shear gradients and non-rectangular velocity profiles (Christen *et al.*, 2010); c_x and c_y were ignored by Christen *et al.*, (2010) due to the mostly insignificant impact on their results. g_z represents gravitational acceleration on the z – axis. S_{gx} and S_{gy} are the accelerations due to gravity, whereas S_{fx} and S_{fy} are the component Voellmy-Salm friction values (derived from equation 10 and equation 11). $ka_{/p}$ is the earth pressure coefficient, given by the equation:

$$ka_{/p} = \tan^2\left(45° \mp \frac{\varphi}{2}\right)$$

Equation 12

where φ is the internal friction angle. This coefficient can either be active (k_a; -), where the flow is dilatant, causing the change in flow velocity to increase ($\nabla \cdot U \geq 0$), or passive

$(k_p; +)$, where the flow is compressive and thus causes the change in flow velocity to decrease ($\nabla \cdot U < 0$).

The basic Voellmy-fluid friction model derives the frictional resistance (S) using the simplified equation:

$$S = \mu \rho H g \cos\varphi + \frac{\rho g U^2}{\xi}$$

Equation 13

where μ is the dry-Coulomb type friction coefficient, ξ the velocity squared drag, ρ the flow density, g the acceleration due to gravity (vertical), H the flow height and U the flow velocity. According to Bartelt *et al.* (2013), μ (Mu) dominates at lower velocities where the flow is close to stopping, whilst ξ (Xi) dominates at higher velocities.

The friction equation has further been adapted to account for material cohesion, based upon chute experiments (Platzer *et al.*, 2007) and real scale experiments at Illgraben. This results in the following equation:

$$S = \mu N + (1 - \mu)\, C - (1 - \mu) C \exp\left(-{}^{N}/_{C}\right) + \frac{\rho g U^2}{\xi}$$

Equation 14

where *C* represents the cohesion (Pa) of the flowing material and N the normal force.

4.2 Model Calibration

April 2015 TLS data was selected for modelling as this represented the pre-failure (prior to Storm Desmond and Storm Frank) surface at RabT. These data lacked sufficient coverage within the gullies on the slope however and so these areas were augmented with data collected using a Riegl VZ-4000 in July 2016, through registration and merging in CloudCompare. The resultant 1 m resolution point cloud was imported into the software Quick Terrain Modeller, from where it was exported as a GEOTIFF raster. The resultant DEM was further processed within ArcMap using the 'Raster to ASCII' tool, formatting the DEM to the particular specification required by the RAMMS-DF. This DEM is of a high resolution, owing to the coverage and density of the TLS data. This compares to significantly lower model resolutions, usually of around 5 m, adopted in other studies utilising RAMMS-DF (Christen *et al.*, 2010; Hussin, 2011; Hussin *et al.*, 2012; Frey *et al.*, 2016). Lower resolution calculation grids, such as a 2 m grid on a 1 m resolution DEM (Klaus *et al.*, 2015; Schraml *et al.*, 2015),

can shorten simulation processing times. A higher resolution (1 m) calculation grid was however favoured due to the relatively small size of the debris flows being modelled.

Figure 4.1 presents a review of Voellmy parameters from different studies, conducted by Scheidl et al. (2013) and gives some initial indication of a realistic parameter value range. A list of calibrated input parameters were compiled from the literature (Table 4.1) and used as guidance alongside those compiled by others (Quan Luna *et al.*, 2010; Scheidl *et al.*, 2013) and those suggested in the RAMMS-DF manual (Bartelt *et al.*, 2013).

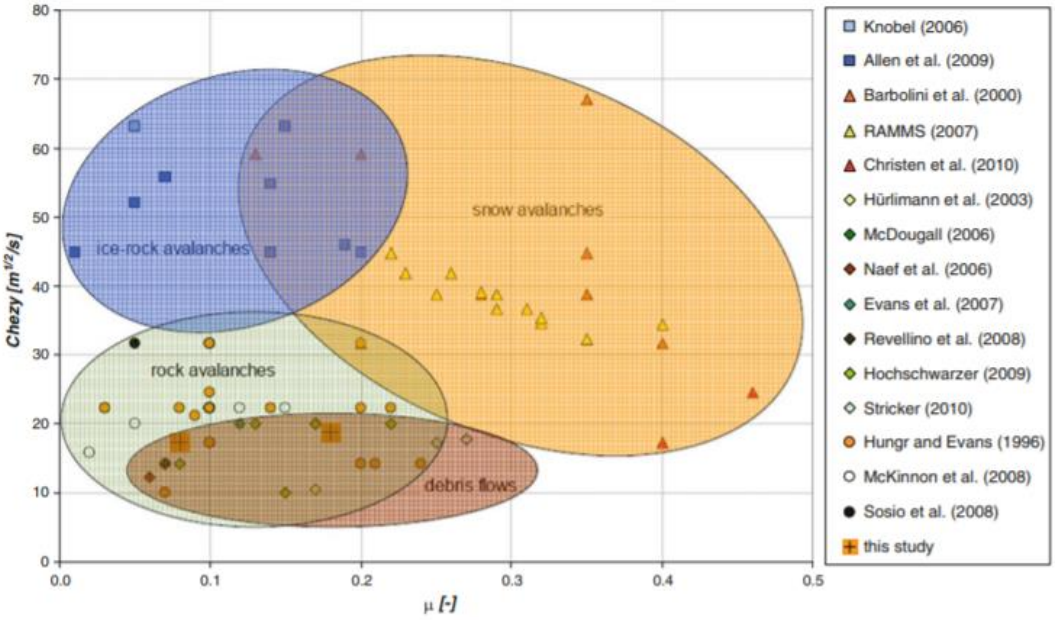

Figure 4.1 – Voellmy rheology parameters used in other studies for landslides and snow avalanches (Scheidl et al., 2013)

The values shown in table 4.1 have been used to inform the initial model parameters, prior to more specific calibration in the back-analysis. During initial testing, it was discovered that block-failure (all volume released instantly) yielded un-realistic initial flow heights, as also found by (Frank *et al.*, 2017). An input hydrograph (delayed mass release) was preferred, although estimation of peak discharge using the empirical equation suggested by Scheidl and Rickenmann (2009) was opted against as this resulted in flows with unrealistically small flow heights. Experimentation with a flow hydrograph found that a four second release period resulted in more realistic initial flow heights, whilst still effectively simulating a mass failure. In the flow hydrograph used (figure 4.2), the maximum discharge increases linearly until two seconds after failure, after which the input declines for a further two seconds. Q_{max} is equivalent to 50 % of the initial flow mass.

Table 4.1 - Some input parameters used to model debris flows in other studies

Reference	Location	Model Type	Parameter	
			Mu (μ)	Xi (ξ)
Deubelbeiss and Graf (2013)	Valais, Switzerland	Single channel	0.225	130
Hussin *et al.* (2012)	Barcelonnette, France	Single channel	0.06	500
Graf and McArdell (2011)	Preonzo, Switzerland	Hillslope and channel	0.1 – 0.3	100 - 400
Loup *et al.* (2012)	Alpnachstad, Rueggisberg and Koniz, Switzerland	Hillslope	0.4, 0.2 and 0.1 respectively	150, 1000 and 500 respectively
Scheuner *et al.* (2011)	Mattenbach, Switzerland	Channel	0.1	200

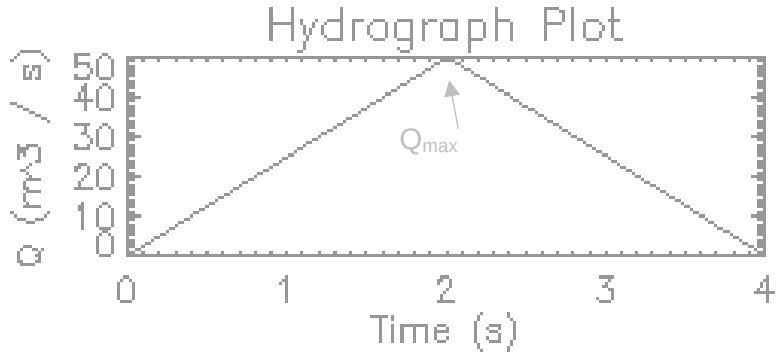

Figure 4.2 - An optimal input hydrograph for simulating block-failure with realistic initial flow heights

A model cessation momentum threshold of 10 % was found to best avoid numerical diffusion (prolonged spreading of the flow mass without deposition). Other studies typically fail to disclose this parameter, which is a critical factor in model deposition, and which may influence whether parameter values from other studies can be directly compared.

Mu (μ), the dry-Coulomb type friction co-efficient, was estimated using tan(α), whereby α is the slope angle (radians) in the deposition zone. This gave a value exceeding the maximum range advised by Bartelt et al. (2017), thus a value towards the upper end of the range (0.35) was adopted. An Xi (ξ) value of 200 m/s^2 was initially used as this marked the threshold between granular and muddy type flow behaviour (Bartelt *et al.*, 2017). A debris flow density of 2000 kg/m^3 is common and was also recommended by Bartelt et al. (2017), and was thus also adopted at this stage.

Table 4.2 – An introduction to the main RAMMS parameters and good starting values (for RabT) around which back-analysis can be conducted

Parameter (symbol/units)	Description	Default value
Mu (μ)	Dry-Coulomb type friction; scales with normal stress.	0.35
Xi (ξ; m/s^2)	Velocity-squared drag *or* viscous-turbulent friction. 200 marks threshold between granular flow and muddy flow.	200
Cohesion (Pa)	Value of 0 represents that of water.	300 - 1800
Density (kg/m^3)	Default parameter given by RAMMS-DF manual. 2000 equivalent to that of wet gravel.	2000

A default cohesion value of 0 Pa resulted in model diffusion (inadequate momentum decay for deposition to occur and the model to stop) on the steep slope of RabT, thus use of this parameter was necessary unlike in most other studies. Cohesion conventionally relates to electrostatic bonds between clay and silt particles (Blasio, 2011), which borehole data show to be abundant within the superficial layer at RabT (BGS, 2009). During laboratory experiments, Hurimann *et al.* (2015) found debris flows to be highly sensitive to changes in clay content. Saturated flows, consisting of fine particles and clays, exhibit cohesion of between 10-400 Pa (Iverson, 2003). Whilst these values should notionally increase with the greater proportion of coarse material (Coussot *et al.*, 1998), such a property is not possible to measure in the lab due to the heterogenous nature of debris flows. Iverson (2003) therefore cautions that incorporation of cohesion delves into the domain of an adjustable model coefficient. Zimmermann *et al.*, (2018) comment that the cohesion parameter has a predictable impact on modelled runout, with the Voellmy parameters still principally controlling this. The parameter was found to yield more realistic simulation of runout areas in some cases (Zimmermann *et al.*, 2018). Bartelt *et al.* (2017) recommend a value between 0 – 2,000 Pa, however a value in excess of 400 Pa is likely suitable due to observations of coarse material in previous flows at RabT.

4.3 Model Application

4.3.1 Sensitivity analysis

Calibration and application of a model such as RAMMS-DF requires an understanding of its sensitivity to individual input parameters. This is particularly important for calibration, as fine-tuning of one parameter often necessitates the considered adjustment of another, particularly to compensate and retain a desired runout distance.

Many studies have previously carried out sensitivity analyses on real-world topographic data, however sudden changes in topography will indiscriminately elongate one model run over another, even if the input parameters only vary marginally. To negate topographic influence, an artificial planar-slope model was constructed with a uniform flow-channel. The model-slope was designed based on the average slope angle (32°) at RabT and thus consisted of an 800 m long slope (horizontal) with a maximum elevation of 500 m. A 6 m wide and 2 m deep gully was included at the centre of the slope to further negate the effect of flow spreading on momentum loss. Co-ordinates representing the corners of each slope segment were manually entered into a spreadsheet before being imported into CloudCompare. The points were meshed into four planes, namely the left-hand side of the slope, the left gully wall, the right gully wall and the right-hand side of the slope (a schematic of these is shown in figure 4.3). A regular 1 m point cloud was sampled from the resultant mesh and imported directly into RAMMS-DF.

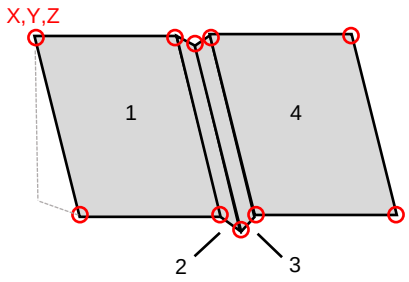

Figure 4.3 - A schematic of the model slope design process, where the label numbers represent each respective plane created from manually calculated co-ordinateS, denoted by the red circles.

A 4 m x 4 m source area was generated at the top of the slope directly at the centre of the channel. From this, 100 m^3 of material was released over a period of four seconds (max discharge of 50 m^3 at t = 2s), representing a maximum flow height of approximately 3 m. A total of 33 sensitivity model runs were conducted, 8 for each model parameter. Models were processed on a desktop PC running Windows 7, with a 3.4 GHz quad-core processor (i7-4770) and 32 GB of RAM. Each sequential model run included a 20 % change in one parameter,

from its default value, whilst all other parameters were locked to their default value. The batch of sensitivity model runs are shown in table 4.3a and 4.3b.

The resulting deposition of each model was viewed and the furthest runout distance of each (X and Y position) was sampled using the cursor position. Raster datasets of deposition were also analysed in ArcMap using a 1 m grid and the Zonal statistics tool, to create plots of deposition depth over longitudinal runout distance.

Table 4.3a – Sensitivity analysis input parameter combinations (Xi and Mu)

Model	**Xi (ξ; m/s^2)**	**Mu (μ)**	**Cohesion (Pa)**	**Density (kg/m^3)**
Default	*200*	*0.2*	*1000*	*2000*
Xi 1	40 (-80%)	*0.2*	*1000*	2000
Xi 2	80 (-60%)	*0.2*	*1000*	2000
Xi 3	120 (-40%)	*0.2*	*1000*	2000
Xi 4	160 (-20%)	*0.2*	*1000*	2000
Xi 5	240 (+20%)	*0.2*	*1000*	2000
Xi 6	280 (+40%)	*0.2*	*1000*	2000
Xi 7	320 (+60%)	*0.2*	*1000*	2000
Xi 8	360 (+80%)	*0.2*	*1000*	2000
Mu 1	*200*	*0.04* (-80%)	*1000*	*2000*
Mu 2	*200*	*0.08* (-60%)	*1000*	2000
Mu 3	*200*	*0.12* (-40%)	*1000*	2000
Mu 4	*200*	*0.16* (-20%)	*1000*	2000
Mu 5	*200*	*0.24* (+20%)	*1000*	2000
Mu 6	*200*	*0.28* (+40%)	*1000*	2000
Mu 7	*200*	*0.32* (+60%)	*1000*	2000
Mu 8	*200*	*0.36* (+80%)	*1000*	2000

Table 4.3b – Sensitivity analysis input parameter combinations (cohesion and density)

Model	Xi (ξ; m/s²)	Mu (μ)	Cohesion (Pa)	Density (kg/m³)
Default	*200*	*0.2*	*1000*	*2000*
Cohesion 1	*200*	*0.3*	200 *(-80%)*	2000
Cohesion 2	*200*	*0.2*	400 (-60%)	2000
Cohesion 3	*200*	*0.2*	600 (-40%)	2000
Cohesion 4	*200*	*0.2*	800 (-20%)	2000
Cohesion 5	*200*	*0.2*	1200 (+20%)	2000
Cohesion 6	*200*	*0.2*	1400 (+40%)	2000
Cohesion 7	*200*	*0.2*	1600 *(+60%)*	2000
Cohesion 8	*200*	*0.2*	*2000 (+80%)*	2000
Density 1	*200*	*0.2*	*1000*	400 *(-80%)*
Density 2	*200*	*0.2*	*1000*	800 (-60%)
Density 3	*200*	*0.2*	*1000*	1200 (-40%)
Density 4	*200*	*0.2*	*1000*	1600 (-20%)
Density 5	*200*	*0.2*	*1000*	2400 (+20%)
Density 6	*200*	*0.2*	*1000*	2800 (+40%)
Density 7	*200*	*0.2*	*1000*	3200 (+60%)
Density 8	*200*	*0.2*	*1000*	3600 *(+80%)*

4.3.1.1 Results and discussion

The sensitivity analysis on a model slope has demonstrated the performance of the RAMMS-DF model in addition to the sensitivity of its individual parameters. The sensitivity plot (figure 4.4) shows a near-linear response to gradual iterative changes in the Voellmy derived input parameters. Slight variations in the lines of the plot however demonstrate that despite the idealised model-slope, outputs are still prone to a degree of volatility. It is suspected that this behaviour could relate to numerical instabilities which became evident when visually inspecting the runout results and observing a tendency for the modelled flows to not conform directly to the centre line of the modelled channel, or to produce a symmetrical terminus deposit.

The steepest line, and thus largest resultant change in runout, is that of the density parameter, with an 80 % reduction in density resulting in an 80 % reduction in runout distance, and an 80 % increase lengthening the runout by almost 60 %. The two vertical black dashed lines in figure 4.4 however show that the realistic range of this parameter is much smaller than that modelled, with only a 2000 kg/m³ ±10 % variation in density being realistic (Wang et al. 2017). Within this range, the difference in runout distance is limited to less than ± 10 %, thus a relatively small range of sensitivity.

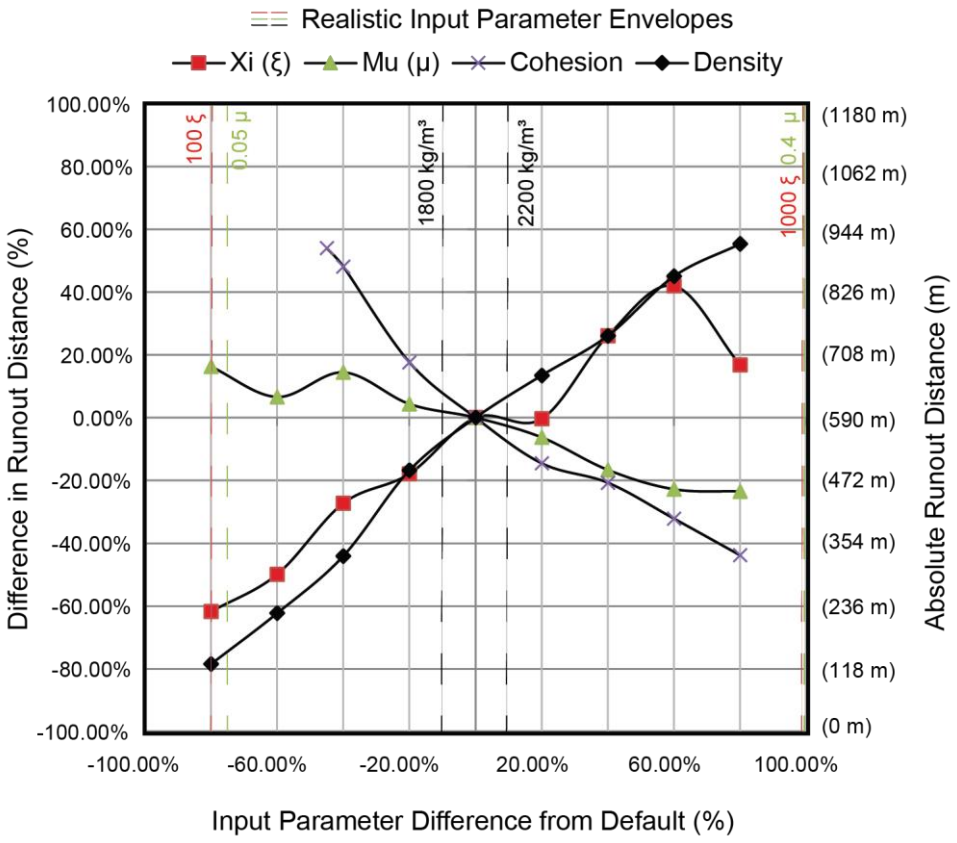

Figure 4.4 - A plot of individual parameter sensitivities. Default values = Mu 0.2, Xi 500, Cohesion 1,000 Pa, Density 2,000 kg/m3. The centre of the plot represents the runout distance where the input parameters are set to their defaults.

A ±20 % variation in cohesion affected the runout distance by ± 16 %, which demonstrates that the model is slightly less sensitive to this parameter. However, a reduction in cohesion of 50 % or more caused the flow to mobilise beyond the 800 m extent of the model, truncating the cohesion line in figure 4.4. A 45 % decrease in cohesion was modelled instead, this yielding a 55 % increase in runout (this fitting within the 800 m model slope extent), whilst the equivalent increase in cohesion yielded a 23 % decrease in runout. Ignoring sensitivity to unrealistic density values, the RAMMS-DF model is clearly most sensitive to changes in the cohesion parameter. The model is also more sensitive to low cohesion values

(particularly 0 - 800 Pa), than changes in high cohesion values, although this appears to relate to the steep slope used in this study, on which low cohesion flows continue to spread (model diffusion). Greater model sensitivity to the cohesion parameter, than the Mu parameter, introduces difficulty to the back-analysis stage, as debris flow deposits rapidly dewater and are often comprised of a sorted assemblage, often including material sourced from heterogeneous glacial deposits (Curry *et al.*, 2009), making a single cohesion value hard to sample in the field. As such, a fixed cohesion value is chosen to represent a simplified and idealised model parameter, rather than a reflection of the true material cohesion.

Of the two principal input parameters Mu and Xi, the modelled runout responded most to changes in the latter, producing a much steeper line in figure 4.4 (Mu = grade of ~0.25, Xi = ~1.5) equating to 500 % greater sensitivity than the Mu parameter. The response of the Xi parameter is non-linear, unlike that of Mu, with the highest Xi value (900 m/s^2) resulting in a reduced runout distance compared to slightly lower values in the range (+ 40-60 % ; 700 – 800 m/s^2). A decrease in Mu principally resulted in an increased runout distance, whilst an increase resulted in the opposite. A ± 80 % change in Mu only resulted in a ~ ± 20 % change in runout distance.

Higher sensitivity to the Xi parameter differs to sensitivity analysis performed by Hürlimann *et al.* (2008) and Borstad and McClung (2009) who found Mu to be more sensitive in other Voellmy rheology based models. The results of this study do correspond to those of Hussin (2011) who also used the RAMMS-DF model however, although it is worth noting that use of natural topography resulted in greater sensitivity variability in his study. It is worth noting that RabT is very steep, as was the model slope (32°), which differs significantly from other studies of relatively low-gradient channels, typically measuring 15-20° (Hussin, 2011; Hussin *et al.*, 2012; Frank *et al.*, 2015; Erika *et al.*, 2017). It is also worth noting that such studies are typically carried out in channels, where large quantities of stream water are likely to dilute any flow mass, thus reducing the requirement for high cohesion values. Frank *et al.* (2017) did however use high Mu values of 0.6 for modelling flows in a channel of a similar gradient to RabT (Meretschibach), with no mention of a cohesion value. This is despite Bartelt *et al.* (2017) commenting that the Mu value should be varied between 0.05 – 0.4, and that values exceeding this rarely yield useful results. Frank *et al.* (2017) meanwhile used a much lower value of 0.3 for a lower gradient stretch of channel (Bondasca). Zimmermann *et al.* (2018) comment that the addition of cohesion can aid modelling in some cases. It appears, based upon this analysis, that use of the cohesion parameter is most applicable to modelling on steep slopes, including open hillslope areas as well as channels.

Figure 4.5 shows a longitudinal plot of deposition binned to 5 m sections. It is notable that modelled runout, on a planar model slope, results in complex longitudinal deposition patterns. The lowest density model results in a significant quantity of deposition just 100 m downslope of the source, this further demonstrating that such low density values are unrealistic. Changes in Mu had a limited effect on the deposition morphology, apart from an increase in Mu resulting in a slight increase in relief between the peak deposition volume and the lowest volume. The Xi parameter affected runout distances more than originally expected, however the parameter also appears to influence the longitudinal distribution of the flowing mass (figure 4.5). In contrast, the Mu parameter did not significantly change the longitudinal distribution.

Low Xi values (~100 m/s^2) resulted in a relatively flat, large depth of deposition over a short distance. The runout distance increased relatively linearly for mid-range Xi values, with a slight increase in variation, or relief, between low and high deposit depths. In contrast, the highest Xi value (+ 80 %; 900 m/s^2) resulted in thicker deposits, with less depth variation, than that of any other model. The highest Xi value also resulted in a random peak of deposition early on, at a distance of ~250 m, a feature of which cannot be observed for any of the other modelled flows. These variations reflect the different flow compositions, with Xi values around 100-200 m/s^2 said to simulate granular flows and higher values said to be more typical of muddy type flows (Bartelt et al. 2017). When modelling the impact of flows, on catch nets for example, this suggests that models with higher Xi values may exert stronger impact pressures. High Xi values, such as those in excess of 900 m/s^2, yielded sporadic deposition results, including a reduction in runout distance and increased bulk of deposition with less longitudinal variation in volume. This diverts from the relatively linear relationship for the rest of the values (100 – 900 m/s^2). Despite Bartelt *et al.* (2017) advising an upper range of 1,000 m/s^2 for the parameter, the findings of this study suggest that a maximum value of around 900 m/s^2 should ensure reliable results, rather than an unpredictable response.

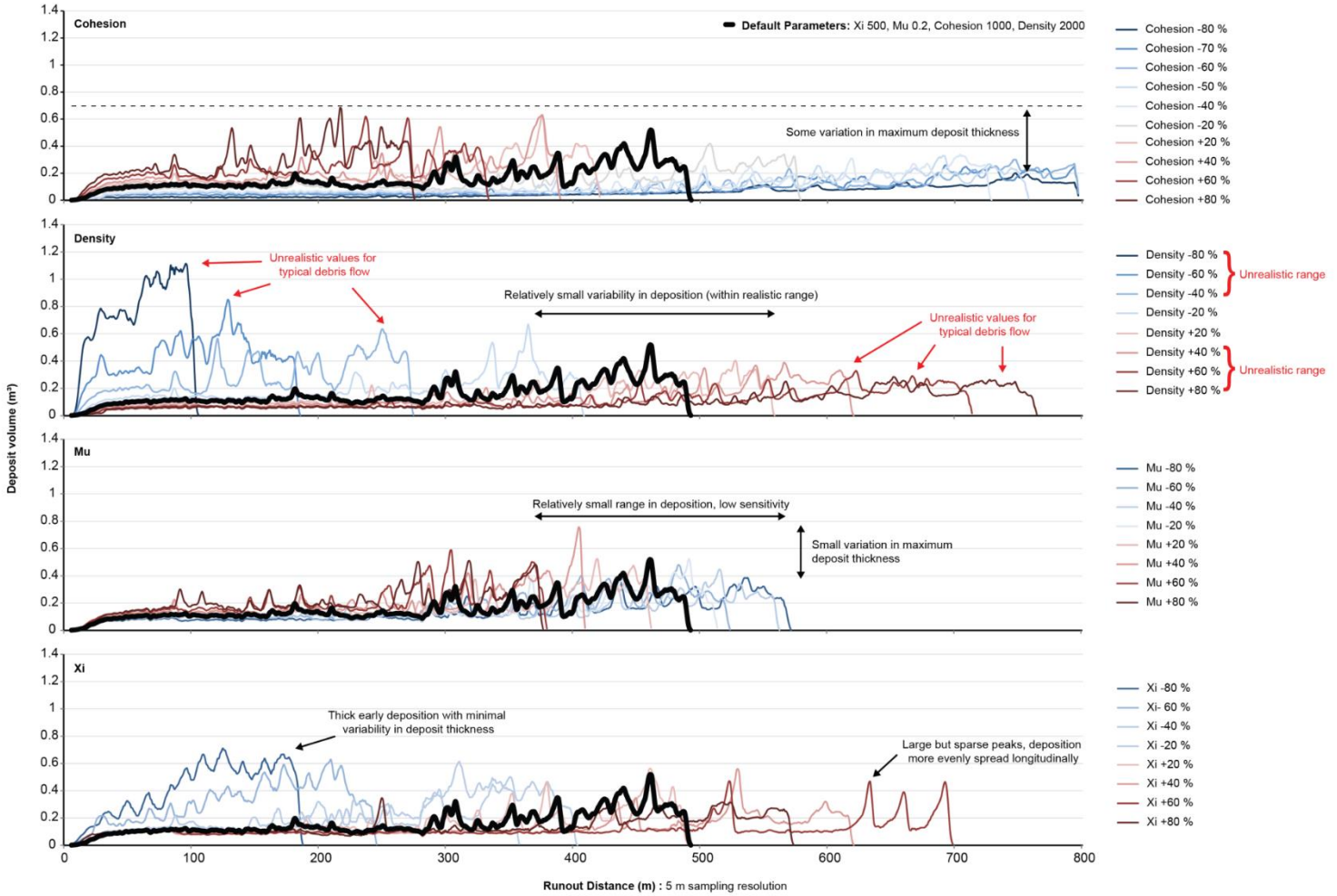

Figure 4.5 - Sensitivity analysis outputs sampled longitudinally to inspect flow height morphology

4.3.2 Back-analysis

No standard objective approach exists for the comparison of simulated runout with actual runout (Heiser *et al.*, 2017), although back-analysis is generally performed through trial and error, whereby changes are sequentially made to subjectively yield satisfactory results (Aaron *et al.*, 2016; Frank *et al.*, 2017). This stage is typically carried out by matching the model output with the actual head of the flow source and the terminus of the flow (i.e. Pirulli, 2005, Simoni *et al.*, 2012; Scheidl *et al.*, 2013), although others have used invasive instrumentation to directly sample flow velocities and other such information for this process (Graf and McArdell, 2011). Alternative statistical approaches are possible, such as that proposed by Aaron *et al.* (2016) in which a Gauss-Marquardt-Levenberg algorithm based parameter estimation package (PEST) was used, however this approach was limited to a combination of just two parameters, whilst this study uses three. Back-analysis results and parameter combinations are commonly analysed through comparison with an approximation of the actual debris flow runout although this is generally limited to comparing runout extents, not small distributed deposit patterns over the flow path. Analysis of the deposition distribution can however be of use (Van Asch *et al.*, 2004) and is the basis of back-analysis in this study.

In this study, monitoring data provides a non-intrusive basis for calibration of RAMMS-DF, using an alternative approach to studies which typically focus on mapping and recreating the runout extent. The runout extent is also taken into account however and is particularly used to validate the back-analysis on an independent event in section 0. Back analysis is corroborated with a more comprehensive data, increasing confidence in the model parameters and results (Christen *et al.*, 2012).

At the time of runout modelling (end of second monitoring year), three main debris flow events had been recorded using TLS. All three of the Storm Desmond events were inhibited in some way by catch nets, ruling out back-analysis via runout extent alone. This necessitated an alternative back-analysis approach, by matching modelled deposition patterns with those of the TLS detected deposits, as outlined in section 0.

The SDLS1 event had a very short runout path along which no significant deposition occurred, immediately ruling it out as a candidate for back-analysis. The SDLS2 event was least inhibited and provided deposition data, above the TLS LoD, to which the model outputs could be compared. Only a limited quantity of material reached a flow net (estimated to be 29 m^3), enabling possible parameter combinations to be constrained (i.e. those resulting in

significantly more deposition could be ruled out). The coherent nature of the SDLS2 source area also enabled the original loss polygon to be directly imported into RAMMS-DF polygon feature. This compares to the SFLS1 source area, which consisted of multiple fragmented polygons due to soil rafts which did not vacate the source, which necessitated processing and subjective simplification. The SFLS1 event was significantly inhibited by a catch net, however upslope deposition patterns did provide a basis for the back-analysis approach described in section 0. The SFLS1 event served as a secondary back-analysis event, for comparison with the SDLS2 back-analysis.

An input hydrograph equivalent to that in figure 4.2, but with a total volume of 334 m^3 and peak discharge of 167 m^3, was set for SDLS2 and a batch of 29 models were prepared. All four of the main parameters were varied about the default values shown in table 4.2 (resembling a similar approach to the sensitivity parameters used; shown in table 4.3). These were run at a 1 m model resolution using RAMMS' batch-run utility. Deposition rasters were exported from RAMMS-DF for analysis, after which the same approach was applied to back-analyse the SFLS1 event for comparison (485.6 m^3 input volume, peach discharge of 242.8 m^3).

Independent comparison event

To assess the two sets of back-analysed rheological parameters, a third debris flow event was modelled. An open hillslope flow occurred at RabT in June 2012, without inhibition by structures such as a debris flow catch net. A source area volume of 80 m^3 was estimated by analysing the scar geometry in TLS data and interpolating across from the margins of the scar. A non-nadir terrestrial photograph was digitised to a hillshade of the slope, with features such as boulders and prominent gully bends used as geo-referencing features. More than twenty features were used, and an affine transformation was applied to the image, after which the source area and runout domain were digitised for comparison with the model outputs.

Model output analysis

Bartelt *et al.* (2017) advise that parameters be incrementally varied around the starting values until satisfactory results are found. Back-analysis in this study was conducted in batch iterations, with the first used to narrow down the parameter range and a subsequent iteration used to refine these values to the optimal combination.

The RAMMS-DF software environment enables transects to be drawn, to analyse deposition depths over the slope. Pirulli and Sorbino (2008), for example, used this approach to compare

different model performances. This was however considered limited, due to it not accounting for the lateral spread and distribution of the flow mass. A pixel by pixel raster comparison was considered as a means to compare each model output with monitoring data, however this was deemed too precise when considering the nuances of numerical models and the potential for small, inconsequential offsets, to be interpreted as poor model performance. Factors such as DEM simplification of true topography (2.5D) and the TLS deposition LoD were also considered to hinder such a precise comparison.

Model outputs were eventually compared, with change detection volumes, using 5 m longitudinal bins. Volumes of deposits within each bin were sampled using ArcMap Zonal Statistics and plotted against monitoring data sampled using the same approach (whole workflow shown in figure 4.6). The RAMMS-DF models generally simulated more diffusive flow behaviour (spreading), resulting in broadly correct volume distributions, although with a larger footprint than observed in reality. Application of a threshold to the model data, equivalent to the TLS LoD threshold, was considered, to enable direct comparison with change detection data. A large threshold was found to filter away most of the flow mass however, due to the diffusive nature (spreading) of the modelled flows. Instead, a 0.05 m threshold was used to isolate and delineate between discrete patches of deposits.

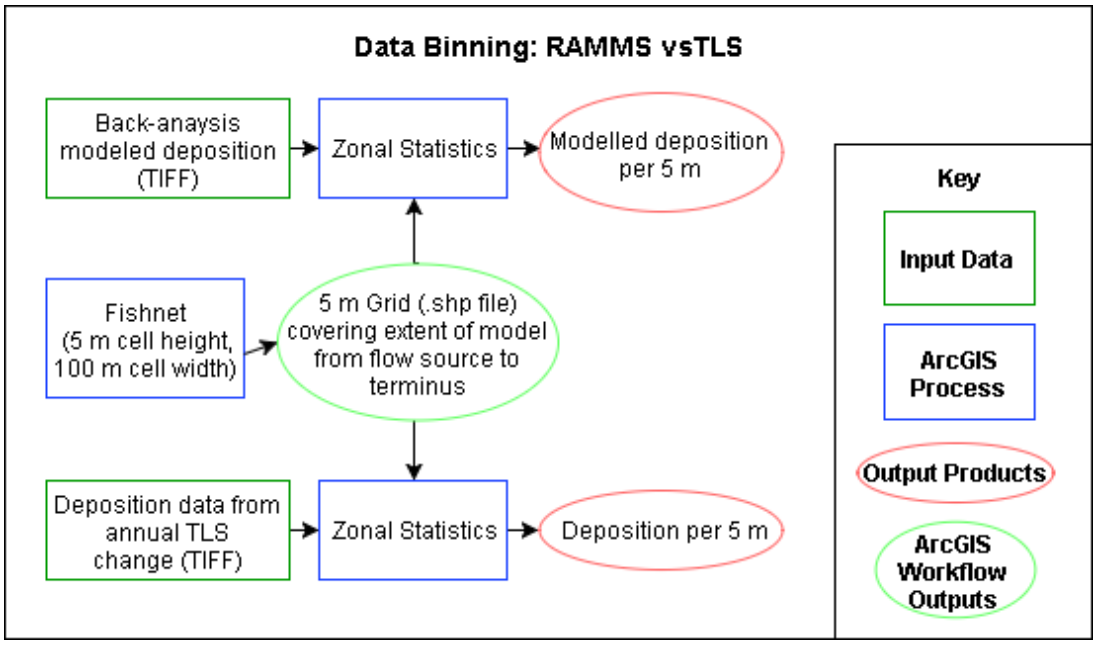

Figure 4.6 - The GIS workflow used to compare back-analysis model outputs with observation data

To account for potential deposition volumes below the TLS LoD threshold, and thus the degree of uncertainty within which back-analysis was conducted, runout areas, in which no deposition was detected, were digitised from a georeferenced photograph taken shortly

after the debris flow events. These areas were converted into volumes, by multiplication with the LoD threshold, and were binned (5 m) to produce a LoD uncertainty range on the resultant plots within section 0 and 0.

Results interpretation

Change detection volumes provided a lower bound, below which models depositing less than this volume were known to be unrealistically small, and thus incorrect. The LoD uncertainty range provided an upper bound beyond which debris flow deposition was considered to be unrealistically large, and thus also incorrect. These bounds were used to rule out certain parameter combinations, leaving just those within an acceptable range. Following this, a number of factors were considered to identify optimal parameter combinations. This primarily included the longitudinal deposition distribution, or shape, relative to the actual recorded deposition distribution (TLS). For example, where one model contained a peak of deposition that matched the monitoring data, whereas another model did not, the former would be considered a better output. Furthermore, the overall volume of deposition was considered. For example, the volume of modelled catch net deposition (SDLS2) was compared to the actual estimate (29 m^3) and values far in excess of this were considered to be unrealistic, providing a further constraining factor.

4.3.2.1 Results

SDLS2 Event

Iteration 1: Initial back analysis

Figure 4.7 shows the results of the first iteration of back-analysis model parameters conducted for the SDLS2 event. All of the models generally follow the same longitudinal distribution as that of the observation data (bold black line), although typically with an offset. Despite the offsets, most of the model results fall within the range of LoD uncertainty (between 15-60 m on the X-axis). Of the 26 model runs shown, six fall outside of the LoD range at a distance of 25 m downslope, whilst 21 of the models fall outside of this range at a distance of 65-70 m downslope. Only cohesion values between 300-900 Pa stay within this range.

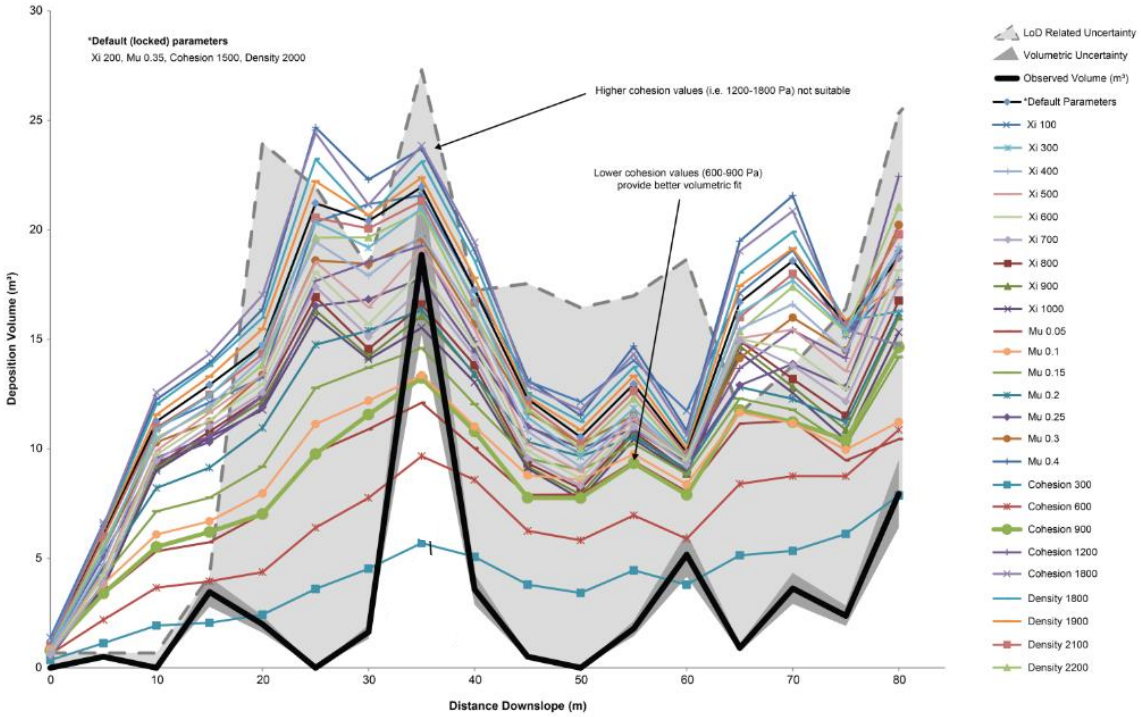

Figure 4.7 - Results from iteration 1 of the back-analysis model runs, binned to a regular 5 m longitudinal spacing orientated parallel to the direction of runout. the black line represents tls data binned using the same approach. this is used to compare modelled results with actual resutls in order to assess parameter performance.

Cohesion values in the range of 1200-1800 Pa were generally found to exceed the overall detected deposition volumes (TLS). Figure 4.8 shows a visual plot (rasters) of the back-analysis results, relating to changes in the cohesion parameter only. The higher values (1200-1800 Pa) promoted significant early deposition, particularly within the source area, which does not match the observation data. These models also failed to reach the gully, which material is known to have entered. The highest cohesion value (1800 Pa) in particular, also did not allow the modelled flow to reach the extent of the furthest (TLS) detected patch of

deposition at 220 m on the Y-axis. These results led to the conclusion that cohesion values of 900 Pa and above were unsuitable for modelling SDLS2.

The lowest cohesion value in (300 Pa) was closest to the overall detected volume of overall deposition (not factoring for LoD uncertainty), exceeding it by 27 %. This model fell considerably short (by 50%) of the large detected deposition peak at a downslope distance (X-axis) of 35 m however. Cohesion values of 600 and 900 Pa also fell short of this peak, however these produced more realistic deposition volumes, especially when accounting for longitudinal spreading between the neighbouring bins (30 m and 40 m bins contained much higher volumes than the black 'observed volume' line). The 600 Pa model appears to be a particularly good fit at this stage, with a similar quantity of deposition, to the monitoring data, over the 30-45 m range (26 m^3 over 15 m, as opposed to 24.1 m^3 over 15 m in the monitoring data). Overall, this model resulted in 145 % more deposition than that detected during TLS change detection, although this is not the actual deposition volume (not accounting for the TLS LoD). The cohesion value of 600 Pa therefore remained within contention at this stage.

Figure 4.9 shows only those results relating to changes in the Xi parameter. All of the models broadly follow the distribution of the observation curve, however there are clear differences such as early or lagged peaks relative to the observation data. Low Xi values (100-300 m/s^2) yield relatively flat longitudinal distributions in the early stages of the model (30 m downslope), these not matching the prominent peak and trough of the observation data. Further downslope (70 m), the highest Xi values (600-1000 m/s^2) yield relatively flat distributions, which also differ from the observation data. The lowest Xi values (particularly 100-300) fall outside of the LoD uncertainty range for at least 10 m (65-70 m), with greater variability in the deposition volume at a distance of 50 – 60 m (the observation data shows variation, between the peak and trough, of ~6 m^3, this compares to the Xi models of 500-1000 m/s^2 which have variability of ~7 m^3, and the 200 m/s^2 Xi model which results in relief of ~8 m^3). An Xi value of ~400 m/s^2 best replicates the peak in the observation curve at a distance of 70 m downslope, without excessive deposition. In the raster figures of the same results (figure 4.10 and figure 4.11), differences in deposition patterns are difficult to discern.

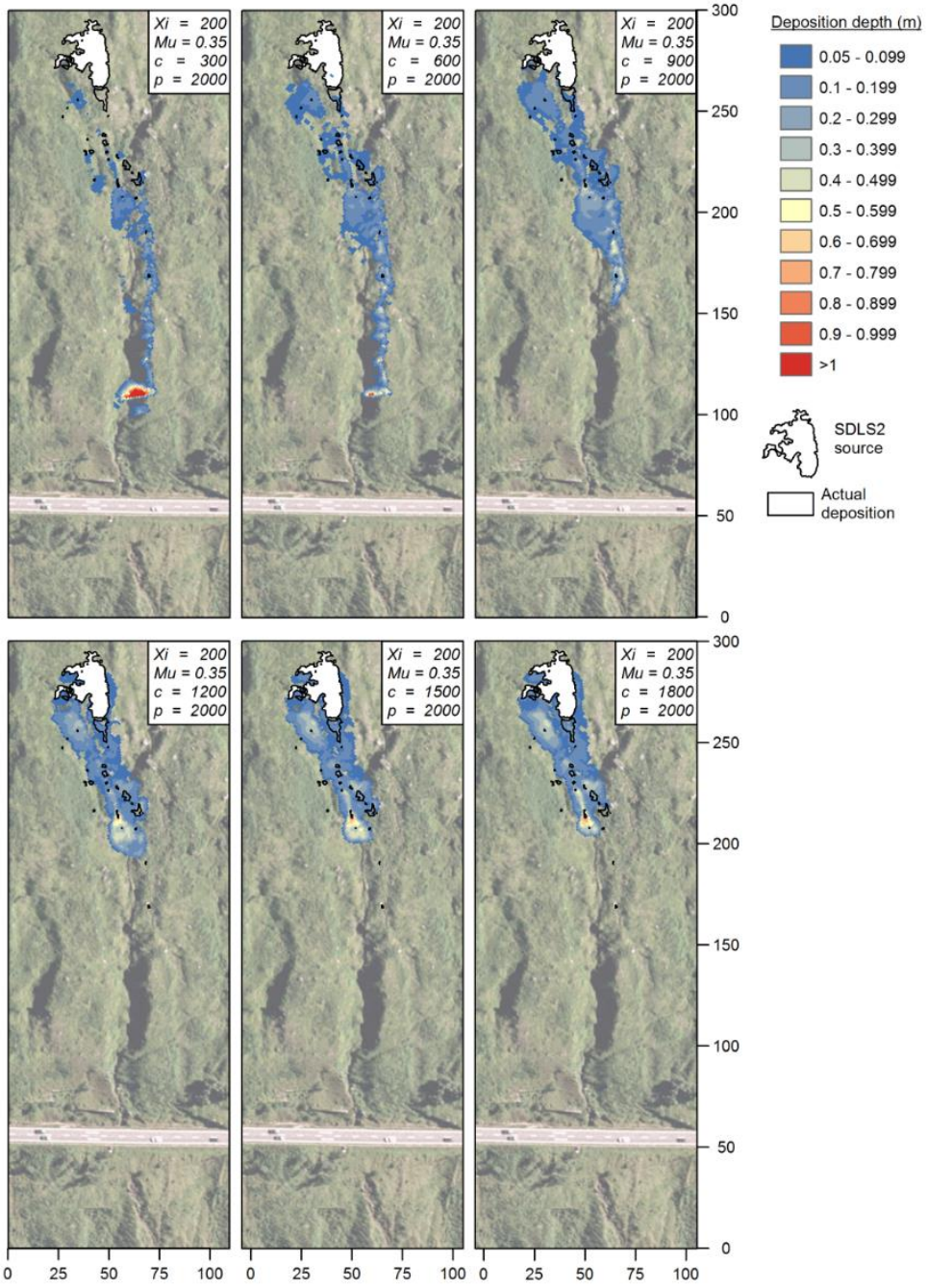

Figure 4.8 - The results of the first iteration back-analysis, where only cohesion values have been varied. In this, the highest cohesion value of 1800 does not allow the flow to reach the furthest detected (TLS) patch of deposition at a distance of around 220 m downslope. The values between 1200 and 1800 also promote deposition within the source area. In contrast, the lowest cohesion value of 300 results in very thin deposits below that of the 0.194 m TLS LoD threshold. This is also visible within the bining analysis plot (Figure 4.7).

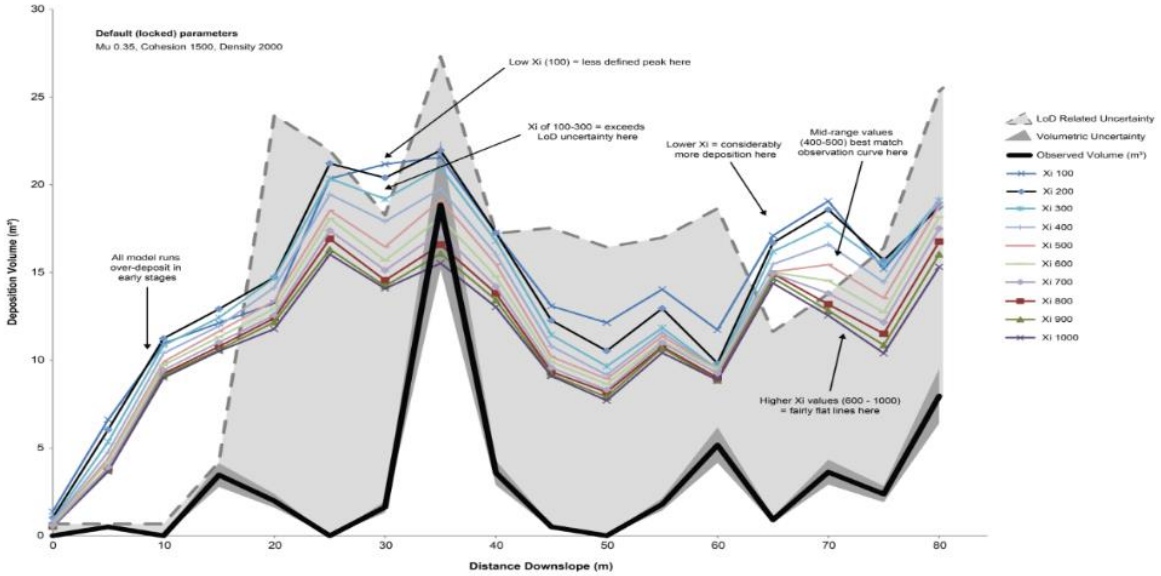

Figure 4.9 - The results of the iteration 1 back-analysis where only Xi values have been changed

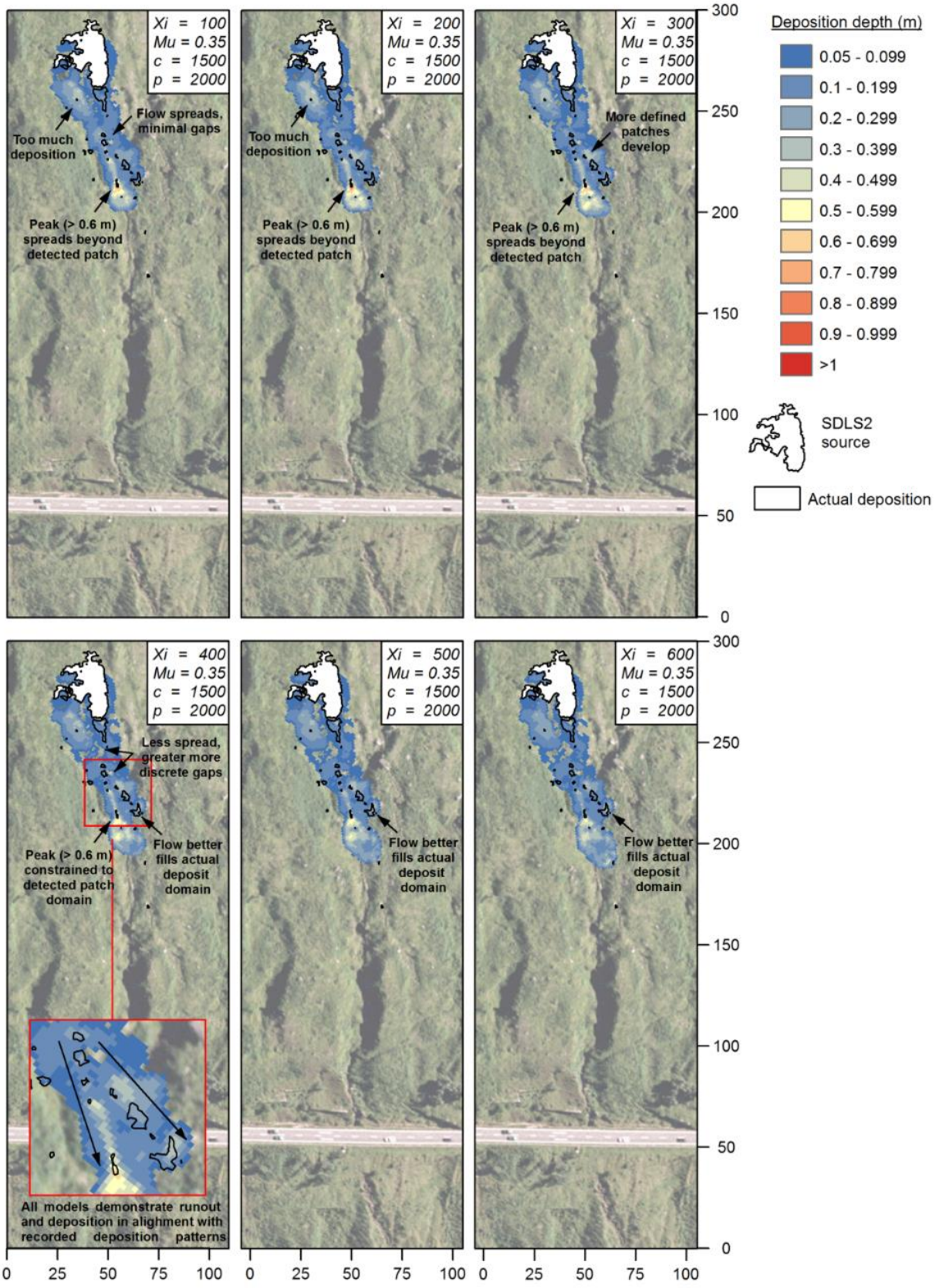

Figure 4.10 - The results of the first iteration back-analysis, where only Xi values have been varied (1 of 2). Higher Xi values promote spreading of the flow, resulting in more discrete patches of deposition, as well as increased runout distances.

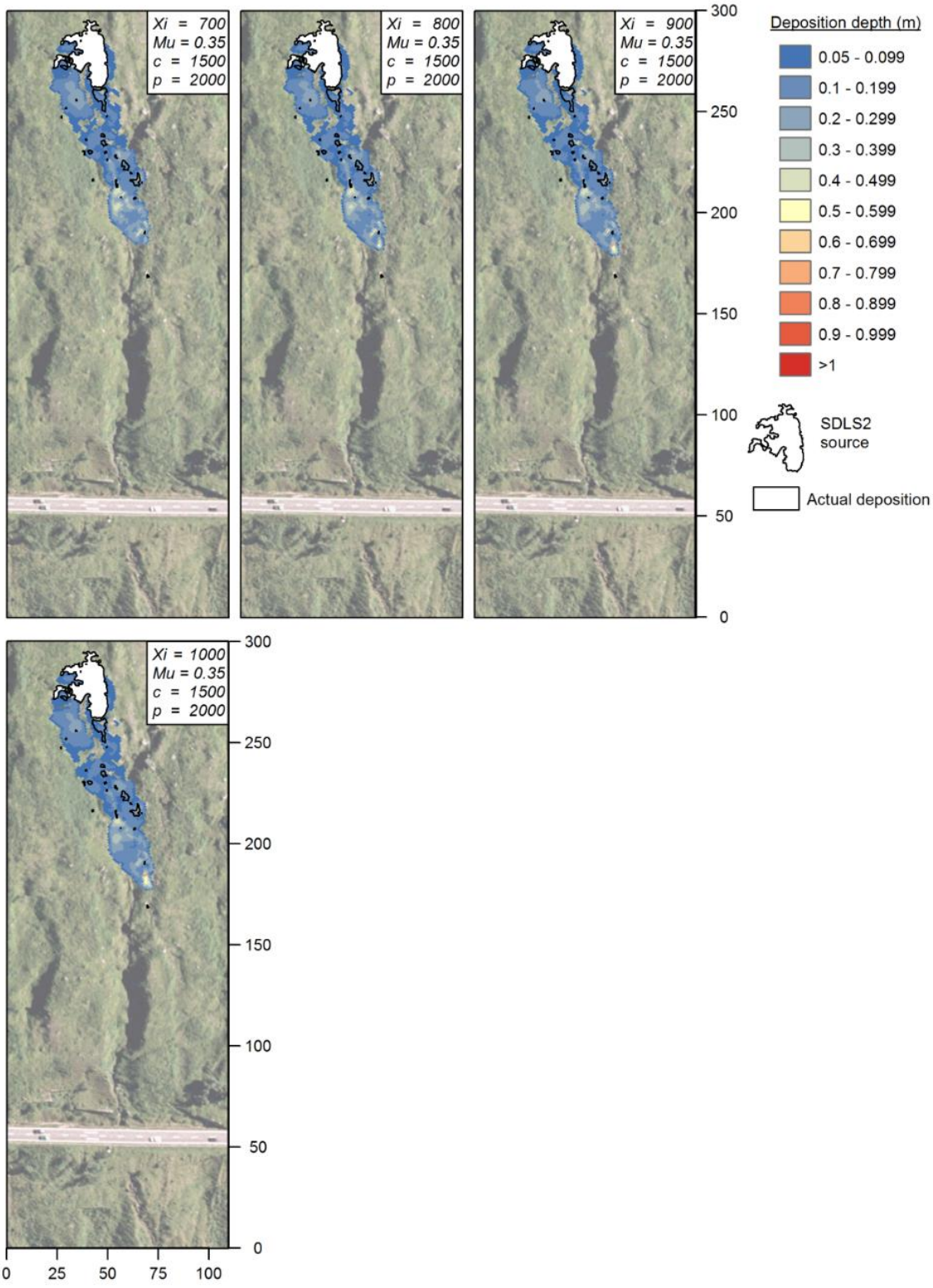

Figure 4.11 - The results of the first iteration back-analysis, where only Xi values have been varied (2 of 2). Differences between these model outputs become harder to identify, except that higher Xi values generally promote increased runout distances.

Figure 4.12 shows the iteration 1 results relating to the Mu (dry-Coulomb type friction coefficient) parameter. In general, the modelled deposition distributions are similar to one another, with higher Mu values (0.4 in particular) resulting in greater quantities of deposition throughout the plot. Differences are however evident in areas of peak deposition, at distances of around 20-35 m and 70 m downslope (X-axis) for example. The greater number of peaks and troughs of the higher Mu values (0.3-0.35), whilst offset volumetrically from the observation data, better resemble the shape or relief of the observation curve. Lower Mu values (0.05 – 0.2) result in smaller relief between deposition peaks and troughs. Low values of 0.05 and 0.1 in particular also result in little increase of deposition towards the end of the 80 m slope extent, whereas the observation data peaks again from a distance of 75 – 80 m.

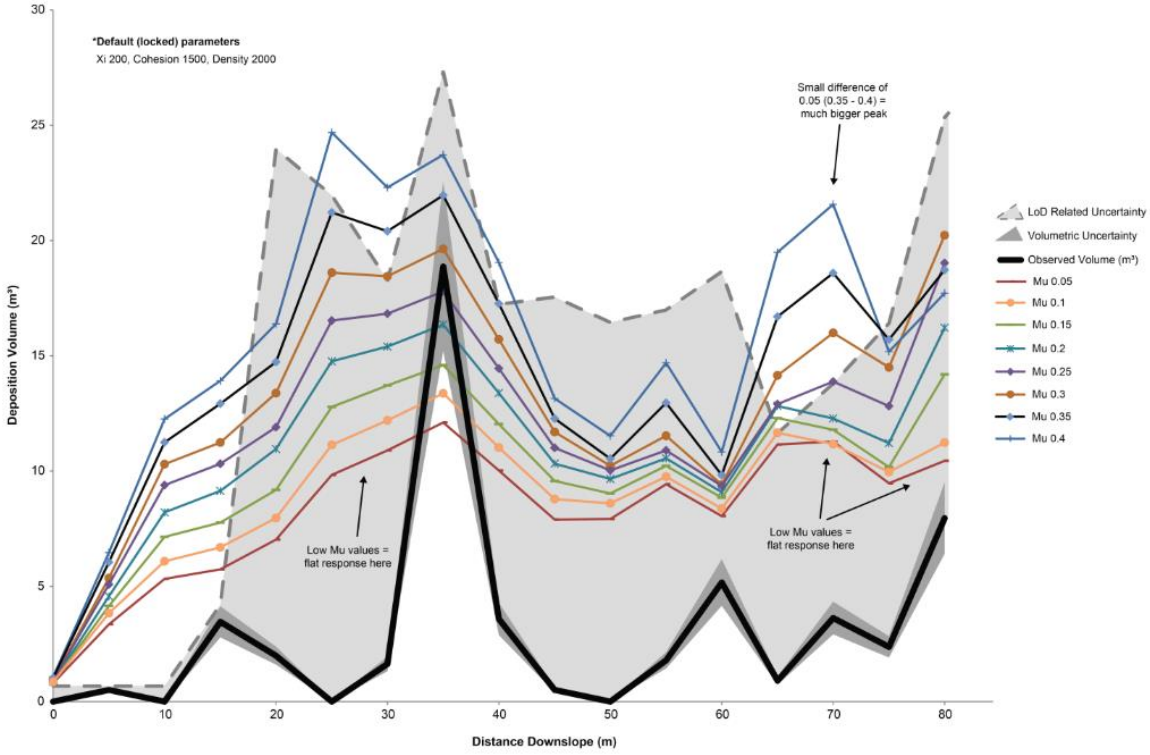

Figure 4.12 – The results of the iteration 1 back-analysis where only Mu values have been changed

Of all the first iteration models, the one with default parameters and a cohesion value of 900 Pa was found to best correlate with the observation curve (coefficient of + 0.533). This set of parameters however resulted in far too much deposition over the 80 m observation range. The slightly lower cohesion value of 600 Pa was thus considered the best best option. An Xi value of 400 m/s^2 and an Mu value of 0.35 were considered to yield the most satisfactory results at this stage. The optimal parameter combination carried forward from iteration 1 are summarised in table 4.4.

Table 4.4 - The combination of parameters carried forward from iteration 1 of the SDLS2 back-analysis and a summary of the justificaitn behind their selection

Parameter	Value	Summary
Mu	0.35	▪ An Mu value of 0.35 best replicated variation in the peak at X = 20-30 m (i.e. larger right peak, with some longitudinal variation; compared to other models which show a flat response). ▪ An Mu value of 0.4 resulted in too large of a peak at X = 25 m and X = 70 m. ▪ RAMMS-DF was found to be least sensitive to the Mu parameter during sensitivity analysis. A value of 0.35, which is towards the upper end of the realistic range, was initially chosen based upon the approximation equation *tan(32°)* and the upper limit both recommended by (Bartelt *et al.*, 2017).
Xi	400	▪ Xi values in excess of 300 m/s² were found to provide the best fit with the major deposition peak at X = 35 m. ▪ Xi values of 400 – 500 m/s² resulted in the best model performance, in terms of replicating a peak at X = 70 m.
Cohesion	600	▪ A cohesion value of 300 Pa resulted in far too little deposition, particularly at peaks in the monitoring data. ▪ Cohesion values of 1200, 1500 and 1800 Pa resulted in deposition beyond the LoD uncertainty range, particularly at X = 70 m, as well as excessive deposition within the source area. ▪ Cohesion values of 600 and 900 Pa were best, with the former model allowing material to reach the gully and catch net downslope.

Iteration 2: Back analysis Refinement

The parameter values in table 4.4 were used as a basis for the second iteration of back-analysis. Figure 4.13 shows all of the results of the second iteration of back-analysis. These model outputs were initially carried out in a methodical manner. The first four models (ordered from top to bottom in the figure key) were conducted to establish which Xi value would result in the model best matching the monitoring data, as the Xi parameter was identified to be the most influential in affecting the deposition morphology during sensitivity analysis. These were combined with a cohesion value of 600 Pa, identified as the optimal value during iteration 1.

The first model run (Xi = 400 m/s^2) was found to yield the greatest variation in deposition volume, between the 15 m mark and 35 m mark, thus best matching that of the observation data. An Xi value of 500 m/s^2 also demonstrated a good fit with that of the observation data. Further downslope, at a distance of 50 – 55 m, this trend continues with Xi values of 600 and 700 m/s^2 showing less volumetric variation, unlike the observation data. At a distance of 70 m downslope, only Xi values of 500 and 600 m/s^2 show kinks in their distribution lines, demonstrating some level of variation, like that in the monitoring data.

It was considered that a different combination of input parameters could yield the same optimal output results (parameter equifinality). Contrasting parameter combinations were therefore tested following models 1-4, these informed by the sensitivity analysis to ensure similar runout distances were achieved. Subsequent parameter combinations in figure 4.13 were therefore more experimental. Models (5-8) were for example conducted to test higher Xi values. The cohesion parameter was varied in some of these models, in an attempt to change the volume of net deposition. Model 13 (Xi = 700 m/s^2, Mu = 0.25, Cohesion = 900 Pa) yielded a similar quantity of deposition to the first four models, but with a much different set of parameters. The deposition distribution from this model was less satisfactory however, particularly early in the model, close to the source area, where greater deposition occurs, and at a distance of 35 m where the peak of deposition, and variation in the line is subdued. Additional model runs, beyond those shown in figure 4.13, were also tested, however did not outperform the existing models. All of the models were considered to be offset from the observation data, however this was clearly skewed by the large deposition peak at X = 35 m.

Model diffusion resulted in greater deposition within neighbouring 5 m bins, resulting in a poor fit between the models and observation data. In an attempt to improve interpretation, the 5 m bins were averaged and re-plotted to a 15 m convention, the result of which is shown

in figure 4.14. In this, the models appear to better match the observation data, within the bounds of the LoD threshold. The parameters used in models 1-4 were considered some of the best combinations, for their closer volumetric fit with large deposition peaks and general longitudinal appearance with the observation data. Figure 4.15 shows the raster outputs from what are considered to be the most optimal parameter combinations for SDLS2 (namely moderls 1-6). Xi values of 400 and 500 m/s^2 are considered to be the best of these, with greater clusters of deposition above the LoD threshold (despite the aforementioned tendency of the model to simulate deposition spreading, perhaps due to the limitations of a DEM or numerical diffusion i.e. Bartelt *et al.*, 2017).

Realistic gully deposition could not be judged due to TLS change detection occlusion and attenuation and a lack of observation data to compare with the model outputs. Estimation of deposition in the downslope net was possible however, to which the model outputs could be compared to further constrain the back-analysis. Figure 4.16 shows that nine models deposited less than 60 m^3, close to the estimated 29 m^3 of actual deposition estimated to have been retained in the net. The remaining 21 models deposited around 100 m^3 within the nets, far exceeding the estimated volume of net deposition. Models 1-4, identified as the most optimal parameter combinations, deposited less than 29 m^3. This was a desirable result, as the model did not account for entrainment or increased runout potential owing to mixing with stream water. As such, model 1 of iteration 2 was selected as the most optimal parameter combination, of which Table 4.5 summarises the respective parameter values.

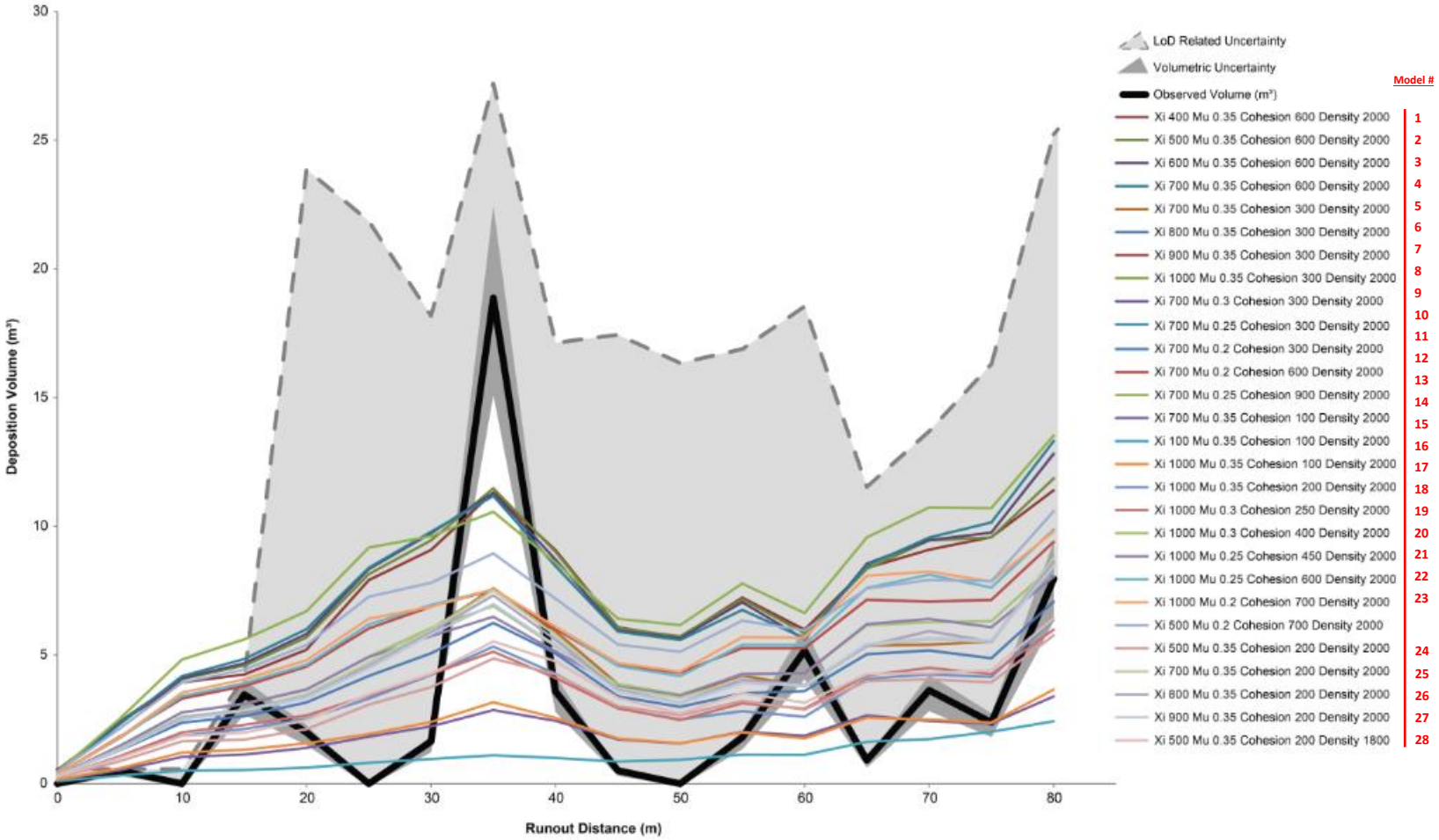

Figure 4.13 - The results of the back-analysis iteration 2. Closer agreement of lines demonstrates the smaller range of cohesion values used; cohesion was previously found to be the most sensitive parameter.

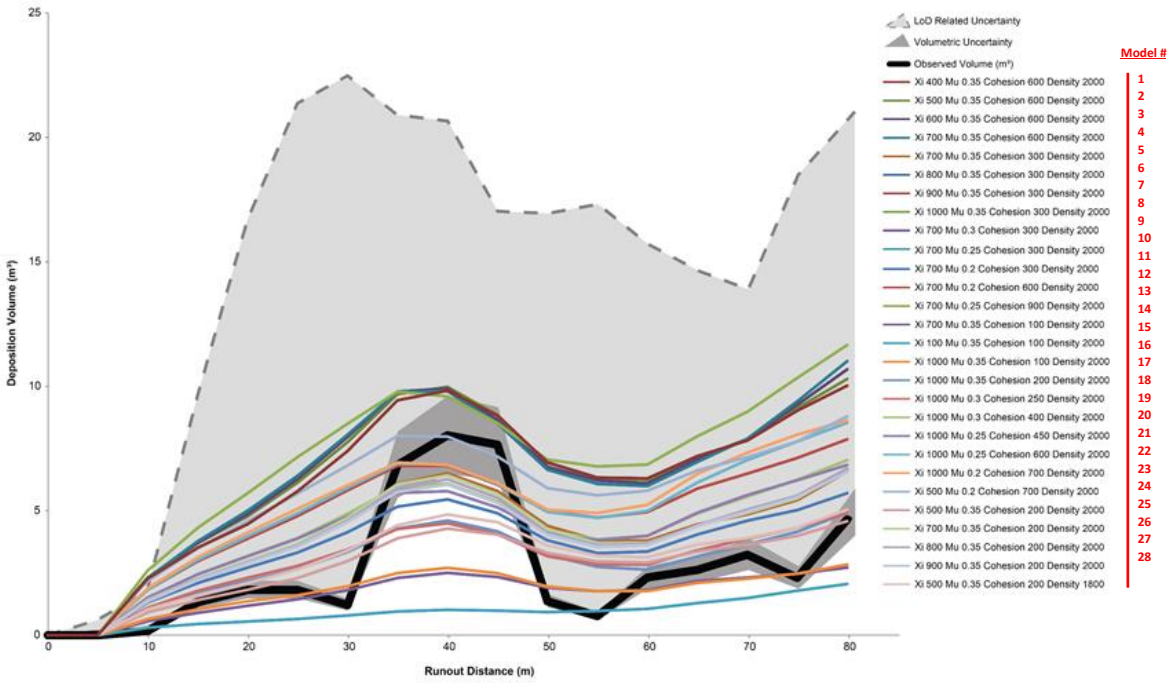

Figure 4.14 - Iteration 2 model results, averaged over the width of three 5 m bins (15 m) to demonstrate how model diffusion (spreading) affects the results, particularly around the peak at X = 40 m.

Table 4.5 - The optimal parameters identified for simulation of the SDLS2 debris flow event

Parameter:	Mu	Xi	Cohesion
	0.35	400	600

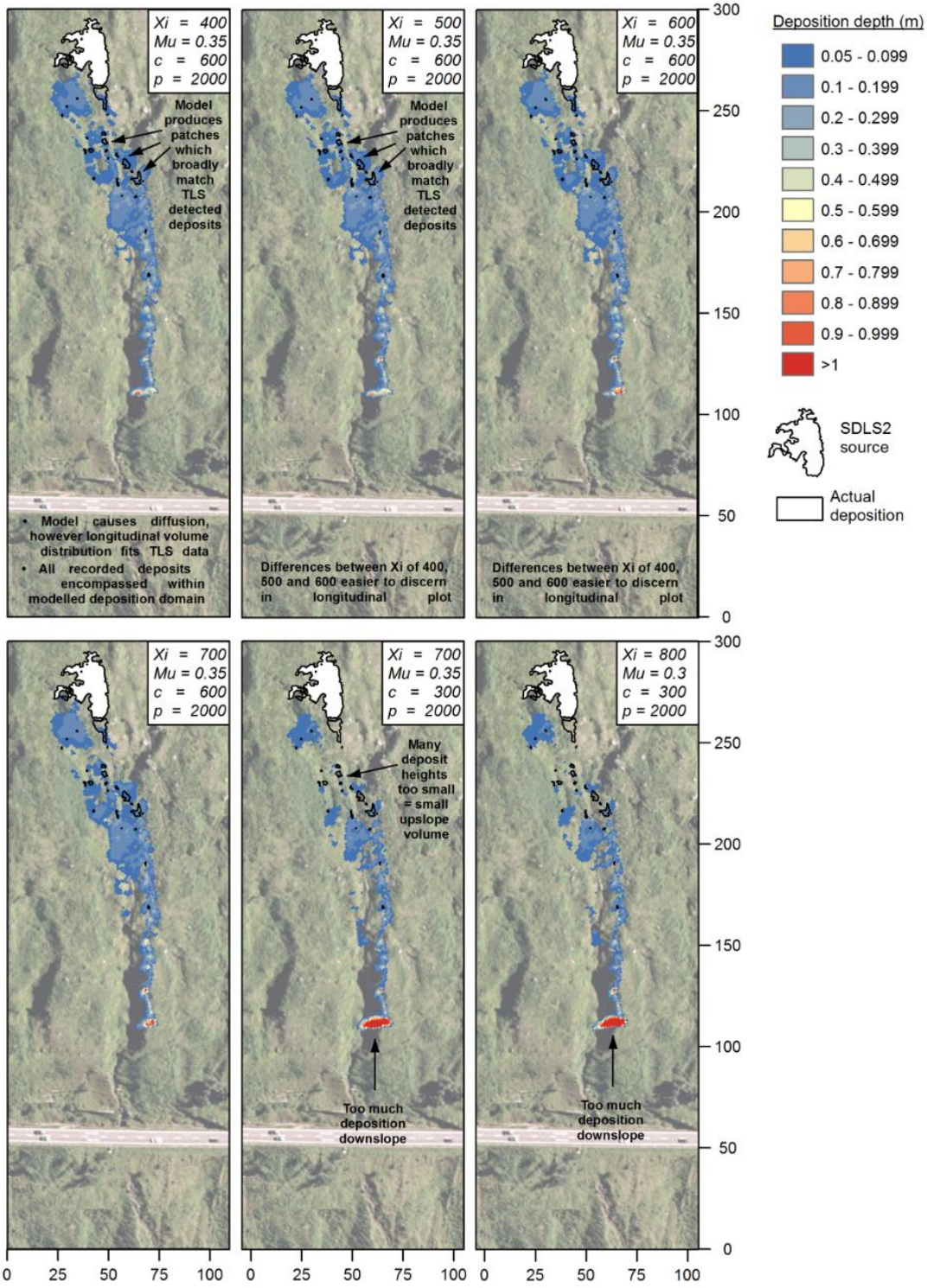

Figure 4.15 - The best performing models from iteration 2 of the SDLS2 back-analysis. Differences are hard to discern by visual means alone and so the longitudinal deposition distributions (binning) are best at this stage.

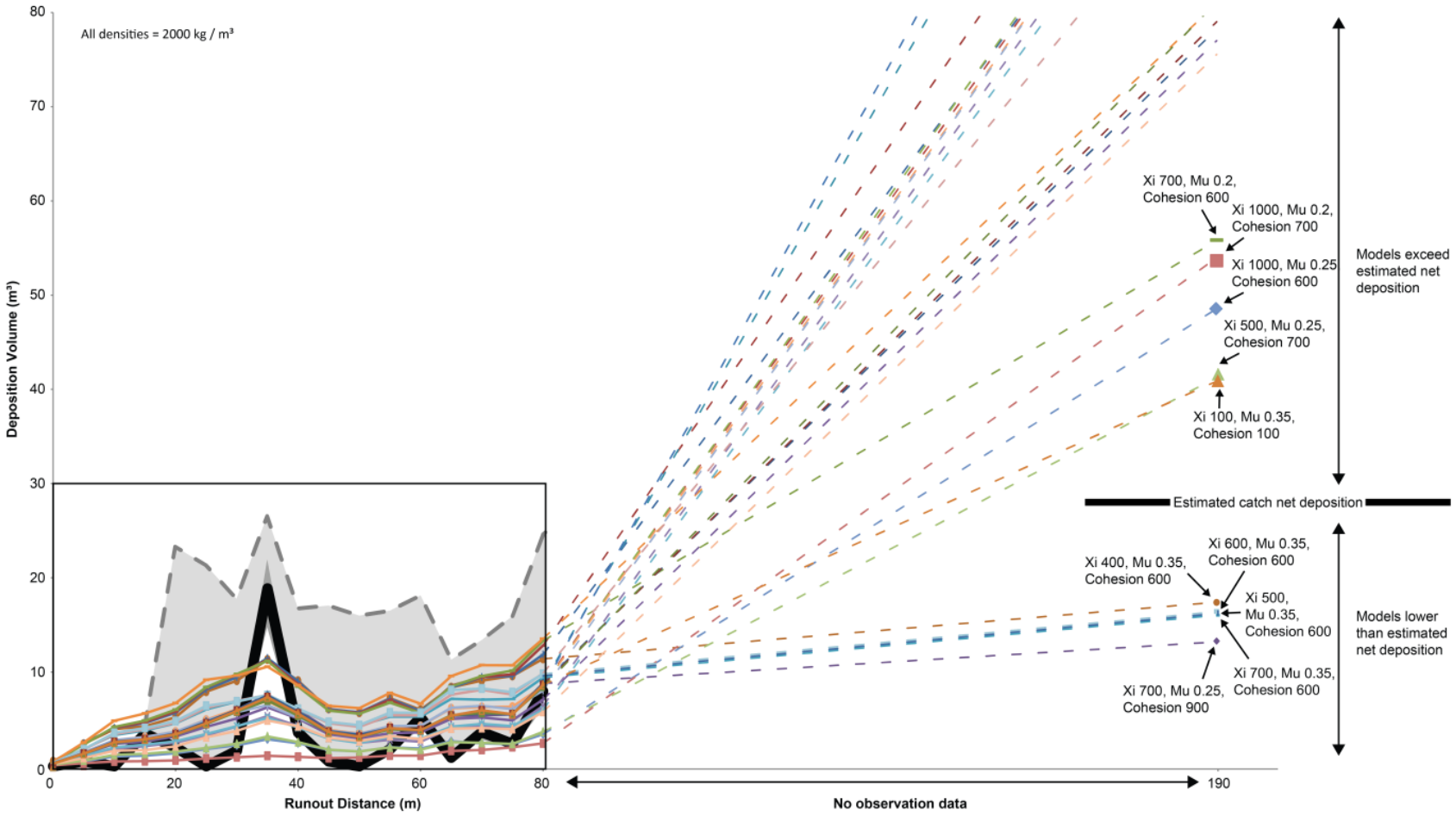

Figure 4.16 - The iteration 2 back-analysis results with deposition volumes from the models sampled behind the phase 1 flow net. Only five models deposited volumes less than that estimated within the net, whilst five additional models deposited greater volumes, within a realistic range of the estimated volume. The remaining 21 models deposited unrealistically large volumes within the net.

SFLS1 Event

The SFLS1 debris flow was further back analysed, for comparison with parameters derived for SDLS1 and an appreciation of rheological variance and model applicability, for runout potential and vulnerability analysis for example. The range of initial values for this event were restricted, based upon the realistic value ranges found for the SDLS1 event.

Iteration 1

Figure 4.17 shows the longitudinal deposition distribution results from the SFLS1 back-analysis. The cohesion parameter has been varied within a smaller range (300 – 1,000 Pa), resulting in a smaller range of variation between the different models than during iteration 1 of the SDLS2 back-analysis. The Mu parameter was also only varied upwards of 0.15, due to low values being ineffective. Xi parameters were varied the same as during iteration 1 for SDLS2 (i.e. Xi 100 – 1,000) as this parameter was particularly influential.

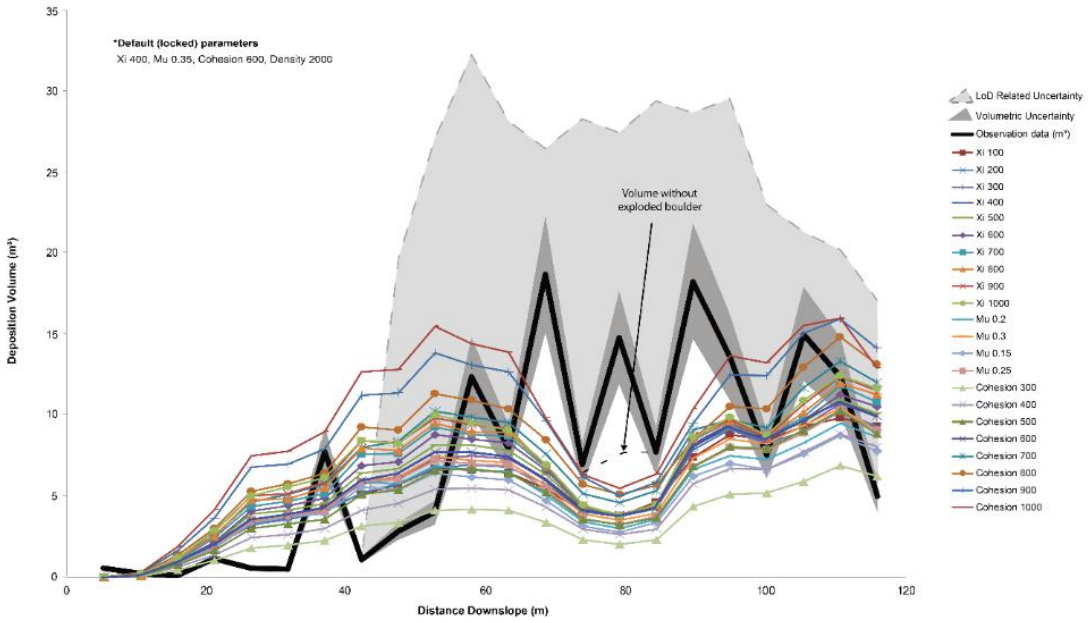

Figure 4.17 - Results from the back-analysis model runs for the SFLS1 event. Data Are binned to a regular 5 m longitudinal spacing, orientated parallel to the direction of runout. the black line represents tls data binned using the same approach.

There are six prominent peaks in the observation data, whilst the model outputs contain four peaks at most. It is worth noting however, that the fourth peak in the observation data, at a downslope distance of X = 80 m, represents a large boulder which was not moved by the SFLS1 debris flow, but which was instead shifted and broken up using explosives as part of hazard mitigation works. The observation data, relating to the 'flow' event, therefore

effectively contains five peaks. When accounting for this boulder related peak, the model results better fit the observation data (the curve without the boulder movement is marked on figure 4.17).

The cohesion parameter was again responsible for the largest source of model variability, with the lowest line representing a value of 300 Pa and the highest line representing a value of 1000 Pa. Values between 300 Pa and 700 Pa resulted in overall deposition volumes below that of the observation data (159 m^3). A value of 800 Pa meanwhile resulted in deposition of 155 m^3, similar to that of the observation data. The 159 m^3 of observed deposition does not account for the range of LoD uncertainty however. Lower cohesion values appear to result in longitudinal deposition distributions with less volumetric variation (peaks and troughs).

Figure 4.18 shows the raster outputs from the models where cohesion has been varied between 300 Pa and 800 Pa. Values between 300 Pa and 500 Pa, in particular, can be seen to not deposit much immediately downslope of the source area (~220 m on the vertical scale). Values of 600 Pa and 700 Pa do promote deposition immediately downslope of the source area, in the same areas as the observation data, however the heights of deposition are generally below 0.1 m. At this point, model outputs can be seen to totally encompass the observation data with very few patches of detected deposition falling outside of the modelled runout domains. A value of 800 Pa also promotes deposition in these areas, with discrete patches beginning to yield heights of 0.1 – 0.19 m, closer to that of the LoD range. Cohesion values of 900 Pa and 1000 Pa led to deposition volumes exceeding the observation data at distances of 40 - 65 m and 95 - 115 m, however the rest of the modelled deposition distribution falls below that of the observation data. The overall deposition volumes of these models are 182 m^3 and 196 m^3 respectively, both exceeding that of the observation data, but falling within the range of LoD uncertainty. Figure 4.19 shows the output rasters from models with cohesion values of 900 Pa and 1,000 Pa. Deposit heights begin to exceed 0.2 m, close to that of the LoD threshold. The observation data (polygons of deposition) were detected due to their heights also exceeding this threshold and so at this stage the modelled flow heights begin to match that of the observation data. The higher cohesion values also result in longitudinal deposition distributions in which the relief better matches that of the observation data.

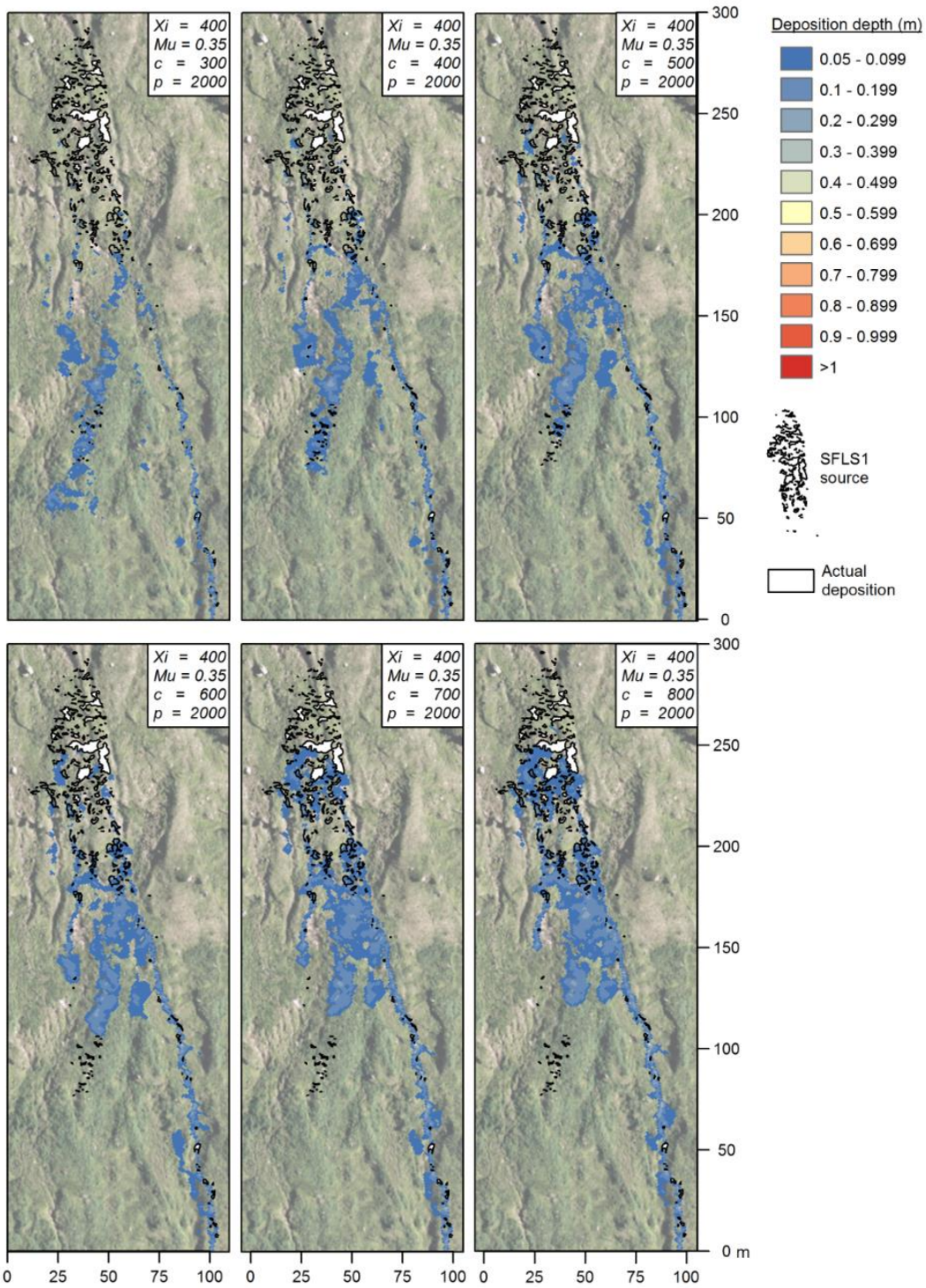

Figure 4.18 - Results from the SFLS1 back-analysis, where only the cohesion parameter has been varied from that of the default parameters (1 of 2)

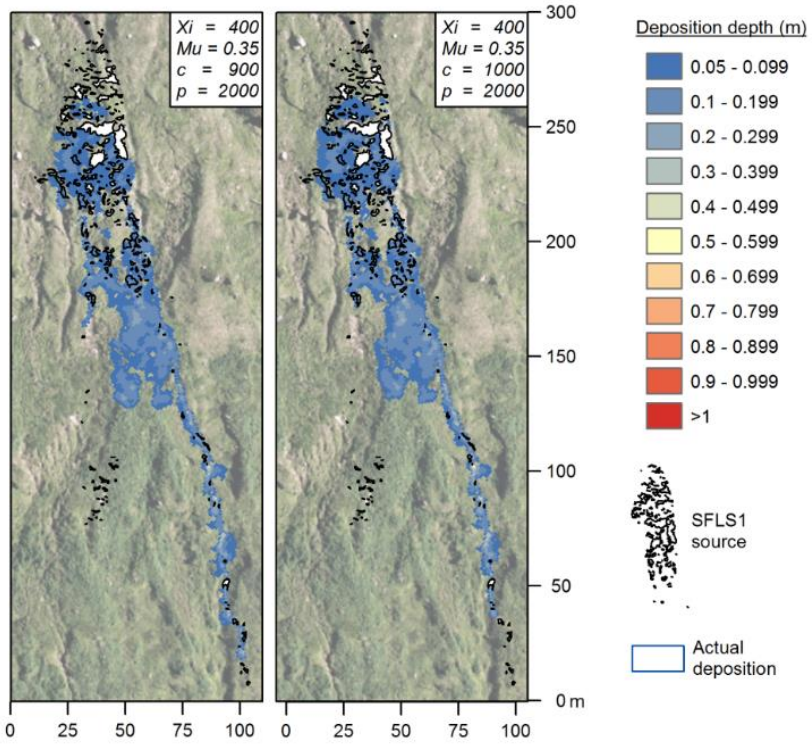

Figure 4.19 - Results from the SFLS1 back-analysis, where only the cohesion parameter has been varied from that of the default parameters (2 of 2)

Figure 4.20 shows a plot of the longitudinal deposition distributions for models relating to the Xi parameter only. Small differences in deposition volumes can be seen. Low Xi values, particularly of 100 and 200 m/s^2, result in flat lines with limited volumetric variation, unlike that of the observation data. Xi values from 300 m/s^2 and upwards begin to introduce greater volumetric variation, although differences are very difficult to discern in the runout raster datasets (these are therefore only provided later in appendix 2). Figure 4.21 shows a plot of the longitudinal deposition distributions for models relating to the Mu parameter only. Changes in the Mu parameter did not appear to correspond to a change longitudinal volumetric variation. Increases in the Mu value only increased the deposition volumes, particularly from a downslope distance of 45 m and onwards. An Mu value of 0.35 was therefore again favoured, particularly due to the low sensitivity of the model to this parameter. The optimal parameter combination carried forward from iteration 1 is summarised in table 4.6.

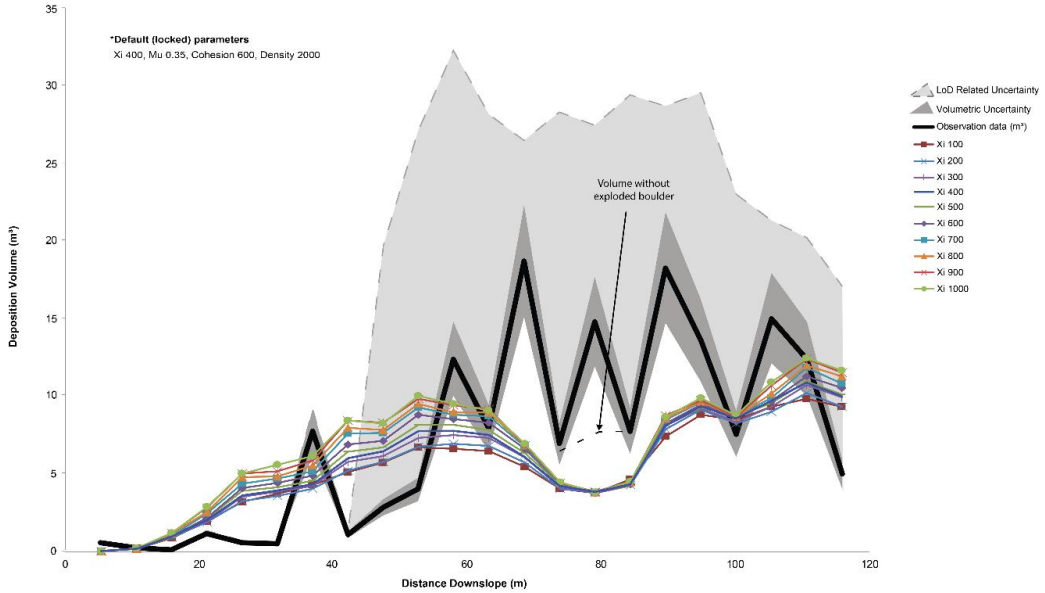

Figure 4.20 – Results from iteration 1 of the back-analysis, from which only models with changes in the Xi values are shown. Higher Xi values show greater variations in the deposition distribution, or peaks and troughs

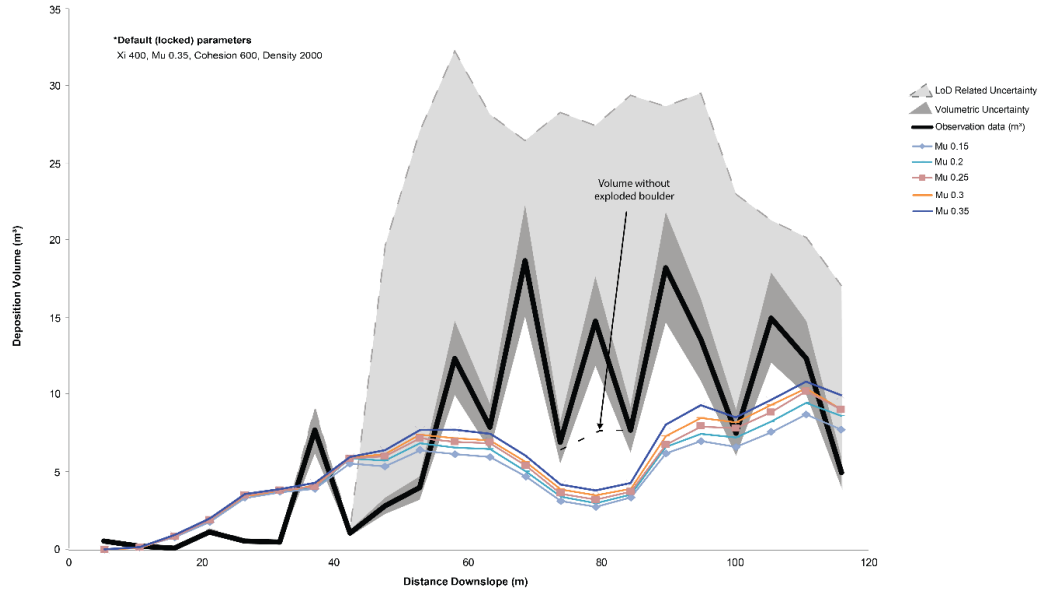

Figure 4.21 - Results from iteration 1 of the back-analysis, from which only models with changes in the Mu values are shown.

Table 4.6 - The combination of parameters carried forward from iteration 1 of the SFLS1 back-analysis and a summary of the justification behind their selection

Parameter	Value	Summary
Mu	0.35	▪ Little variation between changes in Mu, other than overall volume of deposition within plot ▪ RAMMS-DF was found to be least sensitive to the Mu parameter during sensitivity analysis. A value of 0.35, which is towards the upper end of the realistic range, was initially chosen based upon the approximation equation *tan(32°)* and the upper limit both recommended by (Bartelt *et al.*, 2017).
Xi	300 – 900	▪ Low Xi values resulted in longitudinal deposition distributions with very little volumetric variation, unlike that of the observation data. Low values of 100 and 200 m/s² were therefore ruled out. ▪ An Xi value of 1,000 m/s² was tentatively ruled out, due to its unreliable behaviour during sensitivity analysis. It was however carried through to iteration 2 for further testing as it did not perform _ during iteration 1. ▪ Xi values between 300 – 900 m/s² all performed okay during iteration 1, albeit with a lower default cohesion value of 600 Pa during iteration 1. These introduced some volumetric variation, akin to the observation data. These were all still under consideration, and were carried forward to iteration 2 for testing with a larger cohesion value.
Cohesion	900 – 1,000	▪ Cohesion values of 300 – 700 Pa particularly failed to replicate the detected deposition volumes and were therefore ruled out. ▪ Higher cohesion values of 900 – 1,000 Pa resulted in deposition which began to match the observation data (depths above the TLS LoD), whilst still enabling material to enter the gully.

Iteration 2 – Back analysis refinement

The parameter range shown in table 4.6 offered the best combination of values to replicate the observation data, and so these were used as a basis for the second iteration of back-analysis. Figure 4.22 shows the results of the second iteration of back analysis. In this, Xi values have been varied between 300-900 m/s² for both cohesion values of 900 and 1,000 Pa. All of the models again over-estimate deposition in the early stages of runout. All models result in greater total deposition than the observation data, with a cohesion value of 900 Pa resulting in 30 – 50 m^3 more deposition and a value of 1000 Pa resulting in 45 – 60 m^3 more deposition. Cohesion values of 900 Pa and 1000 Pa also resulted in approximately 200 m^3 mobilising into or close to the gully, thus having the potential to reach the A83 where the actual SFLS1 event was known to propagate down to.

Whilst the actual observed deposition decreases slightly from 25 – 30 m downslope, most of the models simulate an increase at the same distance. The model with an Xi value of 400 m/s^2 (regardless of cohesion value) is the only one to not simulate a rise in deposition between 25 – 30 m. Xi values of 300 and 400 m/s^2 (cohesion value of 900 Pa) intersect the observation data at a distance of 35 m downslope, whilst all other models exceed the observed deposition volume. At a distance of 40 – 45m downslope, most of the models simulate a reduction in deposition, whilst the observation data show an increase in deposition over the same range. An Xi value of 400 m/s^2 most closely matches the observation data again, simulating a slight increase in deposition over the 40 - 45 m distance downslope. At a distance of 100 m downslope, Xi values of between 300 and 500 m/s^2 (regardless of the cohesion value), best simulate the drop in deposition volume between two peaks, whilst all other models fail to simulate this.

Figure 4.23 shows the same results averaged over three 5 m bins and therefore replotted to a 15 m convention. A cohesion value of 900 Pa is generally found to best match that of the observation data, although it is noted that this does not fully account for the large uncertainity related to the TLS LoD. Figure 4.24 shows the same results, although only low and high Xi values combined with a cohesion value of 900 Pa. In this, the lower Xi values are shown to best correspond with the observation data, with regards to absolute differences between the peak and low deposition volumes (Xi of 300 and 400 contains the deposition volumes within a smaller volumetric range, more akin to the observation data than Xi values of 900 and 1,000). Overall, the parameter values summarised in table 4.7, and shown in figure 4.25, were found to best replicate the SFLS1 event.

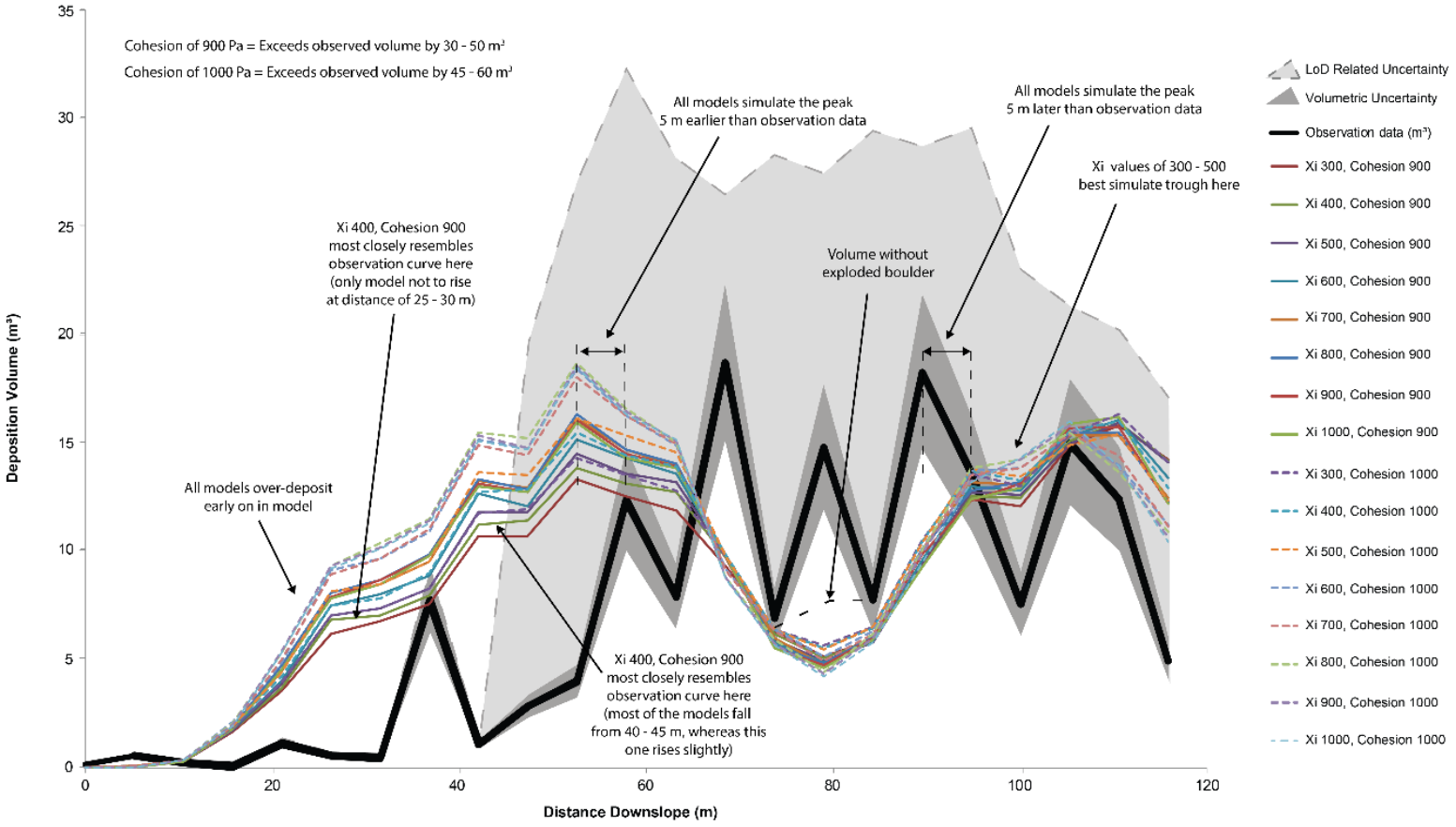

Figure 4.22 - Results from iteration 2 of the SFLS1 back-analysis in which the parameter ranges shown in table 4.6 (optimal parameters from iteration 1) have been tested

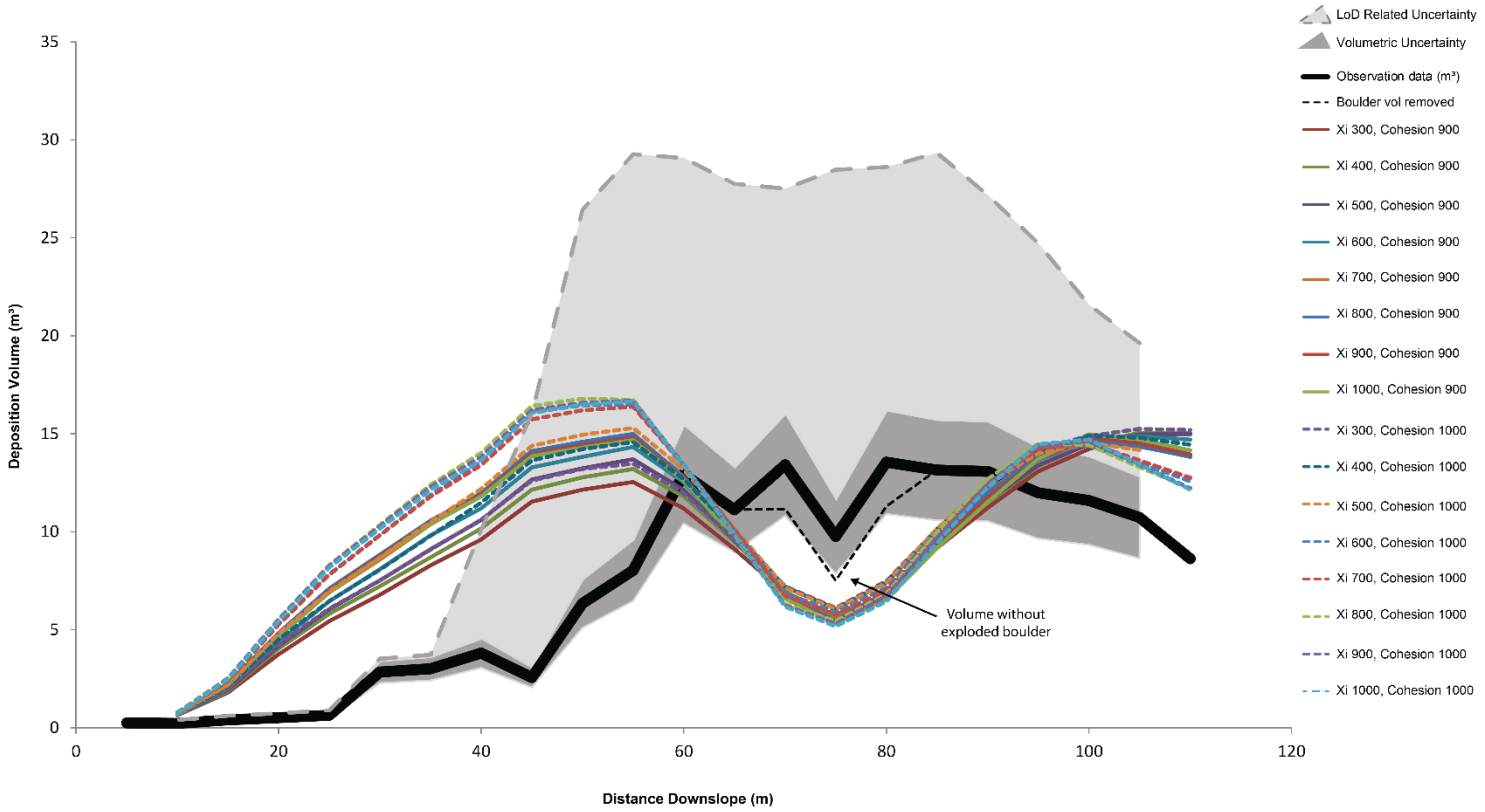

Figure 4.23 - Iteration 2 model results, averaged over the width of three 5 m bins (15 m). In this case, the model clearly deposits material some 15 m earlier than in reality (X = 45 m as opposed to X = 60 m). At the furthest extent of the plot (X = 95 m) deposition clearly occurs later than that in realitywhere the onset is at X = 80 m. Overall, an Xi value of 400 is most satisfactory, as this exhibits the lowest peak of deposition at X = 45 m, closer to that in the observation data, but also exhibits some of the highest

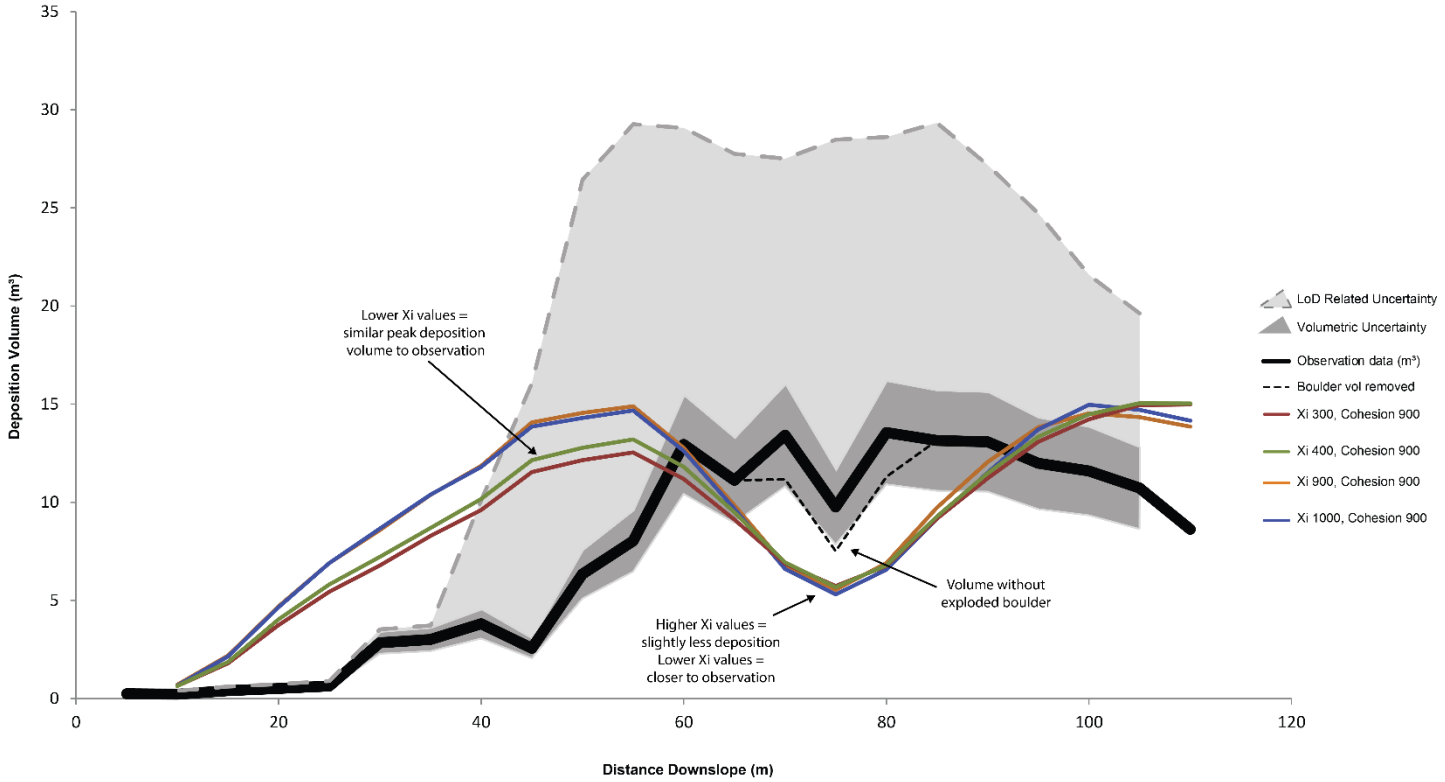

Figure 4.24 - Iteration 2 model results, averaged over the width of three 5 m bins (15 m).In this version, only low and high Xi values are shown for comparison. The lowest values can be seen to be in greater agreement with the observation data volumes, albeit with longitudinal offsets.

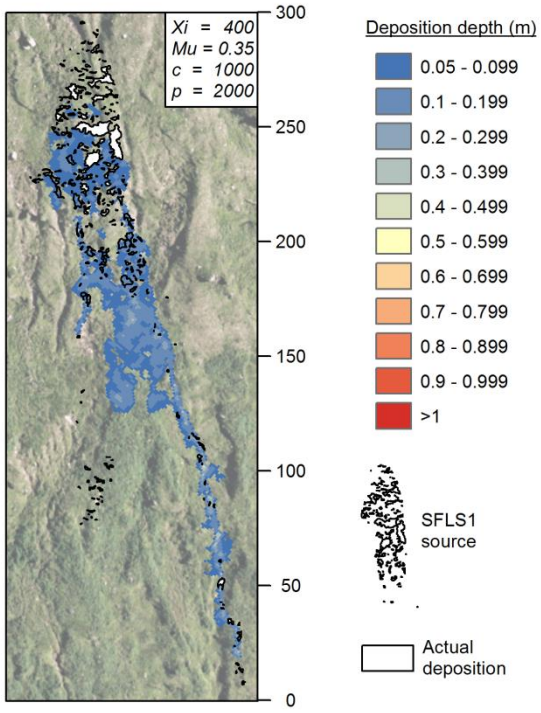

Figure 4.25 - The most optimal modelled runout (Xi 400, Mu 0.35, Cohesion 900, Density 2000)

Table 4.7 - The optimal parameters identified for simulation of the SDLS2 debris flow event

Parameter:	Mu	Xi	Cohesion
	0.35	400	900

Independent validation event

The June 2012 open-hillslope debris flow was modelled with both sets of optimal parameters found earlier in section 4.3.2.1, these including an Mu value of 0.35 and an Xi value of 400 m/s^2. Cohesion values were varied, with values of 300, 600 (SDLS2), 900 (SFLS1) and 1200 Pa used to test the difference this made to the event's runout

Figure 4.26 shows the results of the models in which the optimal Voellmy parameters, derived from the back-analysis, have been applied to an earlier catalogued event. The runout domain of the model with a cohesion values of 300 Pa (top-left), exceeds the actual digitised deposition by more than 10 m. In contrast, the model with a value of 1,200 Pa (bottom-right) simulates runout approximately 10 m shorter than that of the actual runout distance.

The runout domain of the model with a cohesion value of 600 Pa (top-right) best matches that of the digitised deposition domain, with an excess runout distance of around 1 m. The model, with a value of 900 Pa, also closely matches that of the actual runout distance, although ceases approximately 5 m short of the actual runout distance. The back-analysed parameters from the SDLS2 and SFLS1 events therefore appear to replicate the runout distance of another debris flow, at the same site, with some accuracy. However it is notable that all of the models generally fail to replicate the elongate tongue which stretches a further 8 m downslope. The modelled deposition also spreads more laterally. Effective simulation of this event demonstrates the ability to calibrate the RAMMS-DF model using a longitudinal deposition binning approach, despite the overall runout extent being inhibited.

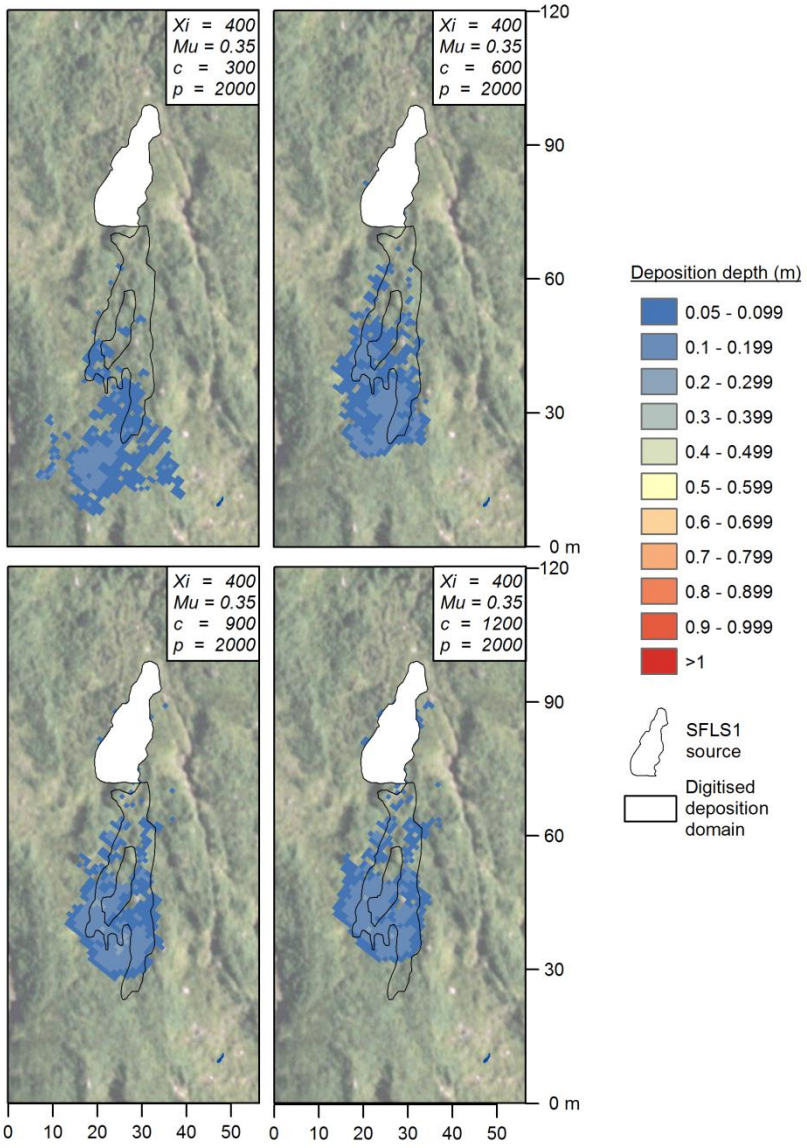

Figure 4.26 – The results of the models in which the optimal back-analysis parameters (Mu of 0.35 and Xi of 400) have been applied to an earlier catalogued hillslope debris flow (June 2012).

4.3.2.2 Discussion

The same Mu and Xi parameters were selected for both the SDLS2 and SFLS1 events, however different cohesion values were required to model both flows, with the SFLS1 event requiring an increase of 300 Pa (900 Pa) relative to that of the SDLS2 event (600 Pa). It is recognised that the back-analysis was a somewhat subjective exercise, and that slightly different parameter combinations may have been deemed optimal by another researcher. That said, a slight change in the more sensitive Xi parameter (± 100 m/s^2), does not appear to significantly affect the runout results and therefore application of the model.

Owing to uncertainty, it is possible that a higher cohesion value would have been effective for modelling the SDLS2 event. These uncertainties relate firstly to the source-proximal LoD threshold. An increase in deposition, proximal to the source area, could be afforded by this uncertainty. An equivalent reduction in deposition downslope within the debris flow catch net would be of no detriment, particularly when considering uncertainty relating to in-channel rheology. It is considered that this LoD uncertainty could be significantly reduced, first by utilising single station scans registered to one another for a reduction in error values, but secondly by not thresholding the data to the same degree, but using more aggressive point cloud cleaning techniques. Although not available at the time of this study, due to the lower density and single return nature of the LMS-Z620 data, more sophisticated echo digitization scanners may enable such an approach in the future. This change to the methodology would likely reduce the subjective nature of back-analysis, through the provision of more defined deposition data which would lend itself to an increased sampling resolution. With more data points, statistical methods of analysis would prove a feasible objective element to the back-analysis process, for instance the utilisation of spatial autocorrelation within ArcMap.

A value of 900 Pa (SFLS1 optimal cohesion) was found to cause excessive deposition during modelling of the SDLS2 event, however a value between 600-900 Pa would also likely prove effective in modelling the flow. This corresponds with the validation model (June 2012) in which a cohesion value slightly higher than 600 Pa would appear to be optimal. Taking this potential uncertainty margin into consideration, any application of the model, to conduct runout potential mapping for example, should focus on the parameters which give-rise to the most mobile flow, thus representing a worst-case scenario.

SDLS1 and SFLS1 demonstrated different depositional behaviour proximal to their sources, for which one common cohesion value could not replicate both events. Further refinement

of the parameter values is unlikely to yield a set of parameters that can model both events. It is important to quantify such variability as this can provide a measure of uncertainty, enabling the continuum model to be applied in a probabilistic manner (Aaron *et al.*, 2016). No other studies are known to have adopted a cohesion value, likely because of the much lower slope angles on which RAMMS-DF has been applied. Addition of the cohesion parameter introduced uncertainty regarding the optimal Mu parameter, because cohesion influenced the runout distance to a greater degree. Bartelt *et al.* (2017) advise an Mu value based upon the tangent of the average slope angle, which proved to be larger for RabT, than an upper advised value of 0.35 / 0.4. A high value within this range (0.35) was maintained, initially to avoid undesired model behaviour which can arise in models when extreme parameter values are adopted. Use of a higher Mu value has since been reconsidered however, on the basis that this can be of benefit (i.e. as demonstrated in a recent study by Frank *et al.*, 2017) without negatively affecting the model results, although this consideration was made after the work presented in this chapter. Assuming runout distances change linearly in relation to Mu changes, the sensitivity analysis suggests that an Mu value of 0.65 would reduce the runout by only around 20 % on a model slope. This reduction in runout would have proved inadequate in promoting adequate source-proximal deposition, necessitating use of a cohesion value regardless of a high Mu value. The cohesion value would likely require compensatory reduction however, to account for an increase in Mu.

Back-analysed rheological parameters can lend insight into the dynamics of a debris flow (Pirulli, 2010). An Xi of 400 m/s^2, suggests a muddy type flow, rather than a granular flow (Bartelt *et al.*, 2017). This is consistent with observations of material downslope, immediately after deposition (BBC, 2014, 2015). An Mu value of 0.35, or higher, falls well beyond the typical range of 0.05 – 0.2 (Quan Luna *et al.*, 2010). This is likely due to the relatively low gradient channel settings within which most runout model studies are conducted.

Although factored, as best possible into the back-analysis, the RAMMS-DF model replicated the hillslope deposition patterns well, but not those in the gullies. For the SFLS1 event, for example, the optimal set of input parameters did not enable material to reach the bottom of the slope. In reality, it is known that material did mobilise to the bottom of the slope, after which some of the mass spilled onto the A83. This poor simulation may relate partially to aforementioned issues with the SFLS1 source area polygon, this leading to too much hillslope deposition. Very small changes in debris flow water content (1-2 %), however, are also known to have a marked effect on flow runout distances (Hurimann *et al.*, 2015). Gully streamflow could conceivably dilute the flow mass, reducing the flow viscosity and thus also increasing

the runout potential. Different rheological zones may prove effective in accounting for differences between the hillslope flow and channelised flow phases, however different rheological combinations may be required for different events, limiting application of the model for runout potential mapping. Alternatively, one set of rheological values can be used, and results can be directly compared to assess relative runout potential, bearing in mind the limitations of the model. RAMMS-DF also currently employs an erosion, or entrainment, module, although this does not currently enable a different rheology to be specified. Entrained material proximal to streamflow, is itself likely to be saturated and therefore of a different rheology anyway. Entrainment of this material alone can increase runout potential (Iverson *et al.*, 2011). Implementation of a different entrainment rheology may therefore be of benefit to a wide range of studies.

This limitation of RAMMS-DF, and any other continuum model such as MassMov2D (Beguería et al., 2009) or DAN-3D (McDougall and Hungr, 2005), between both the open hillslope and channelized runout stages, limits application of the model for analysing impact pressures at road-level for example. The RAMMS-DF model does however provide input hydrograph functionality (Bartelt *et al.*, 2017), which could be applied exclusively to modelling of channelised runout. Should a gully reach be instrumented, with ultrasonic or visual sensors for example (LaHusen, 2005), it would be possible to appropriately calibrate the input hydrograph based upon flow velocity, depth and volume, enabling application of the model to derive impact pressures, thus better informing catch net design specifications and QRAs.

4.3.3 Exhaustive runout potential modelling

Reasonable agreement of rheological parameters, validated on a third independent debris flow event, suggested that RAMMS-DF could be applied to map relative runout potential at RabT. As previously mentioned, this should take into account the worst-case parameters (i.e. lowest cohesion; SDLS2). Furthermore, RAMMS-DF may only be used in this way if the limitations of the model are considered when interpreting the results. The model for example indicates relative mobility, and thus areas of the slope that could pose more of a hazard than other areas. Quantification of the absolute hazard is beyond the capability of the RAMMS-DF model at this stage.

Owing to computing limitations, RAMMS-DF could not model at a high resolution across large spatial extents. An entire slope TLS derived DEM, at a 1 m resolution or less, for example caused the model to crash. Topographic models were therefore cropped to reduce computational demands. The centre of the slope has exhibited significant activity within

recent years, particularly during the TLS monitoring period, and thus this zone was chosen for testing of the new exhaustive runout potential mapping. It is considered

Given that hazard assessments should account for the largest credible event magnitude (Parry 2016), within an appropriate engineering timeframe, the largest event recorded at RabT (473 m^3 in October 2014) was incorporated into the exhaustive runout potential analysis, in the form of a square idealised source area cell. Modelling was conducted using the best-fit parameters found for the SDLS2 event (summarised in table 4.5), as these yielded the most mobile flow and thus represented a 'worst-case' scenario. A grid of 252 source cells were generated using the Fishnet tool within ArcMap. Each cell measured 20 m wide and 23 m long, the former equivalent to the width of the October 2014 event, and the latter equivalent to the average large debris flow source area at RabT. A cell of these dimensions yielded a source area of 460 m^2, and a volume of 473 m^3 when utilising a 1.03 m source depth (also similar to the October 2014 failiure). The grid of cells were split into individual polygons, which were exported from ArcMap and loaded into a new RAMMS-DF model.

Five batches of 50 models were processed, each batch taking approximately six hours to process using a desktop computer with a 3.4 GHz quad-core processor (i7-4770) and 32 GB of RAM. Maximal Flow Height raster datasets were bulk exported from within RAMMS-DF. The large number of models necessitated automation of result processing, thus the workflow shown in figure 4.27 was developed to convert each raster into a representative flow vector (polyline).

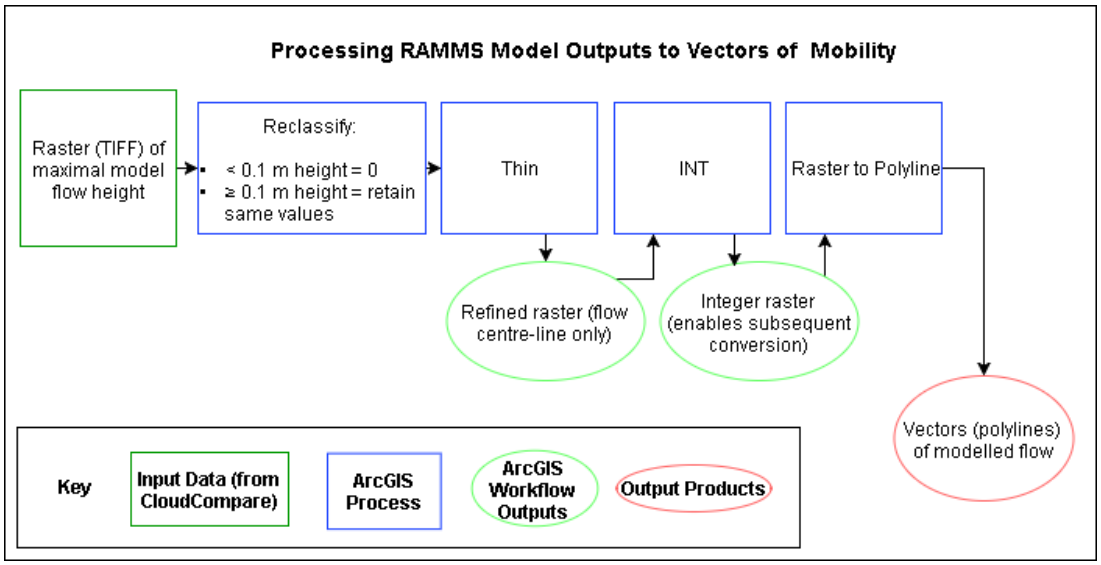

Figure 4.27 - The processing workflow used to convert rasters of maximum flow height into runout vector polylines.

Automation for the high numbers of model runs was achieved using ArcMap's Modelbuilder, to develop a new raster iterator to load in all of the results with just one selection by the user. Raster datasets representing the flow extent were refined using the 'fine' tool in ArcMap, to produce the centreline of each flow. These refined raster datasets were subsequently converted to polylines using the 'raster to polyline' tool and cleaned using the 'Trim line' tool to remove artefacts such as truncate branches. Some vectors were more sinuous than others and contained varying numbers of branches, so a simple calculation of the total line length was not considered to truly represent the flow runout distance. Instead, the longitudinal flow extent of each vector was calculated using bounding boxes ('minimum bounding geometry' tool within ArcMap), the values from which were symbolised on a relative scale. The vectors were subsequently used to compare runout distance with topographic factors. The 1 m resolution slope DEM was converted into a slope angle raster, whilst a 2 m DEM (optimal for this process) was converted into a curvature raster (convergence or divergence perpendicular to the top of the slope). The Zonal Statistics tool was then used to sample the mean of each value for each runout vector polyline. The bands containing the least and most mobile flows (both of which have counts ≤ 5) were omitted from the 'curvature' plot due to the relatively high quantity of raster noise compared to the slope angle raster; hence the requirement for a sufficiently large sample size when calculating a mean value.

4.3.3.1 Results and discussion

Figure 4.28 shows the runout vectors derived from the 252 runout potentila model runs. These have been symbolised using an equal interval colour scale, in which the yellow vectors represent those with the shortest longitudinal runout extent, whilst the red vectors are those with the longest. Of 252 modelled debris flow vectors, 80 reached the road level (31.9 %), 79 (31.5 %) of which were intersected by a digitised catch net, and one model of which (0.4 %) was not. As the analysis was conducted with the worst-case, highest mobility, cohesion value of 600 Pa, it is possible that the flow might not have mobilised onto the carriageway under a different scenario. The benefit of this analysis however, is that this model can be rapidly repeated, to test the quantified level of uncertainty. In this case, the flow still reached the road with the higher cohesion value (900 Pa). This example demonstrates the utility of using one set cohesion value for a 'first look' runout potential assessment, to compare relative mobility across the slope.

Of the debris flow catch nets within the modelled zone, the large P1 net was intersected by the largest number of modelled runout vectors, as seen in table 4.8. The P4 catch nets were intersected by the lowest number of flow vectors (7). This clearly provides an indication that some catch nets may see more use than others. Another metric for this, is the number of runout vectors modelled to intersect each net, normalised per metre length of net. This indicates that the P7 catch net is likely to see the most use and thus affords the most protection to the A83 trunk road. This also suggests that each metre of this structure may be particularly valuable. Furthermore, this may highlight certain nets, or runout zones, that may benefit from reinforcement or being supplemented with additional protection, over others that are less critical. Such analysis helps to demonstrate the value of a mitigation structure, something which Winter (2016) comments is particularly important given that such approaches are cost prohibitive.

Table 4.8 - A breakdown of the debris flow catch nets within the modelled domain and the number of flows intersecting each

Net (net length)	Number of intersecting runout vectors	Runout vectors per metre of net
P1 (65 m)	37	0.57
P7 (32 m)	27	0.85
P8 (43 m)	15	0.35
P4-UPPER (121 m)	3	0.025
P4-LOWER (53 m)	4	0.075

Of the 80 flows modelled to reach the road level, 45 were found to do so via two major gullies. The right-most gully, with the P7 nets at the bottom, is connected to high mobility flows (red vectors) at the very top of the slope. This gully also captures 24 flow vectors. In comparison, the left-most gully, with the P1 net at the bottom, is connected to high mobility flows which begin some 100 m lower down the slope. This gully contains five fewer runout vectors (19). These differences perhaps highlight the more mature and developed state of the right-most (south-east) gully in comparison to that to the left-most (north-west) gully. Should the less developed gully change, then this may represent a more dynamic hazard area.

Analyses of the modelled flow vectors, including use of slope angle and planform convergence rasters, is shown in figure 4.29 and figure 4.30 respectively. Both show that the 151 – 200 m runout distance is most prominent runout distance class with 79 models (31.5 %) falling within this range. The mean runout distance of all the models is 192 m. Only 14 models travel in excess of 300 m, and only five of these travelled in excess of 350 m. The black line in figure 4.29 shows that the mean slope angle for the lowest band of runout distances (50-100 m) is 32.1°, whilst the highest mobility band (351 – 417 m) of flows have a mean slope angle of 35.5°. The flows within the range of 101 – 250 m show no significant difference in mean slope angle. This highlights the potential for a limited number of high gradient tributaries to connect with one another, producing flows of high runout potential, the contributing source areas of which could be further examined for more detailed hazard assessment. The equivalent black line in figure 4.30 demonstrates that the lower mobility flows (101-150 m) mobilise along relatively unconfined regions of the slope. The smallest (50-100 m) and longest bands (351-417 m) of runout distances are omitted from this plot, as

explained in the methodology (small sample size). The degree of curvature increases with each successive increase in runout distance, with equal degrees of confinement for flows between runout distances of 200 – 300 m, but even greater confinement for flows between 301 – 350 m in length. Confinement is known to be an important element of debris flow runout potential (Fannin and Wise, 2001), as also shown by different events presented in the monitoring chapter. This model performance demonstrates that RAMMS-DF is proficient in accounting for such a factor.

In the plot of modelled runout vectors, a clear distinction can be made between open hillslope areas and gully areas, both visible in the backdrop aerial imagery (although this is offset slightly). All five of the most mobile flows, ranging between 350 – 417 m, occur within the left-most gully, the same gully which facilitated the SFLS1 debris flow. The highest mobility flow has a runout distance of 417 m and was found to propagate from a source just 70 m to the north-east, slightly upslope of the SFLS1 source area. The second most mobile flow in this analysis is from a source immediately below this. These flows appear to couple with the same gully into which the SFLS1 event mobilised in December 2015, although the majority of the material reaches the gully in these cases, due to the combination of a confining ridge and a channel which limits flow spreading and branching. In comparison, the SFLS1 event (and modelled flow) spread immediately downslope of the source area, due to a 40 m long area of flat hillslope. Figure 4.28 further highlights that the left hand-side of the modelled slope region is conducive to flow runout diffusion, with this region exclusively containing well dispersed yellow (lowest mobility) flow vectors. This slope region could therefore be considered to pose less of a hazard, if assuming all other conditions (i.e. supply of material) are consistent across the slope. This is likely not the case, however further detailed examination would confirm whether this slope region poses a reduced hazard.

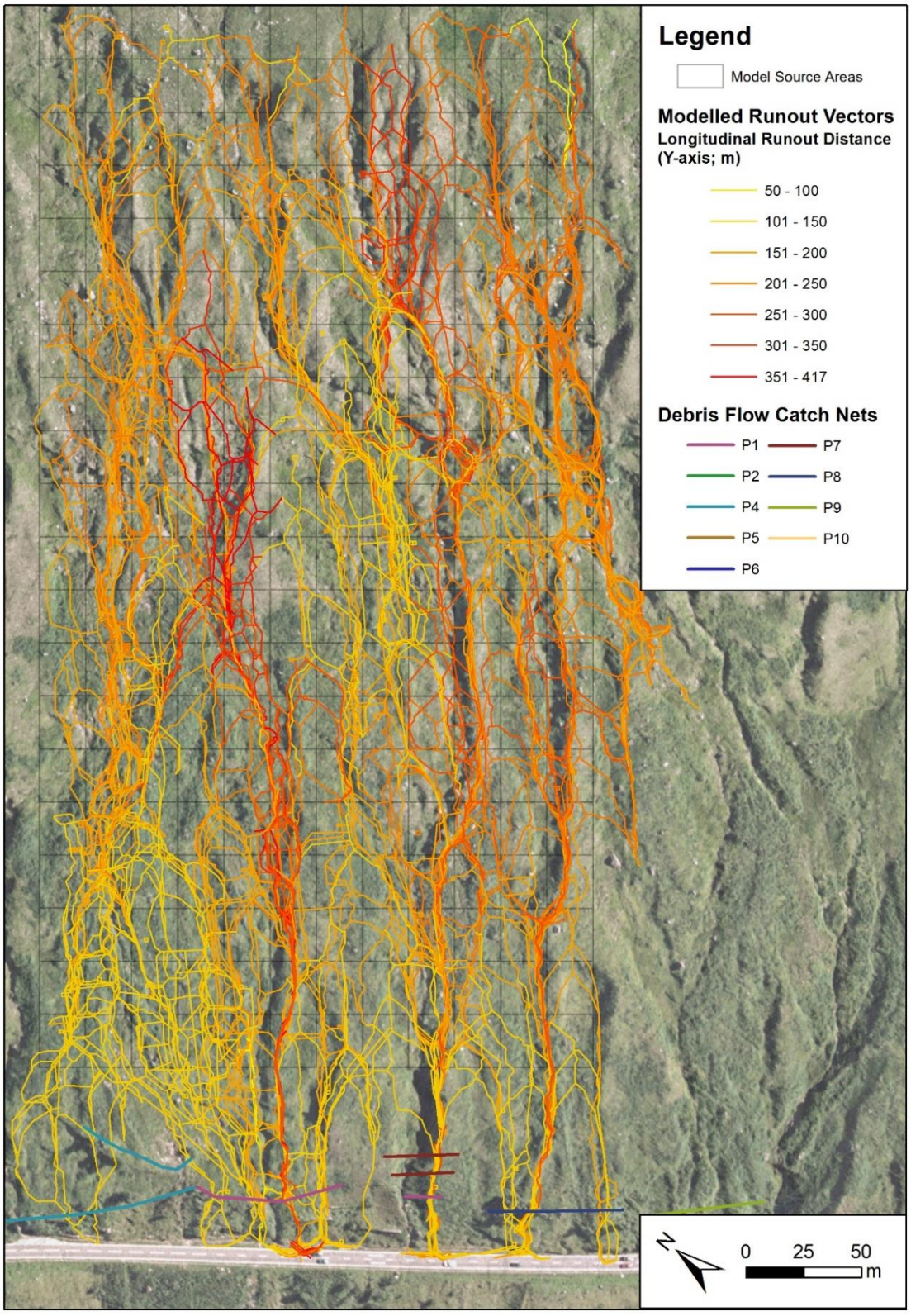

Figure 4.28 – Results of Susceptibility modelling. Modelled runout vectors are displayed, with each line coloured by its respective longitudinal extent.

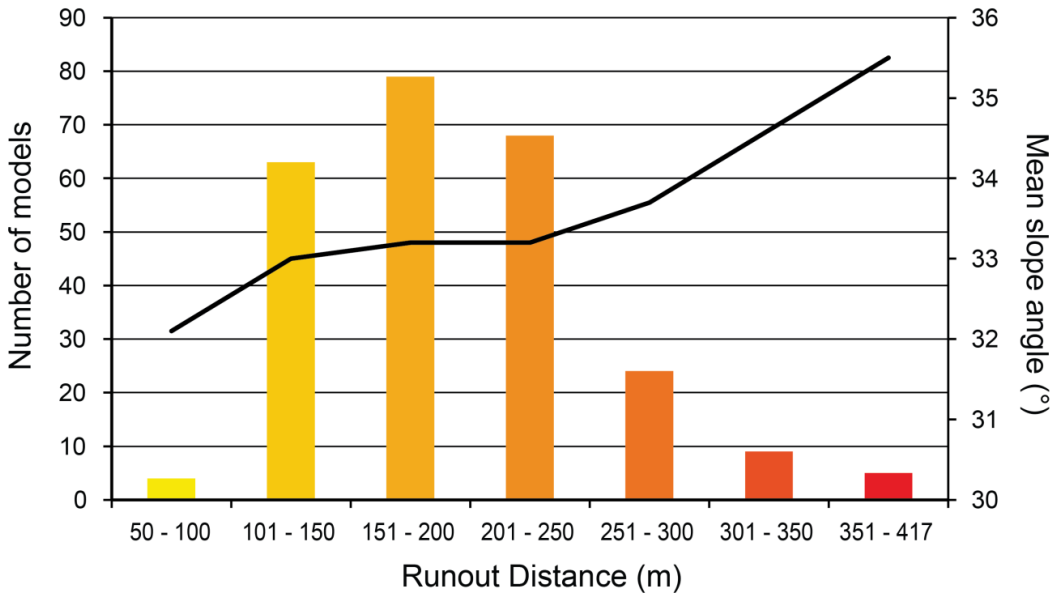

Figure 4.29 – Susceptibility model results by longitudinal runout distance, with the mean slope angle along the runout paths

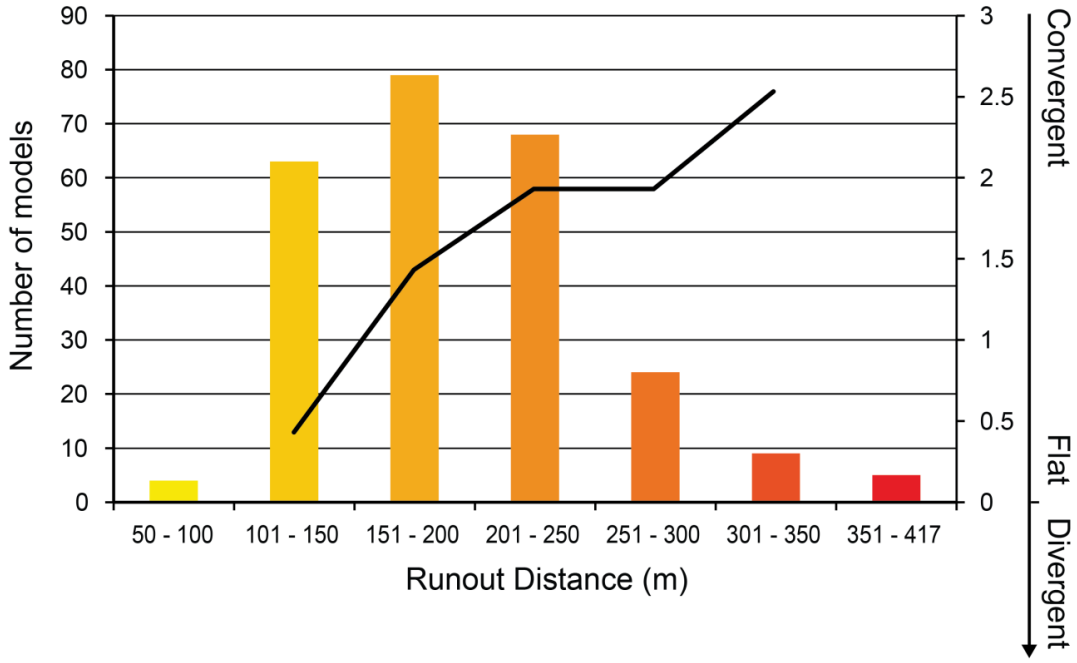

Figure 4.30 – Susceptibility model results by longitudinal runout distance, with a measure of convergence or divergence along the runout paths (Curvature derived from a 2m resolution DEM)

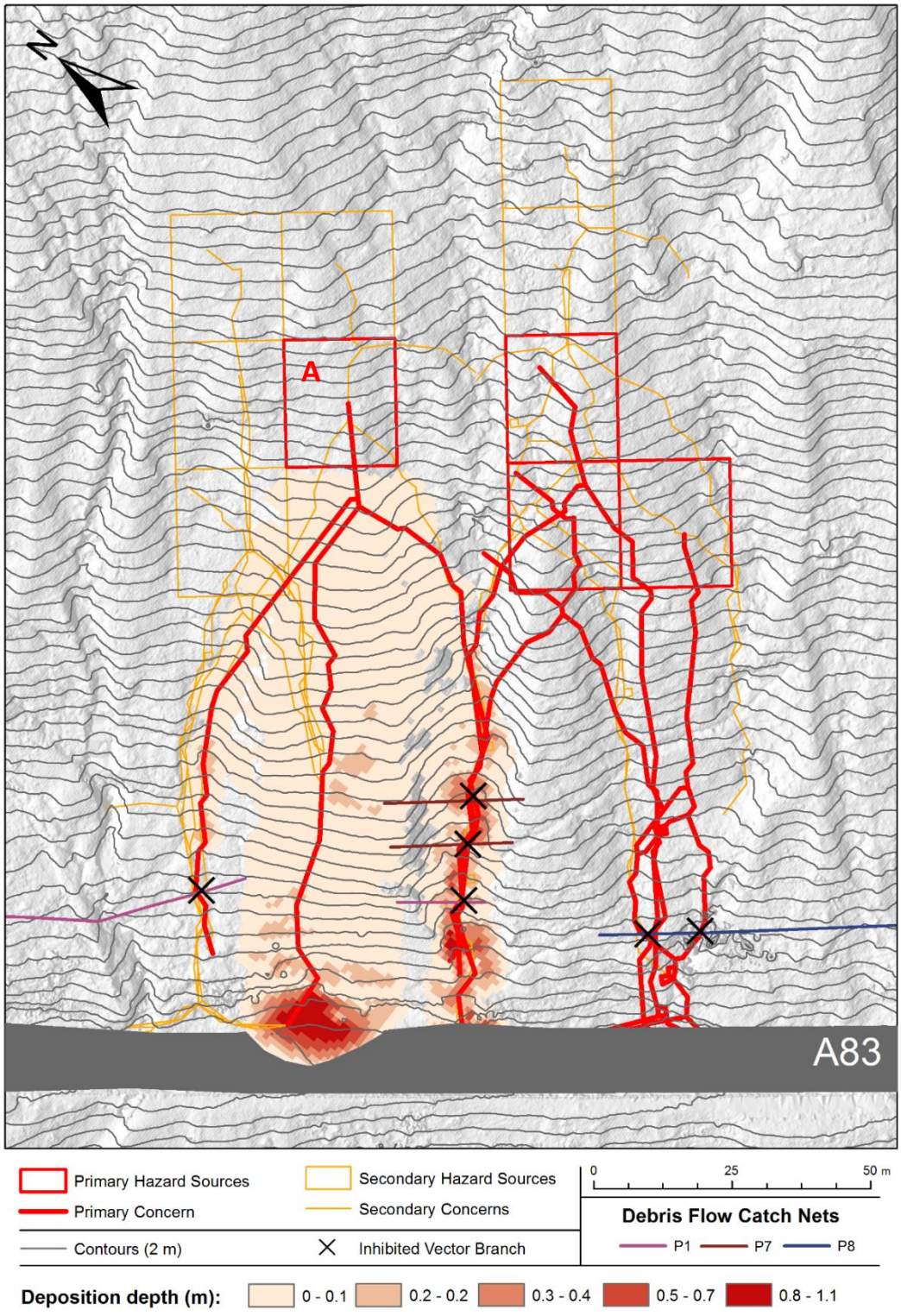

Figure 4.31 - The modelled runout vectors that have been found to circumvent the digitised debris flow catch nets.

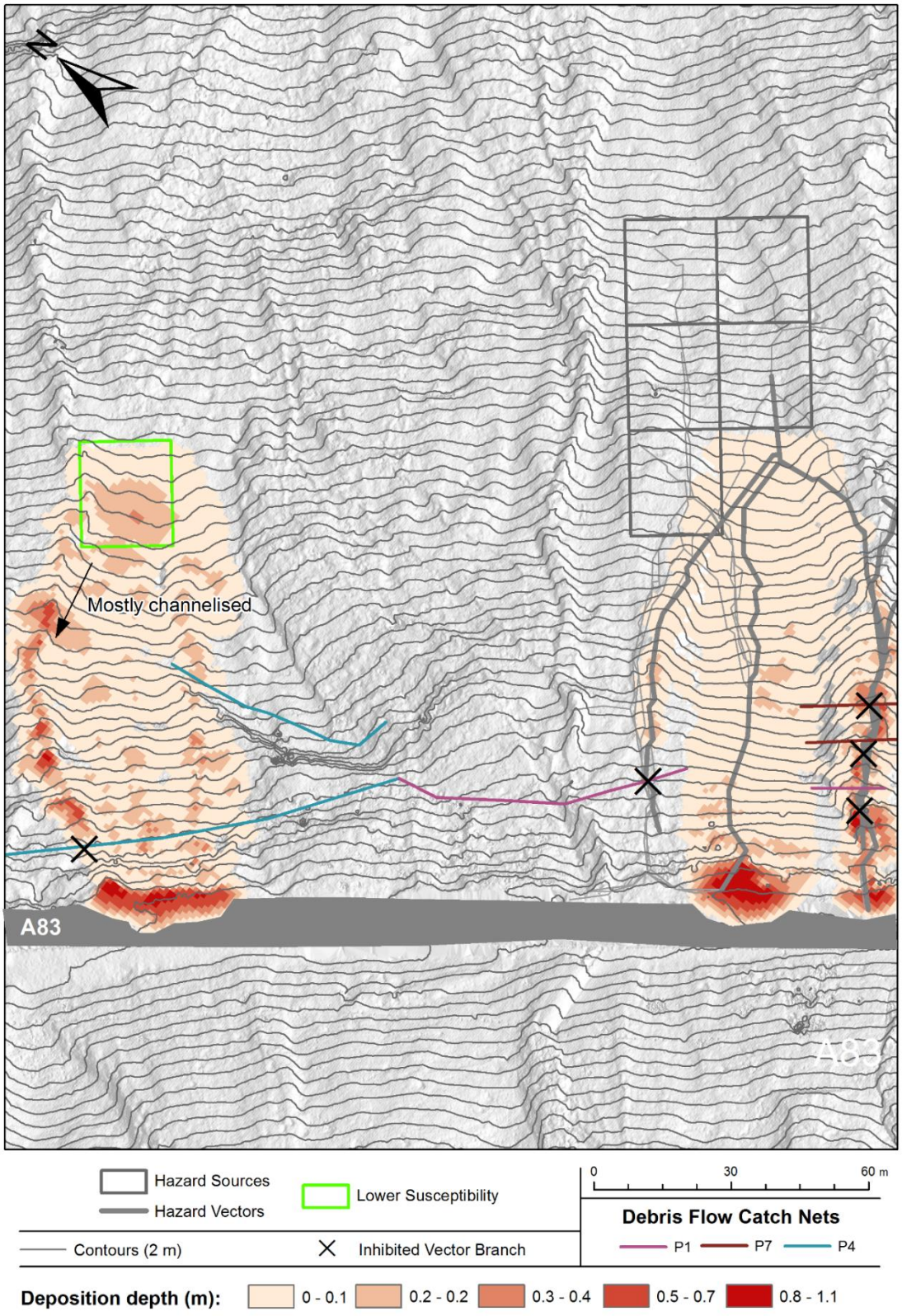

Figure 4.32 – A modelled flow, to the left of the susceptibility modelling domain, mostly propagates into a gully. This was one of only two modelled debris flows found to reach the A83. Given the relatively low runout potential of this region, demonstrated by Figure 4.28, and the presence of a channel, the phase 4 net may be considered excessively large.

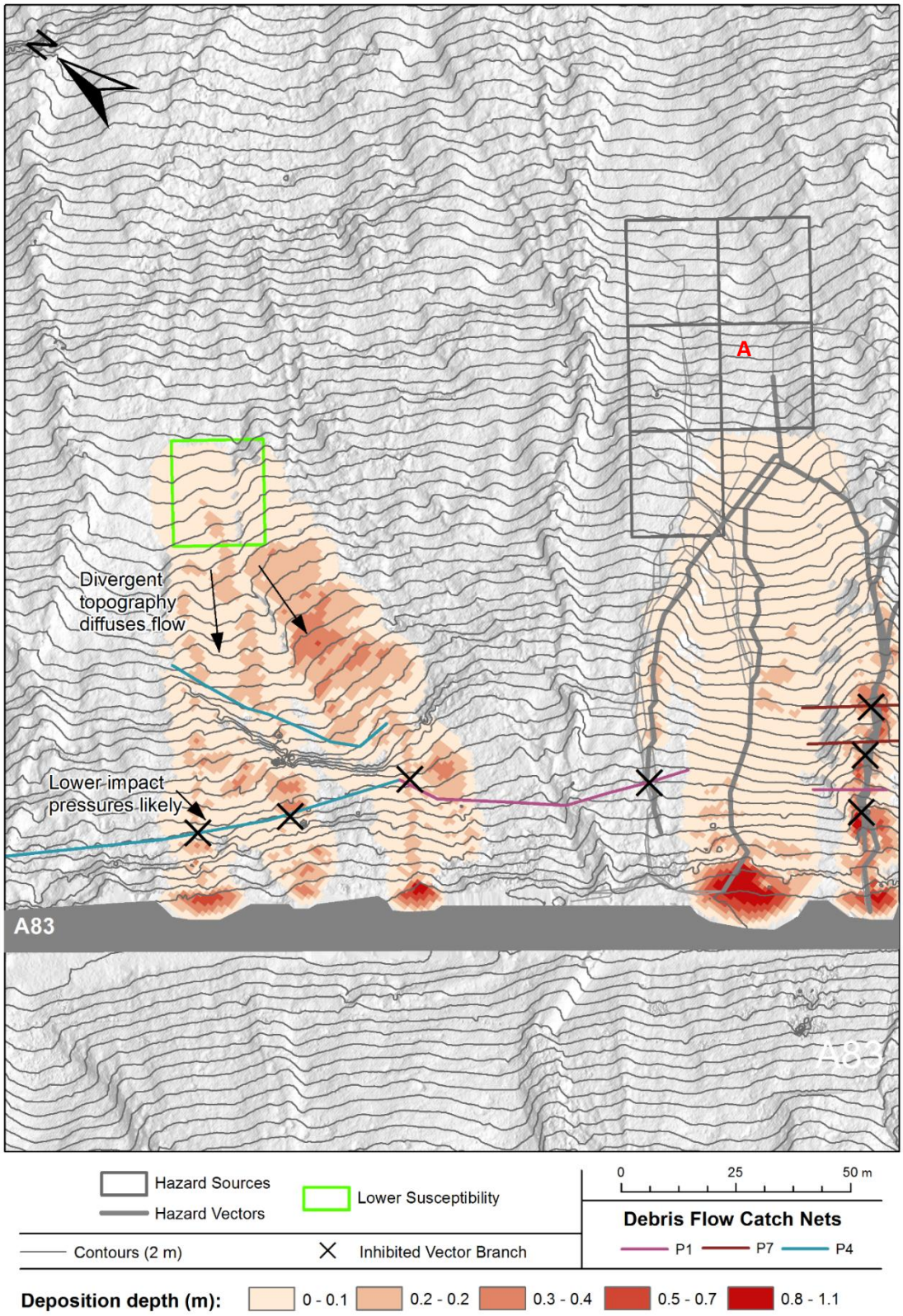

Figure 4.33 - A modelled flow, to the left of the susceptibility modelling domain. The second of only two events to reach the A83 from this region, this flow spreads as a result of divergent topography, with only a small volume of material propagating onto the carriageway (50 m³), this spread between three runout paths. This would result in smaller impact pressures than the unmitigated flow shown to the right.

Figure 4.31 highlights unmitigated vulnerability using models that either reached the road or had potential to reach the road. The vectors marked in orange are those which did not fully mobilise to road level, but which did follow the same path as lower elevation flows with potential to reach the road. The vectors marked in red are those that reached the road, but are considered to represent the most likely flows to potentially propagate beyond the flow nets. Of these, only one runout path is fully intersected by a catch net. Other flows are at least partially inhibited by the ends of the catch nets. The overlap here does not account for spreading of the flow mass however.

The deposition output for the modelled flow which reached the A83 is shown in the centre of figure 4.31 (source cell marked with an 'A'). A large quantity of deposition can be seen on the road, this amounting to 123 m^3, or almost 250 tonnes of material. This flow is neighboured by several other vectors with the potential to propagate to road level, although these are all intersected by catch nets. In contrast, the region to the north-west (the area of relatively low runout potential in figure 4.30), only contains two flow vectors with potential to reach the road. Both of these were both intersected by P4 flow nets. Furthermore, the first of these, shown in figure 4.32, deposited only 106 m^3 on the carriageway, after primarily mobilising into a gully with a culvert. The second of these, shown in figure 4.33, deposited only 50 m^3 onto the carriageway, with this volume being spread across two separate runout paths. These modelled volumes are far smaller than the respective (Phase 4) catch net capacities which total 450 m^3 (Transport Scotland, 2016a). Given that these failures (the only two to the north-west, capable of reaching the road) are more likely to spread out on an open hillslope area or pass through a culvert, it is concluded that the relative vulnerability in this region is low.

4.4 Discussion and conclusions

The sensitivity analysis has demonstrated that a difference in cohesion of 300 Pa (difference between SDLS2 and SFLS1), equates to a 220 m difference in runout on a model slope with a channel. This difference is likely pronounced and would be reduced for a flow initiating on an open slope area with surface variability. Nonetheless, consideration of this sensitivity is important (Hürlimann *et al.*, 2008), especially when applying the model in a predictive manner. It is also worth noting that the back-analysis parameters were unable to account for increased mobility arising from flow dilution. It is therefore possible, that modelled flows found to reach the gullies cease runout prematurely and that a greater number of source areas have potential to mobilise all the way to road level. The model also does not account for entrainment, which could increase both the flow volume and runout distance (Iverson *et al.*, 2011). Such factors may be accounted for, in an idealised way, using RAMMS-DF, however this was avoided for simplicity.

Modelled deposition was generally found to spread in comparison to that of the observation data, although less so with use of the highest stopping momentum threshold and cohesion values. Smoothing of topography by a DEM, regardless of resolution, is considered a significant source of this spreading. McDougall (2017) demonstrates this effect through application of different scale gaussian filters. Modelled flows have previously been found to spill from channels due to this effect (Muñoz-Salinas *et al.*, 2008). Features such as large boulders, with overhangs on the upslope side, might normally accumulate material and promote deposition. DEM rasters are however 2.5D in nature, and thus an overhang will be simplified, often into a feature which enables flow passage with greater ease. Figure 4.34 for example shows how the large sampling size can convert a boulder, with an inhibitory overhang, into a bump with a more ramp-like quality. This reliance on a relatively simplified DEM for modelling is an inherent weakness in many models and could be overcome through utilisation of more advanced terrain representations, for example TINs which are already commonly used in 2D hydraulic models.

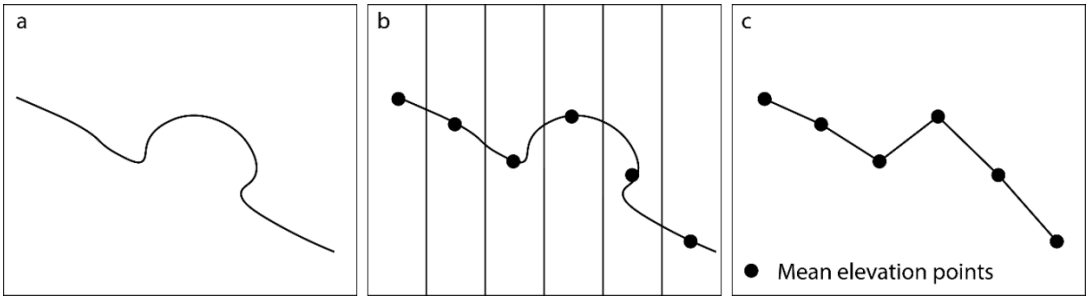

Figure 4.34 – An example of how DEM-related topographic simplification may inhibit deposition. A) True topography. B) An example of the topography sampling. C) Sampled topography reconstituted as a DEM. What was originally an upslope overhang, is now more akin to a ramp. Material travelling over this at a reasonably high velocity is more likely to clear the obstacle, however in reality a proportion of the flow is likely to deposit behind the obstacle.

Another clear source of this spreading is the limitation of a single-phase continuum model. Iverson (2003) explains that the evolving nature of a debris flow cannot be realistically simulated using a single, or continuum, equivalent fluid approach. Debris flows often initiate from shallow translational slides for example, with a complex change from sliding cohesive mass to that of a fluid-like flow which a continuum model cannot account for. Debris flows are also comprised of a heterogeneous mix of solids, amongst fluids, which are prone to sorting during propagation. Whilst more advanced models exist to model such factors, they demand complex parameterisation and are computationally burdensome. Many researchers still opt for single-phase continuum models, which demand fewer inputs and can be calibrated using historic data (Hussin *et al.*, 2012; Fan *et al.*, 2016b), yet which still simulate realistic inundation areas. Bartelt *et al.* (2017) have addressed some concerns relating to continuum models, by enabling variable spatial zones of different rheologies and incorporating an entrainment module for example. As such, continuum models can prove useful in modelling debris flows, as long as the end user is aware of the associated limitations.

The exhaustive runout analysis has demonstrated the role of channels in elongating debris flow runout, with 44 flows (55 %) reaching the bottom of the slope via these features. This is despite the fact that such regions cover just 10 m (4 %) of the 240 m lateral modelling extent. This pattern can also be seen in the comparison of slope convergence and runout distance in figure 4.30. The current mitigation strategy, or placement of nets, does not account for this low spatial distribution of the debris flow geohazard. Two large P4 nets are, for example, installed in a stacked arrangement to the left (north-west) of the modelled area, despite this region of the slope only being susceptible to two sources capable of mobilising onto the road. In comparison, the analysis has highlighted an unmitigated source area, with potential to deposit a larger volume of material onto the road. Furthermore, a larger number of runout

vectors are modelled 60-90 m south-east of this region, close to the gully which facilitated the SFLS1 event. Only one catch net is installed here however.

Debris flow runout is sensitive to the source area position, relative to the downslope topography. Analysis in this chapter has, for example, demonstrated how the mean gradient and confinement of the overall runout path affects runout. The exhaustive modelling approach developed and presented in this chapter does not account for potential source areas that might be offset from the grid used, i.e. with 50 % overlap with two existing cells. A 100 % increase in the number of models would have likely been required to account for this and was not deemed feasible in this study given time constraints. Nonetheless, this more rigorous approach could easily be applied using the existing workflow. Furthermore, it is considered that this exhaustive approach could be implemented directly within the RAMMS-DF software environment.

Interpretation of a large number of results has particularly relied upon the conversion of raster formatted model outputs which would have required multiple separate figures to interpret. Runout vectors can be visualised and compared directly and can be used to highlight areas of variable vulnerability to the debris flow geohazard. Such data can be of significant use to hazard assessments and the strategic implementation of a mitigation approach, such as the design and placement of debris flow catch nets or catch pits. The proof-of-concept modelling approach presented could be integrated into a wider strategic approach to debris flow risk reduction, such as the top down approach outlined by Winter (2016).

CHAPTER 5

Discussion

The principal aim of this research has been to characterise debris flow activity in Scotland, model behaviour of the phenomena and better understand the resultant geohazard providing information that will assist future risk assessment activities. Mapping, monitoring and modelling have thus far provided isolated analysis of debris flow activity and wider topographic and geomorphological factors, including the importance of topographically controlled drainage patterns and gullying. The aim of this chapter is to develop and synthesise a large range of findings into a formalised comprehensive framework of understanding about the debris flow phenomena, geohazard and related processes, as observed primarily at RabT.

5 Debris flow activity at the Rest and be Thankful

A number of findings have been presented throughout this thesis, from an early inventory of recorded events to further detected changes, which thus far have been discussed in isolation from one another. All of the events recorded at RabT, gully extents, estimates of sediment accumulations within four of the gullies, and modelled hydrological flow accumulations are composited and shown in figure 5.1.

The high frequency of activity, particularly detected at RabT during this study, likely represents a perturbation and renewal of paraglaciation, long after the initial paraglacial response (this can happen in waves, as seen in figure 5.2).

This delayed perturbation can be conceptualised by considering a freshly deposited pile of sand, the slopes of which are rapidly evacuated of material until a baseline, or resting angle, is reached. When this pile of sand is subjected to a certain level of wetting, once cohesive forces are overcome, the pile of sand will further evacuate material to reach a lower resting angle, at which point the slope requires a further increase in wetting for a further lowering of its resting angle. Paraglacial sediment stores often react in the same way, rapidly being evacuated to reach a relatively stable state in baseline conditions. However, if said baseline conditions change, due to an increase in rainfall intensities for example, then a large quantity of erodible glacial sediment becomes available for reworking. According to Knight and

Harrison (2018), paraglacial system models have previously overlooked the importance of such geomorphic thresholds and temporal lags.

If the quantity of evacuated sediment is far in excess of background rates of non-glacial sediment evacuation, then this can be considered as a paraglacial perturbation, or renewal. The difficulty with this concept is the quantification of background rates of sediment evacuation. If sediment evacuation, due to increased rainfall, increases only marginally then it can be argued that this activity is not paraglacial, despite the glacigenic origin of the failed material. This problem is confounded by the fact that background sediment evacuation rates are very difficult to quantify in isolation.

Renewed and delayed paraglacial sediment reworking has been observed several thousands of years after deglaciation (Curry, 1998; Jakob and Friele, 2010) and has already been evidenced throughout Scotland (e.g. Brazier *et al.*, 1989; Ballantyne and Benn, 1996; Ballantyne and Whittington, 1999; Curry, 2000). This activity may be expected to continue or worsen in response to climatic changes (Winter and Shearer, 2015) such as shifting rainfall patterns.

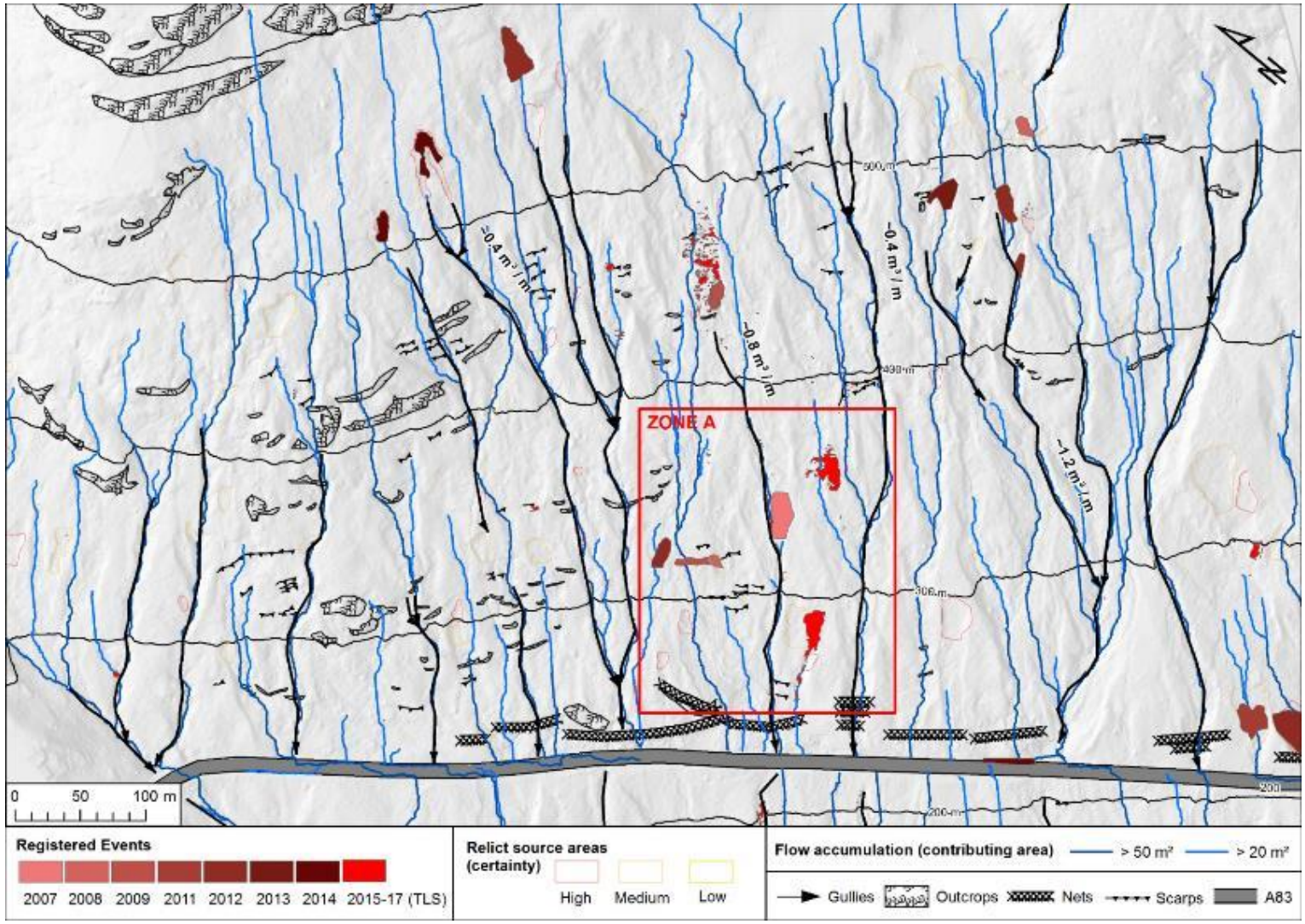

Figure 5.1 - A composite map of slope changes, hydrology, morphology and infrastructure at RabT

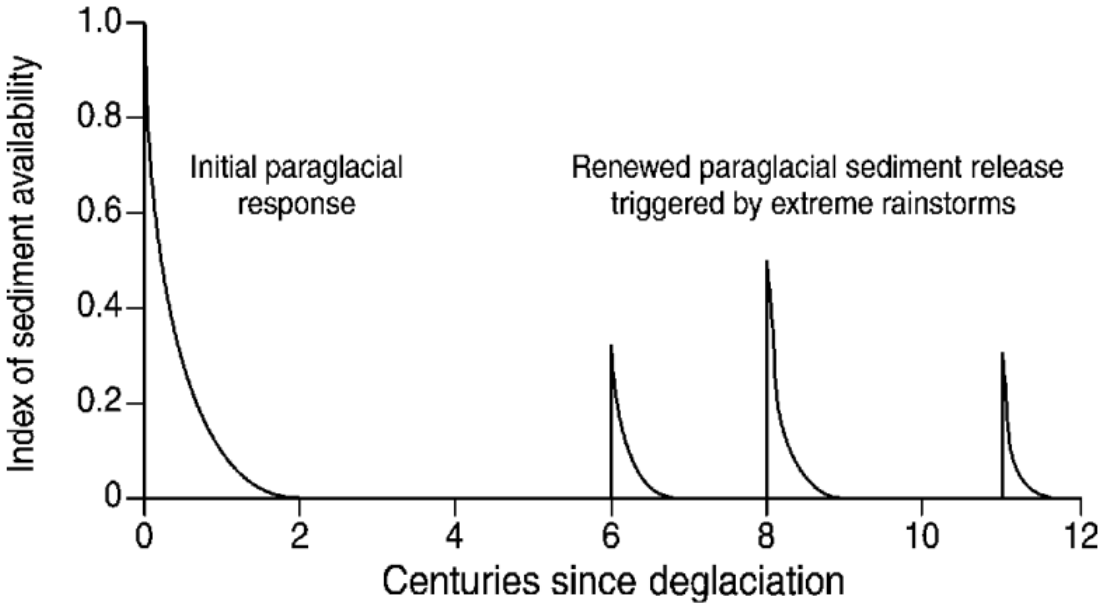

Figure 5.2 – Paraglacial sediment reworking, perturbed by extreme rainstorm events triggering new slope failures after a delay, in this case of several centuries and millenia scale (Ballantyne, 2002). The high frequency of events at RabT appears to represent one of the spikes several millennia after the initial paraglacial response.

There is high confidence that precipitation has increased in the mid-latitudes of the Northern Hemisphere since 1951 (Hartmann et al., 2013), which may explain a recent upturn in slope activity. Rainfall gauge data in England and Wales dates as far back as 1766, and back to 1910 for the whole of the British Isles. Whilst this is insufficient to identify long term trends since deglaciation, this data can be used to contextualise the recent increase in rainfall volume and intensity. For example, rainfall recorded in Cumbria during Storm Desmond, broke the UK record for total rainfall over a 24 hour period since records began in 1910. Natural variability dominates recent changes (last 30 years) in rainfall however (Kendon et al., 2017), making it hard to determine the role of climate change in these recent patterns.

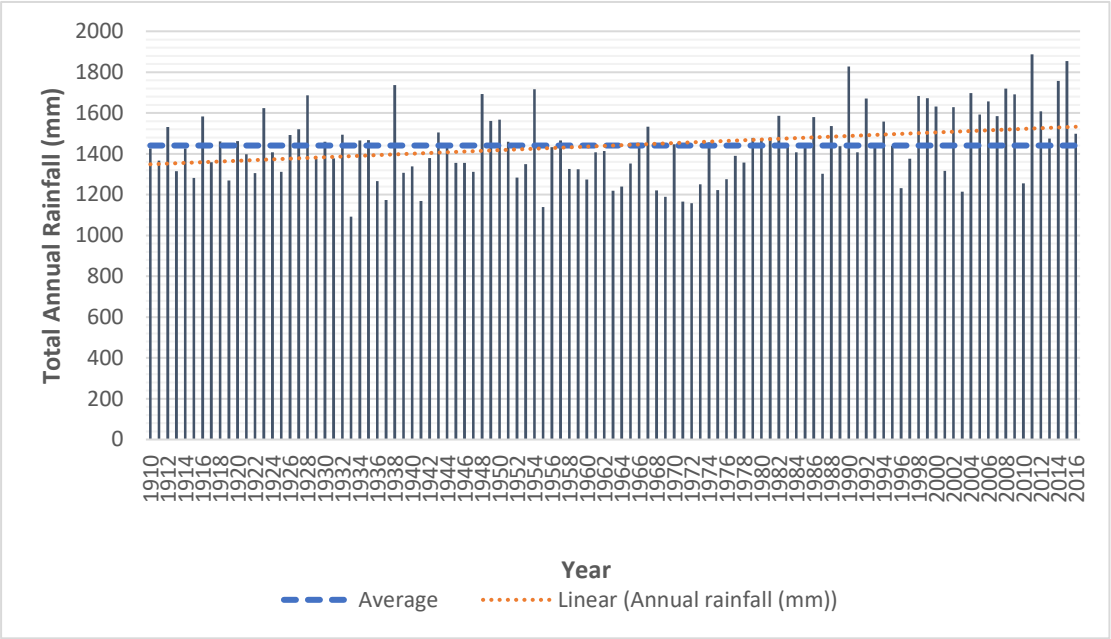

Figure 5.3 – Annual rainfall totals for Scotland from 1910 to 2016. There is no strong trend in this data, however a large number of above average rainfall totals are notable from around 1990 onwards.

Figure 5.3 shows Scottish annual rainfall totals from 1910 to 2016 (Scottish Government, 2017), for which the linear trendline shows a small, perhaps insignificant, increase in totals since records began. In total, over the 106 year record period, the average value is surpassed 50 times, of which 26 of these occurrences have occurred in the 36 years since 1980. Despite these records not yet being statistically significant in terms of climatic change, it is clear to see that annual rainfall has at least increased in recent years, particularly since around 1990, and appears to be linked to an upturn in slope activity. Such activity may explain the observed upturn in slope failures in recent years.

Longer term rainfall records are lacking, however Holocene climate proxy records can provide some further context to current conditions. Charman (2010) for example was able to assemble multiple climate records, including bog oak populations and annual speleothem widths, to determine that the United Kingdom has witnessed a number of warm and wet periods, with the last 400-500 years seemingly representing the beginning of a new wet phase. Such data of course contextualises the recent wet UK climate, but does not shed light on variation in rainfall intensities, of which aforementioned records have recently been broken, albeit over a short record timescale. Charman himself concedes that proxies can be insensitive to very wet periods, with speleothem growth rates for example only slowing to a certain extent during such periods.

RabT has a particularly dense network of gullies (14/km) (Sparkes *et al.*, 2017) compared to other schistose slopes (3/km) (for example, Ballantyne, 2004), and the high frequency and density of slope failures detected in this study may have been significant in their formation.

A lower density of gullies, a surrogate measure of slope modification (Curry *et al.*, 2006), towards the centre of the slope suggests that this area has been prone to less sediment working than other areas (i.e. the north-west of the slope), where the gully density is higher. The main gully at the centre of the slope is also truncated, which is indicative of a less mature feature, if gully length is used as a proxy for paraglacial slope adjustment (Mercier *et al.*, 2009). In comparison, most other gullies stretch to high elevations (>450 m) and correspond with high elevation failures. This also differs from the central truncated gully, which was found to correspond with a lack of high elevation failures (>450 m) prior to monitoring. It appears therefore that shallow landslides at RabT delimit the maximum elevation of the gullies, indicating a potential link between the process and the landforms.

Following production of the inventory map, two low elevation failures were detected at the centre of the slope in December 2015 (SDLS1 and SDLS2), continuing a trend of low elevation failures in the centre of the slope. These events were quickly followed by three new high elevation failures (> 450 m), including the SFLS1 debris flow, resulting in a total of 10 changes being recorded in the centre of the slope. Most of these events have contributed to a general trend of temporal sequencing in the upslope direction. Three events in particular (2007, 2009 and SFLS1; 2016), all mapped along a central truncated gully, have adhered to this trend. Examination of old slope photographs (figure 5.4) indicates that the truncated gully, along which these three debris flows have occurred, has developed rapidly over recent years. A photograph of the 2007 debris flow (figure 5.4a) in particular, shows that the central gully was merely half its current length prior to the 2009 debris flow (figure 5.4b), which has rapidly extended the gully, resulting in an established and active gully region today (figure 5.4c). Little attention has previously been drawn to the connectivity between successive erosive debris flows on longer hillslopes. Johnson *et al.* (2008) for example analysed a debris flow at Wet Swine Gill, UK, which mobilised directly into a headwater stream. Harvey (2001) also mostly presented similar such flows, although two sequential debris flows were documented at Middle Carlingill in 1998. In contrast to activity at RabT, these debris flows occurred sequentially in a downslope direction, and gullying is said to have occurred as a result of post-failure fluvial incision. The sequential debris flow, and connectivity between these, therefore appears to be somewhat unique to RabT in the literature.

A more detailed breakdown of the central slope events and how these sequential failures have joined together, resulting in direct gully extension by debris flow activity, is shown in figure 5.5. Little information about the state of the slope before 2007 is available, however the 2007 debris flow itself is reported to have significantly scoured an existing channel (BGS, 2007), a photo of which is shown in figure 5.7. T1 on figure 5.5 marks the length of the gully in 2007, which measured 216 m from the headscarp of the 2007 failure to the bottom of the slope. The headscarp of the 2009 event represents an extension of 161 m (T2). This new gully region appears to have been significant in the effective channelisation of the subsequent SFLS1 event, with the debris flow mobilising from upslope, travelling through it and eventually reaching the A83 trunk road. Schumm et al. (1984) have previously defined a gully as a relatively deep channel, forming where no well-defined channel had existed before, which has certainly been the case at RabT. The regularity of gully development rates is generally poorly understood (Bull and Kirkby, 1997), however a number of studies have quantified headwall retreat rates of around 0.1-0.2 m/yr^{-1} (Betts & DeRose, 1999; Harvey, 1992; Marzolff & Poesen, 2009; Vandekerckhove et al., 2001) with a median retreat rate of 0.89 m/yr reported in a wide review by Vanmaercke et al. (2016). These give some context to the rapid rates of extensive gullying caused directly by debris flows at RabT.

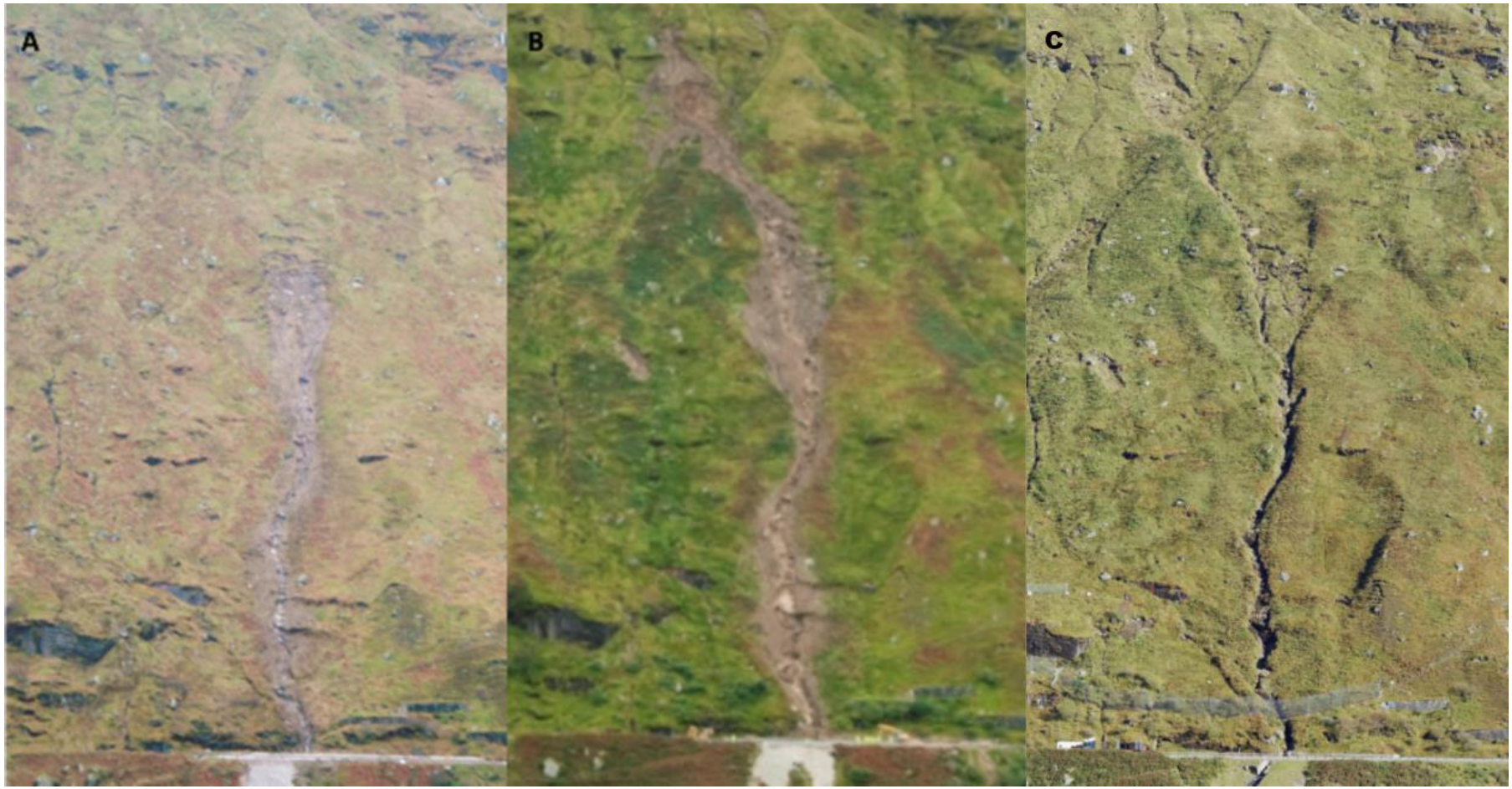

Figure 5.4 - Photographs of the central slope region, encompassing Zone A shown in figure 1. A) Shows a photo taken in 2007 shortly after a large magnitude debris flow at the site (Scotland Transerv, 2007). No gully or channel is evident immediately upslope of the failure. B) Shows a photo taken after a subsequent failure in 2009 (BGS, 2009). C) Shows a new established area of incised gully in 2015.

SFLS1 is known to have scoured some of the existing gully sidewall, however perhaps more importantly, the event has also contributed towards further elongation of the gully, by an additional 60 m (T3 in figure 5.5). Cross sections through the SFLS1 source area (figure 5.8) show a continuous trench along the right-hand margin, measuring up to 1 m in depth and in excess of 20 m in length. The large depth of the feature exceeds that of a smaller ephemeral gully (Poesen, 1993) and exceeds a minimum gully depth threshold of 0.5 m discussed by Bocco (1991). Whilst gully formation has principally been attributed to fluvial incision and upslope propagation (Harvey, 1992) other processes have been recognised as playing a role in their development (Harvey, 1992; Kirkby and Bracken, 2009), albeit to a lesser extent. Debris flows have been found to scour existing gullies (Stock and Dietrich, 2003) and bedrock channels (McCoy et al., 2013), however little evidence of initial gully formation through debris flow activity, as seen at RabT, has been reported.

Strachan (2015) has previously questioned whether debris flows are an effective agent of gully scour, based on observations of the phenomena on the relatively planar slopes of Glen Docherty where larger clasts dominate the hillslope material. The sequencing at RabT (shown in figure 5.5) demonstrates that debris flow are an efficient agent of gullying where finer superficial soils and colluvium are present. The RabT hillslope is heavily undulated (Sparkes *et al.*, 2017), with a large number of convergent sub-basins. Such topographic confinement minimises flow spreading, thus maximising the flow depth which aids debris flow scour (Berger *et al.*, 2011; Schurch *et al.*, 2011). This perhaps explains the lack of debris flow gully propagation observed at the relatively planar Glen Docherty site (Strachan, 2015). Furthermore, research by Johnson and Warburton (2015) has found landslide scars to be highly susceptible to fluvial incision and gully development shortly after failure. Remobilisations within the SFLS1 source area (described in chapter 3) are consistent with this and perhaps indicate the role of an initial debris flow, among other processes, within a wider gully forming continuum, as previously discussed by Poesen *et al.* (2003). Should development fully proceed to the head of SFLS1, as has been observed previously at other sites (Parkner *et al.*, 2006; Menéndez-Duarte *et al.*, 2007; Johnson and Warburton, 2015), then the 2009 and SFLS1 events would have collectively doubled the length of the gully over a short period of time.

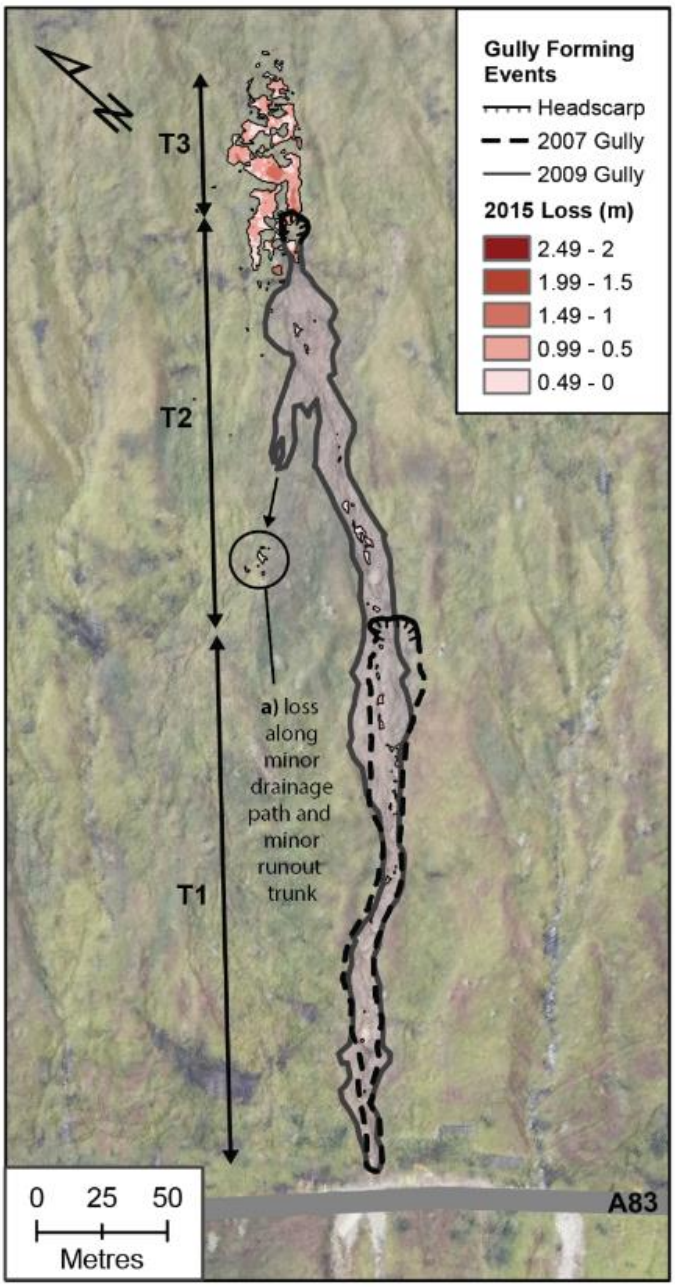

Figure 5.5 - Gully development at the Rest and be Thankful as a result of sequential debris flow runout coupling. T1, T2 and T3 show the vertical gully extents shortly after the time of the slope failures which occurred in 2007, 2009 and 2015 respectively. a) highlights loss detected in 2016 along a secondary propagation path, also an area of modelled hydrology, down which the 2009 event attempted to propagate. Rectified backdrop photograph courtesy of BGS (2009).

Debris flow gully development is further evidenced by the largest debris flow recorded at RabT, in October 2014 (~1,000 m^3; shown in figure 5.9), which appears to have completed extension of a gully by extending it 100 m up to the upper extent of the slope (figure 5.10). This is again a very rapid rate of gully development compared to conventional rates of gully retreat. Given that this event has simultaneously elongated the gully to the top of the slope, whilst also evacuating much of the gully sediment accumulations (Sparkes *et al.*, 2017), this gully region may be considered relatively mature (Mercier *et al.*, 2009). In contrast to the central sequence of debris flow gullying (2007, 2009 and SFLS1) and the October 2014 event, SDLS1 has clearly demonstrated initiation of a completely new gully region, measuring some 40 m in length (figure 5.10). This gully is also truncated, much like the central gully discussed earlier, and has the potential to develop as a result of successive failures, as already observed at the site. Bocco (1991) has previously alluded to the headward retreat of a lower truncated gully, enabling connection with another gully upslope, however there is little research of sequencing in the opposite direction via mass wasting or debris flow. It is considered that the central events (2007, 2009 and SFLS1) represent a near full sequence of debris flow gully propagation, of which an event similar to that in October 2014, could potentially complete the sequence. The SDSL1 event, on the other hand, appears to represent the onset of a new sequence, although this may only be confirmed by continued observations at the site.

According to Ballantyne (2002c), a high gully density is linked to mean annual rainfall, however he also suggests that local hydrological controls may also be influential in the rate of gullying and debris flow activity. A general trend of upslope sequencing could relate to development of the hillslope drainage network. A mapping study by Ng (2006) for example, found that debris flow source area locations corresponded strongly with headward progression of the drainage network, from high order streams up to low order streams. This hypothesis is supported by observations of drainage within several source areas, including tracing through that of SFLS1 (figure 3.52), the RabT1G source area (figure 3.49) and discrete flow through the source area of a landslide in 2012 (figure 5.12). Several researchers have highlighted the role of a large contributing area to instability and landsliding (Montgomery and Dietrich, 1994; Fernandes *et al.*, 2004; Von Ruette *et al.*, 2011; Mandal and Maiti, 2015). Alternatively, flow accumulation could also be indicative of sub-surface drainage patterns. Interestingly, Bull and Kirkby (1997) have previously attributed gully head formation, on steep slopes, to sub-surface flow induced instability. Pipe flow has been observed at RabT, and may explain the lack of an observable stream upslope of the 2007 debris flow where a gully has subsequently formed. According to Jones (1971), soil pipes are particularly

widespread across the UK. Discrete sub-surface drainage, such as pipe flow, is often overlooked due to a similar appearance to an ephemeral gully after collapse (Wilson, 2011), and is thought to be influential in the development of gullies and triggering of slope failures (Wilson et al., 2018). A combination of sub-surface piping and surface flow may explain the discontinuous nature of hydrological flow traced within the vicinity of the SFLS1 source area prior to failure (figure 3.52).

Modelled flow accumulation has also been found to correspond with lesser-developed changes, namely a 2009 inventory event and RabT1F downslope, and the small landslide RabT2C landslide upslope. None of these correspond with an evident mature gully or channel however. Given that landslides can initiate as a progression of smaller precursory events (Fan *et al.*, 2015), it is possible that the these small changes could signal the location of future activity, potentially including further development of the central gully. To the south-east, changes RabT1E and RabT3F both occurred within two years of one another, along the same flow line, perhaps indicating reactivation of the same convergent flow feature. Whilst no evidence pre-existing channel was observed for the 2007 or 2009 debris flows, a small channel does appear to have existed within the vicinity of the large October 2014 landslide source area, prior to failure.

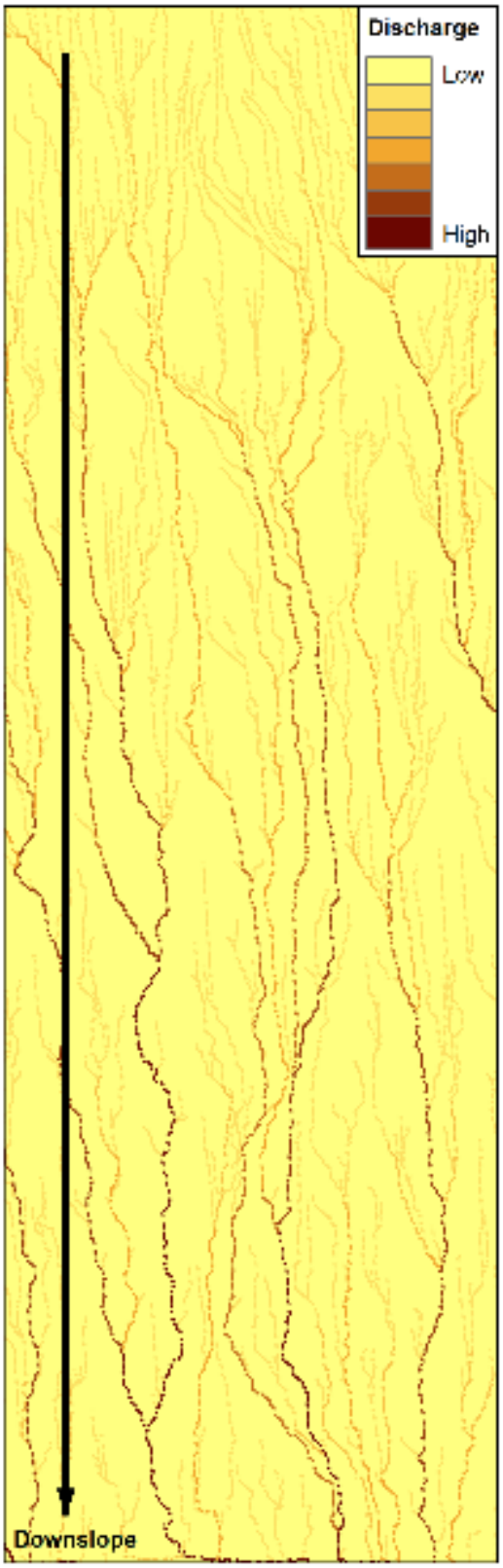

Figure 5.6 - Greater flow discharge occurs with distance downslope, as demonstrated by flow accumulation modelling.

Debris flow sequencing and gully propagation at RabT has occurred in the upslope direction, the cause of which is unclear. A mapping study by Ng (2006) found debris flow activity to correspond with development of the drainage network, from high order streams, up to low order streams. Slope length has also long been known to increase soil loss per unit of area (Zingg, 1940), leading to the use of exponents to estimate soil erosion based upon slope length (Musgrave, 1947). The cumulative increase in contributing area with distance downslope results in greater flow discharge with distance downslope. This is shown in the raw modelled flow accumulation data shown in figure 5.6. Ali *et al.* (2012) performed flume experiments on erodible beds, and have demonstrated the influence of increasing unit discharge, as well as slope gradient and flow velocity, on increased sediment transport capacity. Crosta and Prisco (1999) highlighted increasing flow convergence towards the bottom of the slope as a significant process in the intensification of seepage erosion and soil pipe scour. Furthermore, research by Burke *et al.* (2007) has demonstrated a link between the upslope contributing area, chemical weathering of a soil mantled granite bedrock and thus increased pedogenesis, which can alter the hydraulic transmissivity of a soil and susceptibility to failure (Ballantyne, 2004). It is postulated here that the increased contributing area downslope may intensify erosion and weathering processes, which preferentially reduces the soil shear strength, and thus increase the likelihood of failure (Nettleton *et al.*, 2005). Slower erosion and weathering upslope could therefore result in the delayed failures and upslope sequencing observed at RabT.

Figure 5.7 - Incision relating to the runout of the 2007 landslide event recorded in the inventory (BGS, 2007)

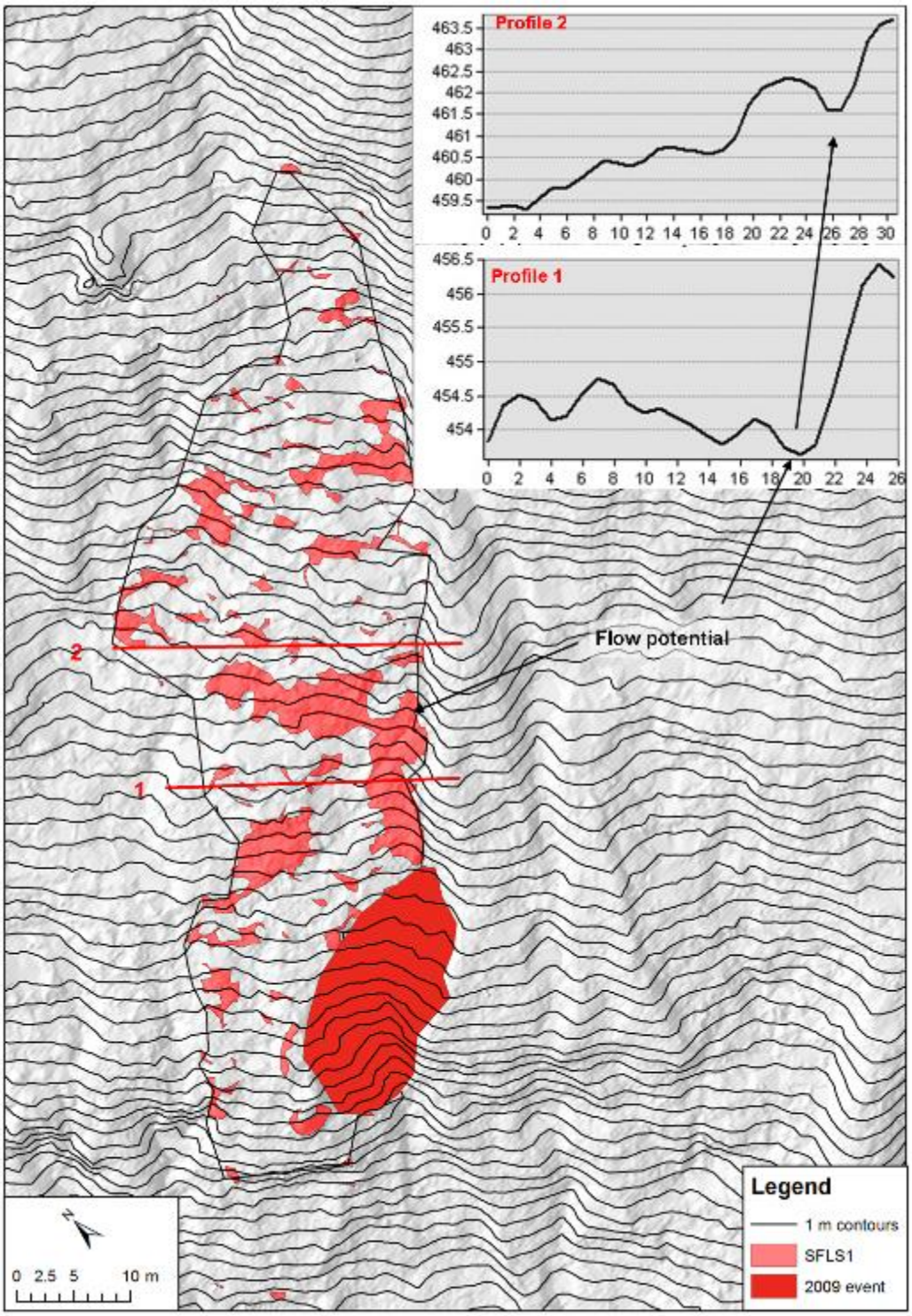

Figure 5.8 - A detailed change map of the SFLS1 event and a failure in 2009, as well as cross sections through the source area of SFLS1, where flow could accumulate and couple with the developing gully directly downslope.

Figure 5.9 - A photograph of the October 2014 debris flow source area and the way in which this has joined with the head of an existing gully

.

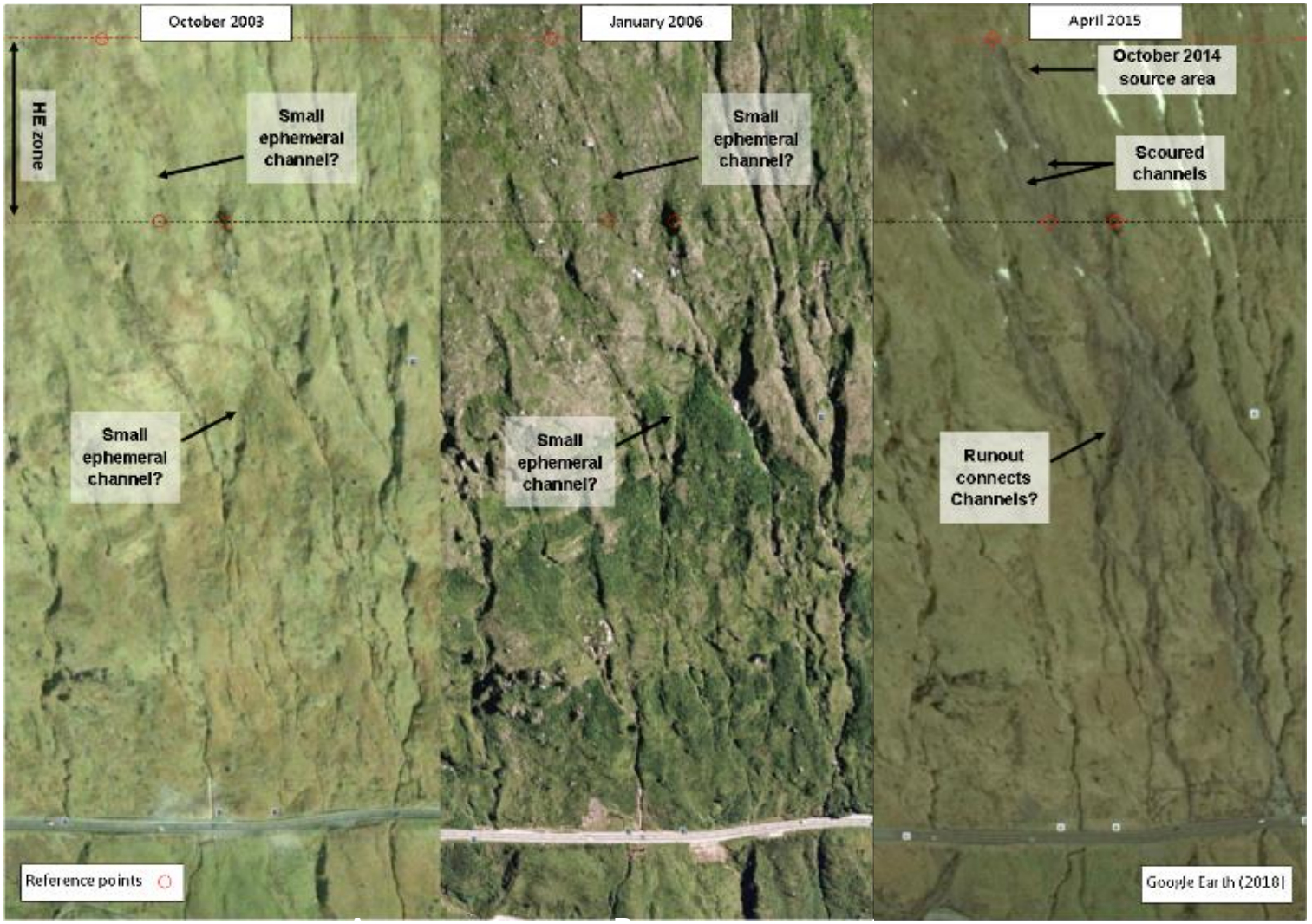

Figure 5.10 - A comparison of historical aerial imagery around the location of the October 2014 debris flow, A) In 2003, B) In 2006 and C) in 2015 (Google Earth, 2018; Digital Globe and GetMapping Plc)

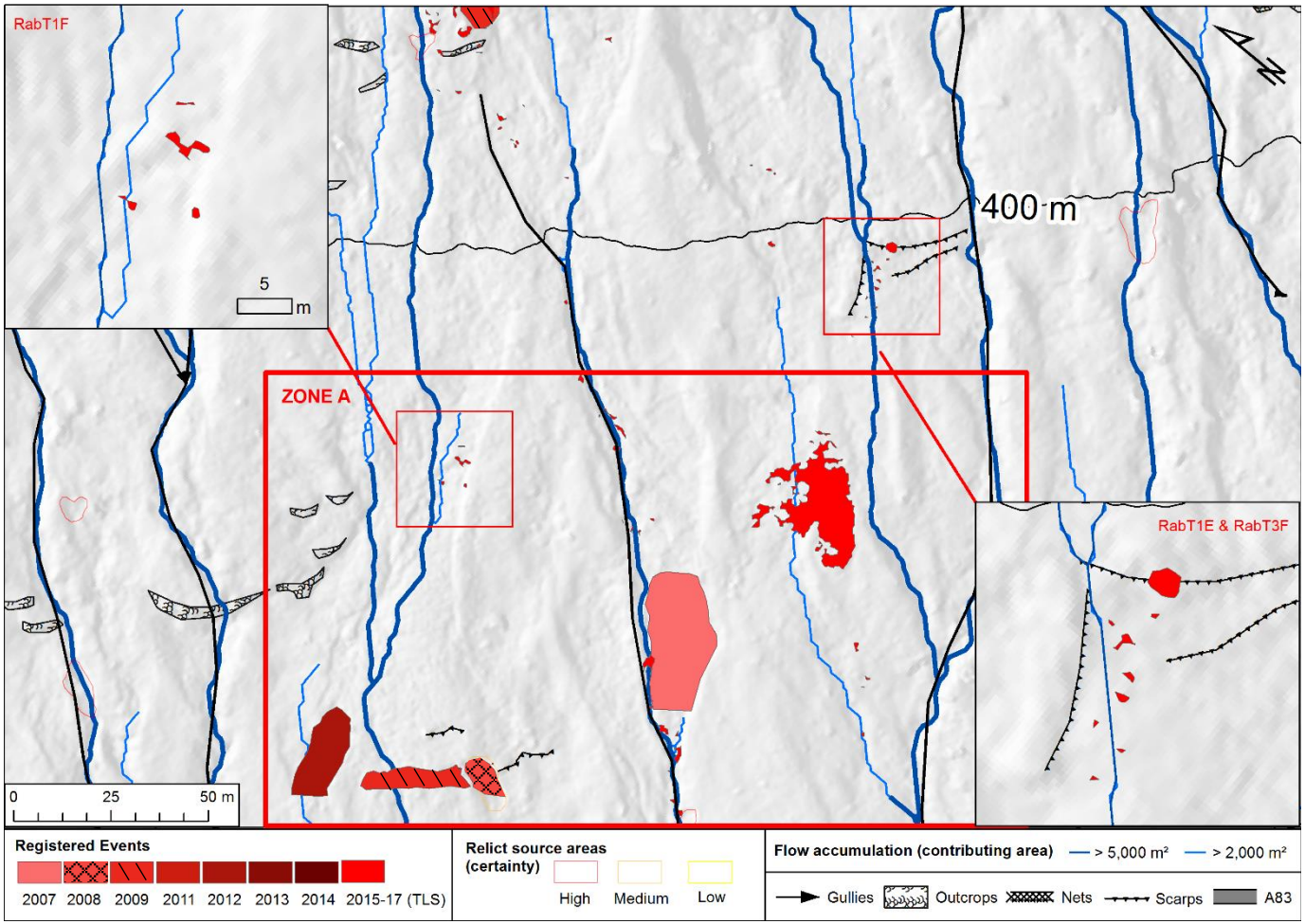

Figure 5.11 – Two areas of loss detected in the centre of the slope, along major modelled flow lines. These have not yet developed into large failures. RabT1F is of major interest, as it was detected along a flow line that runs upslope from the SFLS1 source area and down through another inventory event recorded in 2009.

Figure 5.12 - A photo of hydrological routing directly through the source area of a failure at RabT in 2012 (Unpublished image courtesy of Scotland Transerv, 2012). This is further evidence of water accumulation within the locale of hillslope failure source areas, much like that observed at Glen Ogle (Milne et al., 2010). Such flow accumulation could be concentrated within soil pipes or small channels.

A survey of the deposits within the base of the October 2014 gully, after scour by the 2014 debris flow, shows there to be approximately 0.4 m^3 of material per metre of gully. The SFLS1 gully to the south contains approximately double the quantity of basal deposits per metre of gully. This indicates that the SFLS1 gully is yet to be extensively cleared of sediment accumulations, perhaps because a high elevation failure is yet to have occurred and mobilised down the gully. Furthermore another truncated gully, further to the south-east of the study area, was estimated to contain 1.2 m^3 of material per metre of gully, therefore evidencing a gully system which could yield a large magnitude debris flow should a high elevation failure occur and mobilise into the system

5.1 A conceptual hydro-geomorphological model

The high frequency of activity and the small of the RaBT slope has enabled monitoring of an interconnected suite of hydrological, hydrogeological and geomorphological processes, from source to sink, which would have previously been difficult to record elsewhere. This section presents a conceptual model, which encompasses these processes, and postulates that they are closely interlinked, resulting in debris flow-induced gullying. This model addresses calls for consideration of a more diverse gully forming mechanism (Bergonse and Reis, 2011) and will help shed light on the observed spatial distribution of activity, as well as the potential for future activity and thus slope hazard zonation. It is hoped that this model will form the basis for further research into a wide range of interconnected 'hydrogeomorphic' processes and landforms (Sidle & Onda, 2004).

5.2 Stages of slope development

This conceptual model presents an alternative mechanism by which sequential erosive debris flows couple, instead of conventional upslope headcut migration (Bull and Kirkby, 2002). It is hypothesised here that sequential upslope failures occur within the same sub-basins, which enable accumulation of adequate water for the early development of hydrological or hydrogeological features, along which failures are later triggered. The initial formation of these sub-basins, or depressions, is not of primary concern here, however contributing processes may include the melt and lowering of ice-cored moraines (Mercier *et al.*, 2009), and large magnitude translational failures during or shortly following deglaciation, which have left large cuspate scars (Ballantyne, 2018; figure 5.13a). These features are hypothesised to influence the routing of debris flows, such as the sinuous runout vectors shown during runout modelling (i.e. figure 4.28). Conventionally, once a critical drainage area threshold is surpassed, incision and ephemeral gully formation occur (Patton and Schumm, 1975; Poesen *et al.*, 2003). These features concentrate successive storm rainfall events, reactivating ephemeral gullies and enabling their enlargement (Kirkby and Bracken, 2009). This process may elicit a positive feedback effect by concentrating greater volumes of flow, thus gradually increasing erosive power (Poesen *et al.*, 2003) (figure 5.13b).

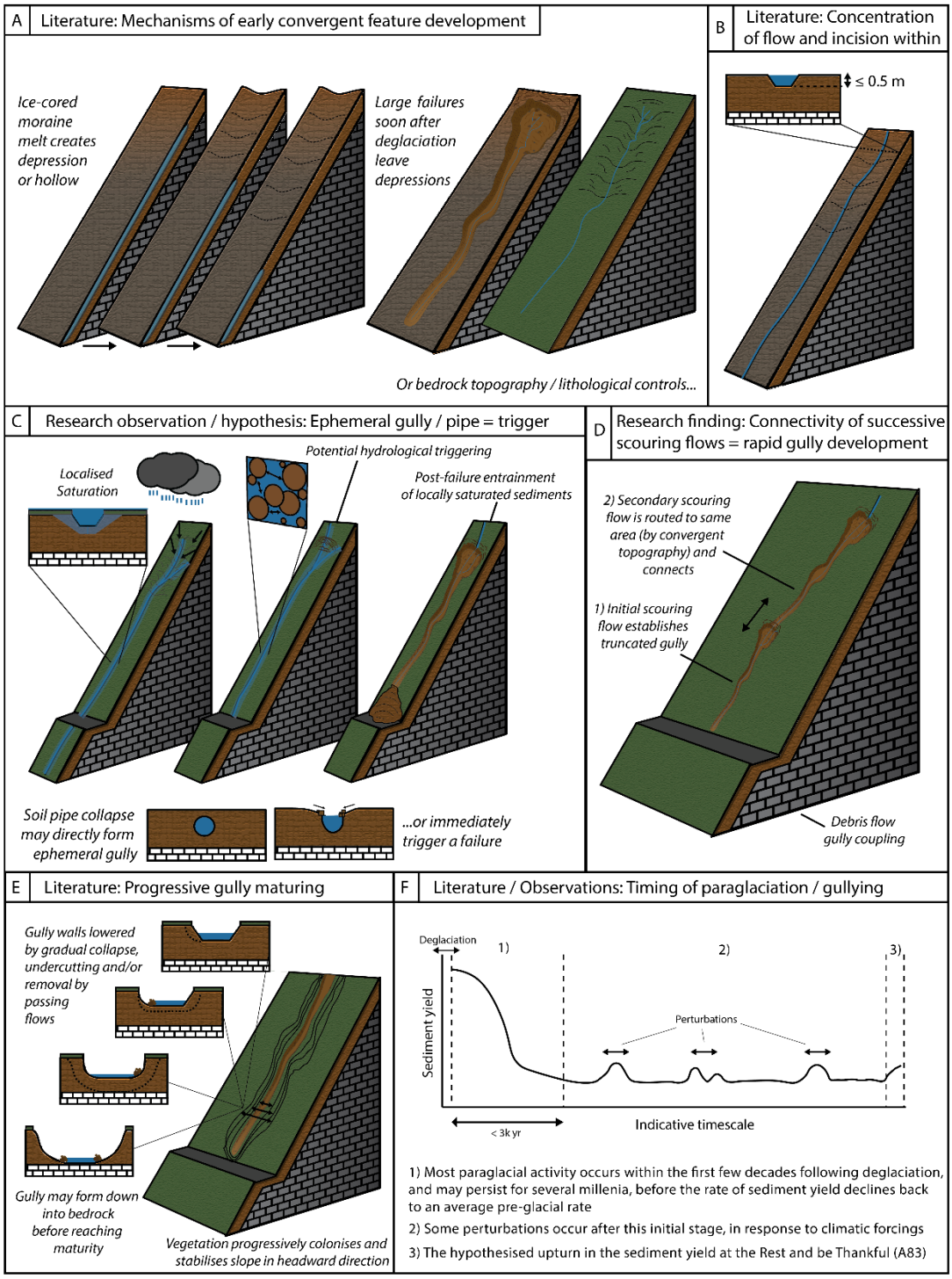

Figure 5.13 - A conceptual model of inter-dependent hydrology, mass wasting and gully development. A) Early formation of features that then influence hydrology and the spatial distribution of failures and gully development. Flow concentrates due to topographic convergence or soil piping. B) Rill formation ensues due to mechanical fluvial erosion, or pipe collapse C) Flow from heavy rainfall concentrates down established flow lines, along which adjacent sediments become heavily saturated. Failures may occur along these flow lines or propagate into them from elsewhere, after which mass entrainment of heavily saturated sediments occurs with relative ease. In the case of saturated basal sediments being overridden by a passing flow, this may lead to a positive feedback effect on both flow magnitude and momentum, as shown by Iverson et al. (2011). D) Successive scouring flows are routed along the same path, connecting to rapidly form long singular gully systems, or new tributaries. E) Gullies widen, deepen, lower and mature over time as a result of multiple factors including the passage of subsequent debris flows, perhaps triggered by the same aforementioned hydrologically forced mechanism. This effect is likely enhanced by the lack of vegetation which was removed by the first flow thus increasing susceptibility to fluvial erosion. F) Most of this activity takes place during the early paraglacial period, however perturbations (2 & 3) renew the activity.

The ephemeral gullies observed at RabT may have formed via this mechanism of successively reactivated flow accumulation and incision, however Wilson (2011) has also observed the collapse of soil pipes to produce features almost indistinguishable from ephemeral gullies. In a detailed investigation of a slope collapse at the edge of a flooded rice field, Crosta and Prisco (1999) highlighted the ingress of water into soil cracks and the development of a soil pipe network as a contributing factor to the failure. These cracks may form sporadically, particularly in peaty soils (Bogaard and Greco, 2016) such as those at RabT (Scottish Natural Heritage, 2016). Swanson et al. (1989) have previously attributed the development of extensive gullying in California to the development and collapse of soil pipes. This, or a combination of both mechanisms, may therefore result in the development of long 'incised' drainage features. Incised lines cannot always be traced continuously, and so the concentrated downslope flow may be distributed intermittently between surface and sub-surface systems, as also observed by Wilson *et al.* (2016).

The third stage of the model (figure 5.13c) involves the triggering of failures within the zero-order basin, by the concentration of hydrological or hydrogeological flow. Hollows, such as that in which SDLS1 was triggered, are known to accumulate thick regolith and subsurface water (Dietrich and Dunne, 1978). The large depth of the SDLS1 event (1.5 m), relative to other detected landslides, and location within a hollow was perhaps indicative of a different triggering mechanism to the other failures detected upslope. The stability of a 1 m thick soil, has been shown to be significantly more sensitive to unsaturated moisture changes than an equivalent soil of 3 m in depth during modelling (Ray *et al.*, 2010). Greater accumulations of water at the bottom of the slope may also influence an initial low-elevation failure (Crosta and Prisco, 1999; Acharya *et al.*, 2009) within a thicker accumulation of material and may represent the first stage of sequential upslope gully formation, such as that outlined earlier in the chapter.

Cracks in the overlying soil surface may provide a route for surface water to infiltrate to the soil-bedrock interface, enabling rapid development of pore pressures (Crosta and Prisco, 1999; Nettleton *et al.*, 2005). Alternatively, failure may be triggered by a so-called 'firehose' effect below a topographic step (Johnson and Rodine, 1984), a process which has been noted to trigger debris flows in Colorado (Godt and Coe, 2007) and Arizona (Griffiths *et al.*, 2004). Soil pipes have been shown to aid stabilisation of a slope, but also to cause instability (Pierson, 1983; Sidle *et al.*, 2006) and debris flows through clogging (Uchida, 2004). These features develop through internal erosion of soil pores (Fox and Wilson, 2010), with clogging also hypothesised as a potential way for bifurcation and new piping to occur (Midgley *et al.*,

2013). The role of clogging and new pipe formation may be significant, as this would result in rapid switching of flow paths, potentially explaining anecdotal observations of channel switching and spatio-temporal variations in stability at RabT. Other internal erosion mechanisms were reviewed by (Crosta and Prisco, 1999), for which several process schematics are shown in figure 5.14. Pipe collapse may aid ephemeral gully formation in second stage of the model (figure 5.13b), but could equally be the direct trigger of a failure and gully development in one rapid action. Observations at Glen Docherty indicate that debris flows exerted little basal erosion during runout (Strachan, 2015), although this was on a slope with more gentle confinement, and more distributed drainage. The SDLS1 event in particular, clearly demonstrated direct gully incision by a debris flow at RabT. This model therefore hypothesises that debris flow runout, through a saturated convergent zero-order basin, results in direct gully incision.

During a prolonged rainfall experiment on a model slope (12 mm/hr), a basalt derived loam soil was found to preferentially saturate around a 1 m deep central trough after 16 hours, whilst the margins of the slope, 3 m away, did not fully saturate. This research demonstrates how more convergent slope areas may preferentially saturate during long duration rainfall events, enabling enhanced scour (Gevaert *et al.*, 2014). Shallow soil stability is particularly sensitive to moisture changes (Ray et al., 2006), thus the confinement of debris flow runout along a saturated convergent path, regardless of channel maturity, would likely result in scour. Crosta *et al.* (2006) detailed debris flows in northern Italy that entrained and scoured surface deposits and vegetation due to soil saturation. Runout through a well-defined gully would also increase the flow magnitude and mobility (Iverson *et al.*, 2011) and thus the potential event magnitude.

The fourth stage of the model (figure 5.13d) entails the coupling of truncated gullies, as a result of successive failures along the same, or linked, convergent topographic zones. This stage rapidly results in the formation of long singular gully systems. Runout modelling, presented earlier in this thesis, demonstrates the ability for convergent topography to facilitate long runout flows, as well as enabling flows in open-hillslope zones to eventually reach existing gullies. Such connectivity has been recognised previously (Bocco, 1991), although not directly and rapidly through mass wasting. This stage of the conceptual model is informed by observations and monitoring of the phenomena, on a few occasions, at RabT. This is the hypothesised development mechanism of long gullies upslope to the upper limit of the drift deposits, after which elongation likely ceases.

Following initiation, gully widening and a reduction in the sidewall angles will ensue (figure 5.13e), developing the gully towards a mature state (Curry, 1999; Johnson and Warburton, 2015). This may occur through the passage and scour by subsequent debris flows which can undercut the gully sidewalls (Hungr et al., 2005). There is limited evidence of debris flows initiating within channels at RabT, therefore gullies may become overloaded with deposits that can only mobilise when a larger hillslope flow passes through (Brayshaw and Hassan, 2009). This might not be possible if high elevation sediments sources have been exhausted. Due to the lower gully density at the centre of the slope at RabT, it is hypothesised that recently monitored activity is working to develop the central-slope gullies to a similar state of maturity as other areas of the slope. The left and right margins of the RabT study area may be considered to be in stage E (figure 5.12) of the conceptual model, whereas observations indicate that the central slope region is currently working through stages C and D.

This model does not account for downslope sequencing, evidence of which has also been found. An example of this was the RabT3A failure (figure 3.32) which clearly occurred below a previous open-hillslope failure. A complex and diverse range of factors influence hillslope hydrological routing (Kim *et al.*, 2016) and may account for failures away from convergent drainage lines. These include spatial heterogeneities in material properties (Montgomery and Dietrich, 1994; Fan et al., 2016b), perched groundwater zones (Gasmo *et al.*, 1999) and geological and lithological influences (Anderson *et al.*, 1997). Jones (1987) also observed that soil pipes do not always honour the surface topography, thus piping may contribute to failures outside of convergent zosnes. Harvey (1992) comments that progressive changes in process interactions occur during gully development. This model does not overlook the role of fluvial action, which has been shown to erode landslide scars after failure events (Johnson and Warburton, 2015). Instead, it is considered that debris flows represent one process amongst a wider continuum of other gully forming processes (Poesen *et al.*, 2003). That said, debris flow gully incision may be a particularly effective process at specific sites, such as RabT.

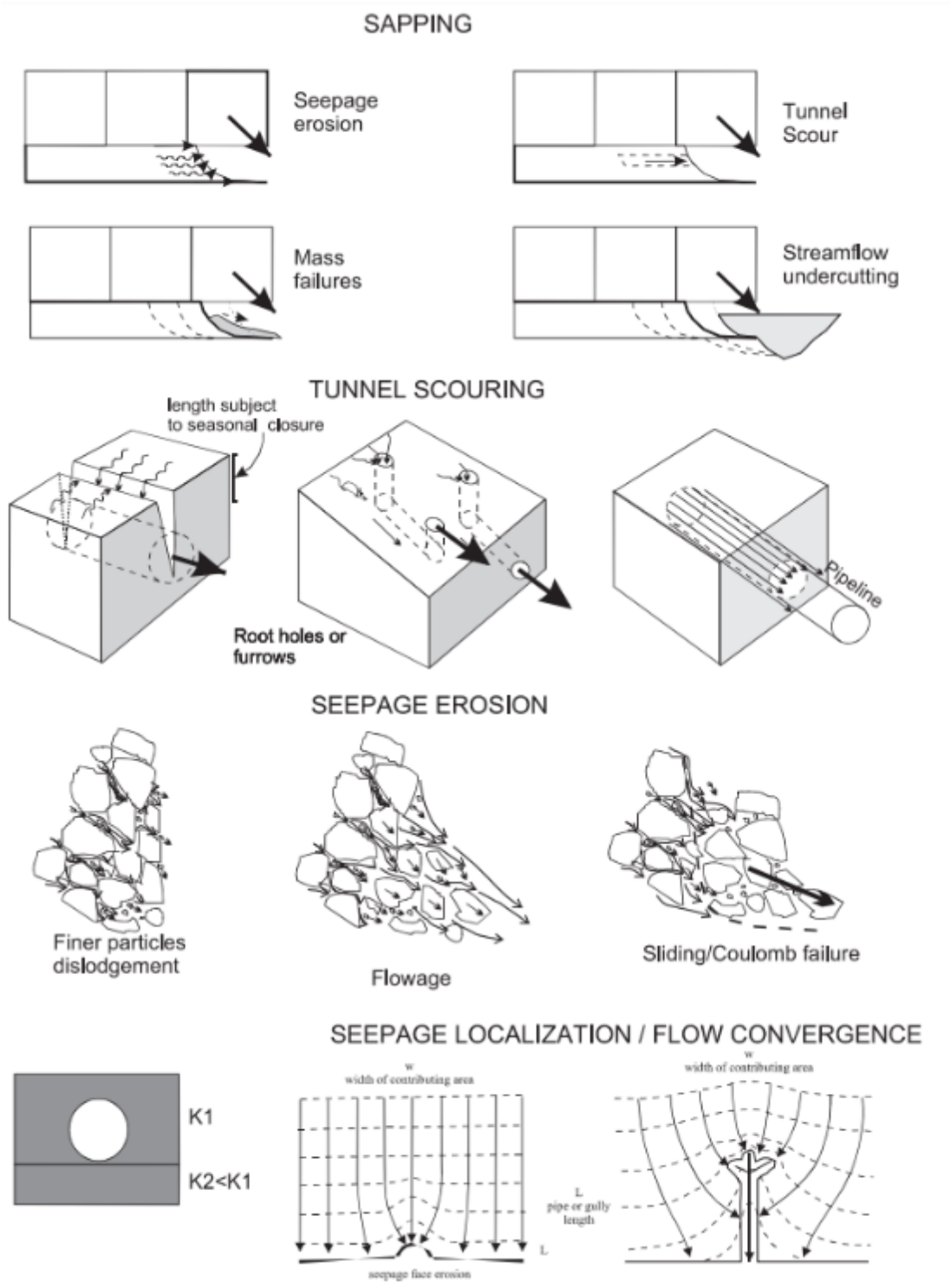

Figure 5.14 – A schematic of possible soil erosion processes, reviewed and presented by (Crosta and Prisco, 1999)

5.3 The debris flow geohazard

5.3.1 Gully accumulations and the conceptual model

Jakob et al. (2005) proposed a recharge rate for gully deposits, however this related to the long-term accumulation of bedrock sources in a supply-limited channel, the majority of which Martin et al. (2017) and Curry (1998) attribute to gully sidewall processes. Monitoring demonstrated that failures input large quantities of sediment into the gullies at RabT, material which may later be remobilised and entrained by the passage of upslope flows. May and Gresswell (2003) previously attributed ~20 % of channel sediments to recent slope failures, however the findings presented in this thesis suggest that the contribution by small failures is more significant. This is a similar conclusion to that made by Brayshaw & Hassan (2009) who found that 40 % of slope failures in British Columbia, contributed sediment to gullies without initiating channelised debris flows. Loye et al. (2016) highlighted seasonal inputs into the Manival torrent from high-magnitude hillslope failures via headwater channels as a significant source of sediment. In accordance with the conceptiual model presented here, the relative contribution of sediment to entrainment varies over time, and may be linked to the state of gully development. Less mature gullies, of lower width and with higher gradient walls, provide more readily erodible sediment whereas mature gullies, with wide gentle sidewalls, produce less sediment and are less susceptible to erosion by a passing debris flow (Curry, 1998). Gully accumulation from small-magnitude failures may therefore be relatively insignificant in less mature gullies.

An acknowledged assumption of the gully recharge rate is that debris flows completely scour accumulations of material (Jakob *et al.*, 2005; Martin *et al.*, 2017). The large October 2014 event appears to have scoured the majority of the basal deposits, resulting in a relatively low accumulation of material, however this research has shown that these gullies still contain approximately 0.4 m^3/m and 0.8 m^3/m of basal deposits respectively. Approximately 137 m^3 of sediment was also estimated to reside within the gully directly downslope of the SFLS1 source area and influx point. The gully along which RabT1I was detected, was found to contain approximately 1.2 m^3/m. A high elevation debris flow down this gully therefore has the potential to entrain more than 400 m^3 of basal deposits. Gully systems containing such sediment accumulations represent an elevated hazard over similar channels that have remained relatively inactive.

The succession of landslides in an upslope direction, as set out in the conceptual model, is of significance to the debris flow geohazard for two reasons. First, the earlier events appear to

erode channels enabling the more efficient runout of subsequent flows. Secondly, these initial events also leave material along the runout path and gully of future flow events. Entrainment has been shown to not only increase the flow magnitude (Reid *et al.*, 2011), but also the mobility (Iverson *et al.*, 2011), both of which would increase the eventual hazard. Conceptually, a succession of failures in the downslope direction might produce a smaller hazard. An initial large-magnitude high elevation failure, from the top of a drift mantled slope, may for example deposit material on the hillslope, particularly due to the lack of a well-defined channel with which it can couple, but also due to a lack of prior readily entrainable material. A subsequent failure, downslope, might entrain some of the material from the preceding failure, however it would not have access to material deposited upslope. This is in contrast to upslope sequencing, where a subsequent flow would have access to all of the previous event's deposits. Exhaustion of upslope material by the initial high elevation failure would also reduce the potential for any deposits to be mobilised at a later date.

The fate of material deposited on the open hillslope is unclear, but also of interest. Cavalli *et al.* (2013) presented a debris flow sediment connectivity index to differentiate between different areas of the hillslope, however such indices do not consider the potential for future changes in connectivity, the potential for which is highlighted by the conceptual model presented in this chapter. Sediments deposited within undeveloped sub-basins basins may, for example, become connected if a gully forms in the same location. In contrast, less convergent areas may simply revegetate and stabilise for the long term.

5.3.2 Coupling efficiency and runout potential

Brayshaw and Hassan (2009) attribute debris flow potential to a low angle of entry into the gully and increased runout gradient. This thesis has also indicated that general topographic confinement of the flow is of particular importance. Runout potential mapping, using the RAMMS-DF numerical model, has highlighted long zones of topographic confinement through which a debris flow could potentially mobilise over long distances. This has shown significant sensitivity to the position of the source area relative to the confining topography. For example, figure 5.15 shows an idealised failure from the source area of the SFLS1 event, which broadly matches the runout trajectory of the actual event. An equivalent failure just 50 m upslope (east) however has significantly greater runout potential. Differences between the controls on flow runouts appear subtle. Despite potential uncertainty in rheological parameters, the numerical model can significantly aid identification of relative mobility differences due to these factors.

The runout models did not account for entrainment, which would increase the magnitude of debris flows. During periods of high rainfall, associated with debris flow triggering, runoff would converge within gullies and saturate basal deposits providing a mechanism through which the debris flow mobility could increase (Iverson *et al.*, 2011). Flows that interact with a drainage network have generally been found to travel further due to the greater availability of surface water and readily mobilised sediment (Coe *et al.*, 2011). The conceptual model presented above also suggests that topographic convergence would influence the coincidence of debris flow runout with hydrological or hydrogeological flow accumulation, regardless of whether a defined channel exists yet. Flume experiments have shown that debris flow runout over dry sediments results in minimal scour, whereas wet sediments with volumetric water contents of 22 % or more give rise to significantly greater scour (Reid *et al.*, 2011). In prolonged rainfall experiments of 12 mm/hr, on a homogenous soil mantled model slope (Gevaert *et al.*, 2014), localised saturation has been to shown to occur around a topographic trough.

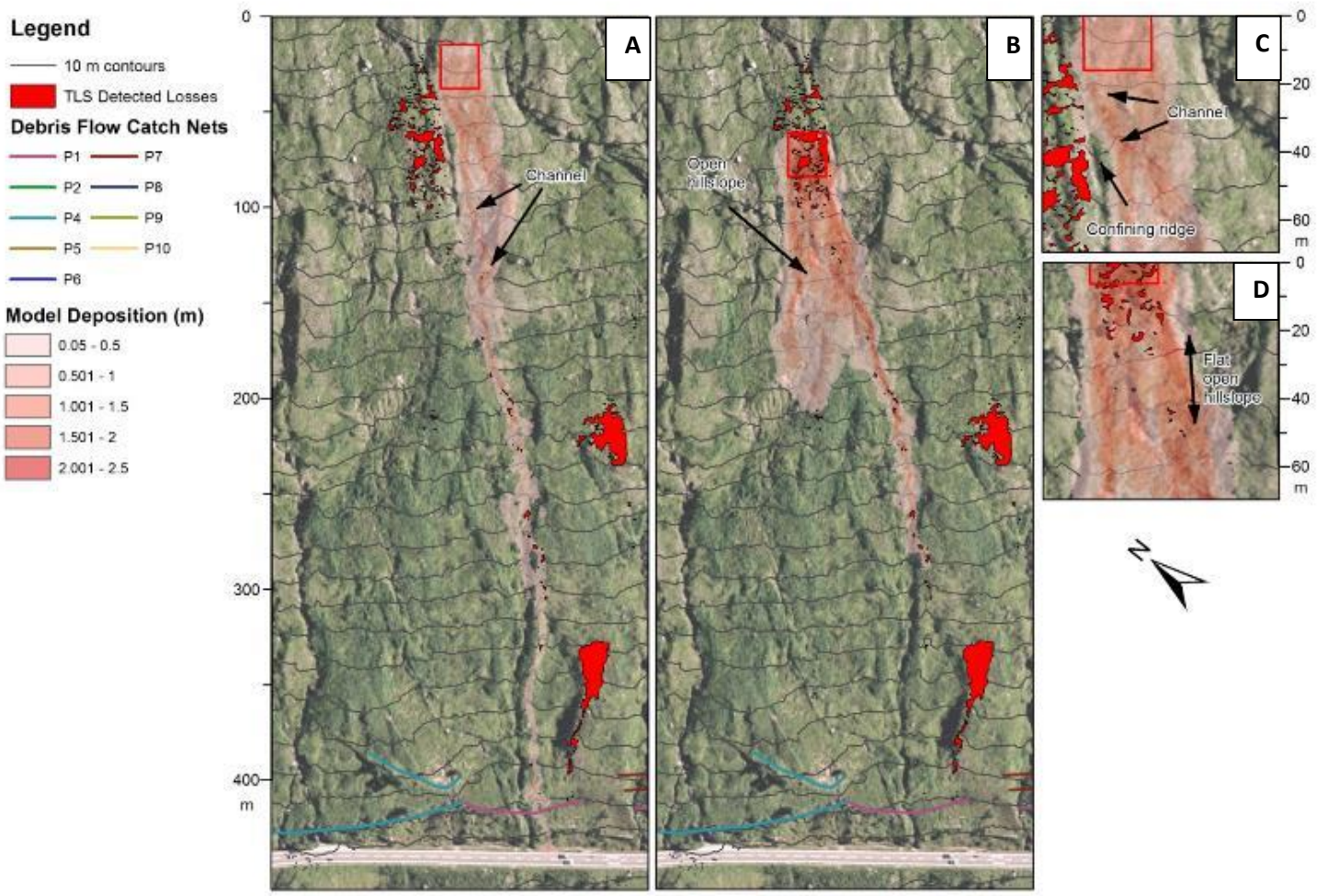

Figure 5.15 - A comparison of RAMMS model outputs, in which the magnitude of both modelled failures is the same. Despite the same input parameters, the runout distance of A is markedly larger than that of B (modelled from a similar source location as that of the real SFLS1 event. This increased runout distance wholly relates to the topography immediately below the source area, with that of A (C) containing one confining feature and that of B (D) being relatively flat, with separate features promoting branching.

5.3.3 The debris flow 'aftershock': source areas as a residual hazard

An additional 42.5 m^3 sediment was also detected to mobilise from the SFLS1 source area and side scarp following initial failure, clearly highlighting continued mobilisation of sediment into the system. A large magnitude failure (224 m^3) also occurred from the source area of SDLS1, within a month of the initial failure. These events, particularly the latter, demonstrate a residual hazard from shallow landslide scars. Recognition of this residual hazard is important where no mitigation structures exist, due to the increased vulnerability of road users. The large remobilisation detected from SDLS1 impacted a catch net which had been recently emptied of a previous deposit. This potentially reduced the effective net capacity when the SFLS1 event mobilised down to the same structure.

5.3.4 Anticipated future activity, slope development and hazard potential

The central slope region at the RabT has shown limited evidence of large, high elevation failures (> 450 m a.s.l), unlike the rest of the slope where large magnitude failures have occurred and mobilised downslope onto the trunk road. Recorded large-magnitude high elevation failures, such as that in October 2014 appear to simultaneously extend and scour gullies. Two shorter gullies, at the centre of the slope, meanwhile contain larger quantities of basal material, perhaps because a large-magnitude high elevation failure has not yet occurred. Combined, the SFLS1 and SDLS1 gullying have gradually increased the gully density at the centre of the slope, progressing it towards a more mature state like the region to the north-west. Should this activity represent a process of sediment reworking (Curry *et al.*, 2006), further such activity may be anticipated at the centre of the slope.

The areas at highest risk of debris flow hazards are those where the slope is modelled to have major flow potential but with little development, areas where there is evidence of past activity, and lower elevation failures and truncated gullies. Observations of gully hydrological flow are highlighted by a flow accumulation model. The model also indicates areas where significant accumulation occurs but no mature drainage features visibly exist. Some of these areas have demonstrated activity, both in the past inventory of change, but also during monitoring. No significant events have been recorded after these small changes have been detected, at least provisionally ruling them out as short-term precursors, as yet however such changes could represent longer term processes. If flow accumulation is a significant factor in the triggering of shallow failures, as indicated by analysis in the monitoring chapter, subsequent debris flows will be routed by the topographic convergence governing this flow, resulting in the rapid erosion and scour of new gully areas.

Figure 5.16 presents the overlap between modelled hydrological flow accumulation and debris flow runout potential. The combination of these datasets enables investigation of specific areas of concern, particularly along modelled flow lines. The TLS detected changes, RabT1E and RabT1F, which overlap modelled flow, are highlighted (figure 16). RabT1E, overlaps an area of low runout potential and thus would be less likely to pose a significant hazard. RabT1F overlaps an area of medium runout potential, below which it also connects with an area of low runout potential.

Zone C highlights an area to the south-east of the SFLS1 source area, separated by an inter-basin divide, in which high runout mobility and modelled flow are both found. The likelihood of failure here, assuming the availability of unstable material, is higher due to the presence of undeveloped flow accumulation. Initiation of a debris flow would also then have a much higher likelihood of reaching the road. In reality, the availability of material in this zone might be low and thus the hazard may actually be lower than predicted. Nonetheless, with targeted field validation this research demonstrates a potential approach for debris flow hazard assessment and mitigation.

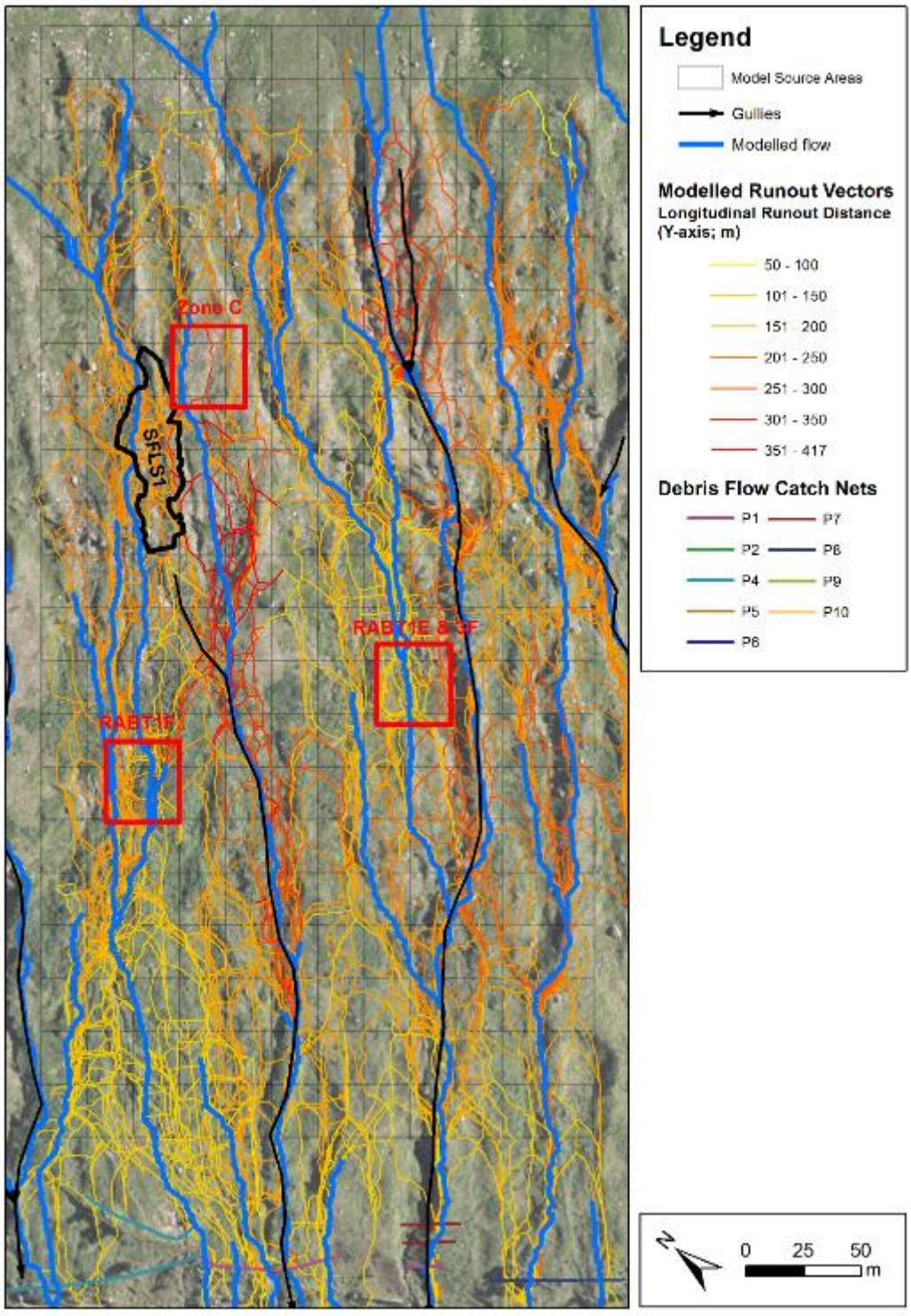

Figure 5.16 - A combined map of modelled flow accumulation and runout susceptibility. Such a product can be used to identify areas of particular susceptibility, such as that in Zone C where no well-defined gully yet exists.

CHAPTER 6

Conclusions

This research presents observations made of a hazardous, landscape evolving phenomena, the propensity of which may be impacted by future climatic changes. A greater understanding of this debris flow phenomena is vital in order to be able to suitably manage the hazard today and adapt to changes in the future. The initial findings presented should be of interest to road management authorities and should prompt further research for a better understanding of the debris flow phenomena and its interaction with other hydrogeomorphological processes. A summary of these findings is presented in this chapter, with suggestions for how further work, beyond the scope of this research, may be carried out.

6 A review of the initial research objectives

The overall objective of this research was to characterise the Scottish debris flow geohazard and the associated geomorphological controls relating to the phenomenon. This has been achieved using a combination of techniques, particularly aimed towards the Rest and be Thankful (A83) study site where a high frequency of activity has been recorded, both prior to and during this project. This thesis is comprised of four principal chapters, with the first three directly relating to at least one of the component research objectives presented in the introduction. The following section provides a summary of the findings presented in each chapter and offers an appraisal of how these have achieved the principal research objectives.

Objective 1: Mapping to collate existing data and build up an understanding of historic activity, as well as to provide an early contextualisation and characterisation of the study sites.

An inventory of events was compiled for all three study sites early in the project. Events at RabT, with available spatial information such as photographs, were subsequently mapped in a GIS, enabling an initial examination of the spatial and temporal distribution of failures.

- An inventory map of activity at RabT demonstrated a high level of activity over the past twenty years, with only limited comparable activity noted at the other two study sites, demonstrating a likely difference in the magnitude-frequency relationship at each.
- The inventory map of RabT also highlighted event zonation, with the north-west extent of the slope in particular experiencing three high elevation failures proximal

to one another, between 2012 and 2014, and an area to the south-east extent of the study site experiencing a similar pattern.

- A central area of the slope also demonstrated zonation, although the majority of events were recorded at a much lower elevation. This zonation suggested that there may be some form of geomorphic, or other, process influencing failures.
- Geomorphological maps comparing RabT and Glen Coe demonstrated the high density of gullies at the former compared to the latter. This was thought to perhaps correspond with the differing magnitude-frequency relationships at each site.
- A geomorphological map of RabT showed limited gully development within the central area of the slope, compared to the areas where high elevations events have been recorded. Shifts in discrete drainage have anecdotally been observed at the site and was initially considered a plausible driver of this zonation, although this was identified as an avenue requiring further investigation.

Objective 2: To build upon the mapping data through development and application of remote monitoring, to provide insight into the differing magnitude-frequency relationships between the sites, as well as to characterise the nature and methods of failure.

1. Seasonal vegetation fluxes were found to be problematic for repeat monitoring exercises, however these could be largely overcome by adoption of a particular survey regime which commences from the point of maximum dieback in early spring.

    - Despite the impact of vegetation and the long range of the surveys, fifteen small magnitude changes were detected, all smaller than those recorded in reports in the seven years prior to the project.
    - This demonstrated that long-range TLS could be applied to monitor such a phenomenon in a vegetated environment where the technique has rarely been applied before.

2. Small-magnitude failures represent a significant contributor towards gully accumulations, while steady-state in-situ sidewall collapses were rarely detected and do not appear to be a significant source. Debris flows at RabT also appear to actively scour the gully sidewalls during runout and are not wholly reliant on a prior supply of sediment.

    - Gully accumulations from sidewalls were identified as a principal source of debris flow entrainment in the literature, with some studies also highlighting inputs from

small failures as a significant source. This research found little in the way of significant accumulations from the gully sidewalls prior to debris flow events, although one of the largest debris flow events recorded during monitoring did appear to actively erode a relatively small quantity of material from the gully sidewalls during runout.

- Several small magnitude failures were detected throughout the monitoring period, with these inputting small quantities of material into the gully system. Further contributions were also found to occur from residual large-magnitude landslide deposits and remobilisations within recent landslide source areas. Continual inputs from such sources would result in significant accumulations over a relatively short decadal timespan.
- The evidence presented suggests that both accumulations and active gully erosion, during debris flow runout, are significant sources of the entrainment budget at RabT, although the relative contribution of material from gully sidewalls likely depends on the maturity of the gully.
- In contrast, accumulations at the Glen Ogle site appear to occur from the more steady-state degradation of exposed gully bedrock surfaces which showed clear entrainment potential during a slope walkover. Such sources were however degraded in-situ, without displacement from their source, potentially explaining the low volume of change detected at the site.
- At Glencoe, a large magnitude rockfall was found to mobilise into a gully, the breakdown of which could contribute to entrainment from a higher elevation failure within the same gully. Recorded debris flow activity at this site has been minimal however and rockfalls onto planar slope areas with an unimpeded trajectory towards the road are likely to pose a more significant hazard in the short term.

3. Shallow landslide source areas pose a residual hazard, due to large magnitude reactivations, potentially a long time after the initial failure (~ 1 year in the case of SFLS1).
    - These reactivations are a significant consideration where catch nets have been deployed, due to their ability to refill the structures after initial failure and clearing, thus potentially reducing the effective net capacity when a subsequent event mobilises into the same structure.

4. Debris flows are an effective agent of direct gully scour, particularly in areas of topographic convergence such as a deep hollow.

- This was demonstrated by the large magnitude SDLS1 event at RabT, whereas another comparable failure (SDLS1) on a flat hillslope area resulted in very little hillslope scour. This likely relates to the combined effect of the topography on maintaining a large erosive flow depth, as well as the localisation of water and elevated pore pressures along the runout path.

5. The topographic convergence of flow appears to be influential in the triggering of some failures, although the precise triggering mechanism is unclear.
   - Concentrated surface and sub-surface flow features were observed at RabT, and were particularly evident around shallow landslide source areas. The overlap between detected shallow failures and modelled flow accumulation was found to be significantly greater than expected using systematic sampling of the random probability.

6. No short-term precursory changes were detected, although it is considered that these may have been detectable at a lower LoD, or shortly before the timing of the landslide events. Other non-landslide changes, were however detected and could yet represent medium to long-term event precursors, or changes indicative of other activity.

7. Several failures, representing approximately 46 % of the landslide volume detected throughout the study at RabT, were found to predominantly deposit material on open hillslope areas, the long term stability of which remains uncertain.

Objective 3: To further understand the nature of the debris flow geohazard, particularly in relation to slope channels and gullies which may be of significance in facilitating runout and hazard development. Furthermore, to be able to critically appraise mitigation efforts

1. The RAMMS model is particularly sensitive to changes in the cohesion parameter, which is a critical component when modelling the runout extent and deposition on a steep hillslope. The Xi (viscous-turbulent friction) parameter meanwhile has a greater influence on the longitudinal distribution and thickness of deposition.
   - Most other studies have looked at debris flow runout within a lower gradient channel or torrent and generally do not discuss use of the cohesion parameter

2. The RAMMS model is capable of simulating debris flow runout across a range of variable topographic areas, however is unable to account for areas in which major rheological changes may take place i.e. when entering gullies containing streamflow.
    - The exhaustive runout modelling results showed a strong connection with slope gradient, but also with topographic convergence and confinement. This corroborates analysis of such factors within the monitoring chapter, in which topographic confinement was identified as a significant factor in the runout potential of two different debris flow events.
    - Large quantities of water accumulate within gullies during storms and intense rainfall. This water is likely to be incorporated into the flowing mass, reducing its viscosity and increasing its runout potential. The model can account for entrainment of solid materials, but precise accounting for the influence of hydrological flow discharge appears to be a challenge.
    - A continuum model such as RAMMS may therefore be best applied to modelling of the hillslope propagation stage, where flow rheologies are likely to be more homogenous, with separate channelised runout modelling. This would enable identification of sources with potential to couple with convergent slope zones, such as gullies, giving an indication of gully influx volumes.
    - For the derivation of engineering values, such as impact pressures for catch net design specifications, separate use of a gully-only model with different rheological parameters would be most suitable. An input hydrograph would be best suited to control the rate of flow down through the gully. This could either be informed by earlier open-hillslope model results, or ideally using data from an actual instrumented channelised debris flow to calibrate the model. Rheological parameters derived from this process may be of use for assessing runout through different gullies.
    - The RAMMS entrainment module may also be a useful addition to the modelling process, however this does not currently account for how the entrained mass may change the bulk flow rheology. A workaround may be to use different rheological zones, available within RAMMS (Bartelt *et al.*, 2017), however this may step into the territory of model overtuning for a specific event, hampering application of parameters to model different events.

3. Considerable mitigation focus (catch nets) appears to be paid to open hillslope areas where the runout potential onto the road appears to be limited. A different configuration of the same mitigation assets may yield a greater reduction in the debris flow geohazard.

    - A numerical debris flow runout model proved to be an effective way to conduct rigorous susceptibility mapping, to highlight relative differences in runout potential across the slope based upon consideration of topographic factors only.
    - A gully in the centre of the slope was found to focus a large number of debris flows, with greater runout potential than diffusive hillslope areas.
    - Only one long net is installed at the bottom of this gully however. This same net was struck by the SFLS1 debris flow, from which material continued to propagate onto the road.
    - Elsewhere, stacked flow nets have been installed, including on a relatively planar slope area where limited runout vectors were modelled. It is considered that single nets may be adequate in such areas and that stacked nets would be better focused on large gullies with much greater runout potential. Furthermore, stacked nets could be installed with greater spacing, with a higher elevation net serving to reduce momentum growth and entrainment at an earlier stage of the channelised runout.

Discussion chapter – Synthesise the different strands of the study and develop a conceptual model to characterise the Scottish debris flow phenomena, geohazard and related processes

1. Debris flow activity at RabT appears to be influenced by hydrological and/or hydrogeological activity on the hillslope. This would appear to explain periodic shifts in activity across the slope and may relate to the affect of material shifts blocking and diverting hydraulic flow paths (like a sluice).
    - Overlapping areas of modelled flow accumulation and high runout mobility can be used for an initial examination of detected changes which may represent a future precursor for a larger event. indicate zones of elevated hazard potential

2. Debris flows are capable of rapidly eroding new gully lengths and sequential upslope coupling of events results in the formation of longer and more mature features
    - Observations have been limited in the past, mostly due to issues in accessing and observing whole slopes from source to sink. TLS has primarily been used to identify

debris flow gullying potential, after which terrestrial photographs and historic aerial imagery have been examined, resulting in the identification of three debris flow gullying examples.

- A conceptual hydrogeomorphological model accounts for a wide range of observations, including the role of convergent topography in accumulating surface or subsurface flows of water, triggering of shallow failures, confinement of debris flows and thus also gully incision.
- Observed ephemeral gullies may be significant in the triggering of slope failures, however these may actually form from the collapse of soil pipes which have also been observed at RabT. Further still, soil pipes themselves may be the direct trigger of slope failure and are prone to sporadic switching during clogging, which could explain changing patterns of activity zonation at RabT over recent years.
- Sequential upslope debris flow activity and gully development can conceptually be explained by greater flow accumulation at the bottom of the slope and the associated acceleration of weathering processes which may act to preferentially reduce the shear strength of the slope bottom before the top.
- Gully development may be significant to the evolving nature of the geohazard at sites such as RabT, and recognition of this may aid anticipation of future hazardous events.

3. The findings of the study do lead to a coherent conceptual model of debris flows and gully development. This model postulates that truncated gullies and undeveloped flow accumulation lines are prone to development and thus may represent future hazard zones
    - Currently disconnected sediment stores within undeveloped zero-order basins may become connected should gully development occur.

6.1 Research limitations

This research project commenced with awareness of some limitations. Whilst attempts have been to minimise these where possible, some limitations are inherent to this type of study and are thus more broadly summarised in this section.

1. The limitations of long-range TLS have been discussed in some detail in the monitoring chapter, however the propagation of these within other areas of the study has not been considered yet.
    - The TLS LoD threshold is considered to have resulted in small changes potentially being overlooked, however little could feasibly be done to reduce the LoD, such as conducting change detection with single-station datasets, without compromising other factors such as complete data coverage. Regardless of this, exhaustive examination of high-resolution photographs throughout this study indicates that most, if not all, fully formed shallow failures have been detected.
    - Limitations in the TLS point density, relative to the change size, has resulted in underestimations of small-magnitude change volumes. This limits the use of such data within a volumetric magnitude-frequency relationship, although it is considered that the small volumes could potentially be corrected.
    - A lack of data coverage in the base of the gullies has limited this study's ability to directly evidence and comment on accumulations, particularly from small failures, although spreading of material would have likely resulted in these accumulations not being detected due to the high LoD. With a higher-range laser scanner, less prone to gully attenuation, such accumulations may surmount the LoD and be detectable over longer time periods.
    - The deposition data derived from long-range TLS was undermined by spreading of the flow mass below the LoD threshold, however this could be estimated through georeferencing and digitisation of flow photographs. This has had a direct impact on subsequent back-analysis of a debris flow runout model.
    - The TLS surveys only focused on the main component of the slope, above which an occluded depression and another area of slope continues beyond the range of the LMS-Z620 laser scanner used. Flow accumulation modelling was therefore not able to account for accumulation from further upslope, which may contribute more water than modelled during this study.

2. Long term observations are required to build a more complete inventory of events for more robust analysis.
    - Magnitude-frequency analysis at this early stage is tenuous and is sensitive to potential anomalies, such as the late 2015 winter events. A longer monitoring period is required in which the actual return period of such storm events is reflected.

- Whilst the overlap between detected events and modelled hydrology is significant, this has been based upon a limited sample size of changes. The modelled hydrological accumulation is also a simplification of actual flow patterns. Further work is required to validate this, particularly for the conceptual model presented.

3. This study presents inductive findings, principally derived from one main study site. More detailed investigative work is required to look at these findings in a more quantitative and deductive light, to support the presented conceptual model and examine its applicability to other sites.
    - This research has been case study, or problem, oriented and builds a conceptual geomorphological model based upon observations and findings that would have been very difficult to collect at another site over a similarly short period of time. This project has followed similar studies at other reliable debris flow sites, such as that of the Illgraben torrent in Switzerland, however it has focused on monitoring the whole hillslope to look at the debris flow phenomena more holistically, unlike any study before it.
    - Such research is invaluable and provides a solid basis for further detailed study, however this type of project inherently does not provide unequivocal answers (Gomez and Jones, 2010). The broad inductive nature of this research project has been a challenge, from the onset where monitoring was not guaranteed to provide insight, to the concluding stages where many interesting further research themes have arisen, but which are unfortunately beyond the scope of the initial project. The inductive nature of this project meant that only broad hypotheses could be considered from the outset and thus at times it has been difficult to objectively gauge progression of the research.
    - Nonetheless, this research project has presented findings which have immediate potential to be incorporated into existing management considerations, such as detailed monitoring of key slope zones and a different approach when designing and deploying mitigation structures such as catch nets. The research also provides a number of areas for further research, from which more deductive, hypothesis led studies can proceed.

6.2 Recommendations

Continued monitoring is recommended for a number of reasons, primarily to accumulate a large and robust record of change at the very active RabT study site. Large samples of activity,

preferably over longer timespans, better aid characterisation of the landslide magnitude-frequency (Evans, 2006) and would also enable further analysis of linking between changes and hydrological accumulation. Continued monitoring would also enable continued examination of gully accumulations, particularly from small-magnitude events, but also to monitor potential further gully development, detailed surveying of which is scarce and has limited our ability to better understand the phenomena (Castillo and Gómez, 2016). Potential medium-long term precursory changes may also be detected. The long term stability of recent hillslope deposits is also uncertain and would benefit from further study. This may be supplemented by collection and stitching of high resolution photographs, which have been invaluable during this study.

Monitoring using TLS in Scotland would best continue at a lower frequency (i.e. annual) due to the influence of seasonally vegetation growth and dieback. A temporally precise approach to monitoring would reduce the need to filter the seasonal vegetation signal, and should focus on collecting a 'base' dataset following winter vegetation dieback. Owing to sequential activity after an initial failure however (such as that found in the case of SDLS1) and the potential for channel incision, high frequency monitoring after events and around the winter intervals would also be considered good practice at a site of high frequency activity. In contrast, sites such as Glen Ogle may benefit from continued monitoring at a much lower frequency, which might enable detection of more significant gully accumulations in response to rainfall events, potentially accumulations above a large level of detection, or simply to more confidently characterise the site as relatively inactive over shorter timescales, with dependence on steady-state gully accumulations. The 2 km range LMS-Z620 and 4 km range VZ-4000 were not able to sample gully floor data with adequate coverage to reliably detect change (likely due to attenuation by oblique, dark and saturated surfaces). The VZ-4000 was an improvement over the LMS-Z620 however and a further improvement in TLS capabilities (range) may aid better data acquisition. It remains a possibility that the sediment budget of such areas could be monitored by a more powerful platform such as the Riegl VZ-6000. Aerial platforms afford opportunities to collect un-obscured photogrammetric data from much shorter ranges, although this can be challenging across a large site with steep terrain and often adverse weather conditions. UAV based Lidar platforms are also an area of development which could show promise for the surveying of gully deposits in the coming years.

Use of ground penetrating radar (GPR) or other investigative methods such as microgravity inspection may prove to be particularly insightful, first to investigate spatial variability in

sediment availability and exhaustion, but also to map the location and extent of sub-surface drainage features such as macropores and pipe networks.

Surveys could be focused around areas of high flow accumulation modelled during this study. Coupling of GPR data with continued TLS monitoring might support the conceptual model presented within this thesis, or present insight for refinement or correction. GPR derived regolith depths would allow a more objective assessment of debris flow potential, particularly if combined with the susceptibility modelling data to identify source cells of high failure potential. New platforms are continually developing to conduct extensive GPR surveys, including heavy-load UAVs. Passive seismic monitoring (i.e. Tromino) may also be of use, particularly to investigate specific active slope zones, and negate the backscatter issues related to coarse grain matrices. Alternatively, Electrical Resistivity Tomography (ERT) surveys could prove useful for the identification of lithologies and groundwater zones which may be influential in hydrological and hydrogeological flow distribution for example.

References

Aaron, J., Hungr, O. and McDougall, S. (2016) 'Development of a systematic approach to calibrate equivalent fluid runout models', in Landslides and Engineered Slopes. Experience, Theory and Practice. pp. 605-620.

Abellán, A., Derron, M.-H., Jaboyedoff, M., Abellán, A., Derron, M.-H. and Jaboyedoff, M. (2016) '"Use of 3D Point Clouds in Geohazards" Special Issue: Current Challenges and Future Trends', Remote Sensing, 8(2), pp. 130. doi: 10.3390/rs8020130.

Abellán, A., Jaboyedoff, M., Oppikofer, T. and Vilaplana, J. M. (2009) 'Detection of millimetric deformation using a terrestrial laser scanner: Experiment and application to a rockfall event', Natural Hazards and Earth System Science, 9(2), pp. 365–372. doi: 10.5194/nhess-9-365-2009.

Abellán, A., Oppikofer, T., Jaboyedoff, M., Rosser, N. J., Lim, M. and Lato, M. J. (2014) 'Terrestrial laser scanning of rock slope instabilities', Earth Surface Processes and Landforms, 39(1), pp. 80–97. doi: 10.1002/esp.3493.

Abellán, A., Vilaplana, J. M., Calvet, J., García-Sellés, D. and Asensio, E. (2011) 'Rockfall monitoring by Terrestrial Laser Scanning - Case study of the basaltic rock face at Castellfollit de la Roca (Catalonia, Spain)', Natural Hazards and Earth System Science, 11(3), pp. 829–841. doi: 10.5194/nhess-11-829-2011.

Acharya, G., Cochrane, T. A., Davies, T. and Bowman, E. (2009) 'The influence of shallow landslides on sediment supply: A flume-based investigation using sandy soil', Engineering Geology. pp. 161-169. doi: 10.1016/j.enggeo.2009.06.008.

Akca, D. (2007) 'Matching of 3D surfaces and their intensities', ISPRS Journal of Photogrammetry and Remote. 62(2). pp 112-121.

Ali, M., Sterk, G., Seeger, M., Boersema, M. and Peters, P. (2012) 'Effect of hydraulic parameters on sediment transport capacity in overland flow over erodible beds', Hydrology and Earth System Sciences. 8(4) pp 6939-6965. doi: 10.5194/hess-16-591-2012.

Anderson, K., Hancock, S., Disney, M. and Gaston, K. J. (2016) 'Is waveform worth it? A comparison of LiDAR approaches for vegetation and landscape characterization', Rocchini, D. and Boyd, D. (eds) Remote Sensing in Ecology and Conservation, 2(1), pp. 5–15. doi: 10.1002/rse2.8.

Anderson, S. P., Dietrich, W. E., Montgomery, D. R., Torres, R., Conrad, M. E. and Loague, K. (1997) 'Subsurface flow paths in a steep, unchanneled catchment', Water Resources Research, 33(12), pp. 2637–2653. doi: 10.1029/97WR02595.

Arattano, M., Marchi, L. and Cavalli, M. (2012) 'Analysis of debris-flow recordings in an instrumented basin: confirmations and new findings', Natural Hazards and Earth System Science. Copernicus GmbH, 12(3), pp. 679–686. doi: 10.5194/nhess-12-679-2012.

Armanini, A., Fraccarollo, L., Larcher, M., Armanini, A., Fraccarollo, L. and Larcher, M. (2005) 'Debris Flow', in Encyclopedia of Hydrological Sciences. pp. 2173-2185 Chichester, UK: John Wiley & Sons, Ltd. doi: 10.1002/0470848944.hsa149.

Arrochar Heritage (2019) History of the Rest and be Thankful. Available at: http://www.arrocharheritage.com/HistoryOfTheRestAndBeThankfulNewRoad.htm (Accessed: 28 July 2019).

van Asch, T. W. ., Buma, J. and Van Beek, L. P. . (1999) 'A view on some hydrological triggering systems in landslides', Geomorphology, 30(1-2), pp. 25–32. doi: 10.1016/S0169-555X(99)00042-2.

van Asch, T. W., Malet, J. P., Remaitre, A. and Maquaire, O. (2004) 'Numerical modelling of the run-out of a muddy debris flow. The effect of rheology on velocity and deposit thickness along the run-out track', in Landslides: Evaluation and Stabilization, Proceedings of the 9th International Symposium on Landslides, pp. 1433–1439.

Ashmore, P. (1993) 'Contemporary erosion of the Canadian landscape', Progress in Physical Geography. 17(2). pp 190-204.

Ashwood, W. (2014) 'Numerical model for the prediction of total dynamic landslide forces on flexible barriers.' University of British Columbia. doi: 10.14288/1.0167322.

Bagnold, R. (1954) 'Experiments on a gravity-free dispersion of large solid spheres in a Newtonian fluid under shear', Proceedings of the Royal Society of. 225(1160). pp. 49-63.

Bagnold, R. (1968) 'Deposition in the Process of Hydraulic Transport', Sedimentology. 10(1). pp. 45-56.

Ballantyne, C. (1981) 'Periglacial landforms and environments on mountains in the Northern Highlands of Scotland.'

Ballantyne, C. (2002a) 'Debris flow activity in the Scottish Highlands: temporal trends and wider implications for dating', Studia Geomorphologica Carpatho-Balcanica, 36, pp. 7–27.

Ballantyne, C. K. (1986) 'Landslides and slope failures in Scotland: A review', Scottish Geographical Magazine. Taylor & Francis Group, 102(3), pp. 134–150. doi: 10.1080/00369228618736667.

Ballantyne, C. K. (1991) 'Holocene geomorphic activity in the Scottish Highlands', Scottish Geographical Magazine, 107(2), pp. 84–98. doi: 10.1080/00369229118736815.

Ballantyne, C. K. (2002b) ‘A general model of paraglacial landscape response’, The Holocene. SAGE Publications, 12(3), pp. 371–376. doi: 10.1191/0959683602hl553fa.

Ballantyne, C. K. (2002c) ‘Paraglacial geomorphology’, Quaternary Science Reviews, 21(18-19), pp. 1935–2017. doi: 10.1016/S0277-3791(02)00005-7.

Ballantyne, C. K. (2003) ‘A Scottish sturzstrom: The Beinn Alligin rock avalanche, Wester Ross’, Scottish Geographical Journal. Taylor & Francis Group , 119(2), pp. 159–167. doi: 10.1080/00369220318737169.

Ballantyne, C. K. (2004) Geomorphological changes and trends in Scotland: debris-flows, Scottish Natural Heritage Commissioned Report No. 052 (ROAME No. F00AC107A). Available at: http://www.snh.org.uk/pdfs/publications/commissioned_reports/F00AC107A.pdf (Accessed: 13 October 2014).

Ballantyne, C. K. (2008) ‘After the Ice: Holocene Geomorphic Activity in the Scottish Highlands’, Scottish Geographical Journal, pp. 8–52. doi: 10.1080/14702540802300167.

Ballantyne, C. K. (2018) After the ice: Lateglacial and Holocene landforms and landscape evolution in Scotland, Transactions of The Royal Society of Edinburgh. pp. 1-39. Edinburgh. Available at: https://www.cambridge.org/core/journals/earth-and-environmental-science-transactions-of-royal-society-of-edinburgh/article/after-the-ice-lateglacial-and-holocene-landforms-and-landscape-evolution-in-scotland/91899F93AA38C525379D2D7C9E0520F2 (Accessed: 12 June 2018).

Ballantyne, C. K. and Benn, D. I. (1994) ‘Paraglacial Slope Adjustment and Resedimentation Following Recent Glacier Retreat, Fabergstolsdalen, Norway’, Arctic and Alpine Research, 26(3), p. 255. doi: 10.2307/1551938.

Ballantyne, C. K. and Benn, D. I. (1996) ‘Paraglacial slope adjustment during recent deglaciation and its implications for slope evolution in formerly glaciated environments’, Advances in hillslope processes, 2, pp. 1173–1195.

Ballantyne, C. K. and Harris, C. (1994) Frost weathering and mountain-top detritus, in ‘The Periglaciation of Great Britain’, pp. 163-192. Cambridge University Press, Cambridge.

Ballantyne, C. K., Sandeman, G. F., Stone, J. O. and Wilson, P. (2014) ‘Rock-slope failure following Late Pleistocene deglaciation on tectonically stable mountainous terrain’, Quaternary Science Reviews, 86, pp. 144–157. doi: 10.1016/j.quascirev.2013.12.021.

Ballantyne, C. K. and Stone, J. O. (2004) ‘The Beinn Alligin rock avalanche, NW Scotland: cosmogenic ¹⁰Be dating, interpretation and significance’, The Holocene. SAGE Publications, 14(3), pp. 448–453. doi: 10.1191/0959683604hl720rr.

Ballantyne, C. K. and Stone, J. O. (2013) 'Timing and periodicity of paraglacial rock-slope failures in the Scottish Highlands', Geomorphology, 186, pp. 150–161. doi: 10.1016/j.geomorph.2012.12.030.

Ballantyne, C. K., Stone, J. O. and Fifield, L. K. (1998) 'Cosmogenic Cl-36 dating of postglacial landsliding at The Storr, Isle of Skye, Scotland', The Holocene. SAGE Publications, 8(3), pp. 347–351. doi: 10.1191/095968398666797200.

Ballantyne, C. and Whittington, G. (1999) 'Late Holocene floodplain incision and alluvial fan formation in the central Grampian Highlands, Scotland: chronology, environment and implications', Journal of Quaternary Science. 14(7). pp. 651-671.

Barla, M., Antolini, F., Bertolo, D., Thuegaz, P., D'Aria, D. and Amoroso, G. (2017) 'Remote monitoring of the Comba Citrin landslide using discontinuous GBInSAR campaigns', Engineering Geology. Elsevier, 222, pp. 111–123. doi: 10.1016/J.ENGGEO.2017.03.019.

Barnhart, T. and Crosby, B. (2013) 'Comparing Two Methods of Surface Change Detection on an Evolving Thermokarst Using High-Temporal-Frequency Terrestrial Laser Scanning, Selawik River, Alaska', Remote Sensing. Multidisciplinary Digital Publishing Institute, 5(6), pp. 2813–2837. doi: 10.3390/rs5062813.

Bartelt, P., Bieler, C., Buhler, Y., Christen, M., Deubelbeiss, Y., Graf, C., McArdell, B., Salz, M. and Schneider, M. (2017) RAMMS Debris Flow User Manual V1.7. Available at: http://ramms.slf.ch/ramms/downloads/RAMMS_DBF_Manual.pdf.

Bartelt, P., Buehler, Y., Christen, M., Deubelbeiss, Y., Graf, C., McArdell, B., Salz, M. and Schneider, M. (2013) 'RAMMS Debris Flow User Manual v1.5.' Available at: http://ramms.slf.ch/ramms/downloads/RAMMS_DBF_Manual.pdf (Accessed: 6 November 2017).

Baum, R. L. and Godt, J. W. (2010) 'Early warning of rainfall-induced shallow landslides and debris flows in the USA', Landslides. Springer-Verlag, 7(3), pp. 259–272. doi: 10.1007/s10346-009-0177-0.

BBC (2014) Efforts to clear 2,000-tonne Rest and Be Thankful landslide. Available at: http://www.bbc.co.uk/news/uk-scotland-glasgow-west-29817282 (Accessed: 15 February 2016).

BBC (2015) Storm Frank: Power cuts and flooding as Scotland battered - BBC News. Available at: http://www.bbc.co.uk/news/uk-scotland-35195275 (Accessed: 13 April 2018).

Beer, A. R., Turowski, J. M. and Kirchner, J. W. (2017) 'Spatial patterns of erosion in a bedrock gorge', Journal of Geophysical Research: Earth Surface, 122(1), pp. 191–214. doi: 10.1002/2016JF003850.

Beguería, S. (2006) 'Changes in land cover and shallow landslide activity: A case study in the

Beguería, S., W. J. Van Asch, T., Malet, J. P. and Gröndahl, S. (2009) 'A GIS-based numerical model for simulating the kinematics of mud and debris flows over complex terrain', Natural Hazards and Earth

System Science, 9(6), pp. 1897–1909. doi: 10.5194/nhess-9-1897-2009. Spanish Pyrenees', Geomorphology. 74(1-4). pp. 196-206. doi: 10.1016/j.geomorph.2005.07.018.

Benda, L. and Dunne, T. (1997) 'Stochastic forcing of sediment supply to channel networks from landsliding and debris flow', Water Resources Research. 33(12). pp. 2849-2863.

Benda, L. E. and Cundy, T. W. (1990) 'Predicting deposition of debris flows in mountain channels', Canadian Geotechnical Journal. NRC Research Press Ottawa, Canada, 27(4), pp. 409–417. doi: 10.1139/t90-057.

Benda, L. E. and Dunne, T. (1987) 'Sediment routing by debris flow', Proceedings of an international symposium on Erosion and sedimentation in the Pacific Rim IAHS-AISH Publication, 165(165), pp. 213–223.

Benjamin, J., Rosser, N. and Brain, M. (2016) 'Rockfall detection and volumetric characterisation using LiDAR', in Aversa, S., Cascini, L., Picarelli, L. and Scavia, C. (eds) Landslides and Engineered Slopes. Experience, Theory and Practice. Napoli, Italy, pp. 12-19.

Benn, D. and Evans, D. (2014) Glaciers and Glaciation. Arnold, London.

Benn, D. I. and Evans, D. J. A. (1998) Glaciers and Glaciation. Arnold, London.

Bennett, G. L., Molnar, P., Eisenbeiss, H. and McArdell, B. W. (2012) 'Erosional power in the Swiss Alps: characterization of slope failure in the Illgraben', Earth Surface Processes and Landforms. John Wiley & Sons, Ltd, 37(15), pp. 1627–1640. doi: 10.1002/esp.3263.

Berger, C., McArdell, B. W. and Schlunegger, F. (2011) 'Direct measurement of channel erosion by debris flows, Illgraben, Switzerland', Journal of Geophysical Research: Earth Surface, 116. doi: 10.1029/2010JF001722.

Bergonse, R. V. and Reis, E. J. (2011) 'Theoretical constraints to gully erosion research: time for a re-evaluation of concepts and assumptions?', Earth Surface Processes and Landforms. John Wiley & Sons, Ltd, 36(11), pp. 1554–1557. doi: 10.1002/esp.2188.

Besl, P. and McKay, N. (1992) 'A method for registration of 3-D shapes', IEEE Transactions on pattern analysis. 1611. pp. 586-607.

Betts, H. and DeRose, R. (1999) 'Digital elevation models as a tool for monitoring and measuring gully erosion', International Journal of Applied Earth Observation. 1(2). pp. 91-101.

BGS (2007) 'Analytical Poster: 2007 Landslide at the Rest and be Thankful.' Available at: http://www.bgs.ac.uk/downloads/start.cfm?id=1245.

BGS (2009) Borehole Record 18378275 - A83 Rest and be Thankful - 223651, 707025. Available at: http://scans.bgs.ac.uk/sobi_scans/boreholes/18378275/images/18380413.html (Accessed: 11 April 2018).

BGS (2017) BGS 1:50,000 Scale Geology of Glencoe. Available at: http://www.bgs.ac.uk/products/digitalmaps/DiGMapGB_50.html (Accessed: 4 June 2017).

BGS (2018) Geology of Britain viewer. Available at: https://www.bgs.ac.uk/discoveringGeology/geologyOfBritain/viewer.html (Accessed: 31 July 2018).

Bickerdike, H. L., Evans, D. J. A., Ó Cofaigh, C. and Stokes, C. R. (2016) 'The glacial geomorphology of the Loch Lomond Stadial in Britain: a map and geographic information system resource of published evidence', Journal of Maps, 12(5), pp. 1178–1186. doi: 10.1080/17445647.2016.1145149.

Blahut, J., Horton, P., Sterlacchini, S. and Jaboyedoff, M. (2010) 'Debris flow hazard modelling on medium scale: Valtellina di Tirano, Italy', Nat. Hazards Earth Syst. Sci, 10, pp. 2379–2390. doi: 10.5194/nhess-10-2379-2010.

Blasio, F. De (2011) Introduction to the physics of landslides: lecture notes on the dynamics of mass wasting. Springer, Heidelberg.

Bocco, G. (1991) 'Gully erosion: processes and models', Progress in Physical Geography. Sage PublicationsSage CA: Thousand Oaks, CA, 15(4), pp. 392–406. doi: 10.1177/030913339101500403.

Bogaard, T. A. and Greco, R. (2016) 'Landslide hydrology: from hydrology to pore pressure', Wiley Interdisciplinary Reviews: Water. 3(3). pp 439-459. doi: 10.1002/wat2.1126.

Borstad, C. P. and McClung, D. M. (2009) 'Sensitivity analyses in snow avalanche dynamics modeling and implications when modeling extreme events', Canadian Geotechnical Journal, 46(9), pp. 1024–1033. doi: 10.1139/T09-042.

Bovis, M. J. and Jakob, M. (1999) 'The role of debris supply conditions in predicting debris flow activity', Earth Surface Processes and Landforms, 24, pp. 1039–1054. doi: 10.1002/(SICI)1096-9837(199910)24:11<1039::AID-ESP29>3.0.CO;2-U.

Bracken, L., Turnbull, L. and Wainwright, J. (2015) 'Sediment connectivity: a framework for understanding sediment transfer at multiple scales', Earth Surface Processes and Landforms. 40(2), pp. 177-188.

Brardinoni, F. and Church, M. (2004) 'Representing the landslide magnitude-frequency relation: Capilano River basin, British Columbia', Earth Surface Processes and Landforms, 29(1), pp. 115–124. doi: 10.1002/esp.1029.

Brasington, J., Vericat, D. and Rychkov, I. (2012) 'Modeling river bed morphology, roughness, and surface sedimentology using high resolution terrestrial laser scanning', Water Resources Research, 48(11). doi: 10.1029/2012WR012223.

Brayshaw, D. and Hassan, M. A. (2009) 'Debris flow initiation and sediment recharge in gullies', Geomorphology, 109(3-4), pp. 122–131. doi: 10.1016/j.geomorph.2009.02.021.

Brazier, V. and Ballantyne, C. K., (1989) 'Late Holocene debris cone evolution in Glen Feshie, western Cairngorm Mountains, Scotland', Transactions of the Royal Society of Edinburgh: Earth Sciences. Royal Society of Edinburgh Scotland Foundation, 80(01), pp. 17–24. doi: 10.1017/S0263593300012244.

Brazier, V., Whittington, G. and Ballantyne, C. K. (1988) 'Holocene debris cone evolution in Glen Etive, Western Grampian Highlands, Scotland', Earth Surface Processes and Landforms. John Wiley & Sons, Ltd, 13(6), pp. 525–531. doi: 10.1002/esp.3290130606.

Bremer, M. and Sass, O. (2012) 'Combining airborne and terrestrial laser scanning for quantifying erosion and deposition by a debris flow event', Geomorphology. Elsevier, 138(1), pp. 49–60. doi: 10.1016/j.geomorph.2011.08.024.

Brodu, N. and Lague, D. (2012) '3D point cloud classification of complex natural scenes using a multi-scale dimensionality criterion: applications in geomorphology', EGU General Assembly Conference. 14. p. 4368. Available at: http://adsabs.harvard.edu/abs/2012EGUGA..14.4368B (Accessed: 11 September 2015).

Brooks, S. M., Anderson, M. G. and Collison, A. J. C. (1995) 'Modelling the role of climate, vegetation and pedogenesis in shallow translational hillslope failure', Earth Surface Processes and Landforms. doi: 10.1002/esp.3290200305.

Brunetti, M. T., Guzzetti, F., Cardinali, M., Fiorucci, F., Santangelo, M., Mancinelli, P., Komatsu, G. and Borselli, L. (2014) 'Analysis of a new geomorphological inventory of landslides in Valles Marineris, Mars', Earth and Planetary Science Letters.405. pp. 156-168. doi: 10.1016/j.epsl.2014.08.025.

Brunetti, M. T., Guzzetti, F. and Rossi, M. (2009) 'Probability distributions of landslide volumes', Nonlinear Processes in Geophysics, 16(2), pp. 179–188. doi: 10.5194/npg-16-179-2009.

Bull, L. J. and Kirkby, M. J. (1997) 'Gully processes and modelling', Progress in Physical Geography. Sage PublicationsSage CA: Thousand Oaks, CA, 21(3), pp. 354–374. doi: 10.1177/030913339702100302.

Bull, L. and Kirkby, M. (2002) Dryland rivers: hydrology and geomorphology of semi-arid channels. Wiley & Sons Ltd, Chichester.

Burke, B. C., Heimsath, A. M. and White, A. F. (2007) 'Coupling chemical weathering with soil production across soil-mantled landscapes', Earth Surface Processes and Landforms, 32(6), pp. 853–873. doi: 10.1002/esp.1443.

Caine, N. (1980) 'The rainfall intensity: duration control of shallow landslides and debris flows', Geografiska Annaler. Series A. Physical Geography, 62, pp. 23–27. Available at: http://www.jstor.org/stable/520449 (Accessed: 21 December 2014).

Calvo, L., Haddad, B., Pastor, M. and Palacios, D. (2015) 'Runout and deposit morphology of Bingham fluid as a function of initial volume: implication for debris flow modelling', Natural Hazards. Springer Netherlands, 75(1), pp. 489–513. doi: 10.1007/s11069-014-1334-x.

Cannon, S. H., Bigio, E. R. and Mine, E. (2001) 'A process for fire-related debris flow initiation, Cerro Grande fire, New Mexico', Hydrological Processes. John Wiley & Sons, Ltd., 15(15), pp. 3011–3023. doi: 10.1002/hyp.388.

Cannon, S. H., Kirkham, R. M. and Parise, M. (2001) 'Wildfire-related debris-flow initiation processes, Storm King Mountain, Colorado', Geomorphology, 39(3-4), pp. 171–188. doi: 10.1016/S0169-555X(00)00108-2.

Capra, L., Borselli, L., Varley, N., Gavilanes-Ruiz, J. C., Norini, G., Sarocchi, D., Caballero, L. and Cortes, A. (2010) 'Rainfall-triggered lahars at Volcán de Colima, Mexico: Surface hydro-repellency as initiation process', Journal of Volcanology and Geothermal Research, 189(1), pp. 105–117. doi: 10.1016/j.jvolgeores.2009.10.014.

Carbonneau, P. E., Lane, S. N. and Bergeron, N. E. (2003) 'Cost-effective non-metric close-range digital photogrammetry and its application to a study of coarse gravel river beds', International Journal of Remote Sensing, 24(14), pp. 2837–2854. doi: 10.1080/01431160110108364.

Casalí, J., Giménez, R. and Campo-Bescós, M. (2015) 'Gully geometry: what are we measuring?', Soil. 1(2) pp. 509-513.

Castagnetti, C. and Bertacchiniab, E. (2014) 'A reliable methodology for monitoring unstable slopes: the multi-platform and multi-sensor approach', Earth Resources and Envionmental Remote Sensing/GIS Applications. 9245.

Castellanos, A. (2008) Multi-scale landslide risk assessment in Cuba. Utrecht. Available at: https://dspace.library.uu.nl/handle/1874/30890 (Accessed: 5 April 2018).

Castillo, C. and Gómez, J. A. (2016) 'A century of gully erosion research: Urgency, complexity and study approaches', Earth-Science Reviews. 160. pp. 300-319. doi: 10.1016/j.earscirev.2016.07.009.

Cavalli, M., Trevisani, S., Comiti, F. and Marchi, L. (2013) 'Geomorphometric assessment of spatial sediment connectivity in small Alpine catchments', Geomorphology, 188, pp. 31–41. doi: 10.1016/j.geomorph.2012.05.007.

Centre for Environmental Data Analysis (2017) 'Rest and be Thankul - Daily Rainfall Data.' Available at: http://www.ceda.ac.uk/.

Chen, C.-W., Saito, H. and Oguchi, T. (2015b) 'Rainfall intensity–duration conditions for mass movements in Taiwan', Progress in Earth and Planetary Science. Springer Berlin Heidelberg, 2(1), p. 14. doi: 10.1186/s40645-015-0049-2.

Chen, N., Chen, M., Li, J., He, N., Deng, M., Iqbal Tanoli, J. and Cai, M. (2015a) 'Effects of human activity on erosion, sedimentation and debris flow activity - A case study of the Qionghai Lake watershed, southeastern Tibetan Plateau, China', The Holocene. SAGE Publications, 25(6), pp. 973–988. doi: 10.1177/0959683615574893.

Chen, N. S., Zhou, W., Yang, C. L., Hu, G. S., Gao, Y. C. and Han, D. (2010) 'The processes and mechanism of failure and debris flow initiation for gravel soil with different clay content', Geomorphology, 121(3), pp. 222–230. doi: 10.1016/j.geomorph.2010.04.017.

Christen, M., Bühler, Y., Bartelt, P., Leine, R., Glover, J., Schweizer, A., Graf, C., Mcardell, B. W., Gerber, W., Deubelbeiss, Y. and Feistl, T. (2012) 'Integral hazard management using a unified software environment. Numerical simulation tool "RAMMS" for gravitational natural hazards', Proceedings Vol 1 12th Congress INTERPRAEVENT 2012 Grenoble France 23th 26th April 2012, pp. 77–86. doi: ISBN 978-3-901164-19-4.

Christen, M., Kowalski, J. and Bartelt, P. (2010) 'RAMMS: Numerical simulation of dense snow avalanches in three-dimensional terrain', Cold Regions Science and Technology, 63(1-2), pp. 1–14. doi: 10.1016/j.coldregions.2010.04.005.

Church, M., Ham, D., Hassan, M. and Slaymaker, O. (1999) 'Fluvial clastic sediment yield in Canada: scaled analysis', Canadian Journal of Earth Sciences. NRC Research Press Ottawa, Canada , 36(8), pp. 1267–1280. doi: 10.1139/e99-034.

Church, M. and Ryder, J. M. (1972) 'Paraglacial sedimentation: A consideration of fluvial processes conditioned by glaciation', Bulletin of the Geological Society of America, 83, pp. 3059–3072. doi: 10.1130/0016-7606(1972)83[3059:PSACOF]2.0.CO;2.

Church, M. and Slaymaker, O. (1989) 'Disequilibrium of Holocene sediment yield in glaciated British Columbia', Nature. 337. pp. 452-454.

Clark, C. D., Hughes, A. L. C., Greenwood, S. L., Jordan, C. and Sejrup, H. P. (2012) 'Pattern and timing of retreat of the last British-Irish Ice Sheet', Quaternary Science Reviews. 44. pp/ 112-146. doi: 10.1016/j.quascirev.2010.07.019.

CloudCompare (2018) 'CloudCompare v 2.9.1.' Available at: http://www.danielgm.net/cc/.

Coe, J. A., Glancy, P. A. and Whitney, J. W. (1997) 'Volumetric analysis and hydrologic characterization of a modern debris flow near Yucca Mountain, Nevada', Geomorphology, 20(1-2), pp. 11–28. doi: Doi 10.1016/S0169-555x(97)00008-1.

Coe, J. A., Reid, M. E., Brien, D. L. and Michael, J. A. (2011) 'Assessment of topographic and drainage network controls on debris-flow travel distance along the west coast of the United States', in Proceedings of the 5th International Conference on Debris Flow Hazards Mitigation, Mechanics, Prediction and Assessmemt, pp. 199–209. doi: 10.4408/IJEGE.2011-03.B-024.

Collins, B., Kayen, R., Reiss, T. and Sitar, N. (2007) Terrestrial LIDAR investigation of the December 2003 and January 2007 activations of the Northridge Bluff landslide, Daly City, California, Open-File Report. U.S. Dept. of the Interior. Available at: https://pubs.er.usgs.gov/publication/ofr20071079 (Accessed: 13 October 2017).

Condon, L. E. and Maxwell, R. M. (2015) 'Evaluating the relationship between topography and groundwater using outputs from a continental-scale integrated hydrology model', Water Resources Research. 51. pp. 6602-6621. doi: 10.1002/2014WR016774.

Cook, K. L. (2017) 'An evaluation of the effectiveness of low-cost UAVs and structure from motion for geomorphic change detection', Geomorphology. Elsevier, 278, pp. 195–208. doi: 10.1016/J.GEOMORPH.2016.11.009.

Coquin, J., Mercier, D., Bourgeois, O., Cossart, E. and Decaulne, A. (2015) 'Gravitational spreading of mountain ridges coeval with Late Weichselian deglaciation: impact on glacial landscapes in Tröllaskagi, northern Iceland', Quaternary Science Reviews, 107, pp. 197–213. doi: 10.1016/j.quascirev.2014.10.023.

Corominas, J. and Moya, J. (2008) 'A review of assessing landslide frequency for hazard zoning purposes', Engineering Geology, 102(3-4), pp. 193–213. doi: 10.1016/j.enggeo.2008.03.018.

Corominas, J., van Westen, C., Frattini, P., Cascini, L., Malet, J. P., Fotopoulou, S., Catani, F., Van Den Eeckhaut, M., Mavrouli, O., Agliardi, F., Pitilakis, K., Winter, M. G., Pastor, M., Ferlisi, S., Tofani, V., Hervás, J. and Smith, J. T. (2014) 'Recommendations for the quantitative analysis of landslide risk', Bulletin of Engineering Geology and the Environment, 73(2), pp. 209–263. doi: 10.1007/s10064-013-0538-8.

Corsini, A., Castagnetti, C., Bertacchini, E., Rivola, R., Ronchetti, F. and Capra, A. (2013) 'Integrating airborne and multi-temporal long-range terrestrial laser scanning with total station measurements for mapping and monitoring a compound slow moving rock slide', Earth Surface Processes and Landforms, 38(11), pp. 1330–1338. doi: 10.1002/esp.3445.

Cossart, E. (2008) 'Landform connectivity and waves of negative feedbacksduring the paraglacial period, a case study: the Tabuc subcatchment since the end of the Little Ice Age (massif des Écrins, France)', Géomorphologie : relief, processus, environnement, 14(4), pp. 249–260. doi: 10.4000/geomorphologie.7430.

Cossart, E. and Fort, M. (2008) 'Consequences of landslide dams on alpine river valleys: examples and typology from the French Southern Alps', Norsk Geografisk Tidsskrift-Norwegian Journal. 62 (2). pp. 75-88. Available at: http://www.tandfonline.com/doi/abs/10.1080/00291950802094882 (Accessed: 7 October 2016).

Cossart, E., Mercier, D., Decaulne, A., Feuillet, T., Jónsson, H. P. and Saemundsson, Þ. (2014) 'Impacts of post-glacial rebound on landslide spatial distribution at a regional scale in northern Iceland (Skagafjörður)', Earth Surface Processes and Landforms, 39(3), pp. 336–350. doi: 10.1002/esp.3450.

Coussot, P., Laigle, D., Arattano, M., Deganutti, A. and Marchi, L. (1998) 'Direct Determination of Rheological Characteristics of Debris Flow', Journal of Hydraulic Engineering, 124(8), pp. 865–868. doi: 10.1061/(ASCE)0733-9429(1998)124:8(865).

Crosta, G. B., Chen, H. and Lee, C. F. (2006) 'Erosional effects on runout of fast landslides, debris flows and avalanches: a numerical investigation', Géotechnique, 56(5), pp. 305–322. doi: 10.1680/geot.2006.56.5.305.

Crosta, G. B., Imposimato, S. and Roddeman, D. (2009) 'Numerical modelling of entrainment/deposition in rock and debris-avalanches', Engineering Geology. Elsevier, 109(1-2), pp. 135–145. doi: 10.1016/j.enggeo.2008.10.004.

Crosta, G. and Prisco, C. di (1999) 'On slope instability induced by seepage erosion', Canadian Geotechnical Journal, 36(6), pp. 1056–1073. doi: 10.1139/t99-062.

Cruden, D. M. and Hu, X. Q. (1993) 'Exhaustion and steady state models for predicting landslide hazards in the Canadian Rocky Mountains', Geomorphology. Elsevier, 8(4), pp. 279–285. doi: 10.1016/0169-555X(93)90024-V.

Cruden, D. and Varnes, D. (1996) 'Landslides: investigation and mitigation. Chapter 3-Landslide types and processes', Transportation research board special report. pp. 36-75. Available at: https://trid.trb.org/view.aspx?id=462501 (Accessed: 27 September 2016).

Curry, A. (2000) ‘Holocene reworking of drift-mantled hillslopes in the Scottish Highlands’, Journal of Quaternary Science, 10(5), pp. 509–518. Available at: http://onlinelibrary.wiley.com/doi/10.1002/1099-1417(200007)15:5%3C529::AID-JQS531%3E3.0.CO;2-D/abstract (Accessed: 29 December 2014).

Curry, A. M. (1998) Paraglacial modification of drift-mantled hillslopes. The University of St Andrews. Available at: https://research-repository.st-andrews.ac.uk/handle/10023/7115 (Accessed: 21 September 2015).

Curry, A. M. (1999) ‘Paraglacial modification of slope form’, Earth Surface Processes and Landforms, 24, pp. 1213–1228. doi: 10.1002/(SICI)1096-9837(199912)24:13<1213::AID-ESP32>3.0.CO;2-B.

Curry, A. M., Cleasby, V. and Zukowskyj, P. (2006) ‘Paraglacial response of steep, sediment-mantled slopes to post-’Little Ice Age' glacier recession in the central Swiss Alps’, Journal of Quaternary Science, 21(3), pp. 211–225. doi: 10.1002/jqs.954.

Curry, A. M., Sands, T. B. and Porter, P. R. (2009) ‘Geotechnical controls on a steep lateral moraine undergoing paraglacial slope adjustment’, Geological Society, London, Special Publications. Geological Society of London, 320(1), pp. 181–197. doi: 10.1144/SP320.12.

D’Elia, B., Picarelli, L. and Leroueil, S. (1998) ‘Geotechnical characterisation of slope movements in structurally complex clay soils and stiff jointed clays’, Rivista Italiana di Geotecnica. 32(3). pp. 5-47. Available at: http://associazionegeotecnica.it/sites/default/files/rig/RIG_1998_3_5.pdf (Accessed: 7 October 2016).

Darling, F. (1968) ‘Ecology of land use in the highlands and islands’ in D. S. Thomson and I. Grimble (eds), The Future of the Highlands, London pp. 27-56.

Davies, T. R. H. (1982) ‘Spreading of rock avalanche debris by mechanical fluidization’, Rock Mechanics Felsmechanik Mecanique des Roches. Springer-Verlag, 15(1), pp. 9–24. doi: 10.1007/BF01239474.

Davies, T. R. H. (1986) ‘Large debris flows: A macro-viscous phenomenon’, Acta Mechanica. Springer-Verlag, 63(1-4), pp. 161–178. doi: 10.1007/BF01182546.

Densmore, A., Anderson, R. and McAdoo, B. (1997) ‘Hillslope evolution by bedrock landslides’, Science. 175(5298). pp. 369-372.

Deubelbeiss, Y. and Graf, C. (2013) ‘Two different starting conditions in numerical debris flow models–Case study at Dorfbach, Randa (Valais, Switzerland)’, GRAF, C.(Red.) Mattertal–ein Tal in Bewegung. Publikation zur Jahrestagung der Schweizerischen Geomorphologischen Gesellschaft. 29. pp. 125–138. Available at: http://www.wsl.ch/wsl/dienstleistungen/publikationen/pdf/12488.pdf (Accessed: 25 November 2014).

Dietrich, A. and Krautblatter, M. (2017) 'What does control debris-flow channel-bed erosion? A LiDAR-based change detection compared to velocity, momentum and pressure derived from a calibrated model.', 19th EGU General Assembly, EGU2017, proceedings from the conference held 23-28 April, 2017 in Vienna, Austria., p.15155. Available at: http://adsabs.harvard.edu/abs/2017EGUGA..1915155D (Accessed: 16 October 2017).

Dietrich, W. and Dunne, T. (1978) 'Sediment budget for a small catchment in a mountainous terrain.' in Slaymaker, O. (ed) Fluvial Geomorphology. pp. 191-206. Routledge, London.

Dowling, C. A. and Santi, P. M. (2014) 'Debris flows and their toll on human life: a global analysis of debris-flow fatalities from 1950 to 2011', Natural Hazards. Springer Netherlands, 71(1), pp. 203–227. doi: 10.1007/s11069-013-0907-4.

Dunning, S. A., Rosser, N. J. and Massey, C. I. (2010) 'The integration of terrestrial laser scanning and numerical modelling in landslide investigations', Quarterly Journal of Engineering Geology and Hydrogeology. Geological Society of London, 43(2), pp. 233–247. doi: 10.1144/1470-9236/08-069.

Dunning, S., Massey, C. and Rosser, N. (2009) 'Structural and geomorphological features of landslides in the Bhutan Himalaya derived from terrestrial laser scanning', Geomorphology. 103(1). pp. 17-29.

Van Den Eeckhaut, M., Kerle, N., Poesen, J. and Hervás, J. (2012) 'Object-oriented identification of forested landslides with derivatives of single pulse LiDAR data', Geomorphology, 173-174, pp. 30–42. doi: 10.1016/j.geomorph.2012.05.024.

Ekwue, E. I. (1990) 'Organic-matter effects on soil strength properties', Soil and Tillage Research. Elsevier, 16(3), pp. 289–297. doi: 10.1016/0167-1987(90)90102-J.

Erika, D. F., Paola, G. and Laur, S. (2017) 'Forecasting the Hydrogeological Hazard in the Anomalous Basin-Fan System of Sernio (Northern Italy)', in Advancing Culture of Living with Landslides. Cham: Springer International Publishing, pp. 1051–1059. doi: 10.1007/978-3-319-53498-5_119.

Etienne, S., Mercier, D. and Voldoire, O. (2008) 'Temporal scales and deglaciation rhythms in a polar glacier margin, Baronbreen, Svalbard', Norsk Geografisk Tidsskrift - Norwegian Journal of Geography, 62(2), pp. 102–114. doi: 10.1080/00291950802095111.

Evans, S. G. (2006) 'Single-event landslides resulting from massive rock slope failure: characterising their frequency and impact on society', in Landslides from Massive Rock Slope Failure. Dordrecht: Springer, pp. 53–73.

Fan, L., Lehmann, P., McArdell, B. and Or, D. (2016b) 'Linking rainfall-induced landslides with debris flows runout patterns towards catchment scale hazard assessment', Geomorphology, 280, pp. 1–15. doi: 10.1016/j.geomorph.2016.10.007.

Fan, L., Lehmann, P. and Or, D. (2015) 'Effects of hydromechanical loading history and antecedent soil mechanical damage on shallow landslide triggering', Journal of Geophysical Research F: Earth Surface, 120(10), pp. 1990–2015. doi: 10.1002/2015JF003615.

Fan, L., Lehmann, P. and Or, D. (2016a) 'Effects of soil spatial variability at the hillslope and catchment scales on characteristics of rainfall-induced landslides', Water Resources Research, 52(3), pp. 1781–1799. doi: 10.1002/2015WR017758.

Fan, L., Powrie, W., Smethurst, J., Atkinson, P. M. and Einstein, H. (2014) 'The effect of short ground vegetation on terrestrial laser scans at a local scale', ISPRS Journal of Photogrammetry and Remote Sensing, 95, pp. 42–52. doi: 10.1016/j.isprsjprs.2014.06.003.

Fang, H.-Y. (1991) Foundation Engineering Handbook. 2nd edn, Fang, H. (ed.). New York: Springer Science & Business Media. Available at: https://books.google.com/books?id=vDboBwAAQBAJ&pgis=1 (Accessed: 3 September 2015).

Fannin, R. J. and Wise, M. P. (2001) 'An empirical-statistical model for debris flow travel distance', Canadian Geotechnical Journal, 38(5), pp. 982–994. doi: 10.1139/t01-030.

Faulkner, H. (2006) 'Piping hazard on collapsible and dispersive soils in Europe', Soil erosion in Europe. pp. 537-562. Available at: http://onlinelibrary.wiley.com/doi/10.1002/0470859202.ch40/summary (Accessed: 7 October 2016).

Fell, R., Corominas, J., Bonnard, C., Cascini, L., Leroi, E. and Savage, W. Z. (2008) 'Guidelines for landslide susceptibility, hazard and risk zoning for land use planning', Engineering Geology, 102(3-4), pp. 85–98. doi: 10.1016/j.enggeo.2008.03.022.

Fernandes, N. F., Guimarães, R. F., Gomes, R. A. T., Vieira, B. C., Montgomery, D. R. and Greenberg, H. (2004) 'Topographic controls of landslides in Rio de Janeiro: Field evidence and modeling', Catena. pp. 163–181. doi: 10.1016/S0341-8162(03)00115-2.

Fey, C. and Wichmann, V. (2017) 'Long-range terrestrial laser scanning for geomorphological change detection in alpine terrain - handling uncertainties', Earth Surface Processes and Landforms, 42(5), pp. 789–802. doi: 10.1002/esp.4022.

Fischer, M., Huss, M., Kummert, M. and Hoelzle, M. (2016) 'Application and validation of long-range terrestrial laser scanning to monitor the mass balance of very small glaciers in the Swiss Alps', Cryosphere, 10(3), pp. 1279–1295. doi: 10.5194/tc-10-1279-2016.

Fleming, R. W., Ellen, S. D. and Algus, M. A. (1989) 'Transformation of dilative and contractive landslide debris into debris flows—An example from marin County, California', Engineering Geology. Elsevier, 27(1), pp. 201–223. doi: 10.1016/0013-7952(89)90034-3.

ForArgyll (2015) Argyll News: A83 now closed with landslide at Rest & Be Thankful | For Argyll. Available at: http://forargyll.com/?p=103727 (Accessed: 19 October 2017).

Forde, T. C., Nedimović, M. R., Gibling, M. R. and Forbes, D. L. (2016) 'Coastal Evolution Over the Past 3000 Years at Conrads Beach, Nova Scotia: the Influence of Local Sediment Supply on a Paraglacial Transgressive System', Estuaries and Coasts. Springer US, 39(2), pp. 363–384. doi: 10.1007/s12237-015-0016-6.

Fox, G. A. and Wilson, G. V. (2010) 'The Role of Subsurface Flow in Hillslope and Stream Bank Erosion: A Review', Soil Science Society of America Journal, 74(3), p. 717. doi: 10.2136/sssaj2009.0319.

Frank, F., McArdell, B. W., Huggel, C. and Vieli, A. (2015) 'The importance of entrainment and bulking on debris flow runout modeling: examples from the Swiss Alps', Natural Hazards and Earth System Sciences, 15, pp. 2569–2583.

Frank, F., McArdell, B. W., Oggier, N., Baer, P., Christen, M. and Vieli, A. (2017) 'Debris-flow modeling at Meretschibach and Bondasca catchments, Switzerland: Sensitivity testing of field-data-based entrainment model', Natural Hazards and Earth System Sciences, 17(5), pp. 801–815. doi: 10.5194/nhess-17-801-2017.

Franz, M., Carrea, D., Abellán, A., Derron, M.-H. and Jaboyedoff, M. (2016) 'Use of targets to track 3D displacements in highly vegetated areas affected by landslides', Landslides. Springer Berlin Heidelberg, 13(4), pp. 821–831. doi: 10.1007/s10346-016-0685-7.

Frattini, P. and Crosta, G. B. (2013) 'The role of material properties and landscape morphology on landslide size distributions', Earth and Planetary Science Letters. 361. pp. 310-319. doi: 10.1016/j.epsl.2012.10.029.

Fredlund, D. G., Xing, A., Fredlund, M. D. and Barbour, S. L. (1996) 'The relationship of the unsaturated soil shear to the soil-water characteristic curve', Canadian Geotechnical Journal. NRC Research Press Ottawa, Canada , 33(3), pp. 440–448. doi: 10.1139/t96-065.

Frey, H., Huggel, C., Bühler, Y., Buis, D., Burga, M. D., Choquevilca, W., Fernandez, F., García Hernández, J., Giráldez, C., Loarte, E., Masias, P., Portocarrero, C., Vicuña, L. and Walser, M. (2016) 'A robust debris-flow and GLOF risk management strategy for a data-scarce catchment in Santa Teresa, Peru', Landslides, 13(6), pp. 1493–1507. doi: 10.1007/s10346-015-0669-z.

Froese, C. R., Corey, R., Poncos, V., Skirrow, R., Mansour, M. and Martin, D. (2008) 'Characterizing complex deep seated landslide deformation using corner reflector InSAR (CR-INSAR): Little Smoky Landslide, Alberta', in Canadian Geotechnical Society: Engineering Geology Division (ed.) Proceedings of the 4th Canadian Conference on Geohazards, pp. 1–4.

Gabet, E. J. and Bookter, A. (2008) 'A morphometric analysis of gullies scoured by post-fire progressively bulked debris flows in southwest Montana, USA', Geomorphology, 96(3), pp. 298–309. doi: 10.1016/j.geomorph.2007.03.016.

Gabet, E. and Mudd, S. (2006) 'The mobilization of debris flows from shallow landslides', Geomorphology. 74. pp/ 207-218.

Galeandro, A., Šimůnek, J. and Simeone, V. (2013) 'Analysis of rainfall infiltration effects on the stability of pyroclastic soil veneer affected by vertical drying shrinkage fractures', Bulletin of Engineering Geology and the Environment. Springer Berlin Heidelberg, 72(3-4), pp. 447–455. doi: 10.1007/s10064-013-0492-5.

Gao, L., Zhang, L. M. and Cheung, R. W. M. (2018) 'Relationships between natural terrain landslide magnitudes and triggering rainfall based on a large landslide inventory in Hong Kong', Landslides, 15(4), pp. 727–740. doi: 10.1007/s10346-017-0904-x.

Gasmo, J., Hritzuk, K. J., Rahardjo, H. and Leong, E. C. (1999) 'Instrumentation of an Unsaturated Residual Soil Slope', Geotechnical Testing Journal. 22(2). pp. 134-143. doi: 10.1520/GTJ11272J.

Gevaert, A. I., Teuling, A. J., Uijlenhoet, R., DeLong, S. B., Huxman, T. E., Pangle, L. A., Breshears, D. D., Chorover, J., Pelletier, J. D., Saleska, S. R., Zeng, X. and Troch, P. A. (2014) 'Hillslope-scale experiment demonstrates the role of convergence during two-step saturation', Hydrology and Earth System Sciences, 18(9), pp. 3681–3692. doi: 10.5194/hess-18-3681-2014.

Ghestem, M., Sidle, R. C. and Stokes, A. (2011) 'The Influence of Plant Root Systems on Subsurface Flow: Implications for Slope Stability', BioScience. doi: 10.1525/bio.2011.61.11.6.

Gili, J. A., Corominas, J. and Rius, J. (2000) 'Using Global Positioning System techniques in landslide monitoring', Engineering Geology, 55(3), pp. 167–192. doi: 10.1016/S0013-7952(99)00127-1.

Giussani, A. and Scaioni, M. (2004) 'Application of TLS to support landslides study: survey planning, operational issues and data processing', Archives of Photogrammetry, Remote Sensing and Spatial Information Sciences. (36). pp. 318-323.

Glade, T. (2005) 'Linking debris-flow hazard assessments with geomorphology', Geomorphology, 66(1), pp. 189–213. doi: 10.1016/j.geomorph.2004.09.023.

Glendell, M., McShane, G., Farrow, L., James, M. R., Quinton, J., Anderson, K., Evans, M., Benaud, P., Rawlins, B., Morgan, D., Jones, L., Kirkham, M., DeBell, L., Quine, T. A., Lark, M., Rickson, J. and Brazier, R. E. (2017) 'Testing the utility of structure-from-motion photogrammetry reconstructions using small unmanned aerial vehicles and ground photography to estimate the extent of upland soil erosion', Earth Surface Processes and Landforms, 42(12), pp. 1860–1871. doi: 10.1002/esp.4142.

Glira, P., Pfeifer, N. and Mandlburger, G. (2016) 'Rigorous Strip Adjustment of UAV-based Laserscanning Data Including Time-Dependent Correction of Trajectory Errors', Photogrammetric Engineering & Remote Sensing, 82(12), pp. 945–954. doi: 10.14358/PERS.82.12.945.

Godt, J. W. and Coe, J. A. (2007) 'Alpine debris flows triggered by a 28 July 1999 thunderstorm in the central Front Range, Colorado', Geomorphology. 84(1-2). pp. 80-97. doi: 10.1016/j.geomorph.2006.07.009.

Gomez, B. and Jones, J. P. (2010) Research methods in geography : a critical introduction, Critical introductions to geography. 6. doi: 10.1080/13563475.2011.561066.

Goodwin, N. R., Armston, J., Stiller, I. and Muir, J. (2016) 'Assessing the repeatability of terrestrial laser scanning for monitoring gully topography: A case study from Aratula, Queensland, Australia', Geomorphology, 262, pp. 24–36. doi: 10.1016/j.geomorph.2016.03.007.

Google Earth (2018) 'Aerial / Satellite imagery.' Available at: https://www.google.com/earth/.

Graf, C. and McArdell, B. W. (2011) 'Debris-flow monitoring and debris-flow runout modelling before and after construction of mitigation measures: an example from an instable zone in the Southern Swiss Alps', in La géomorphologie alpine: entre patrimoine et contrainte. Actes du colloque de la Société Suisse de Géomorphologie, 3-5 septembre 2009, Olivone (Géovisions n° 36). Institut de géographie, Université de Lausanne, p. 11. Available at: https://www.unil.ch/files/live/sites/igd/files/shared/Geovisions/Geovisions36/16_Graf_McArdell.pdf.

Gregoretti, C., Degetto, M. and Boreggio, M. (2016) 'GIS-based cell model for simulating debris flow runout on a fan', Journal of Hydrology, 534, pp. 326–340. doi: 10.1016/j.jhydrol.2015.12.054.

Griffiths, P. G., Webb, R. H. and Melis, T. S. (2004) 'Frequency and initiation of debris flows in Grand Canyon, Arizona', Journal of Geophysical Research, 109(F4), p. F04002. doi: 10.1029/2003JF000077.

Grissinger, E. (1996) 'Rill and gullies erosion', in Agassi, M. (ed) Soil Erosion, Conservation, and Rehabilitation. pp. 153-167. Marcel Dekker Inc, New York.

Grove, J. M. (1972) 'The Incidence of Landslides, Avalanches, and Floods in Western Norway during the Little Ice Age', Arctic and Alpine Research, 4(2), pp. 131–138. doi: 10.2307/1550396.

Guthrie, R. H., Hockin, A., Colquhoun, L., Nagy, T., Evans, S. G. and Ayles, C. (2010) 'An examination of controls on debris flow mobility: Evidence from coastal British Columbia', Geomorphology, 114, pp. 601–613. doi: 10.1016/j.geomorph.2009.09.021.

Guzzetti, F., Ardizzone, F., Cardinali, M., Rossi, M. and Valigi, D. (2009) 'Landslide volumes and landslide mobilization rates in Umbria, central Italy', Earth and Planetary Science Letters. 279(3-4). pp. 222-229. doi: 10.1016/j.epsl.2009.01.005.

Guzzetti, F., Malamud, B. D., Turcotte, D. L. and Reichenbach, P. (2002) 'Power-law correlations of landslide areas in central Italy', Earth and Planetary Science Letters. 195(3-4). pp. 169-183. doi: 10.1016/S0012-821X(01)00589-1.

Guzzetti, F., Peruccacci, S., Rossi, M. and Stark, C. P. (2008) 'The rainfall intensity–duration control of shallow landslides and debris flows: an update', Landslides. Springer-Verlag, 5(1), pp. 3–17. doi: 10.1007/s10346-007-0112-1.

Guzzetti, F., Reichenbach, P., Cardinali, M., Galli, M. and Ardizzone, F. (2005) 'Probabilistic landslide hazard assessment at the basin scale', Geomorphology, 72(1), pp. 272–299. doi: 10.1016/j.geomorph.2005.06.002.

de Haas, T., Braat, L., Leuven, J. R. F. W., Lokhorst, I. R. and Kleinhans, M. G. (2015) 'Effects of debris flow composition on runout, depositional mechanisms, and deposit morphology in laboratory experiments', Journal of Geophysical Research: Earth Surface, 120(9), pp. 1949–1972. doi: 10.1002/2015JF003525.

de Haas, T. and van Woerkom, T. (2016) 'Bed scour by debris flows: Experimental investigation of effects of debris-flow composition', Earth Surface Processes and Landforms, 41(13), pp. 1951–1966. doi: 10.1002/esp.3963.

Haeberli, W., Wegmann, M. and Vonder Muhll, D. (1997) 'Slope stability problems related to glacier shrinkage and permafrost degradation in the Alps', Eclogae Geologicae Helvetiae, 90(3), pp. 407–414. doi: 10.5169/seals-168172.

Harbor, J. and Warburton, J. (1993) 'Relative Rates of Glacial and Nonglacial Erosion in Alpine Environments', Arctic and Alpine Research, 25(1), p. 1. doi: 10.2307/1551473.

Harp, E. L., Wells II, W. G. and Sarmiento, J. G. (1990) 'Pore pressure response during failure in soils', Geological Society of America Bulletin. Geological Society of America, 102(4), pp. 428–438. doi: 10.1130/0016-7606(1990)102<0428:PPRDFI>2.3.CO;2.

Hartmann, D. L., Klein Tank, A. M. G., Rusticucci, M., Alexander, L. V., Brönnimann, S., Charabi, Y. A. R., Dentener, F. J., Dlugokencky, E. J., Easterling, D. R., Kaplan, A., Soden, B. J., Thorne, P. W., Wild, M. and Zhai, P. (2013) 'Observations: Atmosphere and surface', in Climate Change 2013 the Physical Science Basis: Working Group I Contribution to the Fifth Assessment Report of the Intergovernmental Panel on Climate Change. doi: 10.1017/CBO9781107415324.008.

Hartzell, P. J., Gadomski, P. J., Glennie, C. L., Finnegan, D. C. and Deems, J. S. (2015) 'Rigorous error propagation for terrestrial laser scanning with application to snow volume uncertainty', Journal of Glaciology, 61(230), pp. 1147–1158. doi: 10.3189/2015JoG15J031.

Harvey, A. (1992) 'Process interactions, temporal scales and the development of hillslope gully systems: Howgill Fells, northwest England', Geomorphology. 5(35). pp. 323-344.

Harvey, A. M. (2001) 'Coupling between hillslopes and channels in upland fluvial systems: implications for landscape sensitivity, illustrated from the Howgill Fells, northwest England', CATENA, 42(2), pp. 225–250. doi: 10.1016/S0341-8162(00)00139-9.

Heald, A. and Parsons, J. (2005) 'Key contributory factors to debris flows', in Winter, M. G., Macgregor, F., and Shackman, L. (eds) Scottish Road Network Landslide Study, pp. 68–80. Available at: http://www.scotland.gov.uk/Publications/2005/07/08131738/17492.

Hein, C. J., FitzGerald, D. M., Carruthers, E. A., Stone, B. D., Barnhardt, W. A. and Gontz, A. M. (2012) 'Refining the model of barrier island formation along a paraglacial coast in the Gulf of Maine', Marine Geology, 307, pp. 40–57. doi: 10.1016/j.margeo.2012.03.001.

Heiser, M., Scheidl, C. and Kaitna, R. (2017) 'Evaluation concepts to compare observed and simulated deposition areas of mass movements', Computational Geosciences, 21(3), pp. 335–343. doi: 10.1007/s10596-016-9609-9.

Helsen, M. M., Koop, P. J. M. and Van Steijn, H. (2002) 'Magnitude-frequency relationship for debris flows on the fan of the Chalance torrent, Valgaudemar (French Alps)', Earth Surface Processes and Landforms, 27(12), pp. 1299–1307. doi: 10.1002/esp.412.

Hencher, S. R., Lee, S. G., Carter, T. G. and Richards, L. R. (2011) 'Sheeting joints: Characterisation, shear strength and engineering', Rock Mechanics and Rock Engineering, 44(1), pp. 1–22. doi: 10.1007/s00603-010-0100-y.

Herrera, G., López-Davalillo, J. C. G., Fernández-Merodo, J. A., Béjar-Pizarro, M., Allasia, P., Lollino, P., Lollino, G., Guzzetti, F., Álvarez-Fernández, M. I., Manconi, A., Duro, J., Sánchez, C. and Iglesias, R. (2017) 'The Differential Slow Moving Dynamic of a Complex Landslide: Multi-sensor Monitoring', in Advancing Culture of Living with Landslides. Cham: Springer International Publishing, pp. 219–225. doi: 10.1007/978-3-319-53498-5_25.

Hewitt, K. (2006) 'Disturbance regime landscapes: mountain drainage systems interrupted by large rockslides', Progress in Physical Geography. 30(3). pp. 365-393.

Hinchliffe, S. (1999) 'Timing and significance of talus slope reworking, Trotternish, Skye, northwest Scotland', Holocene, 9(4), pp. 483–494. doi: 10.1191/095968399671220239.

Hodge, R., Brasington, J. and Richards, K. (2009) 'In situ characterization of grain-scale fluvial morphology using Terrestrial Laser Scanning', Earth Surface Processes and Landforms, 34(7), pp. 954–968. doi: 10.1002/esp.1780.

Hoffmann, T. (2015) 'Sediment residence time and connectivity in non-equilibrium and transient geomorphic systems', Earth-Science Reviews, 150, pp. 609–627. doi: 10.1016/j.earscirev.2015.07.008.

Hovius, N., Stark, C. P. and Allen, P. A. (1997) 'Sediment flux from a mountain belt derived by landslide mapping', Geology. 25(3). pp. 231-234. doi: 10.1130/0091-7613(1997)025<0231:SFFAMB>2.3.CO;2.

Hungr, O. (2000) 'Analysis of debris flow surges using the theory of uniformly progressive flow', Earth Surface Processes and Landforms. John Wiley & Sons, Ltd., 25(5), pp. 483–495. doi: 10.1002/(SICI)1096-9837(200005)25:5<483::AID-ESP76>3.0.CO;2-Z.

Hungr, O. (2005) 'Classification and terminology', in Jakob, M. and Hungr, O. (eds) Debris-flow Hazards and Related Phenomena. Chichester: Praxis Publishing Ltd, pp. 9–23.

Hungr, O., Evans, S. G., Bovis, M. J. and Hutchinson, J. N. (2001) 'A review of the classification of landslides of the flow type', Environmental & Engineering Geoscience. Association of Environmental & Engineering Geologists, 7(3), pp. 221–238. doi: 10.2113/gseegeosci.7.3.221.

Hungr, O., Leroueil, S. and Picarelli, L. (2013) 'The Varnes classification of landslide types, an update', Landslides, 11(2), pp. 167–194. doi: 10.1007/s10346-013-0436-y.

Hungr, O., McDougall, S. and Bovis, M. (2005) 'Entrainment of material by debris flows', in Jakob, M. and Hungr, O. (eds) Entrainment of material by debris flows. New York: Springer Berlin Heidelberg, pp. 135–158.

Hungr, O., McDougall, S., Wise, M. and Cullen, M. (2008) 'Magnitude–frequency relationships of debris flows and debris avalanches in relation to slope relief', Geomorphology, 96(3), pp. 355–365. doi: 10.1016/j.geomorph.2007.03.020.

Hurimann, M., McArdell, B. W. and Rickli, C. (2015) 'Field and laboratory analysis of the runout characteristics of hillslope debris flows in Switzerland', Geomorphology, 232, pp. 20–32. doi: 10.1016/j.geomorph.2014.11.030.

Hürlimann, M., Rickenmann, D., Medina, V. and Bateman, A. (2008) 'Evaluation of approaches to calculate debris-flow parameters for hazard assessment', Engineering Geology, 102(3-4), pp. 152–163. doi: 10.1016/j.enggeo.2008.03.012.

Hussin, H. Y. (2011) 'Probabilistic Run-out Modeling of a Debris Flow in Barcelonnette, France. University of Twente Faculty of Geo-Information and Earth Observation (ITC). Available online: https://webapps.itc.utwente.nl/librarywww/papers_2011/msc/aes/hussin.pdf (Accessed: 28 August 2018).

Hussin, H. Y., Quan Luna, B., van Westen, C. J., Christen, M., Malet, J.-P. and van Asch, T. W. J. (2012) 'Parameterization of a numerical 2-D debris flow model with entrainment: a case study of the Faucon catchment, Southern French Alps', Natural Hazards and Earth System Science, 12(10), pp. 3075–3090. doi: 10.5194/nhess-12-3075-2012.

Hutchinson, J. N. (1988) 'General report: Morphological and geotechnical parameters of landslides in relation to geology and hydrogeology', International Journal of Rock Mechanics and Mining Sciences & Geomechanics Abstracts, 26(2), pp. 3–35.

Hyde, K., Woods, S. W. and Donahue, J. (2007) 'Predicting gully rejuvenation after wildfire using remotely sensed burn severity data', Geomorphology, 86(3), pp. 496–511. doi: 10.1016/j.geomorph.2006.10.012.

Innes, J. L. (1983) 'Lichenometric dating of debris-flow deposits in the Scottish Highland', Earth Surface Processes and Landforms, 8(6), pp. 579–588. doi: 10.1002/esp.3290080609.

Iturrizaga, L. (2008) 'Paraglacial landform assemblages in the Hindukush and Karakoram Mountains', Geomorphology, 95(1), pp. 27–47. doi: 10.1016/j.geomorph.2006.07.030.

Iverson, N. R., Mann, J. E. and Iverson, R. M. (2010) 'Effects of soil aggregates on debris-flow mobilization: Results from ring-shear experiments', Engineering Geology, 114(1-2), pp. 84–92. doi: 10.1016/j.enggeo.2010.04.006.

Iverson, R. M. (2003) 'The debris-flow rheology myth', in Rickenmann, D. and Chen, C. L. (eds) Debris-flow hazards mitigation: mechanics, prediction and assessment. 1. pp. 303-314.

Iverson, R. M. (2005a) 'Regulation of landslide motion by dilatancy and pore pressure feedback', Journal of Geophysical Research: Earth Surface. 110(F2).

Iverson, R. M. (1997) 'The physics of debris flows', Reviews of Geophysics, 35(3), p. 245. doi: 10.1029/97RG00426.

Iverson, R. M. (2000) 'Acute Sensitivity of Landslide Rates to Initial Soil Porosity', Science, 290(5491), pp. 513–516. doi: 10.1126/science.290.5491.513.

Iverson, R. M. (2005b) 'Debris-flow mechanics', in Debris-flow Hazards and Related Phenomena. Berlin, Heidelberg: Springer Berlin Heidelberg, pp. 105–134. doi: 10.1007/3-540-27129-5_6.

Iverson, R. M. (2013) 'Mechanics of debris flows and rock avalanches', Handbook of Environmental Fluid Dynamics, 1, pp. 573–587.

Iverson, R. M. (2014) 'Debris flows: behaviour and hazard assessment', Geology Today, 30(1), pp. 15–20. doi: 10.1111/gto.12037.

Iverson, R. M. and Denlinger, R. P. (2001) 'Flow of variably fluidized granular masses across three-dimensional terrain: 1. Coulomb mixture theory', Journal of Geophysical Research: Solid Earth, 106(B1), pp. 537–552. doi: 10.1029/2000JB900329.

Iverson, R. M., Logan, M., LaHusen, R. G. and Berti, M. (2010) 'The perfect debris flow? Aggregated results from 28 large-scale experiments', Journal of Geophysical Research, 115(F3). doi: 10.1029/2009JF001514.

Iverson, R. M. and Ouyang, C. (2015) 'Entrainment of bed material by Earth-surface mass flows: Review and reformulation of depth-integrated theory', Reviews of Geophysics, 53(1), pp. 27–58. doi: 10.1002/2013RG000447.

Iverson, R. M., Reid, M. E., Logan, M., LaHusen, R. G., Godt, J. W. and Griswold, J. P. (2011) 'Positive feedback and momentum growth during debris-flow entrainment of wet bed sediment', Nature Geoscience, pp. 116–121. doi: 10.1038/ngeo1040.

Iverson, R. M. and Vallance, J. W. (2001) 'New views of granular mass flows', Geology, 29(2), p. 115. doi: 10.1130/0091-7613(2001)029<0115:NVOGMF>2.0.CO;2.

Jaafar, H. A., Meng, X. and Sowter, A. (2018) 'Terrestrial laser scanner error quantification for the purpose of monitoring', Survey Review. Taylor & Francis, 50(360), pp. 232–248. doi: 10.1080/00396265.2016.1259721.

Jaboyedoff, M., Oppikofe, T., Abellán, A., Derron, M.-H., Loye, A., Metzger, R. and Pedrazzini, A. (2012) 'Use of LIDAR in landslide investigations: a review', Natural Hazards, 61(1), pp. 5–28. Available at: http://link.springer.com/article/10.1007/s11069-010-9634-2.

Jakob, M. (2005) 'A size classification for debris flows', Engineering Geology, 79(3), pp. 151–161. doi: 10.1016/j.enggeo.2005.01.006.

Jakob, M., Bovis, M. and Oden, M. (2005) 'The significance of channel recharge rates for estimating debris-flow magnitude and frequency', Earth Surface Processes and Landforms. John Wiley & Sons, Ltd., 30(6), pp. 755–766. doi: 10.1002/esp.1188.

Jakob, M. and Friele, P. (2010) 'Frequency and magnitude of debris flows on Cheekye River, British Columbia', Geomorphology, 114(3), pp. 382–395. doi: 10.1016/j.geomorph.2009.08.013.

Jakob, M., Stein, D. and Ulmi, M. (2012) 'Vulnerability of buildings to debris flow impact', Natural Hazards. Springer Netherlands, 60(2), pp. 241–261. doi: 10.1007/s11069-011-0007-2.

James, M. R. and Robson, S. (2012) 'Straightforward reconstruction of 3D surfaces and topography with a camera: Accuracy and geoscience application', Journal of Geophysical Research: Earth Surface. 117(F3). doi: 10.1029/2011JF002289.

James, M. R., Robson, S., d'Oleire-Oltmanns, S. and Niethammer, U. (2017) 'Optimising UAV topographic surveys processed with structure-from-motion: Ground control quality, quantity and bundle adjustment', Geomorphology. doi: 10.1016/j.geomorph.2016.11.021.

Jeong, S. W. and Park, S.-S. (2016) 'On the viscous resistance of marine sediments for estimating their strength and flow characteristics', Geosciences Journal. The Geological Society of Korea, 20(2), pp. 149–155. doi: 10.1007/s12303-015-0032-3.

Johnson, A. M. and Rahn, P. H. (1970) 'Mobilization of debris flow', Zeitschrift fur Geomorphologie, 9, pp. 168–186.

Johnson, A. M. and Rodine, J. R. (1984) 'Debris Flow', in Brunsden, D. and Prior, D. (eds) Slope instability. Chichester: John Wiley & Sons, Ltd, pp. 257–361. Available at: https://trid.trb.org/view/267068 (Accessed: 23 June 2018).

Johnson, R. M. and Warburton, J. (2015) 'Sediment erosion dynamics of a gullied debris slide: a medium-term record', CATENA, 127, pp. 152–169. doi: 10.1016/j.catena.2014.12.018.

Johnson, R. M., Warburton, J. and Mills, A. J. (2008) 'Hillslope-channel sediment transfer in a slope failure event: Wet Swine Gill, Lake District, northern England', Earth Surface Processes and Landforms, 33(3), pp. 394–413. doi: 10.1002/esp.1563.

Jones, A. (1971) 'Soil Piping and Stream Channel Initiation', Water Resources Research. 7(3). pp. 602-610. doi: 10.1029/WR007i003p00602.

Jones, J. A. A. (1987) 'The effects of soil piping on contributing areas and erosion patterns', Earth Surface Processes and Landforms. 12(3). pp. 229-248. doi: 10.1002/esp.3290120303.

Jones, J. A. A., Richardson, J. M. and Jacob, H. J. (1997) 'Factors controlling the distribution of piping in Britain: a reconnaissance', Geomorphology. Elsevier, 20(3), pp. 289–306. doi: 10.1016/S0169-555X(97)00030-5.

Kaasalainen, S., Jaakkola, A., Kaasalainen, M., Krooks, A. and Kukko, A. (2011) 'Analysis of Incidence Angle and Distance Effects on Terrestrial Laser Scanner Intensity: Search for Correction Methods', Remote Sensing. Molecular Diversity Preservation International, 3(12), pp. 2207–2221. doi: 10.3390/rs3102207.

Kaiser, A., Neugirg, F., Rock, G., Müller, C., Haas, F., Ries, J. and Schmidt, J. (2014) 'Small-scale surface reconstruction and volume calculation of soil erosion in complex moroccan Gully morphology using structure from motion', Remote Sensing. 6(8). pp. 7050-7080. doi: 10.3390/rs6087050.

Kaitna, R., Palucis, M. and Hill, K. (2016) 'Effects of coarse grain size distribution and fine particle content on pore fluid pressure and shear behavior in experimental debris flows', Journal of Geophysical Research: Earth Surface. 121(2). pp. 415-441.

Kean, J. W., McCoy, S. W., Tucker, G. E., Staley, D. M. and Coe, J. A. (2013) 'Runoff-generated debris flows: Observations and modeling of surge initiation, magnitude, and frequency', Journal of Geophysical Research: Earth Surface, 118(4), pp. 2190–2207. doi: 10.1002/jgrf.20148.

Kendon, E. J., Blenkinsop, S. and Fowler, H. J. (2018) 'When will we detect changes in short-duration precipitation extremes?', Journal of Climate. doi: 10.1175/JCLI-D-17-0435.1.

Kim, M. S., Onda, Y., Uchida, T. and Kim, J. K. (2016) 'Effects of soil depth and subsurface flow along the subsurface topography on shallow landslide predictions at the site of a small granitic hillslope', Geomorphology, 271, pp. 40–54. doi: 10.1016/j.geomorph.2016.07.031.

Kirkby, M. J. and Bracken, L. J. (2009) 'Gully processes and gully dynamics', Earth Surface Processes and Landforms. John Wiley & Sons, Ltd., 34(14), pp. 1841–1851. doi: 10.1002/esp.1866.

Klaus, S., Barbara, T., Brian, M., Christoph, G., Hungr, O. and Roland, K. (2015) 'Modeling Debris-Flow Runout Pattern on a Forested Alpine Fan with Different Dynamic Simulation Models'. Springer, Cham.

Knight, J. and Harrison, S. (2018) 'Transience in cascading paraglacial systems', Land Degradation and Development. doi: 10.1002/ldr.2994.

Knighton, D. (2014) Fluvial Forms and Processes : a New Perspective. Routledge, London.

Kogelnig, A., Hübl, J., Suriñach, E., Vilajosana, I. and McArdell, B. W. (2014) 'Infrasound produced by debris flow: Propagation and frequency content evolution', Natural Hazards, 70(3), pp. 1713–1733. doi: 10.1007/s11069-011-9741-8.

Korup, O., Clague, J. J., Hermanns, R. L., Hewitt, K., Strom, A. L. and Weidinger, J. T. (2007) Giant landslides, topography, and erosion, Earth and Planetary Science Letters. 261(3-4). pp. 578-589. doi: 10.1016/j.epsl.2007.07.025.

Kovanen, D. and Slaymaker, O. (2015) 'The paraglacial geomorphology of the Fraser Lowland, southwest British Columbia and northwest Washington', Geomorphology, 232, pp. 78–93. doi: 10.1016/j.geomorph.2014.12.021.

Kromer, R. A., Abellan, A., Hutchinson, D. J., Lato, M., Chanut, M.-A., Dubois, L. and Jaboyedoff, M. (2017) 'Automated Terrestrial Laser Scanning with Near Real-Time Change Detection & Monitoring of the Séchilienne Landslide', Earth Surface Dynamics Discussions. 5(2). pp. 1–33. doi: 10.5194/esurf-2017-6.

Kromer, R. A., Abellán, A., Hutchinson, D. J., Lato, M., Edwards, T. and Jaboyedoff, M. (2015) 'A 4D filtering and calibration technique for small-scale point cloud change detection with a terrestrial laser scanner', Remote Sensing, 7(10), pp. 13029–13058. doi: 10.3390/rs71013029.

Lague, D., Brodu, N. and Leroux, J. (2013) 'Accurate 3D comparison of complex topography with terrestrial laser scanner: Application to the Rangitikei canyon (N-Z)', ISPRS Journal of Photogrammetry and Remote Sensing, 82, pp. 10–26. doi: 10.1016/j.isprsjprs.2013.04.009.

LaHusen, R. G. (2005) 'Debris-flow instrumentation', in Jakob, M. and Hungr, O. (eds) Debris-flow Hazards and Related Phenomena. Berlin, Heidelberg: Springer, pp. 291–304.

Larcan, E., Mambretti, S. and Pulecchi, M. (2006) 'A procedure for the evaluation of debris flow stratification', in Monitoring, Simulation, Prevention and Remediation of Dense and Debris Flows. Southampton, UK: WIT Press (WIT Transactions on Ecology and the Environment, Vol 90), pp. 81–88. doi: 10.2495/DEB060081.

Lari, S., Frattini, P. and Crosta, G. B. (2014) 'A probabilistic approach for landslide hazard analysis', Engineering Geology. Elsevier, 182, pp. 3–14. doi: 10.1016/J.ENGGEO.2014.07.015.

Larsen, I. J., Montgomery, D. R. and Korup, O. (2010) 'Landslide erosion controlled by hillslope material', Nature Geoscience, 3(4), pp. 247–251. doi: 10.1038/ngeo776.

Larsson, S. (1982) 'Geomorphological effects on the slopes of Longyear Valley, Spitsbergen, after a heavy rainstorm in July 1972', Geografiska Annaler. Series A: Physical Geography, 64, pp. 105–125.

Legros, F. (2002) 'The mobility of long-runout landslides', Engineering Geology, 63(3), pp. 301–331. doi: 10.1016/S0013-7952(01)00090-4.

Leica (2019) Leica FlexLine TS10 Manual Total Station. Available at: https://leica-geosystems.com/en-gb/products/total-stations/manual-total-stations/leica-flexline-ts10 (Accessed: 28 July 2019).

Leroueil, S. (2001) 'Natural slopes and cuts: movement and failure mechanisms', Géotechnique, 51(3), pp. 197–243. doi: 10.1680/geot.2001.51.3.197.

Leroueil, S. (2004) 'Geotechnics of slopes before failure', Landslides: Evaluation and Stabilization, Proceedings of the 9th International Symposium on Landslides, 2, pp. 863–884.

Li, L., Lan, H. and Wu, Y. (2016) 'How sample size can effect landslide size distribution', Geoenvironmental Disasters, 3(1), p. 18. doi: 10.1186/s40677-016-0052-y.

Liang, Y.-B., Zhan, Q.-M., Che, E.-Z., Chen, M.-W. and Zhang, D.-L. (2014) 'Automatic Registration of Terrestrial Laser Scanning Data Using Precisely Located Artificial Planar Targets', IEEE Geoscience and Remote Sensing Letters, 11(1), pp. 69–73. doi: 10.1109/LGRS.2013.2246134.

Lichti, D. D., Gordon, S. J. and Tipdecho, T. (2005) 'Error Models and Propagation in Directly Georeferenced Terrestrial Laser Scanner Networks', Journal of Surveying Engineering, 131(4), pp. 135–142. doi: 10.1061/(ASCE)0733-9453(2005)131:4(135).

Lichti, D. D. and Jamtsho, S. (2006) 'Angular resolution of terrestrial laser scanners', The Photogrammetric Record, 21(114), pp. 141–160. doi: 10.1111/j.1477-9730.2006.00367.x.

Lim, M., Petley, D. N., Rosser, N. J., Allison, R. J., Long, A. J. and Pybus, D. (2005) 'Combined Digital Photogrammetry and Time-of-Flight Laser Scanning for Monitoring Cliff Evolution', The Photogrammetric Record. Blackwell Publishing Ltd, 20(110), pp. 109–129. doi: 10.1111/j.1477-9730.2005.00315.x.

Liu, J., Li, Y., Su, P., Cheng, Z. and Cui, P. (2009) 'Temporal variation of intermittent surges of debris flow', Journal of Hydrology, 365(3), pp. 322–328. doi: 10.1016/j.jhydrol.2008.12.005.

Lorente, A., García-Ruiz, J. M., Begueria, S. and Arnaez, J. (2002) 'Factors explaining the spatial distribution of hillslope debris flows: A case study in the Flysch Sector of the Central Spanish Pyrenees', Mountain Research and Development. 22(1). pp. 32-39.

Loup, B., Egli, T. and Stucki, M. (2012) 'Impact pressures of hillslope debris flows', Proceedings of 12th Congres INTERPRAEVENT, pp. 225–236. Available at: http://www.interpraevent.at/palm-cms/upload_files/Publikationen/Tagungsbeitraege/2012_1_225.pdf (Accessed: 25 November 2014).

Lourenço, S. D. N., Sassa, K. and Fukuoka, H. (2006) 'Failure process and hydrologic response of a two layer physical model: Implications for rainfall-induced landslides', Geomorphology, 73(1), pp. 115–130. doi: 10.1016/j.geomorph.2005.06.004.

Loye, A., Jaboyedoff, M., Isaac Theule, J. and Liébault, F. (2016) 'Headwater sediment dynamics in a debris flow catchment constrained by high-resolution topographic surveys', Earth Surface Dynamics, 4(2), pp. 489–513. doi: 10.5194/esurf-4-489-2016.

Lu, N. and Godt, J. (2013) Hillslope hydrology and stability. Cambridge University Press, Cambridge.

Luna, B. Q., Blahut, J., Kappes, M., Akbas, S. O., Malet, J.-P., Remaître, A., van Asch, T. and Jaboyedoff, M. (2014) 'Methods for Debris Flow Hazard and Risk Assessment', In Asch, T. V.,

Cormonias, J., Greiving, S., Malet, J-P. and Sterlacchini, Sl. (eds) Mountain Risks: From Prediction to Management and Governance, pp. 133-177. Springer, Dordrecht, 2014.

Malamud, B. D., Turcotte, D. L., Guzzetti, F. and Reichenbach, P. (2004) 'Landslide inventories and their statistical properties', Earth Surface Processes and Landforms, 29(6), pp. 687–711. doi: 10.1002/esp.1064.

Malet, J. P., Maquaire, O., Locat, J. and Rema??tre, A. (2004) 'Assessing debris flow hazards associated with slow moving landslides: Methodology and numerical analyses', Landslides, 1(1), pp. 83–90. doi: 10.1007/s10346-003-0005-x.

Mandal, S. and Maiti, R. (2015) 'Impact Assessment of Hydrologic Attributes and Slope Instability', in Semi-Quantitative Approaches for Landslide Assessment and Prediction, pp. 95–121. doi: 10.1007/978-981-287-146-6.

Mangeney, A., Roche, O., Hungr, O., Mangold, N., Faccanoni, G. and Lucas, A. (2010) 'Erosion and mobility in granular collapse over sloping beds', Journal of Geophysical Research, 115(F3), p. F03040. doi: 10.1029/2009JF001462.

Marchi, L., Arattano, M. and Deganutti, A. M. (2002) 'Ten years of debris-flow monitoring in the Moscardo Torrent (Italian Alps)', Geomorphology. Elsevier, 46(1-2), pp. 1–17. doi: 10.1016/S0169-555X(01)00162-3.

Martin, Y. E., Johnson, E. A. and Chaikina, O. (2017) 'Gully recharge rates and debris flows: A combined numerical modeling and field-based investigation, Haida Gwaii, British Columbia', Geomorphology, 278, pp. 252–268. doi: 10.1016/j.geomorph.2016.11.012.

Martinius, A. W. and Naess, A. (2005) 'Uncertainty analysis of fluvial outcrop data for stochastic reservoir modelling', Petroleum Geoscience, 11(3), pp. 203–214. doi: 10.1144/1354-079303-615.

Marzolff, I. and Poesen, J. (2009) 'The potential of 3D gully monitoring with GIS using high-resolution aerial photography and a digital photogrammetry system', Geomorphology, 111(1-2), pp. 48–60. doi: 10.1016/j.geomorph.2008.05.047.

Matsushi, Y., Hattanji, T. and Matsukura, Y. (2006) 'Mechanisms of shallow landslides on soil-mantled hillslopes with permeable and impermeable bedrocks in the Boso Peninsula, Japan', Geomorphology, 76(1), pp. 92–108. doi: 10.1016/j.geomorph.2005.10.003.

Mattson, L. E. and Gardner, J. S. (1991) 'Mass Wasting on Valley-Side Ice-Cored Moraines, Boundary Glacier, Alberta, Canada', Geografiska Annaler. Series A, Physical Geography, 73(3/4), p. 123. doi: 10.2307/521017.

May, C. L. and Gresswell, R. E. (2003) 'Processes and rates of sediment and wood accumulation in headwater streams of the Oregon Coast Range, USA', Earth Surface Processes and Landforms, 28(4), pp. 409–424. doi: 10.1002/esp.450.

McColl, S. T. (2012) 'Paraglacial rock-slope stability', Geomorphology, 153, pp. 1–16. doi: 10.1016/j.geomorph.2012.02.015.

McCoy, S. W., Kean, J. W., Coe, J. A., Staley, D. M., Wasklewicz, T. A. and Tucker, G. E. (2010) 'Evolution of a natural debris flow: In situ measurements of flow dynamics, video imagery, and terrestrial laser scanning', Geology. GeoScienceWorld, 38(8), pp. 735–738. doi: 10.1130/G30928.1.

McCoy, S. W., Kean, J. W., Coe, J. A., Tucker, G. E., Staley, D. M. and Wasklewicz, T. A. (2012) 'Sediment entrainment by debris flows: In situ measurements from the headwaters of a steep catchment', Journal of Geophysical Research: Earth Surface, 117(F3). doi: 10.1029/2011JF002278.

McCoy, S. W., Tucker, G. E., Kean, J. W. and Coe, J. A. (2013) 'Field measurement of basal forces generated by erosive debris flows', Journal of Geophysical Research: Earth Surface, 118(2), pp. 589–602. doi: 10.1002/jgrf.20041.

McDonnell, J. J. (1990) 'A Rationale for Old Water Discharge Through Macropores in a Steep, Humid Catchment', Water Resources Research, 26(11), pp. 2821–2832. doi: 10.1029/WR026i011p02821.

McDougall, S. and Hungr, O. (2005) 'Dynamic modelling of entrainment in rapid landslides', Canadian Geotechnical Journal, 42(5), pp. 1437–1448. doi: 10.1139/t05-064.

McDougall, S. (2017) '2014 Canadian Geotechnical Colloquium: Landslide runout analysis — current practice and challenges', Canadian Geotechnical Journal, 54(5), pp. 605–620. doi: 10.1139/cgj-2016-0104.

Menéndez-Duarte, R., Marquínez, J., Fernández-Menéndez, S. and Santos, R. (2007) 'Incised channels and gully erosion in Northern Iberian Peninsula: Controls and geomorphic setting', CATENA, 71(2), pp. 267–278. doi: 10.1016/j.catena.2007.01.002.

Mercier, D., Étienne, S., Sellier, D. and André, M.-F. (2009) 'Paraglacial gullying of sediment-mantled slopes: a case study of Colletthøgda, Kongsfjorden area, West Spitsbergen (Svalbard)', Earth Surface Processes and Landforms. John Wiley & Sons, Ltd., 34(13), pp. 1772–1789. doi: 10.1002/esp.1862.

Met Office (2016) UK Climate Averages 1981-2010. Available at: http://www.metoffice.gov.uk/public/weather/climate/ (Accessed: 28 September 2016).

Midgley, T. L., Fox, G. A., Wilson, G. V., Felice, R. M. and Heeren, D. M. (2013) 'In Situ Soil Pipeflow Experiments on Contrasting Streambank Soils', Transactions of the ASABE. 56(2). pp. 479-488. doi: 10.13031/2013.42685.

Milenković, M., Karel, W., Ressl, C. and Pfeifer, N. (2016) 'A Comparison of UAV and TLS Data for Soil Roughness Assessment', in ISPRS Annals of the Photogrammetry, Remote Sensing and Spatial Information Sciences, pp. 145–152. doi: 10.5194/isprs-annals-III-5-145-2016.

Milne, F. (2008) Topographic and material controls on the Scottish debris flow geohazard. University of Dundee. Available at: http://ethos.bl.uk/OrderDetails.do?uin=uk.bl.ethos.578723 (Accessed: 17 October 2014).

Milne, F. D., Brown, M. J., Davies, M. C. R. and Cameron, G. (2015) 'Some key topographic and material controls on debris flows in Scotland', Quarterly Journal of Engineering Geology and Hydrogeology. 48. pp. 212-223. doi: 10.1144/qjegh2013-095.

Milne, F. D., Brown, M. J., Knappett, J. A. and Davies, M. C. R. (2012) 'Centrifuge modelling of hillslope debris flow initiation', CATENA, 92, pp. 162–171. doi: 10.1016/j.catena.2011.12.001.

Milne, F. D., Brown, M. J. and Werritty, A. (2010) 'A hazardous channelized debris flow in Glen Ogle, Stirlingshire', Scottish Journal of Geology. Geological Society of London, 46(2), pp. 181–189. doi: 10.1144/0036-9276/01-409.

Milne, F. D., Werritty, A., Davies, M. C. R. and Brown, M. J. (2009) 'A recent debris flow event and implications for hazard management', Quarterly Journal of Engineering Geology and Hydrogeology, 42(1), pp. 51–60. doi: 10.1144/1470-9236/07-073.

Mitchell, W. W., Petley, D. N., Rosser, N. J., Dunning, S. A. and Kausar, A. B. (2005) 'The Development of Tension Crack Arrays Associated with the mw 7.6 Kashmir Earthquake, October 2005: Implications for Future Slope Stability', in Sassa, K. and Canuti, P. (eds) Landslides - Disaster Risk Reduction. Berlin, Heidelberg: Springer, pp. 397–398.

Montgomery, D. R. and Dietrich, W. E. (1994) 'A physically based model for the topographic control on shallow landsliding', Water Resources Research, 30(4), pp. 1153–1171. doi: 10.1029/93WR02979.

Montgomery, D. R., Dietrich, W. E., Torres, R., Anderson, S. P., Heffner, J. T. and Loague, K. (1997) 'Hydrologic response of a steep, unchanneled valley to natural and applied rainfall', Water Resources Research, 33(1), pp. 91–109. doi: 10.1029/96WR02985.

Montreuil, A.-L., Bullard, J. E., Chandler, J. H. and Millett, J. (2013) 'Decadal and seasonal development of embryo dunes on an accreting macrotidal beach: North Lincolnshire, UK', Earth Surface Processes and Landforms, 38(15), pp. 1851–1868. doi: 10.1002/esp.3432.

Mukhlisin, M., Kosugi, K., Satofuka, Y. and Mizuyama, T. (2006) 'Effects of Soil Porosity on Slope Stability and Debris Flow Runout at a Weathered Granitic Hillslope', Vadose Zone Journal. Soil Science Society, 5(1), p. 283. doi: 10.2136/vzj2005.0044.

Muñoz-Salinas, E., Castillo, M., Sanderson, D. and Kinnaird, T. (2013) 'Unraveling paraglacial activity on Sierra de Gredos, Central Spain: A study based on geomorphic markers, stratigraphy and OSL', CATENA, 110, pp. 207–214. doi: 10.1016/j.catena.2013.06.018.

Muñoz-Salinas, E., Renschler, C. S., Palacios, D. and Namikawa, L. M. (2008) 'Updating channel morphology in digital elevation models: Lahar assessment for Tenenepanco-Huiloac Gorge, Popocatépetl volcano, Mexico', in Natural Hazards, pp. 309–320. doi: 10.1007/s11069-007-9162-x.

Musgrave, G. W. (1947) 'The quantitative evaluation of factors in water erosion - a first approximation', Journal of Soil and Water Conservation, 2(3), pp. 133–138.

Nadal-Romero, E., Revuelto, J., Errea, P. and López-Moreno, J. I. (2015) 'The application of terrestrial laser scanner and SfM photogrammetry in measuring erosion and deposition processes in two opposite slopes in a humid badlands area (central Spanish pyrenees)', SOIL, 1(2), pp. 561–573. doi: 10.5194/soil-1-561-2015.

Napolitano, E., Fusco, F., Baum, R. L., Godt, J. W. and De Vita, P. (2016) 'Effect of antecedent-hydrological conditions on rainfall triggering of debris flows in ash-fall pyroclastic mantled slopes of Campania (southern Italy)', Landslides. Springer Berlin Heidelberg, 13(5), pp. 967–983. doi: 10.1007/s10346-015-0647-5.

Nettleton, I. M., Martin, S., Hencher, S. and Moore, R. (2005) 'Debris flow types and mechanisms', in Winter, M. G., Macgregor, F., and Shackman, L. (eds) Scottish Road Network Landslide Study, pp. 45–119. Available at: http://www.scotland.gov.uk/Publications/2005/07/08131738/17492.

Neugirg, F., Kaiser, A., Huber, A., Heckmann, T., Schindewolf, M., Schmidt, J., Becht, M. and Haas, F. (2016) 'Using terrestrial LiDAR data to analyse morphodynamics on steep unvegetated slopes driven by different geomorphic processes', Catena. Elsevier, 142, pp. 269–280. doi: 10.1016/j.catena.2016.03.021.

Ng, K. Y. (2006) 'Landslide locations and drainage network development: A case study of Hong Kong', Geomorphology, 76(1-2), pp. 229–239. doi: 10.1016/j.geomorph.2005.10.008.

Nguyen, H. T., Fernandez-Steeger, T. M., Wiatr, T., Rodrigues, D. and Azzam, R. (2011) 'Use of terrestrial laser scanning for engineering geological applications on volcanic rock slopes - An example from Madeira island (Portugal)', Natural Hazards and Earth System Science, 11(3), pp. 807–817. doi: 10.5194/nhess-11-807-2011.

Nyman, P., Sheridan, G. J., Smith, H. G. and Lane, P. N. J. (2011) 'Evidence of debris flow occurrence after wildfire in upland catchments of south-east Australia', Geomorphology, 125(3), pp. 383–401. doi: 10.1016/j.geomorph.2010.10.016.

Okuda, S., Suwa, H., Okunishi, K., Yokoyama, K., Hamana, S. and Tanaka, K. (1978) 'Synthetic observation on debris flow, Part 7, Observation at valley Kamikamihorizawa of Mt. Yakedake in 1977: Annuals DPRI, 21B-1', pp. 157–204.

Olsen, M., Wartman, J., McAlister, M., Mahmoudabadi, H., O'Banion, M., Dunham, L. and Cunningham, K. (2015) 'To Fill or Not to Fill: Sensitivity Analysis of the Influence of Resolution and Hole Filling on Point Cloud Surface Modeling and Individual Rockfall Event Detection', Remote Sensing. Multidisciplinary Digital Publishing Institute, 7(9), pp. 12103–12134. doi: 10.3390/rs70912103.

Ordnance Survey (2017) Ordnance Survey. Available at: https://www.ordnancesurvey.co.uk/gps/os-net-rinex-data/ (Accessed: 26 January 2018).

Orwin, J. F. and Smart, C. C. (2004) 'The evidence for paraglacial sedimentation and its temporal scale in the deglacierizing basin of Small River Glacier, Canada', Geomorphology, 58(1), pp. 175–202. doi: 10.1016/j.geomorph.2003.07.005.

Parkner, T., Page, M. J., Marutani, T. and Trustrum, N. A. (2006) 'Development and controlling factors of gullies and gully complexes, East Coast, New Zealand', Earth Surface Processes and Landforms. John Wiley & Sons, Ltd., 31(2), pp. 187–199. doi: 10.1002/esp.1321.

Parry, S. (2016) 'Landslide hazard assessments: problems and limitations. Examples from Hong Kong', Geological Society, London, Engineering Geology Special Publications. Geological Society of London, 27(1), pp. 135–145. doi: 10.1144/EGSP27.12.

Patton, P. C. and Schumm, S. A. (1975) 'Gully Erosion, Northwestern Colorado: A Threshold Phenomenon', Geology. GeoScienceWorld, 3(2), p. 88. doi: 10.1130/0091-7613(1975)3<88:GENCAT>2.0.CO;2.

Pelletier, J. D. (1997) 'Scale-invariance of soil moisture variability and its implications for the frequency-size distribution of landslides', Engineering Geology. 48(3-4). pp. 255-268. doi: 10.1016/S0013-7952(97)00041-0.

Perroy, R. L., Bookhagen, B., Asner, G. P. and Chadwick, O. A. (2010) 'Comparison of gully erosion estimates using airborne and ground-based LiDAR on Santa Cruz Island, California', Geomorphology. 118(3-4). pp. 288-300. doi: 10.1016/j.geomorph.2010.01.009.

Pesci, A. and Teza, G. (2008) 'Effects of surface irregularities on intensity data from laser scanning: An experimental approach', Annals of Geophysics, 51(5-6), pp. 839–848. doi: 10.4401/ag-4462.

Pesci, A., Teza, G. and Bonali, E. (2011) 'Terrestrial laser scanner resolution: Numerical simulations and experiments on spatial sampling optimization', Remote Sensing. 3(1). pp. 167-184.

Petley, D. (2012) 'Global patterns of loss of life from landslides', Geology. Geological Society of America, 40(10), pp. 927–930. doi: 10.1130/G33217.1.

Pierson, T. C. (1983) 'Soil pipes and slope stability', Quarterly Journal of Engineering Geology and Hydrogeology. 16(1). pp. 1-11.

Pierson, T. C. (2005) 'Hyperconcentrated flow — transitional process between water flow and debris flow', in Debris-flow Hazards and Related Phenomena. Berlin, Heidelberg: Springer Berlin Heidelberg, pp. 159–202. doi: 10.1007/3-540-27129-5_8.

Pierson, T. C. and Costa, J. E. (1987) 'A rheologic classification of subaerial sediment-water flows', in Reviews in Engineering Geology. Geological Society of America, pp. 1–12. doi: 10.1130/REG7-p1.

Pierson, T. and Scott, K. (1985) 'Debris Flow to Hyperconcentrated Streamflow', Water resources research. 21(10). pp. 1511-1524.

Pirotti, F., Guarnieri, A. and Vettore, A. (2013) 'Vegetation filtering of waveform terrestrial laser scanner data for DTM production', Applied Geomatics. 5(4). pp. 311-322.

Pirulli, M. (2005) Numerical modelling of landslide runout: a continuum mechanics approach. Politecnico di Torino. Available at: https://pdfs.semanticscholar.org/aca5/b08f314464ba6730433d701f997eaa0d3279.pdf (Accessed: 5 April 2018).

Pirulli, M. (2010) 'On the use of the calibration-based approach for debris-flow forward-analyses', Natural Hazards and Earth System Science, 10(5), pp. 1009–1019. doi: 10.5194/nhess-10-1009-2010.

Pirulli, M. and Sorbino, G. (2008) 'Assessing potential debris flow runout: A comparison of two simulation models', Natural Hazards and Earth System Science, 8(4), pp. 961–971. doi: 10.5194/nhess-8-961-2008.

Platzer, K., Bartelt, P. and Kern, M. (2007) 'Measurements of dense snow avalanche basal shear to normal stress ratios (S/N)', Geophysical Research Letters. Wiley-Blackwell, 34(7). doi: 10.1029/2006GL028670.

Poesen, J. (1993) 'Gully typology and gully control measures in the European loess belt', Farm Land Erosion in Temperate Plains Environments. pp. 221-239.

Poesen, J., Nachtergaele, J., Verstraeten, G. and Valentin, C. (2003) 'Gully erosion and environmental change: importance and research needs', Catena. 50(2-4). pp. 91-133.

Procter, J. N., Cronin, S. J., Zernack, A. V., Lube, G., Stewart, R. B., Nemeth, K. and Keys, H. (2014) 'Debris flow evolution and the activation of an explosive hydrothermal system; Te Maari, Tongariro,

New Zealand', Journal of Volcanology and Geothermal Research, 286, pp. 303–316. doi: 10.1016/j.jvolgeores.2014.07.006.

Pudasaini, S. (2012) 'A general two-phase debris flow model', Journal of Geophysical Research: Earth. 117(F3).

Qi, J., Ma, W. and Song, C. (2008) 'Influence of freeze–thaw on engineering properties of a silty soil', Cold Regions Science and Technology, 53(3), pp. 397–404. doi: 10.1016/j.coldregions.2007.05.010.

Quan Luna, B., Westen, C. J. Van, Jetten, V. and Asch, T. W. J. Van (2010) 'A preliminary compilation of calibrated rheological parameters used in dynamic simulations of landslide run-out', in Mountain risks: bringing science to society. Proceedings of the Mountain Risks International Conference. Firenze, Italy: CERG Strasbourg, pp. 255–260.

Rahardjo, H., Indrawan, I. G. B., Leong, E. C. and Yong, W. K. (2008) 'Effects of coarse-grained material on hydraulic properties and shear strength of top soil', Engineering Geology, 101(3), pp. 165–173. doi: 10.1016/j.enggeo.2008.05.001.

Rahardjo, H., Lim, T. T., Chang, M. F. and Fredlund, D. G. (1995) 'Shear-strength characteristics of a residual soil', Canadian Geotechnical Journal. NRC Research Press Ottawa, Canada , 32(1), pp. 60–77. doi: 10.1139/t95-005.

Ray, R., Jacobs, J. and Alba, P. de (2010) 'Impacts of unsaturated zone soil moisture and groundwater table on slope instability', Journal of Geotechnical and Geoenvironmental Engineering. 136(10). pp. 1448-1458.

Reid, E. and Thomas, M. F. (2006) 'A chronostratigraphy of mid- and late-Holocene slope evolution: Creagan a' Chaorainn, Northern Highlands, Scotland', The Holocene. SAGE Publications, 16(3), pp. 429–444. doi: 10.1191/0959683606hl939rp.

Reid, M., Brien, D. and LaHusen, R. (2003) 'Debris-flow initiation from large, slow-moving landslides', Rickenmann, D. and Chen, C. l. (ed.), Debris-Flow Hazards Mitigation: Mechanics, Prediction, and Assessment. 1. pp. 155-156.

Reid, M. E., Baum, R. L., LaHusen, R. G. and Ellis, W. L. (2008) 'Capturing landslide dynamics and hydrologic triggers using near-real-time monitoring', Landslides and Engineered Slopes. From the Past to the Future. 1. pp. 179–191. doi: 10.1201/9780203885284-c10.

Reid, M. E., LaHusen, R. G. and Iverson, R. M. (1997) 'Debris-Flow Initiation Experiments Using Diverse Hydrologic Triggers', Debris-Flow Hazards Mitigation: Mechanics, Prediction and Assessment, pp. 1–11.

Reid, M., Iverson, R. and Logan, M. (2011) 'Entrainment of bed sediment by debris flows: Results from large-scale experiments', Debris-flow Hazards. In Genevois, R., Hamilton, D. L., and Prestinizi, A. (eds) Fifth International Conference on Debris-flow Hazards Mitigation, Mechanics, Prediction and Assessment, Casa Editrice Universita La Sapienza, Rome. pp. 367-374.

Reynolds, O. (1886) 'Dilatancy', Nature, 33, pp. 429–430.

Richardson, S. and Reynolds, J. (2000) 'An overview of glacial hazards in the Himalayas', Quaternary International. 65. pp. 31-47.

Rickenmann, D. (2005) 'Runout prediction methods', in Jakob, M. and Hungr, O. (eds) Debris-flow Hazards and Related Phenomena. Berlin, Heidelberg: Springer-Verlag, pp. 305–321.

Riegl (2010) LMS-Z620 Data Sheet. Available at: http://www.riegl.com/uploads/tx_pxpriegldownloads/11_DataSheet_Z620_03-05-2010.pdf (Accessed: 14 May 2018).

Riegl (2011) 'RiScan Pro.' Available at: http://www.riegl.com.

Riegl (2017a) RIEGL - VZ-6000. Available at: http://www.riegl.com/nc/products/terrestrial-scanning/produktdetail/product/scanner/33/ (Accessed: 17 October 2017).

Riegl (2017b) VZ-4000 Data Sheet. Available at: http://www.riegl.com/uploads/tx_pxpriegldownloads/RIEGL_VZ-4000_Datasheet_2017-09-01.pdf (Accessed: 14 May 2018).

Rosser, N. J. (2010) 'Landslides and Rockfalls', in Burt, T. and Allison, R. (eds) Sediment cascades: an integrated approach. Oxford: John Wiley & Sons, Ltd, pp. 55–88.

Rosser, N. J., Petley, D. N., Lim, M., Dunning, S. A. and Allison, R. J. (2005) 'Terrestrial laser scanning for monitoring the process of hard rock coastal cliff erosion', Quarterly Journal of Engineering Geology and Hydrogeology. Geological Society of London, 38(4), pp. 363–375. doi: 10.1144/1470-9236/05-008.

Rosser, N., Lim, M., Petley, D., Dunning, S. and Allison, R. (2007) 'Patterns of precursory rockfall prior to slope failure', Journal of Geophysical Research, 112(F4). doi: 10.1029/2006JF000642.

Le Roux, O., Schwartz, S., Gamond, J. F., Jongmans, D., Bourles, D., Braucher, R., Mahaney, W., Carcaillet, J. and Leanni, L. (2009) CRE dating on the head scarp of a major landslide (Séchilienne, French Alps), age constraints on Holocene kinematics, Earth and Planetary Science Letters. 280(1-4). pp. 236-245. doi: 10.1016/j.epsl.2009.01.034.

von Ruette, J., Papritz, A., Lehmann, P., Rickli, C. and Or, D. (2011) 'Spatial statistical modeling of shallow landslides-Validating predictions for different landslide inventories and rainfall events', Geomorphology, 133(1-2), pp. 11–22. doi: 10.1016/j.geomorph.2011.06.010.

Saito, H., Korup, O., Uchida, T., Hayashi, S. and Oguchi, T. (2014) 'Rainfall conditions, typhoon frequency, and contemporary landslide erosion in Japan', Geology, 42(11), pp. 999–1002. doi: 10.1130/G35680.1.

Salm, B. (1993) 'Flow, flow transition and run-out distances of flowing avalanches', Annals of Glaciology, 18, pp. 221–226. doi: 10.1017/S0260305500011551.

Sanchez, G., Rolland, Y., Corsini, M., Braucher, R., Bourlès, D., Arnold, M. and Aumaître, G. (2010) 'Relationships between tectonics, slope instability and climate change: Cosmic ray exposure dating of active faults, landslides and glacial surfaces in the SW Alps', Geomorphology, 117(1), pp. 1–13. doi: 10.1016/j.geomorph.2009.10.019.

Santana, D., Corominas, J., Mavrouli, O. and Garcia-Sellés, D. (2012) 'Magnitude-frequency relation for rockfall scars using a Terrestrial Laser Scanner', Engineering Geology, 144-145, pp. 50–64. doi: 10.1016/j.enggeo.2012.07.001.

Sasahara, K. and Sakai, N. (2014) 'Development of shear deformation due to the increase of pore pressure in a sandy model slope during rainfall', Engineering Geology, 170, pp. 43–51. doi: 10.1016/j.enggeo.2013.12.005.

Sassa, K. (2000) 'Mechanism of flows in granular soils', ISRM International Symposium. Available at: https://www.onepetro.org/conference-paper/ISRM-IS-2000-043 (Accessed: 8 October 2016).

Scheidl, C. and Rickenmann, D. (2009) 'Empirical prediction of debris-flow mobility and deposition on fans', Earth Surface Processes and Landforms. 35(2). pp. 157-173. doi: 10.1002/esp.1897.

Scheidl, C., Rickenmann, D. and McArdell, B. W. (2013) 'Runout prediction of debris flows and similar mass movements', in Landslide Science and Practice: Spatial Analysis and Modelling. Berlin, Heidelberg: Springer Berlin Heidelberg, pp. 221–229. doi: 10.1007/978-3-642-31310-3-30.

Scheuner, T., Schwab, S. and Mcardell, B. W. (2011) 'Application of a two-dimensional numerical model in risk and hazard assessment in Switzerland', 5th DFHM, pp. 993–1001. doi: 10.4408/IJEGE.2011-03.B-108.

Schofield, A. and Wroth, P. (1968) 'Critical state soil mechanics'. 310. McGraw-Hill. London. Available at: http://civil.dept.shef.ac.uk/current/module/CIV6505.pdf (Accessed: 7 October 2016).

Schraml, K., Thomschitz, B., McArdell, B. W., Graf, C. and Kaitna, R. (2015) 'Modeling debris-flow runout patterns on two alpine fans with different dynamic simulation models', Natural Hazards and Earth System Science. Copernicus GmbH, 15(7), pp. 1483–1492. doi: 10.5194/nhess-15-1483-2015.

Schulz, W. H., McKenna, J. P., Kibler, J. D. and Biavati, G. (2009) 'Relations between hydrology and velocity of a continuously moving landslide—evidence of pore-pressure feedback regulating landslide motion?', Landslides. Springer-Verlag, 6(3), pp. 181–190. doi: 10.1007/s10346-009-0157-4.

Schumm, S., Harvey, M. and Watson, C. (1984) Incised Channels: Initiation, Evolution, Dynamics, and Control, Water Resources Publication. Littleton, Colorado.

Schürch, P., Densmore, A. L., Rosser, N. J., Lim, M. and McArdell, B. W. (2011) 'Detection of surface change in complex topography using terrestrial laser scanning: application to the Illgraben debris-flow channel', Earth Surface Processes and Landforms. John Wiley & Sons, Ltd, 36(14), pp. 1847–1859. doi: 10.1002/esp.2206.

Schurch, P., Densmore, A. L., Rosser, N. J. and McArdell, B. W. (2011) 'Dynamic controls on erosion and deposition on debris-flow fans', Geology. Geological Society of America, 39(9), pp. 827–830. doi: 10.1130/G32103.1.

Scottish Government (2017) Annual Precipitation 1910-2016. Available at: https://www2.gov.scot/seso (Accessed: 28 September 2019).

Scottish Natural Heritage (2016) Carbon and Peatland 2016 map. Available at: http://map.environment.gov.scot/Soil_maps (Accessed: 4 July 2018).

Sharp, R. and Nobles, L. (1953) 'Mudflow of 1941 at Wrightwood, southern California', Geological Society of America. 64(5). pp. 547-560.

Sidle, R. C. (2005) 'Influence of forest harvesting on debris avalanches and flows', in Jakob, M. and Hungr, O. (eds) Debris-flow Hazards and Related Phenomena. Berlin, Heidelberg: Springer, pp. 387–403.

Sidle, R. C. and Bogaard, T. A. (2016) 'Dynamic earth system and ecological controls of rainfall-initiated landslides', Earth-Science Reviews, 159, pp. 275–291. doi: 10.1016/j.earscirev.2016.05.013.

Sidle, R. C. and Onda, Y. (2004) 'Hydrogeomorphology: overview of an emerging science', Hydrological Processes, 18(4), pp. 597–602. doi: 10.1002/hyp.1360.

Sidle, R. C., Ziegler, A. D., Negishi, J. N., Nik, A. R., Siew, R. and Turkelboom, F. (2006) 'Erosion processes in steep terrain - Truths, myths, and uncertainties related to forest management in Southeast Asia', Forest Ecology and Management, 224(1-2), pp. 199–225. doi: 10.1016/j.foreco.2005.12.019.

Sidle, R., Noguchi, S. and Tsuboyama, Y. (2001) 'A conceptual model of preferential flow systems in forested hillslopes: Evidence of self-organization', Hydrological. 15(10). pp. 1675-1692.

Sidle, R. and Ochiai, H. (2006) 'Landslides: processes, prediction, and land use', in Sidle, R. C., and Pearce, A. J. and O'Loughlin, C. L. (eds) Hillslope Stability and Land Use. 11.

Simoni, A., Mammoliti, M. and Graf, C. (2012) 'Performance of 2D debris flow simulation model RAMMS. Back-analysis of field events in Italian Alps', in Conference Proceedings on 1st Annual International Conference on Geological & Earth Sciences. Global Science Technology Forum. doi: 10.5176/2251-3361_GEOS12.59.

Slaymaker, O. (1987) 'Sediment and solute yields in British Columbia and Yukon: their geomorphic significance reexamined'. pp. 925–945.

Slaymaker, O. and Kelly, R. E. J. (2007) The cryosphere and global environmental change, Water. Blackwell Publishing, Oxford. doi: 10.1111/j.1475-4762.2008.875_5.x.

Smout, T. C. (T. C., MacDonald, A. R. and Watson, F. J. (2007) A history of the native woodlands of Scotland, 1500-1920. Edinburgh University Press.

Soudarissanane, S., Lindenbergh, R., Menenti, M. and Teunissen, P. (2011) 'Scanning geometry: Influencing factor on the quality of terrestrial laser scanning points', ISPRS Journal of Photogrammetry and Remote Sensing, 66(4), pp. 389–399. doi: 10.1016/j.isprsjprs.2011.01.005.

Sparkes, B., Dunning, S., Lim, M. and Winter, M. G. (2017) 'Characterisation of Recent Debris Flow Activity at the Rest and Be Thankful, Scotland', in Advancing Culture of Living with Landslides. Springer International Publishing, Cham. pp. 51–58. doi: 10.1007/978-3-319-53483-1_8.

Staley, D. M., Wasklewicz, T. A. and Kean, J. W. (2014) 'Characterizing the primary material sources and dominant erosional processes for post-fire debris-flow initiation in a headwater basin using multi-temporal terrestrial laser scanning data', Geomorphology, 214, pp. 324–338. doi: 10.1016/j.geomorph.2014.02.015.

Stark, C. P. and Hovius, N. (2001) 'The characterization of landslide size distributions', Geophysical Research Letters, 28(6), pp. 1091–1094. doi: 10.1029/2000GL008527.

Stark, T. D. and Eid, H. T. (1994) 'Drained Residual Strength of Cohesive Soils', Journal of Geotechnical Engineering. American Society of Civil Engineers, 120(5), pp. 856–871. doi: 10.1061/(ASCE)0733-9410(1994)120:5(856).

Steger, S., Brenning, A., Bell, R. and Glade, T. (2017) 'The influence of systematically incomplete shallow landslide inventories on statistical susceptibility models and suggestions for improvements', Landslides, 14(5), pp. 1767–1781. doi: 10.1007/s10346-017-0820-0.

Stock, J. D. and Dietrich, W. E. (2006) 'Erosion of steepland valleys by debris flows', Geological Society of America Bulletin. Geological Society of America, 118(9-10), pp. 1125–1148. doi: 10.1130/B25902.1.

Stock, J. and Dietrich, W. (2003) 'Valley incision by debris flows: Evidence of a topographic signature', Water Resources Research. 39(4). Available at: http://onlinelibrary.wiley.com/doi/10.1029/2001WR001057/full (Accessed: 1 May 2017).

Stoffel, M. (2010) 'Magnitude-frequency relationships of debris flows - A case study based on field surveys and tree-ring records', Geomorphology, 116(1-2), pp. 67–76. doi: 10.1016/j.geomorph.2009.10.009.

Stoffel, M. and Huggel, C. (2012) 'Effects of climate change on mass movements in mountain environments', Progress in Physical Geography. SAGE Publications, 36(3), pp. 421–439. doi: 10.1177/0309133312441010.

Strachan, G. J. (2015) 'Debris flow activity and gully propagation: Glen Docherty, Wester Ross', Scottish Journal of Geology. Geological Society of London, 51(1), pp. 69–80. doi: 10.1144/sjg2014-013.

Strozzi, T., Farina, P., Corsini, A., Ambrosi, C., Thüring, M., Zilger, J., Wiesmann, A., Wegmüller, U. and Werner, C. (2005) 'Survey and monitoring of landslide displacements by means of L-band satellite SAR interferometry', Landslides. 2(3). pp. 193–201. doi: 10.1007/s10346-005-0003-2.

Sun, H. yue, Wong, L. N. Y., Shang, Y. quan, Shen, Y. jiang and Lü, Q. (2010) 'Evaluation of drainage tunnel effectiveness in landslide control', Landslides. 7(4). pp. 445–454. doi: 10.1007/s10346-010-0210-3.

Swanson, M. L., Kondolf, G. M. and Boison, P. J. (1989) 'An example of rapid gully initiation and extension by subsurface erosion: Coastal San Mateo County, California', Geomorphology, 2(4), pp. 393–403. doi: 10.1016/0169-555X(89)90023-8.

Takahashi, T. (1991) Debris flow. Leiden: Balkema.

Takahashi, T. (2014) Debris flow: mechanics, prediction and countermeasures. CRC Press, London.

Take, W. A., Beddoe, R. A., Davoodi-Bilesavar, R. and Phillips, R. (2015) 'Effect of antecedent groundwater conditions on the triggering of static liquefaction landslides', Landslides. Springer Berlin Heidelberg, 12(3), pp. 469–479. doi: 10.1007/s10346-014-0496-7.

Taylor, J. (1997) Introduction to error analysis, the study of uncertainties in physical measurements. University Science Books, Sausalito CA.

Telling, J., Lyda, A., Hartzell, P. and Glennie, C. (2017) 'Review of Earth science research using terrestrial laser scanning', Earth-Science Reviews. 169. pp. 35–68. doi: 10.1016/j.earscirev.2017.04.007.

Teza, G., Galgaro, A. and Zaltron, N. (2007) 'Terrestrial laser scanner to detect landslide displacement fields: a new approach', International Journal of Remote Sensing. 28(16). pp. 3425-3446.

Theule, J. I., Liébault, F., Laigle, D., Loye, A. and Jaboyedoff, M. (2015) 'Channel scour and fill by debris flows and bedload transport', Geomorphology. Elsevier, 243, pp. 92–105. doi: 10.1016/J.GEOMORPH.2015.05.003.

Theule, J., Liébault, F. and Loye, A. (2012) 'Sediment budget monitoring of debris-flow and bedload transport in the Manival Torrent, SE France', Natural Hazards and Earth System Sciences. 12. pp. 731-749.

Tonini, M. and Abellan, A. (2014) 'Rockfall detection from terrestrial LiDAR point clouds: A clustering approach using R', Journal of Spatial Information Science. (8). pp. 95-110. doi: 10.5311/JOSIS.2014.8.123.

Transport Scotland (2016a) Debris flow fences - 'How much debris are they capable of holding?' Available at: https://www.transport.gov.scot (Accessed: 1st November 2016).

Transport Scotland (2016b) Enhanced landslide mitigation for A83 - Further investment outlined. Available at: https://www.transport.gov.scot/news/enhanced-landslide-mitigation-for-a83-further-investment-outlined/ (Accessed: 13 April 2018).

Travelletti, J., Delacourt, C., Allemand, P., Malet, J.-P., Schmittbuhl, J., Toussaint, R. and Bastard, M. (2012) 'Correlation of multi-temporal ground-based optical images for landslide monitoring: Application, potential and limitations', ISPRS Journal of Photogrammetry and Remote Sensing, 70, pp. 39–55. doi: 10.1016/j.isprsjprs.2012.03.007.

Trenter, N. A. (1999) Engineering in Glacial Tills. CIRIA Publication C504. Construction Industry Research and Information Association, London.

Tsukamoto, Y., Ohta, T. and Noguchi, H. (1982) 'Hydrological and geomorphological studies of debris slides on forested hillslopes in Japan', International Association of Hydrological Sciences Publication. 137. pp. 89-98.

Uchida, T. (2004) 'Clarifying the role of pipe flow on shallow landslide initiation', Hydrological Processes. John Wiley & Sons, Ltd., 18(2), pp. 375–378. doi: 10.1002/hyp.5214.

Uchida, T., Kosugi, K. and Mizuyama, T. (2001) 'Effects of pipeflow on hydrological process and its relation to landslide: a review of pipeflow studies in forested headwater catchments', Hydrological Processes. John Wiley & Sons, Ltd., 15(11), pp. 2151–2174. doi: 10.1002/hyp.281.

Vallance, J. W. and Scott, K. M. (1997) 'The Osceola Mudflow from Mount Rainier: Sedimentology and hazard implications of a huge clay-rich debris flow', Geological Society of America Bulletin, 109(2), pp. 143–163. doi: 10.1130/0016-7606(1997)109.

Vandekerckhove, L., Poesen, J., Oostwoud Wijdenes, D. and Gyssels, G. (2001) 'Short-term bank gully retreat rates in Mediterranean environments', CATENA, 44(2), pp. 133–161. doi: 10.1016/S0341-8162(00)00152-1.

Vanmaercke, M., Poesen, J. and Mele, B. Van (2016) 'How fast do gully headcuts retreat?', Earth-Science Reviews. 154. pp. 336-355.

Varnes, D. J. (1954) 'Landslide types and processes', in Eckel, E. B. (ed) Landslides and Engineering Practice, Special Report 28. Washington DC: Highway Research Board, National Academy of Sciences, pp. 20–47.

Varnes, D. J. (1978) 'Slope Movement Types and Processes', Transportation Research Board Special Report, (176). Available at: http://trid.trb.org/view.aspx?id=86168 (Accessed: 14 October 2014).

Vennari, C., Mc Ardell, B., Parise, M., Santangelo, N. and Santo, A. (2016) 'Implementation of the RAMMS Debris Flow to Italian case studies', EGU General Assembly 2016, held 17-22 April, 2016 in Vienna Austria. 18. p. 11378.

Veyrat-Charvillon, S. and Memier, M. (2006) 'Stereophotogrammetry of archive data and topographic approaches to debris-flow torrent measurements: Calculation of channel-sediment states and a partial sediment budget for Manival torrent (Isère, France)', Earth Surface Processes and Landforms, 31(2), pp. 201–219. doi: 10.1002/esp.1322.

Wagner, W., Hollaus, M., Briese, C. and Ducic, V. (2008) '3D vegetation mapping using small-footprint full-waveform airborne laser scanners', International Journal of Remote Sensing. Taylor & Francis. 29(5), pp. 1433–1452. doi: 10.1080/01431160701736398.

Wang, B., Li, Y., Liu, D. and Liu, J. (2017) 'Debris flow density determined by grain composition', Landslides. Springer Berlin Heidelberg, pp. 1–9. doi: 10.1007/s10346-017-0912-x.

Wang, G. and Sassa, K. (2003) 'Pore-pressure generation and movement of rainfall-induced landslides: effects of grain size and fine-particle content', Engineering Geology, 69(1), pp. 109–125. doi: 10.1016/S0013-7952(02)00268-5.

Wartmann, S. and Salzmann, H. (2002) Debris Flow and Floating Tree Impacts on Flexible Barriers. Hong Kong: IMMM Press. Available at: https://www.tib.eu/en/search/id/BLCP%3ACN071822495/Debris-Flow-and-Floating-Tree-Impacts-on-Flexible/ (Accessed: 13 April 2018).

Wendeler, C., McArdell, B., Rickenmann, D., Volkwein, A., Roth, A. and Denk, M. (2006) 'Field testing and numerical modeling of flexible debris flow barriers', Physical Modelling in Geotechnics - 6th ICPMG '06, pp. 1573–1578. Available at: https://www.dora.lib4ri.ch/wsl/islandora/object/wsl:12365 (Accessed: 13 April 2018).

van Westen, C. J., van Asch, T. W. J. and Soeters, R. (2005) 'Landslide hazard and risk zonation - Why is it still so difficult?', Bulletin of Engineering Geology and the Environment, 65(2), pp. 167–184. doi: 10.1007/s10064-005-0023-0.

Westoby, M., Brasington, J., Glasser, N. and Hambrey, M. (2012) '"Structure-from-Motion"photogrammetry: A low-cost, effective tool for geoscience applications', Geomorphology. 179. pp. 300-314. Available at: http://www.sciencedirect.com/science/article/pii/S0169555X12004217 (Accessed: 22 September 2017).

Westoby, M., Dunning, S. and Hein, A. (2016) 'Interannual surface evolution of an Antarctic blue-ice moraine using multi-temporal DEMs', Earth Surface Dynamics. 4(2). pp. 515-529.

Wicherski, W., Dethier, D. P. and Ouimet, W. B. (2016) 'Erosion and channel changes due to extreme flooding in the Fourmile Creek catchment, Colorado', Geomorphology. Elsevier, 294, pp. 87–98. doi: 10.1016/j.geomorph.2017.03.030.

Wieczorek, G. F. (1987) 'Effect of rainfall intensity and duration on debris flows in central Santa Cruz Mountains, California', in Reviews in Engineering Geology. Geological Society of America. 7. pp. 93–104. doi: 10.1130/REG7-p93.

Wieczorek, G. F. and Glade, T. (2005) 'Climatic factors influencing occurrence of debris flows', in Debris-flow Hazards and Related Phenomena. Berlin, Heidelberg: Springer Berlin Heidelberg, pp. 325–362. doi: 10.1007/3-540-27129-5_14.

Williams, J. G., Rosser, N. J., Hardy, R. J., Brain, M. J. and Afana, A. A. (2017) 'Optimising 4D Approaches to Surface Change Detection: Improving Understanding of Rockfall Magnitude-Frequency', Earth Surface Dynamics Discussions, July, pp. 1–36. doi: 10.5194/esurf-2017-43.

Wilson, G. (2011) 'Understanding soil-pipe flow and its role in ephemeral gully erosion', Hydrological Processes. John Wiley & Sons, Ltd., 25(15), pp. 2354–2364. doi: 10.1002/hyp.7998.

Wilson, G., Nieber, J. and Sidle, R. (2013) 'Internal erosion during soil pipeflow: State of the science for experimental and numerical analysis', Transactions of the ASABE. 56(2). pp. 465-478.

Wilson, G. V., Rigby, J. R., Ursic, M. and Dabney, S. M. (2016) 'Soil pipe flow tracer experiments: 1. Connectivity and transport characteristics', Hydrological Processes. 30(8). pp. 1265-1279. doi: 10.1002/hyp.10713.

Wilson, G. V., Wells, R., Kuhnle, R., Fox, G. and Nieber, J. (2018) 'Sediment detachment and transport processes associated with internal erosion of soil pipes', Earth Surface Processes and Landforms. 43(1) pp. 45–63. doi: 10.1002/esp.4147.

Wilson, R. C. (1989) 'Rainstorms, pore pressures, and debris flows: a theoretical framework', in Sadler, P. M. and Morton, D. M. (eds) Landslides in semi-arid environment. Riverside: Inland Geologic Society, pp. 101–117.

Wilson, R. C. and Wieczorek, G. F. (1995) 'Rainfall Thresholds for the Initiation of Debris Flows at La Honda, California', Environmental & Engineering Geoscience, 1(1). pp. 11-27.

Winter, M. G., Dent, J. and Macgregor, F. (2010) 'Debris flow, rainfall and climate change in Scotland', Quarterly Journal of Engineering geology and Hydrogeology. 43(4). pp. 429-446.

Winter, M. G. (2014) 'A strategic approach to landslide risk reduction', International Journal of Landslide and Environment, 2(1), pp. 14–23.

Winter, M. G. (2016) 'A Strategic Approach to Debris Flow Risk Reduction on the Road Network', in Procedia Engineering. 143. pp. 759–768. doi: 10.1016/j.proeng.2016.06.121.

Winter, M. G. and Bromhead, E. N. (2012) 'Landslide risk: Some issues that determine societal acceptance', Natural Hazards, 62(2), pp. 169–187. doi: 10.1007/s11069-011-9987-1.

Winter, M.G., Heald, A.P., Parsons, J.A., Shackman, L. & MacGregor, F. (2006). 'Scottish Debris Flow Events of August 2004'. Quarterly Journal of Engineering Geology and Hydrogeology. 39(1) pp. 73-78.

Winter, M. G., Kinnear, N., Shearer, B., Lloyd, L. and Helman, S. (2013) 'A technical and perceptual evaluation of wig-wag signs at the A83 Rest and be Thankful', in Published Project Report PPR 664. TRL, Wokingham.

Winter, M. G., Macgregor, F. and Shackman, L. (2005) Scottish Road Network Landslide Study . Edinburgh: The Scottish Executive. Available at: http://www.scotland.gov.uk/Resource/Doc/55971/0015351.pdf (Accessed: 14 October 2014).

Winter, M. G. and Shearer, B. (2015) 'Climate Change and Landslide Hazard and Risk in Scotland', in Lollino, G., Manconi, A., Clague, J., Shan, W., and Chiarle, M. (eds) Engineering Geology for Society

and Territory - Volume 1: Climate Change and Engineering Geology. London: Springer International Publishing, pp. 411–414. doi: 10.1007/978-3-319-09300-0_78.

Winter, M. G. and Shearer, B. (2017) 'An Extended and Updated Technical Evaluation of Wig-Wag Signs at the A83 Rest and be Thankful.' Available at: https://trid.trb.org/view/1458164 (Accessed: 12 June 2018).

Winter, M. G., Troughton, V., Bayliss, R., Golightly, C., Spasic-Gril, L., Hobbs, P. R. N. and Privett, K. D. (2017) 'Design and construction considerations', in Griffiths, J. S. and Martin, C. J. (eds) Engineering Geology and Geomorphology of Glaciated and Periglaciated Terrains: Engineering Group Working Party Report. 28th edn. London: Geological Society, pp. 831–885.

Winter, M. G., Macgregor, F. and Shackman, L. (2009) Scottish road network landslides study: implementation. Transport Scotland, Glasgow. Available at: http://www.transportscotland.gov.uk/sites/default/files/documents/rrd_reports/uploaded_reports/j10107/j10107.pdf (Accessed: 13 October 2014).

Winter, M. G., Shearer, B., Palmer, D. and Peeling, D. (2016) 'The Economic Impact of Landslides and Floods on the Road Network', Procedia engineering. 143. pp. 1425-1434.

Wolf, P. and Ghilani, D. (2006) 'Adjustment Computations Spatial Data Analysis', New Jersey: John Wiley & Sons, Inc.

Wu, L. Z., Huang, R. Q., Xu, Q., Zhang, L. M. and Li, H. L. (2015) 'Analysis of physical testing of rainfall-induced soil slope failures', Environmental Earth Sciences. Springer Berlin Heidelberg, 73(12), pp. 8519–8531. doi: 10.1007/s12665-014-4009-8.

Wyrwoll, K. (1977) 'Causes of rock-slope failure in a cold area: Labrador-Ungava', Geological Society of America Reviews in Engineering Geology. 3. pp. 59-67.

Xenaki, V. C. and Athanasopoulos, G. A. (2003) 'Liquefaction resistance of sand–silt mixtures: an experimental investigation of the effect of fines', Soil Dynamics and Earthquake Engineering, 23(3), pp. 1–12. doi: 10.1016/S0267-7261(02)00210-5.

Zhou, G. G. D., Cui, P., Chen, H. Y., Zhu, X. H., Tang, J. B. and Sun, Q. C. (2013) 'Experimental study on cascading landslide dam failures by upstream flows', Landslides. Springer Berlin Heidelberg, 10(5), pp. 633–643. doi: 10.1007/s10346-012-0352-6.

Zimmermann, F., McArdell, B., Rickli, C. and Hübl, J. (2018) 'Does cohesion improve the accuracy of runout of hillslope debris flows? A systematic comparison using well-documented events in Switzerland.', in. EGU: Geophysical Research Abstracts. Available at: https://meetingorganizer.copernicus.org/EGU2018/EGU2018-15001.pdf (Accessed: 8 March 2018).

Zimmermann, M., Mani, P. and Romang, H. (1997) ‘Magnitude-frequency aspects of alpine debris flows’, Eclogae Geologicae Helvetiae. 90(3). pp. 415-420.

Zingg, A. W. (1940) ‘Degree and length of land slope as it affects soil loss in run-off.’, Agricultural Engineering. 21(2). pp. 59–64.

Appendix 1

Table 0.1 - RabT year 1 loss values (m^3)

3D Area (m^2)	Mean depth (m)	Volume (m^3)	Adjusted volume (m^3)
429.00	-1.47	-630.17	**-630.17**
419.58	-0.76	-320.30	**-320.30**
58.15	-0.56	-32.83	**-32.83**
27.47	-0.61	-16.69	**-16.69**
119.48	-1.28	-152.59	**-152.59**
28.76	-0.57	-16.44	**-16.44**
153.47	-0.97	-149.57	**-149.57**
20.96	-0.59	-12.37	**-12.37**
11.14	-0.38	-4.24	**-5.08**
16.29	-0.50	-8.17	**-9.28**
5.33	-0.37	-1.99	**-2.54**
6.53	-0.42	-2.75	**-3.46**
7.17	-0.65	-4.68	**-5.85**
5.24	-0.35	-1.85	**-2.37**
49.68	-0.76	-37.74	**-37.74**
12.57	-0.68	-8.51	**-10.05**
6.23	-0.41	-2.57	**-3.26**
5.02	-0.64	-3.21	**-4.12**
44.17	-0.71	-31.17	**-31.17**
1.92	-0.40	-0.76	**-1.09**

26.47	-0.69	-18.23	**-18.23**
10.34	-0.59	-6.11	**-7.39**
4.06	-0.58	-2.35	**-3.04**
4.55	-0.62	-2.81	**-3.63**
20.79	-0.90	-18.82	**-18.82**
1.97	-0.51	-1.01	**-1.43**
12.02	-0.73	-8.73	**-10.37**
3.01	-0.70	-2.12	**-2.78**
2.06	-0.39	-0.81	**-1.13**
11.46	-1.65	-18.92	**-22.60**
2.07	-0.35	-0.72	**-1.00**
4.59	-0.57	-2.61	**-3.37**
8.44	-0.71	-5.98	**-7.38**
1.51	-0.38	-0.57	**-0.91**
0.94	-0.43	-0.40	**-0.77**
11.88	-0.54	-6.44	**-7.66**
2.32	-0.39	-0.90	**-1.20**
7.05	-0.58	-4.10	**-5.14**
1.49	-0.56	-0.83	**-1.33**
1.01	-0.50	-0.51	**-0.95**
3D Area (m^2)	**Mean depth (m)**	**Volume (m^3)**	**Adjusted volume (m^3)**
0.69	-0.41	-0.28	**-0.59**

1.94	-0.63	-1.22	**-1.74**
1.43	-0.42	-0.60	**-0.98**
1.86	-0.37	-0.70	**-1.02**
5.57	-0.86	-4.82	**-6.14**
4.23	-0.48	-2.03	**-2.62**
1.51	-0.39	-0.58	**-0.93**
2.11	-0.41	-0.87	**-1.20**
0.71	-0.55	-0.39	**-0.81**
0.58	-0.49	-0.29	**-0.63**
0.92	-0.37	-0.35	**-0.67**
4.65	-1.13	-5.26	**-6.77**
1.25	-0.87	-1.08	**-1.88**
6.70	-1.08	-7.24	**-9.11**
1.70	-0.45	-0.77	**-1.16**
3.29	-0.54	-1.78	**-2.33**
0.50	-0.36	-0.18	**0.00**
4.89	-0.72	-3.51	**-4.51**
6.66	-0.74	-4.93	**-6.20**
1.67	-0.76	-1.27	**-1.94**
0.28	-0.77	-0.22	**0.00**
3.38	-1.04	-3.52	**-4.60**
1.32	-0.76	-1.01	**-1.71**
0.45	-0.30	-0.14	**0.00**
0.79	-0.49	-0.39	**-0.78**

0.76	-0.27	-0.21	**-0.42**
4.37	-0.65	-2.84	**-3.68**
0.84	-0.45	-0.38	**-0.76**
2.78	-1.14	-3.16	**-4.16**
0.44	-0.39	-0.17	**0.00**
0.57	-0.57	-0.32	**-0.70**
0.99	-0.59	-0.58	**-1.10**
1.13	-0.59	-0.67	**-1.20**
0.31	-0.34	-0.10	**0.00**
0.97	-0.80	-0.77	**-1.46**
2.22	-0.55	-1.22	**-1.62**
0.31	-0.44	-0.13	**0.00**
2.19	-0.70	-1.52	**-2.05**
0.64	-0.45	-0.29	**-0.61**
2.24	-0.35	-0.78	**-1.03**
0.63	-0.37	-0.23	**-0.50**
0.98	-0.41	-0.40	**-0.75**
8.69	-0.85	-7.42	**-9.13**

3D Area (m^2)	**Mean depth (m)**	**Volume (m^3)**	**Adjusted volume (m^3)**
2.71	-0.63	-1.70	**-2.24**
0.60	-0.53	-0.32	**-0.69**
1.14	-0.32	-0.37	**-0.66**

1.50	-0.55	-0.82	**-1.32**
0.47	-0.50	-0.23	**0.00**
0.25	-0.67	-0.17	**0.00**
0.15	-0.46	-0.07	**0.00**
0.18	-0.52	-0.09	**0.00**
2.82	-1.52	-4.28	**-5.63**
1.79	-1.19	-2.13	**-3.17**
1.67	-1.08	-1.81	**-2.78**
0.35	-0.46	-0.16	**0.00**
0.45	-0.45	-0.20	**0.00**
0.50	-0.34	-0.17	**-0.38**
0.23	-0.30	-0.07	**0.00**
1.84	-1.14	-2.10	**-3.08**

3D Area (m^2)	Mean depth (m)	Volume (m^3)	Adjusted Volume (m^3)
0.47	-0.47	-0.22	**0.00**
2.55	-0.57	-1.46	**-1.92**
0.27	-0.53	-0.14	**0.00**
2.13	-1.28	-2.71	**-3.70**
0.37	-0.25	-0.09	**0.00**
0.46	-0.55	-0.25	**0.00**
0.71	-0.28	-0.20	**-0.42**

1.81	-0.60	-1.09	**-1.61**
0.22	-0.36	-0.08	**0.00**
3.00	-0.51	-1.53	**-2.01**
0.72	-0.46	-0.33	**-0.69**
0.53	-0.55	-0.29	**-0.65**
0.73	-0.31	-0.23	**-0.47**
2.21	-0.33	-0.74	**-0.98**
0.98	-0.65	-0.64	**-1.20**
0.19	-0.38	-0.07	**0.00**
0.18	-0.47	-0.08	**0.00**
0.18	-0.48	-0.09	**0.00**
0.53	-0.43	-0.23	**-0.51**
0.19	-0.36	-0.07	**0.00**
0.20	-0.53	-0.11	**0.00**
0.08	-0.34	-0.03	**0.00**
0.32	-0.60	-0.19	**0.00**
1.13	-0.47	-0.53	**-0.95**
0.32	-0.38	-0.12	**0.00**
1.75	-0.52	-0.92	**-1.37**
0.21	-0.37	-0.08	**0.00**
1.55	-1.22	-1.89	**-3.00**
0.71	-0.55	-0.39	**-0.81**
0.59	-0.45	-0.27	**-0.58**
0.85	-0.83	-0.71	**-1.39**

0.14	-0.52	-0.07	**0.00**
0.11	-0.46	-0.05	**0.00**
0.23	-0.49	-0.11	**0.00**
0.15	-0.34	-0.05	**0.00**
0.46	-1.86	-0.85	**0.00**
0.49	-0.92	-0.45	**0.00**
0.69	-0.69	-0.48	**-1.00**
0.11	-0.39	-0.04	**0.00**
0.90	-0.65	-0.58	**-1.12**

3D Area (m^2)	**Mean depth (m)**	**Volume (m^3)**	**Adjusted Volume (m^3)**
0.22	-0.36	-0.08	**0.00**
1.09	-0.52	-0.56	**-1.03**
1.02	-1.55	-1.57	**-2.93**
0.78	-0.37	-0.29	**-0.59**
0.16	-0.37	-0.06	**0.00**
0.40	-0.65	-0.26	**0.00**
0.09	-0.71	-0.06	**0.00**
0.25	-0.48	-0.12	**0.00**
0.35	-0.38	-0.13	**0.00**
0.54	-0.42	-0.23	**-0.50**
0.17	-0.44	-0.08	**0.00**
0.19	0.00	0.00	**0.00**
0.13	-1.82	-0.24	**0.00**

0.30	-0.36	-0.11	**0.00**
0.79	-0.54	-0.43	**-0.86**
0.54	-0.82	-0.44	**-0.98**
0.40	-0.50	-0.20	**0.00**
1.13	-0.71	-0.80	**-1.45**
0.14	-0.42	-0.06	**0.00**
0.31	-0.61	-0.19	**0.00**
0.36	-0.91	-0.33	**0.00**
0.42	-0.60	-0.25	**0.00**
0.41	-1.02	-0.42	**0.00**
0.28	-0.44	-0.12	**0.00**
1.20	-0.36	-0.43	**-0.76**
0.51	-0.75	-0.38	**-0.85**
0.24	-1.72	-0.41	**0.00**
0.10	-0.73	-0.07	**0.00**
0.31	-0.79	-0.25	**0.00**
0.19	-1.05	-0.20	**0.00**
0.19	-0.27	-0.05	**0.00**
0.07	-0.59	-0.04	**0.00**
0.90	-0.50	-0.46	**-0.88**
0.44	-1.10	-0.48	**0.00**
0.44	-0.37	-0.16	**0.00**
0.29	-0.98	-0.28	**0.00**
0.41	-0.36	-0.15	**0.00**

0.20	-0.55	-0.11	**0.00**
0.30	-0.53	-0.16	**0.00**
0.15	-0.54	-0.08	**0.00**
0.45	-0.46	-0.20	**0.00**
0.17	0.00	0.00	**0.00**
0.16	-0.68	-0.11	**0.00**

3D Area (m^2)	**Mean depth (m)**	**Volume (m^3)**	**Adjusted Volume (m^3)**
0.07	-0.65	-0.04	**0.00**
0.27	-0.66	-0.18	**0.00**
0.21	-1.39	-0.29	**0.00**
0.27	-0.82	-0.22	**0.00**
0.15	-1.22	-0.19	**0.00**
0.12	-0.36	-0.04	**0.00**
0.10	-0.69	-0.07	**0.00**
0.52	-0.43	-0.22	**-0.50**
0.17	-2.02	-0.35	**0.00**
0.07	-1.17	-0.08	**0.00**
1.83	-0.36	-0.67	**-0.98**
0.11	-0.64	-0.07	**0.00**
0.11	-1.18	-0.13	**0.00**
0.13	0.00	0.00	**0.00**
0.26	-0.30	-0.08	**0.00**
0.05	0.00	0.00	**0.00**

0.052712	-0.414625	-0.021856	**0**

Table 0.2 - RabT year 2 loss values (m^3)

3D Area (m^2)	Mean depth (m)	Volume (m^3)	Adjusted Volume (m^3)
35.17	-0.74	-25.91	**-25.91**
13.52	-0.59	-7.93	**-9.27**
15.04	-0.43	-6.49	**-7.47**
8.31	-0.58	-4.85	**-5.99**
6.68	-0.72	-4.83	**-6.08**
6.78	-0.60	-4.05	**-5.09**
9.21	-0.41	-3.76	**-4.60**
5.95	-0.57	-3.41	**-4.33**
5.67	-0.47	-2.68	**-3.41**
6.14	-0.42	-2.56	**-3.25**
4.04	-0.62	-2.50	**-3.24**
1.59	-0.80	-1.28	**-2.00**
1.56	-0.63	-0.98	**-1.55**
2.84	-0.34	-0.98	**-1.29**
1.37	-0.57	-0.79	**-1.31**
1.70	-0.41	-0.70	**-1.06**
0.66	-0.99	-0.65	**-1.38**

0.24	-2.52	-0.61	**0.00**
0.25	-2.27	-0.56	**0.00**
1.47	-0.34	-0.51	**-0.82**
0.72	-0.70	-0.51	**-1.04**
0.76	-0.61	-0.47	**-0.95**

3D Area (m^2)	Mean depth (m)	Volume (m^3)	Adjusted Volume (m^3)
0.21	-1.93	-0.41	**0.00**
0.72	-0.54	-0.39	**-0.80**
1.17	-0.32	-0.38	**-0.67**
0.87	-0.42	-0.36	**-0.71**
1.06	-0.33	-0.35	**-0.65**
0.61	-0.55	-0.34	**-0.73**
0.51	-0.58	-0.29	**-0.66**
0.18	-1.63	-0.29	**0.00**
0.71	-0.39	-0.28	**-0.58**
0.57	-0.46	-0.27	**-0.58**
0.46	-0.50	-0.23	**0.00**
0.62	-0.32	-0.20	**-0.43**
0.59	-0.32	-0.19	**-0.41**
0.36	-0.45	-0.16	**0.00**
0.42	-0.33	-0.14	**0.00**

0.25	-0.39	-0.10	**0.00**
0.26	-0.34	-0.09	**0.00**
0.16	-0.36	-0.06	**0.00**
0.13	-0.36	-0.05	**0.00**
0.12	-0.29	-0.04	**0.00**
0.06	-0.56	-0.03	**0.00**